

REPORT DOCUMENTATION PAGE				Form Approved OMB NO. 0704-0188	
<p>The public reporting burden for this collection of information is estimated to average 1 hour per response, including the time for reviewing instructions, searching existing data sources, gathering and maintaining the data needed, and completing and reviewing the collection of information. Send comments regarding this burden estimate or any other aspect of this collection of information, including suggestions for reducing this burden, to Washington Headquarters Services, Directorate for Information Operations and Reports, 1215 Jefferson Davis Highway, Suite 1204, Arlington VA, 22202-4302. Respondents should be aware that notwithstanding any other provision of law, no person shall be subject to any penalty for failing to comply with a collection of information if it does not display a currently valid OMB control number.</p> <p>PLEASE DO NOT RETURN YOUR FORM TO THE ABOVE ADDRESS.</p>					
1 REPORT DATE (DD MM YYYY) 08-12-2010		2 REPORT TYPE Final Report		3. DATES COVERED (From - To) 1-Aug-2009 31 Jul 2010	
4. TITLE AND SUBTITLE Scalable Multiplexed Ion Traps-Phase II				5a. CONTRACT NUMBER W911NF 08 1 0315	
				5b. GRANT NUMBER	
				5c. PROGRAM ELEMENT NUMBER 411359	
6. AUTHORS RE Slusher, J. Kim, AW Harter, J. Amini, D. Denison, D. Faircloth, H. Hayden, T. Killian A. Ozakin, F. Shaikh, C. Shappert, and C. Volin				5d. PROJECT NUMBER	
				5e. TASK NUMBER	
				5f. WORK UNIT NUMBER	
7. PERFORMING ORGANIZATION NAMES AND ADDRESSES Georgia Tech Applied Research Corporation Office of Sponsored Programs 505 Tenth St , NW Atlanta, GA 30332 -0001				8. PERFORMING ORGANIZATION REPORT NUMBER	
9. SPONSORING/MONITORING AGENCY NAME(S) AND ADDRESS(ES) U.S. Army Research Office P.O. Box 12211 Research Triangle Park, NC 27709-2211				10. SPONSOR/MONITOR'S ACRONYM(S) ARO	
				11. SPONSOR/MONITOR'S REPORT NUMBER(S) 54145-PH-QC.1	
12. DISTRIBUTION AVAILABILITY STATEMENT Approved for Public Release; Distribution Unlimited					
13. SUPPLEMENTARY NOTES The views, opinions and/or findings contained in this report are those of the author(s) and should not be construed as an official Department of the Army position, policy or decision, unless so designated by other documentation.					
14. ABSTRACT The Scalable Multiplexed Ion Trap II (SMIT II) program based at Georgia Tech Research Institute (GTRI) was funded by IARPA during the period from August 2008 through July 2010. The overall goal was to design, fabricate and test surface ion traps through a closely correlated, multi-disciplinary approach involving design, simulation, fabrication and test facilities at GTRI and the Nanotechnology Research Center (NRC) at Georgia Tech. During the SMIT II program, surface ion traps were produced by microfabrication with properties that match the behavior					
15. SUBJECT TERMS ion trap scalable multiplexed microfabricated quantum information					
16. SECURITY CLASSIFICATION OF:			17. LIMITATION OF ABSTRACT UU	15. NUMBER OF PAGES	19a. NAME OF RESPONSIBLE PERSON Richard Slusher
a. REPORT UU	b. ABSTRACT UU	c. THIS PAGE UU			19b. TELEPHONE NUMBER 404-407-6994

## Report Title

### ABSTRACT

The Scalable Multiplexed Ion Trap II (SMIT II) program based at Georgia Tech Research Institute (GTRI) was funded by IARPA during the period from August 2008 through July 2010. The overall goal was to design, fabricate and test surface ion traps through a closely correlated, multi-disciplinary approach involving design, simulation, fabrication and test facilities at GTRI and the Nanotechnology Research Center (NRC) at Georgia Tech. During the SMIT II program, surface ion traps were produced by microfabrication with properties that match the behavior predicted by simulations and are both reproducible and reliable. The trap designs include straight sections that can contain ion chains up to 20 to 50 ions in length using anharmonic electrostatic potentials as well as trap junctions in the form of a 90° cross. Important advances have also been made in integrating optics into the surface trap architecture. Repeated transport over hundreds of microns was demonstrated with no ion loss, facilitated by the optimized software estimates of the required voltages and very accurate control on the microfabricated electrode dimensions. Ion motional frequencies are in good agreement with the simulations. In summary, excellent progress has been made in producing scalable, reliable, reproducible surface ion traps during the SMIT II program.

---

### List of papers submitted or published that acknowledge ARO support during this reporting period. List the papers, including journal references, in the following categories:

#### (a) Papers published in peer-reviewed journals (N/A for none)

1. R. Noek, C. Knoernschild, J. Migacz, T. Kim, P. Maunz, T. Merrill, H. Hayden, C. S. Pai and J. Kim, Multi-scale optics for enhanced light collection from a point source, Optics Letters 35, 2460 (2010).
2. T. H. Kim, P. F. Herskind, T. Kim, J. Kim and I. L. Chuang, A surface electrode point Paul trap, Physical Review A 82, 043412 (2010).

Number of Papers published in peer-reviewed journals: 2.00

---

#### (b) Papers published in non-peer-reviewed journals or in conference proceedings (N/A for none)

Number of Papers published in non peer-reviewed journals: 0.00

---

#### (c) Presentations

1. J. Kim, C. Knoernschild, C. Kim, J. Migacz, R. Noek, K. McKay, and F. Lu, “Optical MEMS technology for scalable quantum information processor”, Invited Talk at Frontiers in Optics, Rochester, NY, October 2008.

2. J. Kim, R. E. Slusher, C. Knoernschild, C. S. Pai, C. Kim and F. Lu, “Microsystems approach to quantum information processing in trapped ions”, Open Poster Session, Solid State Sensors, Actuators and Microsystems Workshop, Hilton Head Island, SC, June, 2008.

3. Richart Slusher, Arkadas Ozakin, Fayaz Shaikh, Douglas Denison, Daniel Faircloth, David Landgren, and Janus Wesenberg, “Geometric Compensation for Planar Ion Traps”, 2nd Workshop on Integrated Atomic Systems, Seattle, WA, February 2009.

4. T. Kim, C. Knoernschild, J. Migacz, R. Noek, M. Silver and J. Kim, “Integrated optics approach to quantum information processing in trapped ions”, Poster Presentation at 2nd Integrated Atomic Systems Workshop, Seattle, WA, February 2009.

5. T. Kim, J. Migacz, R. Noek, C. Knoernschild, M. Silver and J. Kim, “Integrated optics approach towards ion trap quantum computation”, Poster Presentation at APS DAMOP Meeting, Charlottesville, VA, May, 2009.

6. Daniel L. Faircloth, David W. Landgren, Eric J. Kuster, Douglar R. Denison, James G. Maloney, Richard T. Lee, “Implementation and Issues Concerning Higher-Order Moment Method Simulations on CUDA-Enabled GPUs”, Poster Presentation at nVidia GPU Technology Conference, San Jose, CA, October 2009.

7. R. Noek, J. Migacz, C. Knoernschild, T. Kim, and J. Kim, “Enhanced light collection from a point fluorescent source using multiscale optics”, Contributed Talk at Frontiers in Optics, San Jose, CA, October 2009.

8. Fayaz Shaikh, Charlie Doret, Jason Amini, Arkadas Ozakin, Curtis Volin, Douglas Denison, Daniel Faircloth, David Landgren, C.S. Pai, Harley Hayden, Demetris Geddis, Kevin Martin, Alexa Harter, and Richart Slusher, “GTRI Microfabricated Ion Trap Program”, Poster Presentation at SQuInt, Santa Fe, NM, February 2010.

9. T. Kim, P. Maunz, R. Noek, C. Knoernschild, E. Mount, and J. Kim, “Integration of ion trap and optical cavity towards efficient entanglement generation between remote ions”, Poster Presentation at APS DAMOP Meeting, Houston, TX, May 2010.

10. Arkadas Ozakin, Fayaz Shaikh, Daniel Faircloth, Curtis Volin, Jason Amini, Charlie Doret, Douglas Denison, David Landgren, Demetris Geddis, C.S. Pai, Harley Hayden, Alexa Harter, and Richart Slusher, “Ion Stability in Asymmetric Surface Electrode Ion Traps”, Poster Presentation at APS DAMOP Meeting, Houston, TX, May 2010.

11. Fayaz Shaikh, Charlie Doret, Jason Amini, Arkadas Ozakin, Curtis Volin, Douglas Denison, Daniel Faircloth, David Landgren, C.S. Pai, Harley Hayden, Demetris Geddis, Kevin Martin, Alexa Harter, and Richart Slusher, “GTRI Microfabricated Ion Trap Program”, Poster Presentation at APS DAMOP Meeting, Houston, TX, May 2010.

12. R. Noek, C. Knoernschild, J. Migacz, T. Kim, P. Maunz, J. Kim, T. Merrill, H. Hayden and C. S. Pai, “Enhanced light collection from a point source using a micro-mirror for application in trapped ion quantum information processing”, Contributed Talk at APS DAMOP Meeting, Houston, TX May 2010.

13. J. Kim, “Modular Universal Scalable Ion-Trap Quantum Computer (MUSIQ): Engineering a quantum computer”, Invited Talk at the Summer Meeting of the Optical Society of Korea, Busan, Korea, July 2010.]

14. J. Kim, P. Maunz, T. Kim, J. Hussman, R. Noek, A. Mehta, and C. Monroe, “Modular Universal Scalable Ion-Trap Quantum Computer (MUSIQ)”, Contributed Talk at Quantum Communication, Measurement and Computation (QCMC), Brisbane, Australia, July 2010.

Number of Presentations: 14.00

---

Non Peer-Reviewed Conference Proceeding publications (other than abstracts):

Number of Non Peer-Reviewed Conference Proceeding publications (other than abstracts): 0

---

Peer-Reviewed Conference Proceeding publications (other than abstracts):

(d) Manuscripts

Number of Manuscripts:0.00

Patents Submitted

Patents Awarded

Awards

Graduate Students

<u>NAME</u>	<u>PERCENT SUPPORTED</u>
Grahame Vittorini	0.21
Fayaz Shaikh	0.50
<b>FTE Equivalent:</b>	<b>0.71</b>
<b>Total Number:</b>	<b>2</b>

Names of Post Doctorates

<u>NAME</u>	<u>PERCENT SUPPORTED</u>
Harley Hayden	1.00
<b>FTE Equivalent:</b>	<b>1.00</b>
<b>Total Number:</b>	<b>1</b>

Names of Faculty Supported

<u>NAME</u>	<u>PERCENT SUPPORTED</u>	National Academy Member
Jason Amini	0.74	No
Daniel Faircloth	0.06	No
Sean Garrison	0.27	No
Alexa Harter	0.13	No
Harley Hayden	0.82	No
Tyler Killian	0.20	No
David Landgren	0.05	No
Arkadas Ozakin	0.44	No
Chris Shappert	0.14	No
Richart Slusher	0.18	No
Curtis Volin	0.28	No
Kenneth Wright	0.81	No
Douglas Denison	0.03	No
Kevin Martin	0.20	No
<b>FTE Equivalent:</b>	<b>4.35</b>	
<b>Total Number:</b>	<b>14</b>	

---

### Names of Under Graduate students supported

NAME

PERCENT SUPPORTED

**FTE Equivalent:**

**Total Number:**

#### Student Metrics

This section only applies to graduating undergraduates supported by this agreement in this reporting period

The number of undergraduates funded by this agreement who graduated during this period: ..... 0.00

The number of undergraduates funded by this agreement who graduated during this period with a degree in  
science, mathematics, engineering, or technology fields:..... 0.00

The number of undergraduates funded by your agreement who graduated during this period and will continue  
to pursue a graduate or Ph.D. degree in science, mathematics, engineering, or technology fields:..... 0.00

Number of graduating undergraduates who achieved a 3.5 GPA to 4.0 (4.0 max scale):..... 0.00

Number of graduating undergraduates funded by a DoD funded Center of Excellence grant for  
Education, Research and Engineering:..... 0.00

The number of undergraduates funded by your agreement who graduated during this period and intend to  
work for the Department of Defense ..... 0.00

The number of undergraduates funded by your agreement who graduated during this period and will receive  
scholarships or fellowships for further studies in science, mathematics, engineering or technology fields: ..... 0.00

---

### Names of Personnel receiving masters degrees

NAME

Erin Elizabeth Walters

**Total Number:**

1

---

### Names of personnel receiving PHDs

NAME

**Total Number:**

---

### Names of other research staff

NAME

PERCENT SUPPORTED

**FTE Equivalent:**

**Total Number:**

---

### Sub Contractors (DD882)

**Inventions (DD882)**

**Scientific Progress**

See Attachment

**Technology Transfer**

Final Report  
Scalable Multiplexed Ion Trap (SMIT) Program, Phase II

Richart Slusher, Jungsang Kim, and Alexa Harter  
with  
J. Amini, D. Denison, D. Faircloth, H. Hayden, T. Killian  
A. Ozakin, F. Shaikh, C. Shappert, and C. Volin

Signature Technology Laboratory  
Georgia Tech Research Institute  
Atlanta, GA 30332

Project Number: D5802  
Contract Number: W911NF081-0315

December 8, 2010

# Chapter 1

## Introduction

The overall objective of the Scalable Multiplexed Ion Trap (SMIT) program was to design, fabricate and test reliable, scalable surface ion traps that could be used for a variety of applications in quantum information processing. The first phase of the SMIT project was conducted at Bell Laboratories and resulted in a series of silicon fabricated planar ion traps that operated successfully at both room and cryogenic temperatures. The goals of the second phase (SMIT II) were to (1) improve trap reliability, performance and complexity, (2) characterize the trap behavior in detail, and (3) integrate optical elements with the trap. SMIT II was funded by IARPA during the period from August 2008 to July 2010 and work was performed at the Georgia Tech Research Institute (GTRI), the Georgia Tech Nanotechnology Research Center (NRC), and Duke University. Initial cryogenic trap testing was done at MIT in Prof. Isaac Chuang's laboratory.

Under the SMIT II program, the GTRI Quantum Information Systems (QIS) Group developed a comprehensive, tightly-coupled modeling, design, fabrication, and testing capability that allowed us to develop, demonstrate, and deliver novel ion traps that met the primary program objectives. Traps were designed and simulated using advanced in-house electromagnetic modeling codes. These codes were adapted from existing GTRI codes and expanded under the SMIT II program to simulate complex planar trap geometries in reasonable execution times. These codes enabled us to add new complex features to the traps in order to improve trap performance, derive reliable operational parameters, and verify our results numerically before initiating fabrication. Traps were fabricated using scalable silicon VLSI technology based at the Georgia Tech NRC by GTRI and Georgia Tech personnel. Processes were developed under the SMIT II program to fabricate advanced trap features. Traps were tested in GTRI's QIS ion trapping and testing laboratory in order to provide feedback for the design and fabrication teams, verify calculated trapping voltages, and characterize individual traps. The laboratory was built and equipped during the beginning of the SMIT II program<sup>1</sup> and most of the testing and characterization techniques were developed using SMIT II traps.

---

<sup>1</sup>The laboratory was built and equipped using GTRI internal funds, while the testing and characterization techniques were developed using SMIT traps under the SMIT program.



## 1.1 SMIT II goals

Trap **reliability**, **predictability**, and **repeatability** were significantly improved under the SMIT II program. For all traps tested (three first generation linear traps, one second generation linear trap, and one cross junction trap), the trapping parameters remained consistent during testing and showed excellent agreement with simulated values. All traps loaded using the calculated potentials without any modification, and the measured secular frequencies agreed to within 1-10% of the simulated values. A trap tested at GTRI was taken to Prof. Isaac Chuang’s laboratory at MIT and was trapping at cryogenic temperatures within one week using the same trapping voltages calculated and measured at GTRI. Thus far the traps have remained robust in storage, transportation, and testing over periods of many months.

The measured **trap performance** of the SMIT II traps was also improved significantly over the traps produced in the first phase of the program. Ion lifetimes in the dark exceeded a minute; lifetime with cooling was several hours and was possibly limited by frequency drift in the cooling laser. This compares to cooled ion lifetimes measured in the SMIT I traps of 90-300 seconds [1] and of several minutes in the NIST racetrack. While the SMIT II lifetimes are still far shorter than those measured in macroscopic 4-rod traps (or in the anomalous single-zone NIST surface trap; aka the Signe trap), it is far longer than the time required for current QIS experiments. And, as will be discussed in Chapter 4, the ion loss profiles in the SMIT II traps do not follow an exponential single-collision model, which means that expectation of ion loss is extremely low during the time period required to conduct an experiment. We had not developed the capability to take ion heating rate measurements by the end of the SMIT II program, so the heating rate of the SMIT II traps have not been comprehensively tested. The heating rate of a single trap was measured at cryogenic temperatures in Prof. Chuang’s laboratory and, when normalized for ion mass and trap size, was found to be competitive with the lowest measured trap heating rates.

Under SMIT II, we improved the functional **complexity** of surface traps, while simultaneously increasing the **simplicity** of basic trap designs. Four traps were designed and fabricated under the program: two generations of linear traps (the Gen I and Gen II traps), a symmetric cross junction trap, and a trap with an integrated micromirror. The symmetric cross and the mirror trap had a number of complex design features. Both traps shaped the electrodes in transition regions using a genetic algorithm in order to minimize excursions of the pseudopotential and prevent ion perturbations and heating during transport. The mirror trap required an integrated design approach in order to maximize the collection efficiency of the mirror while maintaining the ion height, secular frequency, and other trap properties. This was achieved by carefully selecting the diameter of the mirror and then altering the spacing and width of the RF rails along the trap axis.

A number of complex design features were developed during SMIT II, including:

1. Multi-level electrode addressing using vias between metal electrodes separated by thick oxide layers (Figure 1.1a). Vias provide electrical access to island electrodes. They allow trap designs to include features like segmented DC center electrodes, and are a critical component to scaling up to flexible two dimensional ion trap architectures. The ability to have regions of the trap that are not directly accessible from the chip edge is one of the things that distinguishes surface traps from other trap geometries

like two-layer wafer traps [2], [3], or three-layer traps [4].

2. Recessed wire bonds (Figure 1.1c). This feature increases optical access for lasers across the trap.
3. Through-wafer angled slots (Figure 1.1b). Through-wafer slots with sloped walls permit laser access over a wider range of angles while avoiding scatter off the edges of the trap slot.
4. Shaped loading slots (Figure 1.1d). The Gen II linear trap had a shaped loading slot to minimize potential barriers near the slot and facilitate ion loading.
5. Shaped electrodes designed using a genetic algorithm.
6. Integrated micromirror.

The Gen II linear trap (as well as the linear sections of the mirror and the cross) had a number of new features developed under SMIT II that simplified design and fabrication while maintaining – or even enhancing – functionality. These features include:

1. Top layer ground (Figure 1.1d). Previous to SMIT II, it was commonly believed that in order to have well-defined DC electrodes that did not have exposed leads, that it would be necessary to have a via on each electrode so that the leads could be defined on lower levels of metallization. Instead, we added a top ground layer that covers all metal except for the designed DC electrode geometries. This top layer ensures that the trapping potential will be close to what is calculated and will not be altered by unwanted fields originating from the leads. The top layer has the added benefit of protecting 95% of the trap surface from scratches.
2. Trap symmetries. At the beginning of SMIT II, it was believed that RF rail widths had to have a large asymmetry to facilitate axis rotation to allow for ion cooling across the trap surface. Optimization techniques developed under this program, along with the addition of a DC control rail added parallel to the RF rails, enabled the later generations of SMIT II traps to be designed with symmetric RF rails while still allowing for near-arbitrary axis rotation. This symmetric design has many advantages, particularly when making junctions and traps with integrated components.

One of the primary goals of SMIT II, as reflected in the program name, was to develop ion traps that were, in some sense, **scalable**. While there are myriad definitions of scalability, it is easy to argue that the traps developed under SMIT II advanced the potential scalability of ion trap quantum computing. The critical elements of a flexible, scalable, ion trap architecture must include (1) linear sections, (2) a junction, (3) vias to allow for island electrodes, and (4) the capability to make a trap that performs consistently and predictably. While we have not tested our junction<sup>2</sup>, all of the other requirements were validated under the SMIT II program.

---

<sup>2</sup>At the time this document was being written, the symmetric cross was under testing. Calculated waveforms, with no modification, had taken the ion from the loading slot to within 19  $\mu\text{m}$  of the junction.

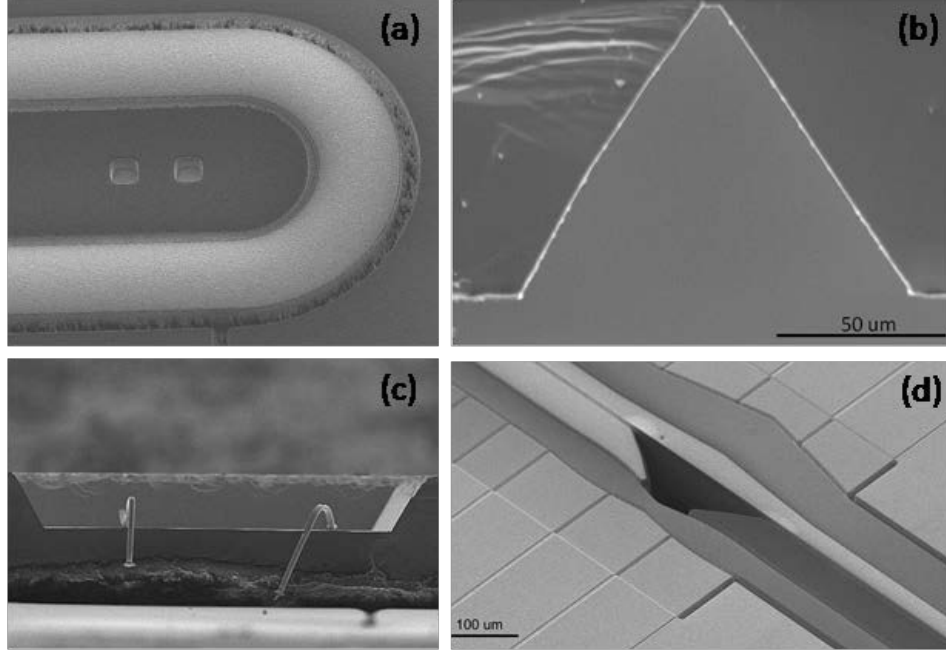


Figure 1.1: Some of the novel features developed under SMIT II. (a) Multi-level vias. (b) An angled through-wafer slot. (c) Recessed wire-bonds. (d) The shaped loading slot and the top level ground.

The traps designed under SMIT II are capable of trapping 1-50 ions. While we did not trap more than five ions at any one time during the SMIT II program, we have designed waveforms that are capable of trapping up to 20 equally spaced ions in the Gen II trap. The mirror trap and the symmetric cross have more electrodes and can trap at least that many ions. However, what makes these traps scalable is that together they make the modular building blocks for a flexible architecture of arbitrary size.

Excellent progress has been made during the SMIT II program on **integrating optics** especially designed for the surface traps. The time required for quantum information processing using ion qubits is often limited by the ion state measurement process that utilizes fluorescent emission from the electronic ion states. Increasing the optics collection efficiency for this fluorescent measurement process is crucial for minimizing quantum information processing times. An optical system was designed for SMIT II that utilizes the notion of multi-scale optics for efficient and scalable detection of ion qubit states. The overall system consists of a conventional imaging system constructed by off-the-shelf optical components and a micromirror located very close to the ion. A large fraction of photons emitted by the ion (point source) located at the focal point of the micromirror is “collimated” by the micromirror and delivered to the detector. The micromirror is fabricated in the silicon substrate and integrated with the ion trap. Using this multi-scale optics scheme, a five-fold collection efficiency increase was demonstrated compared to external lens collection systems used at present. Surface traps have the advantage that the micromirrors can be integrated, enabling scalable qubit detection. Another important advantage of the multi-scale optics

system is a very large improvement in the field of view. At present, large diameter lenses are used to collect the fluorescent light for ion state measurement. The field of view of such a high NA lens is only  $\sim 100 \mu\text{m}$ . The large lens diameter prevents using many lenses to image the ions at various positions. As a result using the large lens collection technique an ion trap architecture using many ions requires that ions be shuttled to remote locations for measurement. Using the multi-scale optics approach, micromirrors can be fabricated into the trap at prescribed locations and a single lens used to collect the fluorescence from all locations. This approach increases the effective field of view by two orders of magnitude to approximately 1 cm and makes it possible to make quantum state measurements on 1000 ions at prescribed positions with a single lens.

A goal for the SMIT II program was to construct a high quality micro-cavity using a small positionable mirror and a second mirror formed by a high reflection coating on a highly polished optical fiber tip. Using micro-cavities designed during the SMIT II program, improvements in coupling efficiency by as much a factor of 50 have evolved. This increased coupling efficiency should result in an increase in remote ion entangling rate by as much as 2500, enough to make the remote entanglement process very interesting for applications. The coupling cavity can be integrated into a surface ion trap. Although this goal has not been entirely accomplished, there has been good progress in understanding the required cavity parameters. An initial design and fabrication process for an integrated ion trap on an optical fiber tip is now being implemented.

## 1.2 Capabilities developed under the SMIT II program

A number of capabilities were developed at GTRI under the SMIT II program in the design, fabrication, and testing of planar ion traps. A number of the techniques are new to the ion trapping community and are unique to GTRI.

### 1.2.1 Design

A number of important innovative advances in trap simulation were made at GTRI during the SMIT II program. Highlights of these advances include:

1. A Method-of-Moments (MoM) solver for the static charges on electrodes due to applied voltages and a post-processor that finds the corresponding electric fields and potentials above the trap. This code forms the foundation of trap modeling at GTRI and its capabilities far exceed that of commercial codes commonly used in the community (such as CPO).
2. Acceleration of the MoM code by a factor of 50 - 500 (depending on the basis function) through execution on graphical processing units (GPU).
3. Addition of the adaptive cross approximation (ACA) to the MoM solver. This improvement makes intractable problems tractable.

4. Implementation of a genetic-algorithm-based RF electrode shape optimizer that tailors RF electrode geometry in the region of complex features (junction, loading slots, integrated mirrors) to maintain the pseudopotential well and reduce heating.
5. Refinement of a particle motion solver to include a more general time-dependence of control waveforms and the ability to artificially cool the ion. These new capabilities were used to both design waveforms and to validate waveform designs derived from properties of the electric fields in the trap.
6. Development of automated waveform design for ion shuttling using particle swarm optimization (PSO) and field fitting approaches. For the PSO, the motion solver is used to evaluate candidate electrode voltages that place the ion along a prescribed trajectory.
7. Implementation of optimization routines to calculate voltages to trap single ions or groups of ions in specified locations, with specified secular frequencies and axis rotations. These optimization codes have been used to calculate the waveforms required to trap equally spaced ion chains with a spacing error of less than 5% and axis rotation variation of less than a few degrees.
8. Analysis of stability criterion for surface ion traps to determine optimal operational parameters.
9. Adoption of a uniform, highly-configurable, dense binary file format (HDF5) for communication between codes and development of routines for direct translation between simulation and mask fabrication geometry definition standards to eliminate translation errors.

The increased speed, capacity and flexibility of this suite of software is essential for studying a broad range of trap designs and parameters, especially for complex trap geometries like trap junctions.

### 1.2.2 Fabrication

Fabrication of advanced ion traps at Georgia Tech began with a transfer of existing process flows and material sets developed at Bell Labs for the SMIT I project to the NRC at Georgia Tech. Subsequent work focused on improving the quality and reliability of each process step, adding additional process modules to increase ion trap design flexibility, and producing multiple generations of ion trap chips for testing at GTRI and throughout the ion trapping community. Current ion trap fabrication capabilities at the Georgia Tech NRC include:

1. Uniform and repeatable multi-layer metal deposition using argon sputtering and electron beam evaporation.
2. Thick, low stress PECVD oxide layers compatible with room temperature and cryogenic testing
3. Low-stress LPCVD nitride.

4. Contact lithography for electrode, loading slot, via and recessed wire bonding pad patterning.
5. Reactive ion etching and inductively coupled plasma etching of metals and dielectrics.
6. High aspect ratio through-silicon etching for backside ion loading slots.
7. Angled backside loading slots for through wafer laser access.
8. Recessed bondpads for increased laser access across the ion trap surface.
9. Integrated micromirrors to enhance photon collection efficiency.
10. Packaging using wire Bonding and AuSn solder die attach compatible with UHV systems.
11. Complete device fabrication characterization utilizing the following equipment:
  - (a) Optical and physical profilometers
  - (b) Optical microscopes
  - (c) Scanning electron microscope
  - (d) Refractometer and ellipsometer for dielectric layer characterization
  - (e) Four-point probe for metal characterization
  - (f) Probe station for initial electrical tests of completed ion traps

### 1.2.3 Testing

At the beginning of the SMIT II program, GTRI built and equipped an on-site  $^{40}\text{Ca}^+$  trapping facility for testing and characterizing ion traps. This facility completes QIS's tight Design/Fabrication/Testing cycle. Our testing methodology includes semi-automated testing of trapping parameters and characteristics, which gives clean, complete data sets for each trap. The QIS trap testing facility's current capabilities include:

1. Photoionization loading of  $^{40}\text{Ca}^+$  ions.
2. Up to 96 DAC channels for ion transport in large traps.
3. Fine tuning transport waveforms.
4. Lifetime measurements with and without laser cooling.
5. Micromotion nulling characterization.
6. Mode frequency measurements.
7. Multiple vacuum systems for rapid trap turnaround.
8. In-house packaging and wire bonding.

A few of the capabilities that were partially developed by the end of SMIT II were:

1. 729 nm laser for resolved sideband cooling and qubit operations.
2. Heating rate measurements.
3. Sympathetic cooling studies.
4. Cryostat for trap characterization at  $<10\text{K}$ .

## 1.3 Facilities used for the SMIT program

### 1.3.1 Design and simulation

GTRI/STL maintains one of the largest, most powerful high performance computing (HPC) labs on the Georgia Tech campus. Currently, STL operates an HPC environment consisting of nine 64-bit Linux clusters and one heterogeneous opportunistic computing cluster. The clusters are organized in groups of 16-36 nodes built from Intel and AMD processors each having 2-24 GB of RAM. These clusters are used to support on-going efforts in ion trap design.

With the advent of general-purpose GPU computing and the CUDA C language extension, STL has procured two GPU clusters comprised of Tesla C1060 cards and the latest generation Fermi series cards. STL has converted several of our in-house codes to make use of this new technology resulting in speed-ups of 10-500X. Our latest generation cluster is made up of nodes containing dual Corei7 Xtreme processors with 24 GB of RAM and two NVIDIA Fermi GPU cards. This new capability allows our engineers and scientists to explore new ion trap designs and perform more rigorous assessments of trap performance in a dramatically reduced timeframe.

### 1.3.2 Fabrication

Ion trap fabrication takes place in the Georgia Tech Nanotechnology Research Center (NRC). The NRC occupies the 190,000 sq. ft Marcus Nanotechnology Building (MNB) and the 100,000 sq. ft Pettit Microelectronics Building (PMB). A complete set of micro- and nano-fabrication and characterization tools are available in the 15,000 sq. ft and 8,000 sq. ft cleanrooms in the MNB and PMB (respectively) and 2,400 sq. ft of optoelectronic and materials testing and metrology labs in the PMB. The NRC capabilities include optical, nanoimprint and electron beam lithography (with sub 10 nm resolution), thin film growth and deposition (metals, oxides, semiconductors), nano structure growth (SiGe and carbon nanotubes, graphene), etching (metals, oxides, semiconductors, polymers), plasma enhanced CVD (oxides and dielectrics), plasma assisted atomic layer deposition (metals, oxides), thermal processing (annealing, RTP) microscopy/imaging (optical, confocal, AFM, sub 1-nm resolution SEMs, dual beam FIB/SEMs, X-ray tomography), thin film characterization (ellipsometry, stress, tribology), materials characterization (XPS, EDX, confocal Raman,

FTIR, mass spec, QCM, XRF, XRD) and packaging (dicing, flip chip bonding, wirebonding). The NRC cleanroom and supporting labs are available to users from Georgia Tech and outside institutions (universities, federal labs and companies).

### 1.3.3 Testing

The QIS trap testing facility provides detailed characterization of trap properties. The core of the facility is a  $^{40}\text{Ca}^+$  trapping system with a flexible in-house developed FPGA based timing system and a 96-channel DAC source for ion transport in large traps. Semi-automated characterization processes provide complete and detailed trap information. A second trapping system will soon characterize traps at cryogenic temperatures. This facility also features rapid trap turnaround with multiple trapping chambers, a furnace for uniform chamber bakeout, trap mounting and wire bonding equipment, and chip and carrier level probes for testing of trap electrical connections.

## 1.4 Traps developed under the SMIT program

Surface ion traps were pioneered by the Wineland ion trapping group at NIST [5] with the vision that they would provide scalability to large numbers of trapped ions that can be shuttled over relatively long distances. Vias in the surface trap go to multi-level electrode layers and allow for flexible architectures, unlike multi-level traps that preclude layouts with enclosed electrodes. A number of trap configurations have been designed and fabricated by different research groups since the initial proposal of planar traps. These traps cover a wide range of materials, configurations, and size scales.

We set the dimensions of the traps designed at GTRI using two key parameters. First, laser beams used to cool and control the ion quantum state are beamed across the surface of the trap. This requires that the ion be at least high enough above the surface to avoid light scattering from the surface electrode roughness. Early experiments and simulations show that for a trap chip that is 1 cm across this requires that the ion height be  $> 50\ \mu\text{m}$  above the surface. The trap heights in the SMIT II program are typically 60 to  $70\ \mu\text{m}$ . Second, the ion motional heating rate is dominated by electric field fluctuations on the surface electrodes whose effect on ion heating varies approximately as the fourth power of the distance of the ion from the metal electrodes. In order to achieve heating times long enough for many quantum information tasks, this limiting heating process requires that the ion be higher than approximately  $40\ \mu\text{m}$  at room temperature and  $10\ \mu\text{m}$  at cryogenic temperatures.

Selection of an ion height places restrictions on the size and location of the RF electrodes. The optimum choice for RF rail width and spacing must balance the influences of pseudopotential well depth, which generally favors a wider rail; capacitance and RF dissipation, which generally favor a smaller rail; and through-chip optical access, which generally favors a wide spacing.



### 1.4.1 Evolution of linear trap designs

This section describes the decision-making process in the design of linear traps developed under the SMIT programs. The technical details supporting these decisions are described elsewhere in this report.

#### 1.4.1.1 SMIT I trap

The first phase of the SMIT project produced a series of silicon fabricated planar ion traps that operated successfully at both room and cryogenic temperatures. Figure 1.2 shows microscope images of the SMIT I trap that was successfully used to trap ions at several research groups. The optional  $700 \times 70 \mu\text{m}$  loading slot is not present in this trap.

This trap features symmetric,  $20 \mu\text{m}$  wide RF rails that step down to produce null heights of approximately 75, 61, 49, and  $37 \mu\text{m}$ . These steps were intended to allow testing of heating rates at different heights within the same trap, although this experiment was never performed. The Aluminum RF rails are very narrow and are placed on top of a  $10 \mu\text{m}$   $\text{SiO}_2$  pedestal in order to reduce capacitance to the RF ground (DC electrodes). Low capacitance was understood to reduce RF currents on the DC electrodes and to reduce dissipation on the RF electrodes.

The symmetric DC (control) electrodes are  $150 \mu\text{m}$  long (first three) or  $100 \mu\text{m}$  long (all others) and are terminated to leads at a distance approximately  $250 \mu\text{m}$  from the ion trapping location. DC electrodes were spaced by  $2 \mu\text{m}$  gaps.

It was found to be difficult to rotate the secular axes beyond  $10^\circ$  in the SMIT I trap without exceeding the 10V DC limit imposed by hardware. Much of this difficulty can be attributed to the limited tools available for electrostatic field simulation and waveform design under this program.

**Testing:** Multiple SMIT I traps were tested by a different ion trapping groups. Ion lifetimes with cooling were measured to be from  $56 \pm 6 \text{ s}$  to  $300 \pm 30 \text{ s}$  at room temperature, and  $4.5 \pm 1.1 \text{ hours}$  at 6 K. The motional heating rate for  $^{25}\text{Mg}^+$  at room temperature and a trap frequency of 1.6 MHz is measured to be  $7 \pm 3$  quanta per millisecond. For  $^{88}\text{Sr}^+$  at 6 K and 540 kHz the heating rate is measured to be  $220 \pm 30$  quanta per second.

#### 1.4.1.2 The first generation SMIT II trap

Several lessons learned from the SMIT I trap were applied to the design of the first generation (Gen I) SMIT II trap. The exposed oxide layers on the sides of the pedestal were postulated to contribute to the short observed ion lifetime, although no conclusive evidence exists. The raised pedestals also contributed substantially to light scatter in the vicinity of the ion, which would have ultimately limited the utility of these traps for QIP applications. Therefore, for the Gen I trap, the RF rail was brought into the same plane as the DC electrodes and the entire electrode plane was spaced above the ground by a  $10 \mu\text{m}$  thick oxide layer. A third metal layer (the capacitive control electrode) was placed under the DC electrodes in order to increase their capacitance, effectively shorting induced RF currents to ground at the electrode. In order to maximize this capacitance, the DC electrodes were extended as close as possible to the edge of the trap.

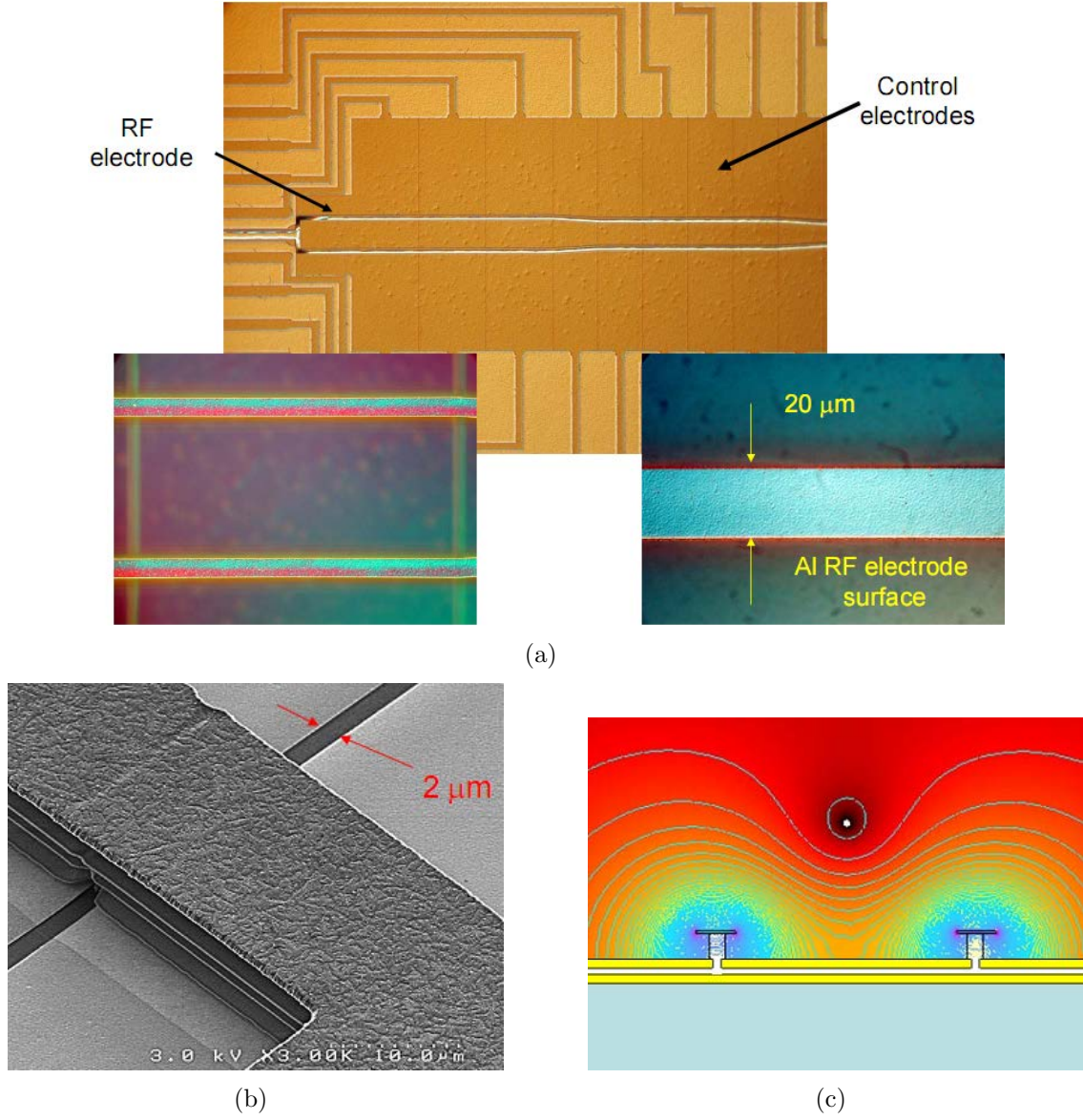


Figure 1.2: (a) Microscope images of the SMIT I trap distributed to testing groups. (b) SEM image of the raised RF rail. (c) diagram of the electrodes with illustration of the RF pseudopotential.

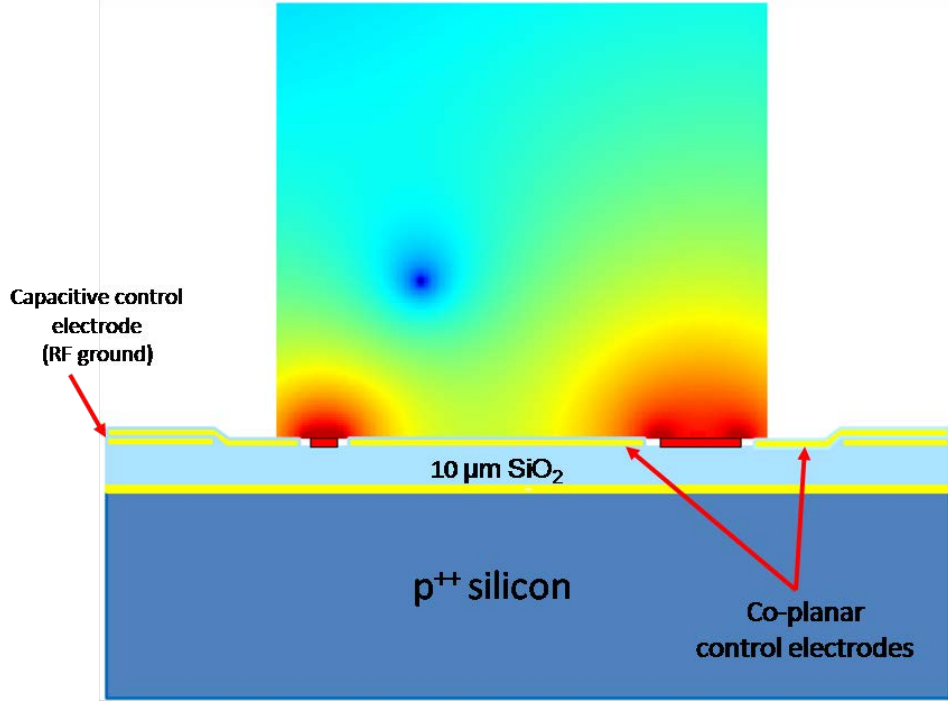


Figure 1.3: Diagram of the cross-section of the SMIT II, Gen I trap. The RF electrodes are red, control and ground electrodes are yellow.

The RF rails were made asymmetric in the Gen I trap in order to facilitate axis rotation. The rails are  $10\ \mu\text{m}$  and  $30\ \mu\text{m}$  wide, resulting in approximately  $30^\circ$  rotation of the RF field axes (while preserving the overall low capacitance of the RF rail). Because the RF field axes make no actual contribution to the secular axis rotation, the secular axis rotation realized in this trap is facilitated by the asymmetry of the DC electrodes with respect to the location of the ion position in the RF null (see Figure 4a). The use of substantially better modeling and design tools developed under SMIT II eliminated the difficulty in generating rotated secular axes in traps with symmetric RF rails.

The RF rails have only one step, from a nominal height of  $68\ \mu\text{m}$  in the wide section to  $50\ \mu\text{m}$  in the narrow section. Along the axial direction, DC electrodes are semi-infinite (first one),  $150\ \mu\text{m}$  long (next two) and  $80\ \mu\text{m}$  long (all others). Electrodes in the load zone were wider to create larger, deeper potential wells in order to facilitate loading. Gaps between DC electrodes are  $4\ \mu\text{m}$  near the trap center. The gaps are stepped out to  $10\ \mu\text{m}$  at a distance of several 100s of microns from the trap center in order to reduce the probability of shorts (this was a precautionary step since shorts were frequently observed in SMIT I traps, but were not conclusively attributed to gaps). The loading slot is  $310\ \mu\text{m}$  long and  $100\ \mu\text{m}$  wide.

One large (2mm square) ground pad was left open to the bottom ground in order to permit heat sinking of the chip in cryogenic experiments. Two other pads were left open to the capacitive control (M3) ground layer (under the control electrodes) as surfaces that could be used for a packaging tool; however, these were not used.

**Testing:** The bulk of the trap testing facility was developed with the GTRI SMIT

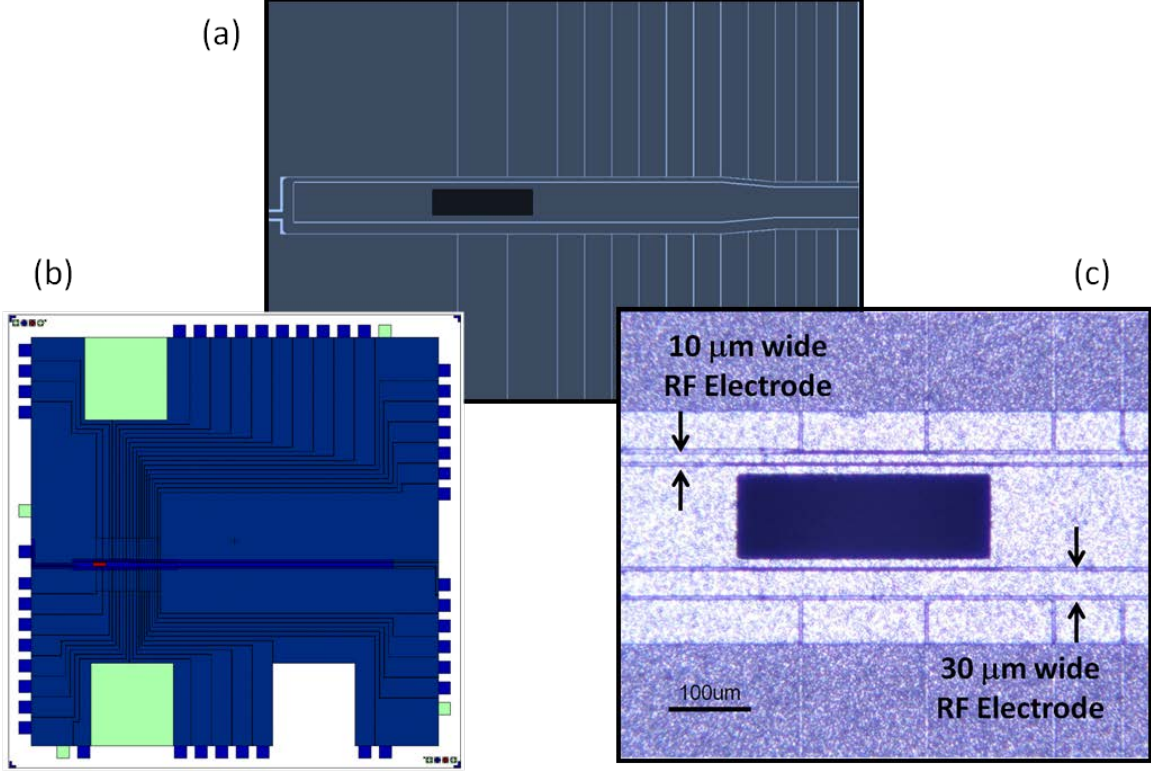


Figure 1.4: (a) CAD image of the trap surface. (b) CAD drawing of the control electrode plane. The open square is the ground pad on the bottom (Metal 1) layer for heat sinking and the green pads are grounds on the capacitive control (M3) layer. (c) Microscope image of the Gen I loading slot.

Gen I traps. Cryogenic testing at MIT was also performed on this generation of trap. Ions were loaded into three Gen I traps, although two of them had floating electrodes that prevented extensive testing. The floating electrodes were caused by wire bonds that broke during bakeout. This issue was resolved by acquiring our own wire bonding capability and developing improved processes. In the third trap, we demonstrated a thousand  $600\ \mu\text{m}$  transports from the load zone without loss or tweaking of trap potentials. Ion lifetimes in the dark exceeded a minute (the lifetime measurement is described later along with the results for this trap) and lifetime with cooling was several hours and possibly limited by frequency drift in the cooling laser. This trap was tested at cryogenic temperatures in Prof. Isaac Chuang's laboratory at MIT. Mode measurements (2 radial and 1 axial) matched calculations to within 2%. The heating rate was  $58 \pm 12$  quanta/s ( $68\ \mu\text{m}$  ion-trap distance, 0.8 MHz trap mode frequency), which is consistent with the best heating rates measured at cryogenic temperatures. No electrical shorts were observed in this trap.

#### 1.4.1.3 The second generation SMIT II trap

The Gen II trap design was completed prior to testing the Gen I trap. Therefore, design decisions for this trap were made based on improved analytical and numerical models of the

ion trapping system, as well as suggested revisions from the fabrication team. Substantial revisions included:

1. The RF rail width was increased to  $50\text{ }\mu\text{m}$ . The use of wider rails allows the experiment to use much lower RF amplitude and decreases fabrication error, since it is difficult to reliably fabricate a  $10\text{ }\mu\text{m}$  wide rail. This, in turn, ensures that calculated voltages will be in better agreement with measurement. It was determined that using RF rails as narrow as  $10\text{ }\mu\text{m}$  was not necessary or desirable to reduce RF dissipation.
2. The step-down in height was eliminated in order to produce a trap capable of experiments with many ions (i.e., one with an isotropic RF pseudopotential tube across the trap). The step-down causes significant pseudopotential barriers and complicates the alignment of laser beams across multiple sections of the trap. A height of  $63\text{ }\mu\text{m}$  was chosen based on optical simulations to maintain a very low level of scattered light and chip-edge diffraction.
3. The capacitive control electrode was moved to the top layer (“top level ground”). First suggested by the fabrication team to simplify the fabrication process, this change offers numerous practical advantages including shielding of the ion from fields produced by leads (thereby increasing the probability of model and measurement agreement), protecting the leads from contamination and damage during packaging, permitting asymmetric DC electrodes with symmetric RF electrodes, and equalizing the shunt capacitance on all control electrodes.
4. The loading slot was made smaller to reduce undesirable effects above and in the vicinity of the loading zone, including reduced height and axial RF electric fields. The slot was shaped using a downhill gradient algorithm in order to maintain a nearly isotropic pseudopotential above the slot. The identification of a region of isolated metal on the back of the Gen I loading slot was resolved by leaving a  $\sim 50\text{ }\mu\text{m}$  thick layer of Silicon behind the load slot in the Gen II trap. Because this geometry deviates substantially from the design geometry, the advantage gained by slot-shaping was not realized in the fabricated trap.
5. The center DC rail is divided into two parts. The narrower section is used as a control electrode. It was designed to cause a geometric rotation of approximately  $30^\circ$  in the secular principal axes. The wider center rail is a DC ground. The ion is trapped over the center ground, which should minimize the effect of any oxide charging in the gaps between the electrodes.
6. Because there is no lead access for the center ground between the RF feed and the load slot (see Figure 1.5(c)), this chip required a vertical via to connect the center ground to the bottom (M1) ground layer. Two vias are included for redundancy.

Gap sizes, electrode lengths, and the M1 heat sink pad were maintained from the Gen I trap.

The Gen II trap represents several significant new contributions to the architecture of surface ion traps. It is the first trap ever to incorporate 1) vertical vias, 2) a top-level ground,



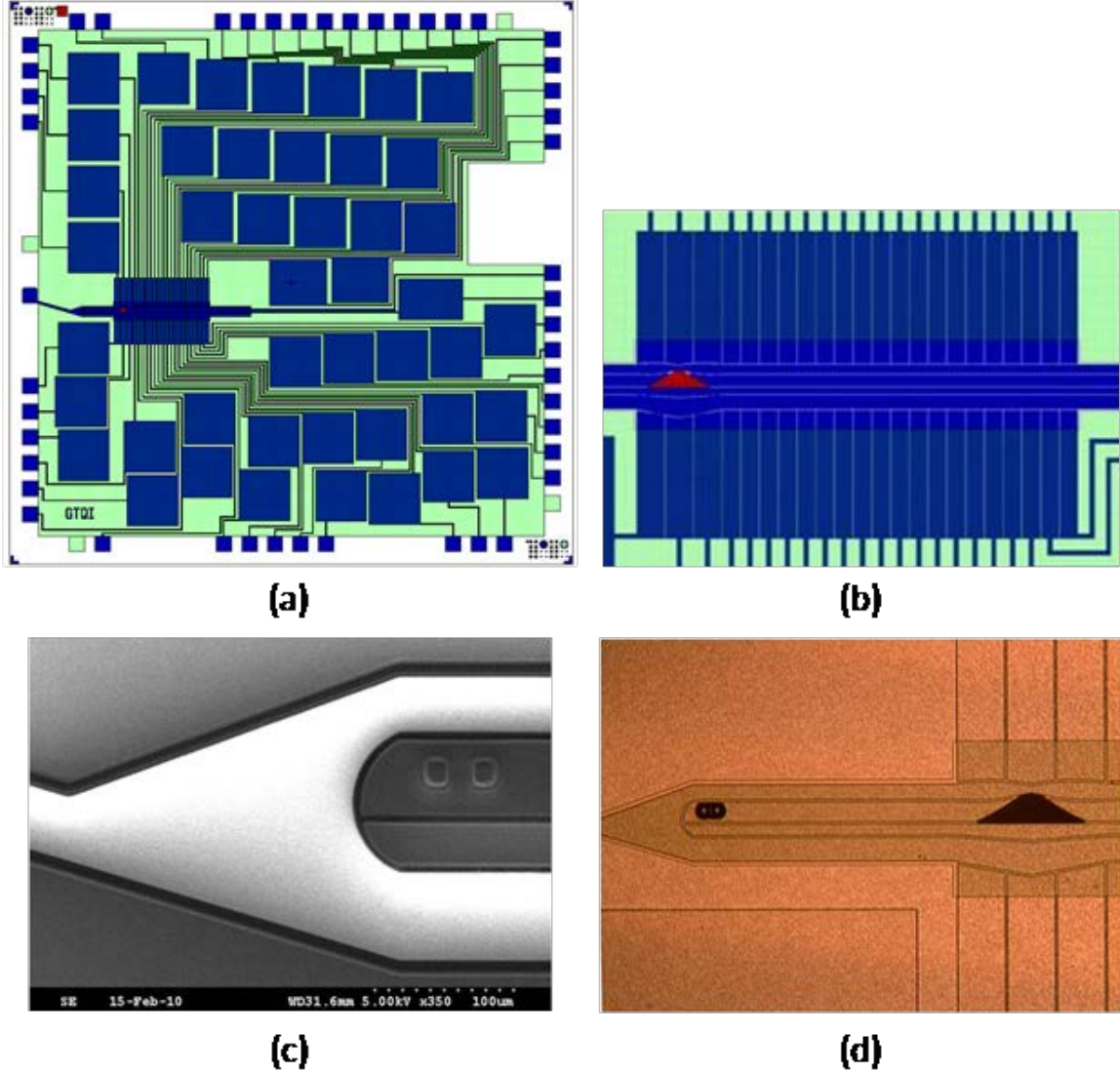


Figure 1.5: (a) The top level ground (M4, green) and electrode layer (M3, blue) layers of the Gen II trap. (b). Detail of the trapping region. The lighter blue region illustrates the part of the electrode layer visible through the top-level ground. (c) SEM image of the RF feed showing the vertical vias. (d) optical microscope image of the RF feed and load zone. Lighter orange is the top level ground, darker orange is the electrode layer.

and 3) equalized RF shunt capacitances. It is also the first five-rail trap to incorporate geometric axis rotation by control electrodes (see Chapter 2); four-rail traps with a semi-infinite RF electrode [6] have axes rotated  $45^\circ$ , but that geometry is not as scalable and is ill-suited to fabrication on silicon due to the size and capacitance of a semi-infinite RF electrode).

**Testing:** A single Gen II trap (GT34 F2) was tested before the end of the SMIT program. As with the Gen I traps, loading was reliable without tweaking the control potentials. This trap demonstrated reliable ion loading in the shaped loading slot, transport along the 1.5 mm region, dark lifetimes  $> 1$  minute, and loading of simple ion chains in a harmonic well.

#### 1.4.1.4 The centered second generation SMIT II trap

This trap is nearly functionally identical to the Gen II trap, with the addition of a pair of biased control electrodes on the top-level ground. These electrodes run the entire length of the trap and can be used for uniform axis rotation, uniform micromotion compensation, and to create long, equally-spaced ion chains. The trap is centered on the die and the pinouts are rearranged in order to match standards that were developed among multiple testing groups at the conclusion of this program. These standards guarantee interoperability of traps and sockets among many organizations.

### 1.4.2 Complex traps

In addition to the linear traps, we developed a symmetric cross trap and a trap with an integrated micromirror. These traps are important elements for developing a scalable quantum computer, and their design and fabrication are considerably more complicated than the linear traps. Both of these traps featured long linear sections that reflected the design principles outlined in the previous sections. However, in addition, their design also had to account for complicated features that added considerable structure to the pseudopotential tube.

#### 1.4.2.1 The symmetric cross trap

Ion trap junctions are crucial for achieving scalable quantum information processing. Recently the NIST ion trapping group has made excellent progress with surface trap junctions incorporated into a racetrack architecture [7]. These racetrack junctions are based on a “Y” geometry. Our powerful optimizing simulations developed during the SMIT II program succeeded in generating a more flexible and space saving junction based on a symmetric “X” geometry.

Once the design parameters for the linear section of the trap are established based on the considerations outlined in the previous section (e.g. RF rail width and separation to provide desired ion height and well depth), it is necessary to shape the RF rails in the region of the junction in order to form a trapping potential without an escape route. To achieve this, we implemented a genetic algorithm that used a multiobjective fitness function that quantified the junction’s performance, with a particular emphasis on minimizing heating (as indicated by the magnitude and rate-of-change of the pseudopotential along the trap

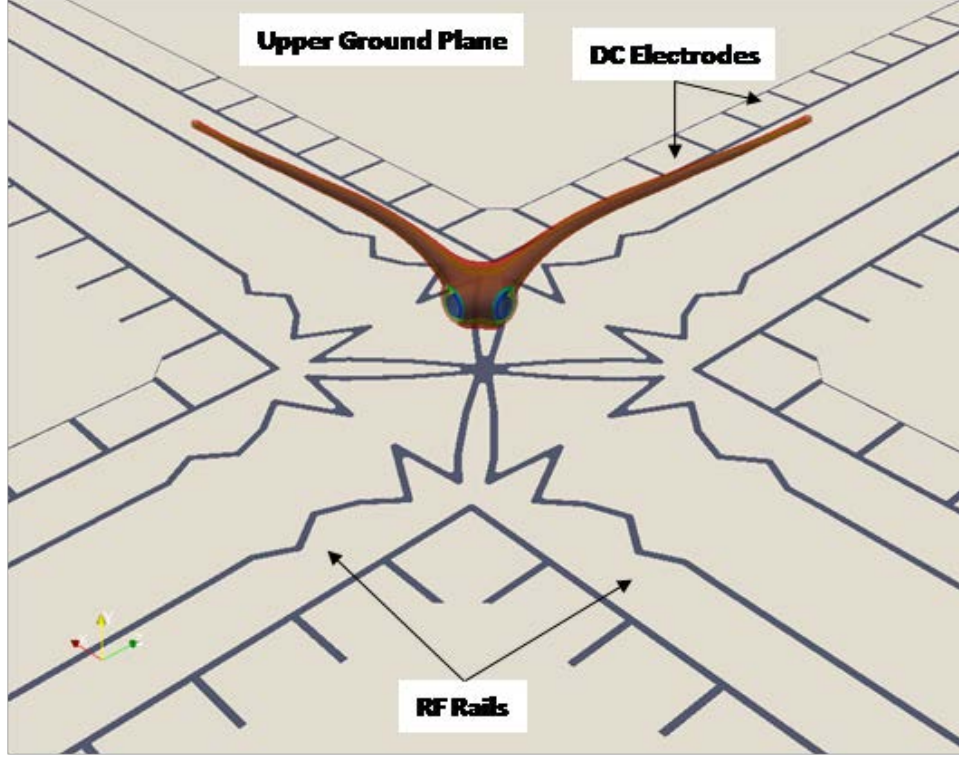


Figure 1.6: Center portion of the symmetric cross junction. A cut-away color map shows the pseudopotential contours for two arms of the trap. This trap includes the upper ground plane process that places a metal sheet  $1\text{ }\mu\text{m}$  above the DC electrode leads to provide shielding and mechanical protection.

axis) and maintaining a uniform trap axis height. This produced RF rails with long fingers that extend into the center of the junction and that have perturbations that taper the fields between the linear section and the center of the junction (Figure 1.6).

**Testing:** Fabrication of the symmetric cross trap was mostly completed under the SMIT II program, and testing is now in progress under a GTRI IRAD. The junction immediately demonstrated efficient loading in a reduced sized slot ( $50\text{ }\mu\text{m} \times 50\text{ }\mu\text{m}$ ) and transport was made multiple times to within  $19\text{ }\mu\text{m}$  of the junction center using the calculated waveforms without any corrections. Figure 1.7 shows the ion trapped at various positions during the transport to the junction center.

#### 1.4.2.2 The mirror trap

The development of sophisticated optical systems for detection of ions in ion trap quantum information research experiments becomes increasingly important as the size and fidelity of experiments increases. Because of interest in entanglement of larger numbers of ions, the field is approaching a threshold beyond which many current optical systems will no longer be adequate. Our approach to address this problem is to integrate a micromirror into the center electrode between the RF rails. The micromirror collects a large NA cone of light



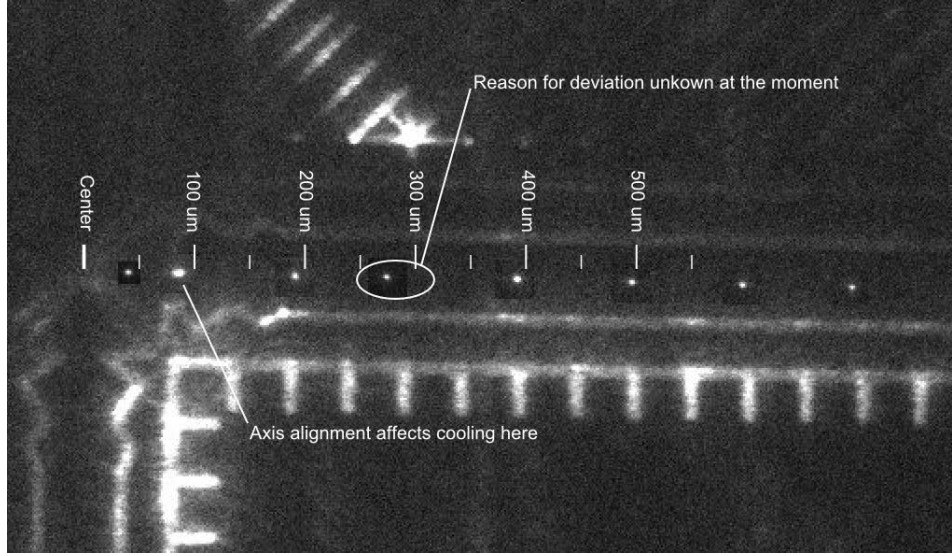


Figure 1.7: Composite image of the trap surface and the ion locations along the leg leading to the load zone. The right-most ion is nominally at  $700\ \mu\text{m}$  from the load zone and the remaining positions are at  $100\ \mu\text{m}$  increments except for the last location on the left which is nominally at  $50\ \mu\text{m}$  from the center. There is a gradual shift of the ion locations from the nominal position as the ion approaches the center. This is under investigation along with the  $300\ \mu\text{m}$  ion which shows a substantial deviation from the expected location.

from the ion, which is then relayed to a detector using a single, large optical system. The same large optical system is capable of relaying light from many individual micromirrors to independent detectors. This approach is referred to as the “multi-scale” optical system. With this approach, the alignment of the optical focus and the ion is entirely the product of design and microfabrication of the trap and is not sensitive to thermomechanical misalignment.

To design the mirror trap, we started from a simple analytic model of the trap and then developed relationships among the critical parameters; including mirror curvature, ion height, and RF rail size and location for the design of simple mirror/trap combinations. To maximize the collection efficiency, the mirror is made as large as possible while maintaining alignment of the pseudopotential null and the mirror focus. A genetic solver was used to optimize the shape of the RF electrodes in the transition region between the linear section and the mirror. The objective of the optimization is to reduce the portion of the linear section which has too much micromotion to perform logical operations on ions while maintaining the alignment of the RF null and the mirror focus. The final design is shown in Figure 1.9. The final trap parameters are mirror ROC =  $150\ \mu\text{m}$ , mirror diameter =  $120\ \mu\text{m}$ , ion height above trap surface =  $63\ \mu\text{m}$ , mirror sag =  $12.5\ \mu\text{m}$ , RF rail width =  $17\ \mu\text{m}$ , geometric collection efficiency = 14%.

Fabrication of the mirror trap was underway at the end of the SMIT II program. The fabrication will be completed in support of the MUSIQ program, and testing will be performed at GTRI and at Duke University.

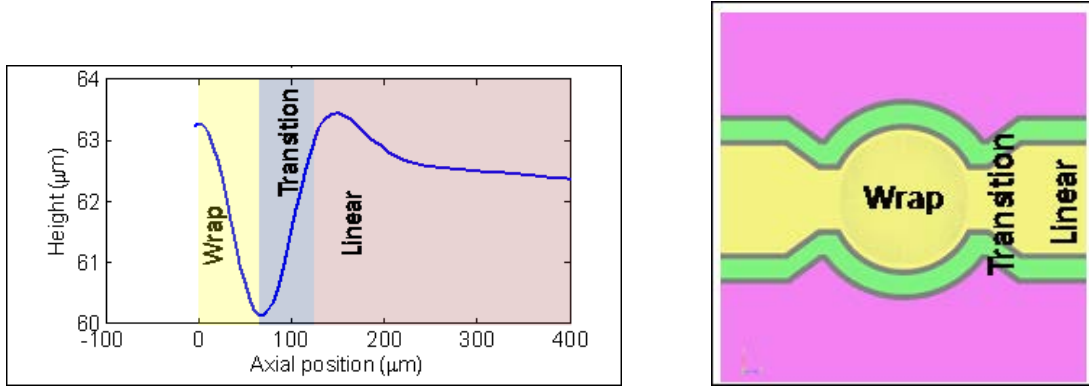


Figure 1.8: (a) Illustration of the three design regions for the mirror trap. (b) Plot of the height of the pseudopotential minimum for the geometry illustrated in (a).

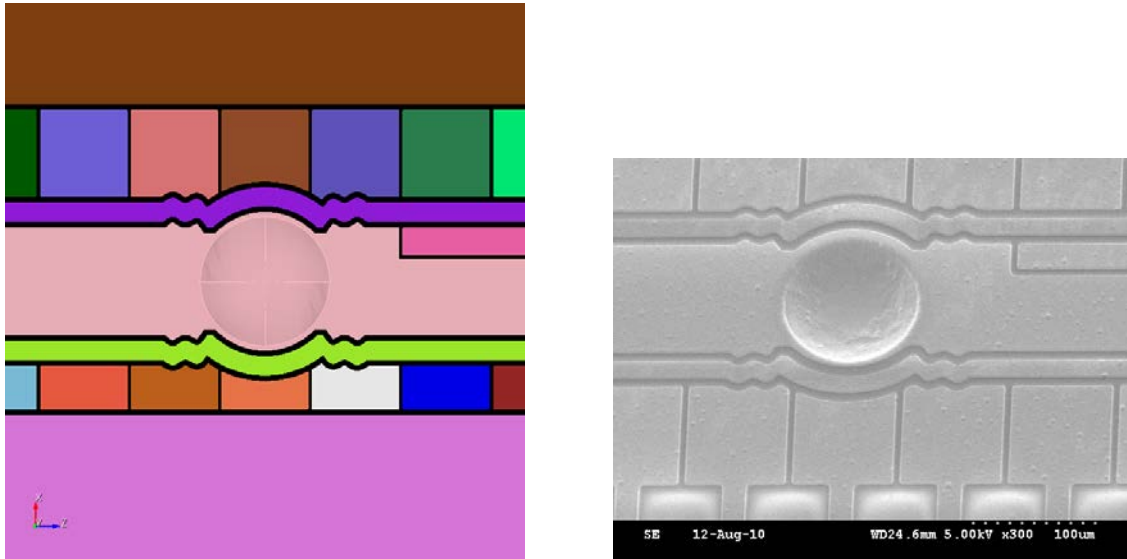


Figure 1.9: (a) Design of the micromirror trap. (b) SEM image of the micromirror trap from the lead wafer. Note that the surface is rough due to incomplete process development; this is corrected in following wafers.

## 1.5 Report organization

This report proceeds as follows. Chapter 2 describes trap design and modeling at GTRI. Chapter 3 describes trap fabrication at NRC. Trap testing at room temperature at GTRI and cryogenic temperatures at MIT is described in Chapter 4. Chapter 5 describes fiber tip traps for high efficiency light collection at Duke and MIT. A stability analysis for surface traps is included in Appendix A. Program goals and results are listed in Appendix B along with a description of how well they were met during the program. Publications and presentations are listed in Appendix C.

# Chapter 2

## Design and Modeling of Surface Electrode Traps

### 2.1 Introduction

Under the SMIT II program, GTRI developed a number of analytic techniques and advanced numerical modeling codes for the design and simulation of RF surface electrode ion traps. Highlights of this work include: software and hardware accelerated method-of-moments electrostatics solvers; models of electrode heating due to RF currents; self-consistent Lorentz force solvers for ion motion; analytic and numerical search approaches to electrode design (including the design of RF rails near integrated mirrors and 90° cross junctions); and analytic and numerical techniques for designing control voltage waveforms for ion shuttling. The following chapter gives details of these advances.

### 2.2 Modeling ion trap fields

GTRI has developed a general purpose electrostatics solver called StaticMoM that computes fields due to voltages impressed on 3-dimensional conductors. This code provides the fields required to characterize RF trapping potentials and design control waveforms. It also serves to generate trap metrics used in ion trap RF electrode geometry design. In the following sections, the motivation, formulation, and state-of-the-art features of StaticMoM are elucidated.

#### 2.2.1 Overview

Accurate and (ideally) rapid numerical modeling of ion traps is a pre-requisite for surface electrode ion trap design and characterization. With proper care, traps can be designed that exhibit properties tailored to the experiment to be performed, thereby yielding faster time to new results and less time spent modifying traps that are inherently suboptimal. However, modeling ion trap electrodynamics with full-wave rigor is an extremely challenging problem due to the electrical size of the ion trap relative to the RF wavelengths involved ( $\sim 1$  mm vs  $\sim 10$  m). Fortunately, even in the near-field region in which the ion exists full-wave simulation

is unnecessary to capture the vast majority of the driving physics since the trap operates well into the quasi-electrostatics limit. To illustrate this point, consider the equation for the electric field radiated by the surface currents and charge density present on the ion trap electrode surfaces. Very generally, this field is given by

$$\mathbf{E}(\mathbf{x}) = -\frac{j\omega\mu_0}{4\pi} \int_S \mathbf{J}_s(\mathbf{x}') \frac{e^{-jk|\mathbf{x}-\mathbf{x}'|}}{|\mathbf{x}-\mathbf{x}'|} dS' - \frac{1}{4\pi\epsilon_0} \nabla \int_S \rho_s(\mathbf{x}') \frac{e^{-jk|\mathbf{x}-\mathbf{x}'|}}{|\mathbf{x}-\mathbf{x}'|} dS' \quad (2.1)$$

where  $S$  is the surface of the trap electrodes,  $\mathbf{J}_s$  is the surface current,  $\rho_s$  is the charge density,  $\omega$  is the radian frequency,  $k$  is the wavenumber, and  $\epsilon_0$  and  $\mu_0$  are the permittivity and permeability of free space, respectively. For electrically small structures such as ion traps, we can significantly simplify this equation by taking the limit as  $k \rightarrow 0$ . To bolster this assumption, we can also consider the fact that the ion resides very near the surface of the ion trap, effectively making this a so-called near-field problem. As such, (2.1) simplifies to

$$\mathbf{E}(\mathbf{x}) = -\frac{1}{4\pi\epsilon_0} \nabla \int_S \rho_s(\mathbf{x}') \frac{1}{|\mathbf{x}-\mathbf{x}'|} dS'. \quad (2.2)$$

Integrating (2.2) yields the familiar expression for Coulomb's Law in terms of an applied voltage  $V$ :

$$V(\mathbf{x}) = \frac{1}{4\pi\epsilon_0} \int_S \rho_s(\mathbf{x}') \frac{1}{|\mathbf{x}-\mathbf{x}'|} dS'. \quad (2.3)$$

### 2.2.2 Method of Moments

A number of techniques exist to solve (2.3) numerically. The finite difference method (FDM), finite element method (FEM), and method of moments (MoM) are among the most popular. All of these techniques are rigorous and with sufficient care can be made equally accurate. Therefore, the selection of which technique to use ultimately simplifies to one of computational efficiency. There are several reasons why one can argue that the MoM is the most efficient. First and foremost, the MoM directly incorporates the boundary conditions of Laplace's equation thus eliminating the need to discretize the space around the ion trap as is required by FDM and FEM. Additionally, the specification of the boundary condition is made difficult for the FDM and FEM since solution accuracy is of paramount importance in ion dynamics modeling. An accurate boundary condition for FDM and FEM would be an expansion of spherical harmonics along the boundary, but this is tedious and difficult to implement. Therefore, most FDM and FEM practitioners implement the boundary condition with a simple Neumann condition which leads to significant errors in the fields. For these reasons, we use the MoM to solve for the charge density on each electrode. From the charge density the fields can be directly calculated at any point in space.

A MoM solution of (2.3) begins by discretizing the electrodes into small elements, usually either quadrilaterals or triangles. In our implementation, we use triangles to better represent curved electrode boundaries without introducing any anisotropy into the basis functions as would be the case with quadrilaterals. An example discretization is shown in Figure 2.1. Since the charge density is known to exhibit a singularity along electrode edges and be fairly

slowly varying in the center of an electrode, a modified meshing scheme is used throughout all simulations to reduce the number of unknowns in the integral equation solution and therefore the overall runtime. This technique involves finely meshing near all edges and tapering to a coarse mesh in the center of electrodes. For very large problems, this technique has the added benefit of reducing numerical precision problems since unnecessary unknowns are removed. An example of this meshing scheme is shown in the figure. For surface electrode ion traps in general, this meshing technique can reduce the unknown count by  $\sim 3\text{-}4\text{X}$  leading to a  $\sim 10\text{-}15\text{X}$  reduction in runtime.

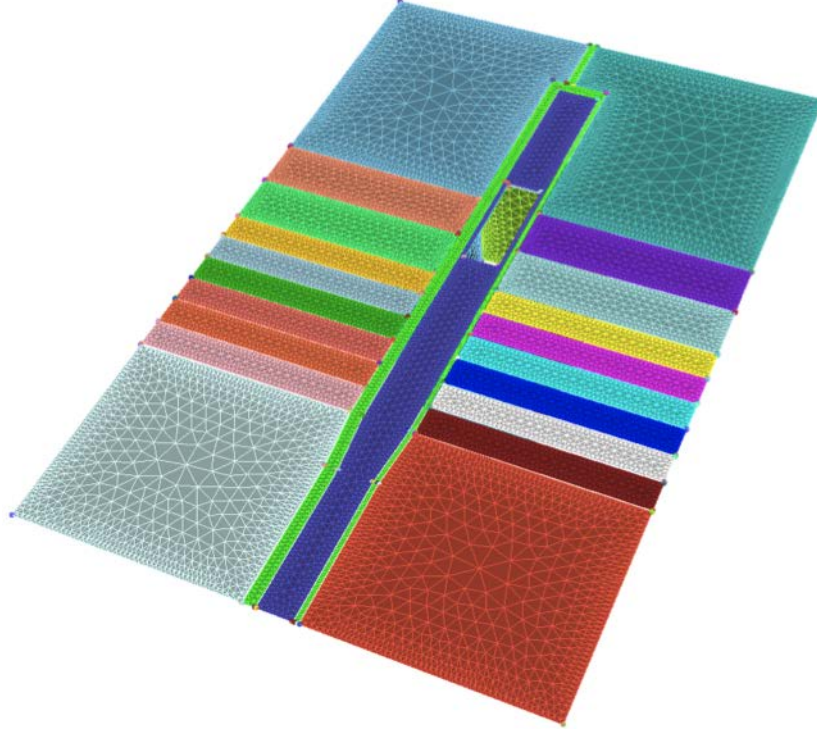


Figure 2.1: SMIT II Gen I surface electrode ion trap with triangular mesh for electrostatic MoM solver. Note that the mesh density is refined near the edges to better resolve the charge singularities.

To describe the charge density on the electrodes, a set of basis functions is defined in the form

$$\rho_s(\mathbf{x}) = \sum_{n=1}^N \rho_n f_n(\mathbf{x}), \quad (2.4)$$

where  $N$  is the total number of basis functions and  $\rho_n$  is the unknown coefficient associated with the  $n^{\text{th}}$  basis function  $f_n(\mathbf{x})$ . Typically, the basis functions are polynomial and are defined over the mesh elements. For example, so-called “pulse” basis functions are associated with a single element and are defined to be constant over the element. The pulse basis function is given by

$$f_n(\mathbf{x}) = \begin{cases} 1 & \mathbf{x} \in \Delta_n, \\ 0 & \text{otherwise} \end{cases}. \quad (2.5)$$

Linear basis functions are linear polynomials associated with the nodes of the mesh. At a given node, that node's basis function has a value of 1 and tapers linearly to 0 at the opposite edges of the triangles shared by that node. Within a given triangle, there are three linear basis functions corresponding to the three nodes as shown in Figure 2.2. The three bases form a linearly-complete set and can therefore represent arbitrary linear functions over the triangle. Higher order basis functions such as quadratic or cubic can be implemented as well. Increasing the order of the basis functions necessarily increases the accuracy of the solution and allows the user to discretize the geometry more coarsely. The overall result is a more accurate solution with a lower unknown count and less solution time. StaticMoM includes formulations for pulse, linear, and quadratic basis functions.

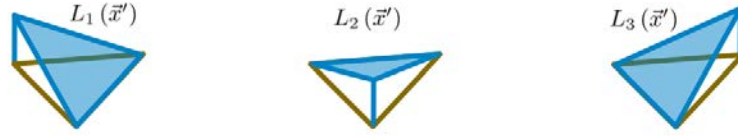


Figure 2.2: Three linear basis functions associated with each node of a triangular element. Each function has a value of 1 at its node and decreases linearly until reaching the opposite edge. This set of functions can represent arbitrary linear variations within an element.

Upon selecting a basis set for the unknown charge density, (2.3) is a single equation with  $N$  unknowns as given by

$$V(\mathbf{x}) = \frac{1}{4\pi\epsilon_0} \sum_{n=1}^N \rho_n \int_{S_n} f_n(\mathbf{x}') \frac{1}{|\mathbf{x} - \mathbf{x}'|} dS'. \quad (2.6)$$

By exciting each electrode and testing the integral equation at  $N$  points over the surface of the trap, an  $N \times N$  matrix equation can be formed. Also, rather than testing at  $N$  points, testing functions can be used yielding

$$\int_{S_m} T_m(\mathbf{x}) V(\mathbf{x}) dS = \frac{1}{4\pi\epsilon_0} \sum_{n=1}^N \rho_n \int_{S_m} T_m(\mathbf{x}) \int_{S_n} f_n(\mathbf{x}') \frac{1}{|\mathbf{x} - \mathbf{x}'|} dS' dS. \quad (2.7)$$

which serves to spread any error over the surface of the geometry. When the testing functions are chosen to be the same as the basis functions, this is known as Galerkin's method and results in a symmetric matrix thereby halving the storage requirement. The resulting matrix equation is given by

$$[Z] \{\rho\} = \{V\} \quad (2.8)$$

where the entries of  $[Z]$  and  $\{V\}$  are given by

$$Z_{mn} = \frac{1}{4\pi\epsilon_0} \int_{S_m} T_m(\mathbf{x}) \int_{S_n} f_n(\mathbf{x}') \frac{1}{|\mathbf{x} - \mathbf{x}'|} dS' dS \quad (2.9)$$

and

$$V_m = \int_{S_m} T_m(\mathbf{x}) V(\mathbf{x}) dS, \quad (2.10)$$

respectively.

The remaining task is then to solve the matrix equation with appropriate excitations in place. To fully characterize the trap, each electrode is excited, in turn, to 1V while holding all other electrodes at 0V. Thus, for a trap with  $N_{elec}$  electrodes, there will be  $N_{elec}$  separate  $V$  vectors resulting in  $N_{elec}$  separate charge density solutions. Arbitrary excitations can be formed by weighted summation of each of these solutions.

To illustrate the accuracy of StaticMoM, consider the sphere shown in Figure 2.3. As the number of unknowns is increased, the percent error in the capacitance (which can be analytically calculated) decreases at the rate expected for pulse and linear basis functions. For completeness, a comparison is shown between StaticMoM and CPO, a commercially available electrostatics code commonly used in the community for ion trap characterization. CPO uses pulse basis functions and is limited to 6000 unknowns. The agreement between the pulse basis StaticMoM results and CPO is excellent.

### 2.2.3 GPU acceleration

At the highest level, the MoM execution can be broken into two steps: 1) matrix fill and 2) matrix solution. The matrix fill step is concerned with the calculation of all the entries  $Z_{mn}$  as given in (2.9). As problem sizes grow, this process scales in memory and computation time like  $O(N^2)$ . For very large problems, this can be intractable in terms of both time and memory. In the design stage, when the user would like to quickly assess many solutions, this  $O(N^2)$  scaling is prohibitive.

Parallelizing the matrix fill step is an attractive option since the computations required to fill each element in the matrix are the same (with possible exception of the singular integral terms). Prior to a few years ago, the only options for parallelization were distributed memory approaches like MPI or shared memory approaches like OpenMP and pthreads. Recently, however, with the advent of general purpose graphics processing units (GPUs), the runtimes of algorithms which exhibit massive parallelism can be dramatically reduced.

The GPU is made up of several multiprocessors each of which has a number of floating point processing cores. For example, NVIDIA's GTX480 GPU has 480 processing cores available for computation. The GPU operates in a single instruction multiple thread (SIMT) mode meaning that many threads execute the same instruction set on different data all in parallel. Unlike modern CPUs, GPUs execute several thousand threads in parallel, which enables the matrix to be filled extremely quickly. To program the GPU, NVIDIA provides a C/C++ language extension called CUDA (Computed Unified Device Architecture) which facilitates creation of relatively simple code constructs to enable matrix element computation.

Table 2.1 shows the speed-up of the GPU implementation of StaticMoM for the pulse and linear formulations compared to the CPU version. Due to the simplicity of the memory



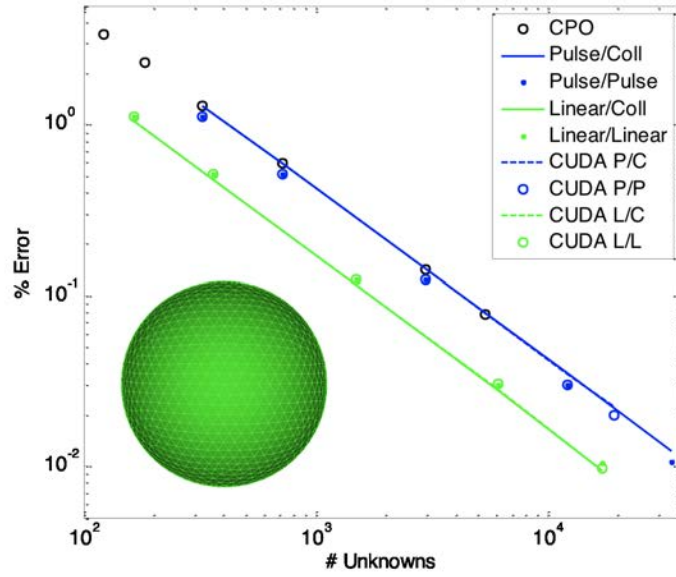


Figure 2.3: Comparison of CPO and four different formulations available in StaticMoM. Pulse basis functions with collocation testing method and pulse testing method are in excellent agreement with CPO. The linear basis functions perform significantly better for both collocation testing and linear testing than the pulse basis. This allows the user to achieve the same accuracy with far fewer unknowns. Results from the GPU version of StaticMoM (labeled CUDA in plot) show excellent agreement with the CPU version.

access pattern in the GPU, the speed increase over the CPU in the pulse basis case is  $\sim 500$ . For the linear basis case, the memory access is quite a bit more complicated, lowering the overall speed-up factor to  $\sim 40$ -150. The accuracy of the pulse and linear basis function implementation within StaticMoM is shown in Figure 2.3. The GPU acceleration thus imposes no degradation in the accuracy of the solution.

Table 2.1: GPU acceleration in StaticMoM Matrix Fill

# Unknowns	CPU Pulse (sec)	GPU Pulse (sec)	Speed-Up
2970	13.9	0.02	<b>695</b>
12194	231	0.49	<b>471</b>
19204	591	1.28	<b>462</b>
# Unknowns	CPU Linear (sec)	GPU Linear (sec)	Speed-Up
1487	9.1	0.98	<b>36.6</b>
6099	157	2.44	<b>64</b>
17105	1207	7.69	<b>157</b>

The GPU can also be applied to the matrix solution process as well which is the second phase of the MoM execution. Two approaches are generally taken for matrix solutions: direct solutions and iterative solutions. Direct solve techniques are typically Cholesky or LU decomposition or Gaussian elimination. Iterative techniques for electrostatic problems are typically conjugate gradient (CG) or GMRES. StaticMoM includes GPU implementations of Cholesky decomposition and CG solvers. For the Cholesky decomposition and CG solvers, the speed-up is  $\sim 50X$  versus the CPU versions.

The GPU is a transformative technology enabling a dramatic reduction in computation time and therefore increasing the fidelity with which simulations can be conducted. As discussed below in Section 2.5, the design of surface electrode geometries requires repeated computation of the fields for each member in a large population of traps; the GPU-enabled StaticMoM is used to enable low turnaround time design of a cross junction surface trap.

### 2.2.4 Adaptive cross approximation

Although the GPU reduces the computation time out-right and opens up possibilities for how to deal with the memory scaling problem, it does not intrinsically reduce the memory requirement. To address this problem, a method is required which can take advantage of information about the physics and matrix properties that result from a MoM formulation to reduce the memory footprint. The Adaptive Cross Approximation (ACA) is one such method. Other techniques include Fast Multipole Method (FMM) and Adaptive Integral Method/Pre-corrected FFT.

The ACA takes advantage of the coupling mechanism between distant groups of elements to form a compressed representation of the matrix that also has the advantage of lowering the required operations count to perform matrix-vector multiplies, etc. To illustrate, consider the ion trap shown in Figure 2.4. In the ACA, elements are grouped together based on spatial separation. The coupling between two groups in the mesh corresponds to a block in

the matrix as shown in the right half of the figure. For distant groups, the coupling from element to element does not vary significantly as the focus is shifted to different element pairs. Thus, the block in the matrix is low rank and need not be described by the full block. To compress the numerical description of a given block, the ACA adaptively forms a pivoted LU decomposition on each block and truncates the LU decomposition based on a convergence tolerance. Geometrically close groups do not compress as well, and the diagonal blocks are not compressed at all. The ACA is in contrast to the FMM in that it is strictly an algebraic technique and is adaptive to the geometry being analyzed, whereas FMM is based on the physics of the problem is not inherently adaptive. GTRI is one of only three groups in the United States that has developed a direct solve technique for the ACA which facilitates rapid solution when the trap has many electrodes. This poses a significant advantage over FMM which relies on iterative techniques.

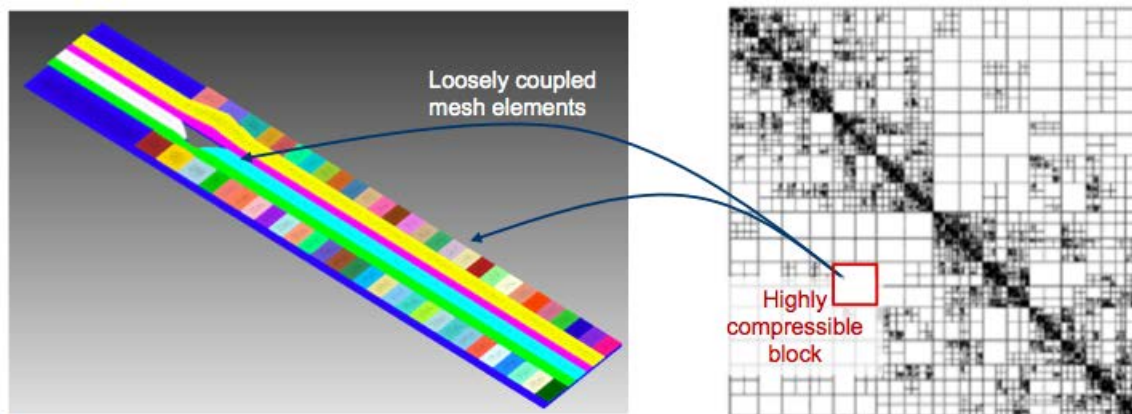


Figure 2.4: A notional matrix block structure due to spatial grouping of elements in the example ion trap. Distant groups can be compressed thereby yielding a much lower memory requirement and reduced solution time.

To illustrate the performance in terms of run times versus increasing unknown count, Figure 2.5 shows a comparison of the scaling of MoM versus ACA as implemented in StaticMoM. The primary benefit of ACA is that it allows much larger problems to be solved. In the figure, the MoM curve cuts off at the point where a single 4GB RAM machine can no longer solve larger problems. The ACA on the other hand, not only handles the maximum MoM problem size but solves it two orders of magnitude faster. In the figure, the largest problem run with ACA had  $\sim 300,000$  unknowns. On a machine with more RAM, GTRI has demonstrated the solution of problems with over one million unknowns.

### 2.2.5 Case study: fabricated cross junction model

During the SMIT II program, GTRI utilized StaticMoM and the Genetic Algorithm (GA) discussed below to design a  $90^\circ$  cross junction surface trap. Upon completion of the initial design phase, the full junction design including DC electrodes, top-level ground plane, screen, and loading zone was implemented in CAD, meshed as described above, and simulated to

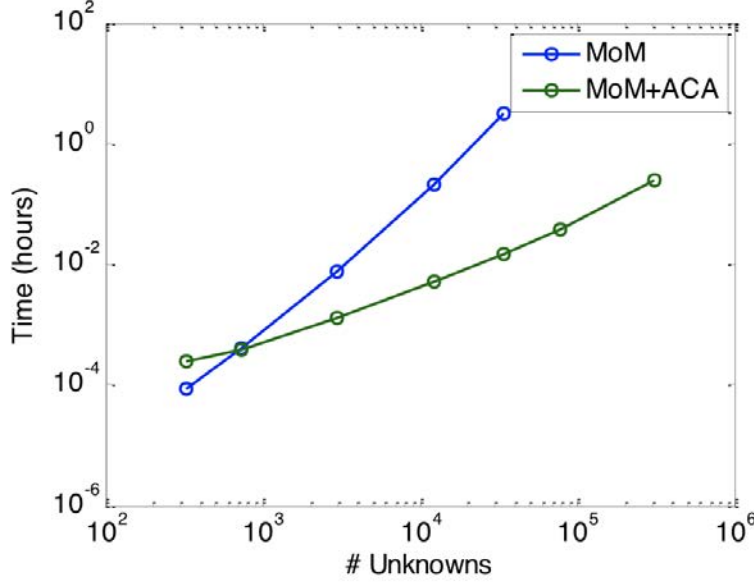


Figure 2.5: Comparison of matrix fill time versus unknown count for StaticMoM using a traditional formulation and an ACA formulation. Note that because of the significantly reduced memory requirement, the ACA can solve much larger problems in less time on a single computer.

facilitate development of shuttling waveforms. The full model is shown in Figure 2.6 with an enlargement of the junction center with mesh shown in Figure 2.7. This simulation is based on the mask files used to fabricate the physical trap so as to eliminate any possible CAD translation errors in the transition from initial design to fabrication (described in Section 2.8).

The resulting mesh was made up of 470,474 triangular elements and 80 independent electrodes (including RF rails and ground electrodes). In a traditional MoM solution, this trap would require 844 GB of RAM and a correspondingly impractical length of time to fill the matrix and solve. Using the ACA solver, the mesh was broken into 572 groups with an average size of 822 elements each. The matrix fill required only 12.9 GB of RAM (98.4% compression) and took 6.7 hours on a Xeon E5345 processor running 2.33 GHz. To generate the charge density solution, the conjugate gradient solver was invoked and required 31.3 hours to solve all 80 solutions. The pseudopotential contour lines are illustrated Figure 2.8. Further discussion of the pseudopotential properties and shuttling are reserved for later sections.

## 2.3 Electrode heating

For trap structures of the size developed under the SMIT program, heat dissipation is not a significant problem; however, it will become a more important consideration as trap structures continue to grow in size and complexity. The traps developed under the SMIT program

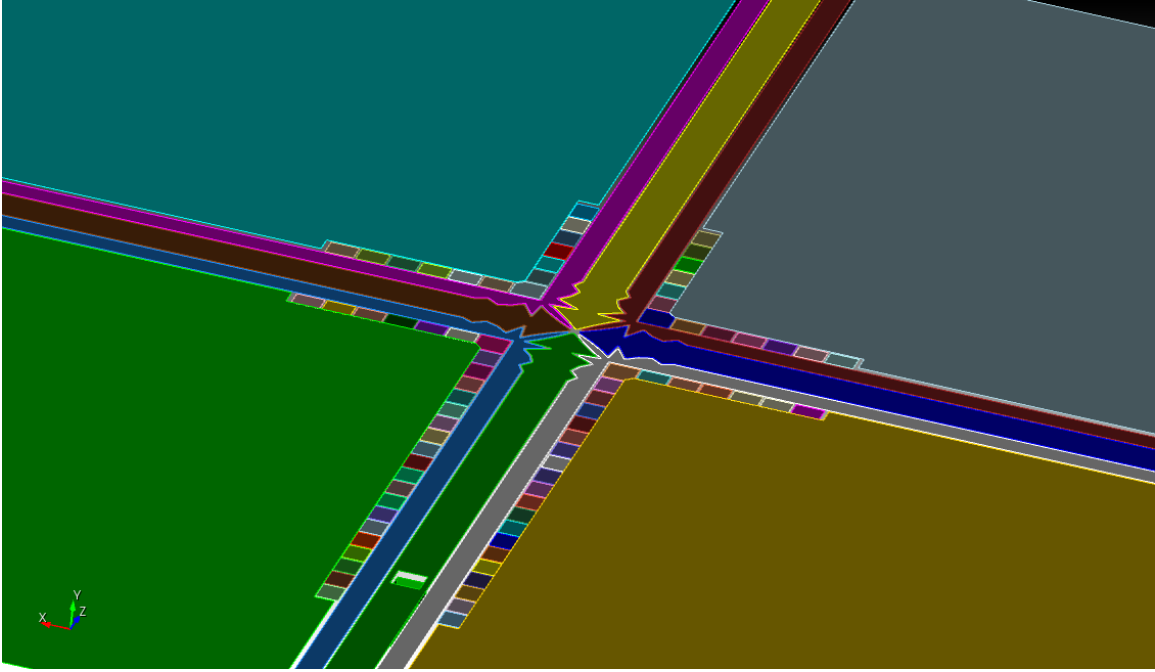


Figure 2.6: CAD rendering of the fabricated cross junction ion trap. Top ground electrodes help to define the extent of the DC electrodes.

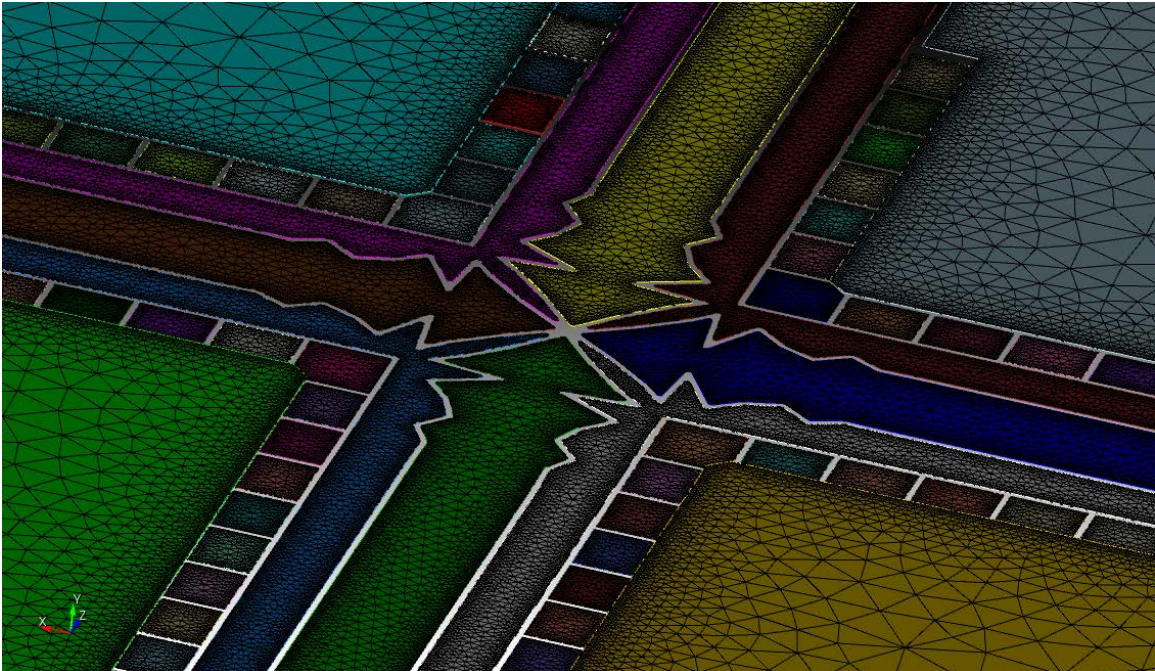


Figure 2.7: The complicated structure of the RF rails serve to control properties of the pseudopotential contours. Meshing is commensurate with the expected charge density distribution thereby reducing the unknown count.



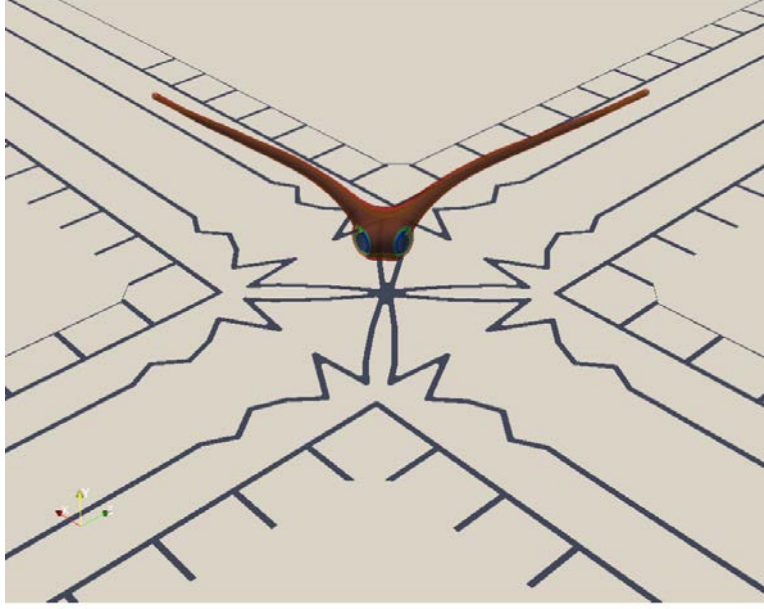


Figure 2.8: CAD rendering of the fabricated cross junction ion trap. Top ground electrodes help to define the extent of the DC electrodes.

are significantly sub-wavelength in size, so low-frequency approximations can capture the relevant effects and dependencies with design and operating parameters. For example, it is not necessary to treat the dissipation as attenuation of a propagating wave. While a complete calculation of heating in the trap structures requires the use of numerical techniques such as FEM, it can be very instructive to examine the problem of dissipation analytically using appropriate approximations.

One source of energy dissipation in the trap is ohmic loss in the RF rail structure. For this discussion, the RF electrode is assumed to be a linear strip of metal of width  $W$ , thickness  $t$ , and length  $L$  insulated from a ground plane by a dielectric of thickness  $d_0$ . A long RF electrode oriented in the  $z$ -direction can be considered as a long series of neighboring capacitors with length  $dz$ , as shown in Figure 2.9.

The lengthwise directed current flowing through any cross-section of this electrode must be equal to the charge required to supply the capacitance between that cross-section and the end of the electrode. For this reason, the  $z$ -directed current decreases linearly along the electrode length according to:

$$I_z = V_{\text{RF}}\omega_{\text{RF}}C = V_{\text{RF}}\omega_{\text{RF}}\frac{\epsilon_r\epsilon_0(W + \delta)}{d_0}z \quad (2.11)$$

where  $z = L$  at the feed point and decreases to zero at the opposite end. The term  $\frac{\epsilon_r\epsilon_0(W + \delta)}{d_0}$  represents a capacitance per unit length, with  $\delta$  as an extra capacitive factor to account for the effects of fringing fields to the ground plane and neighboring grounded electrodes on the trap surface. This factor can be easily determined through numerical models of the cross-sectional trap structure.

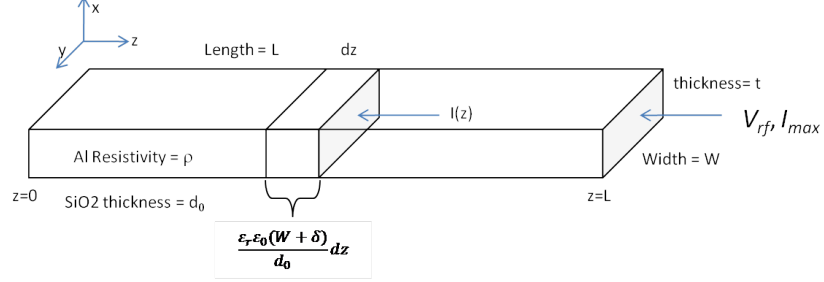


Figure 2.9: Schematic of single RF electrode with uniform cross section with a single RF voltage supply at  $z = L$ .

For room temperature operation, the electrode skin depth is much larger than the electrode height, and  $I_z$  can be considered uniformly distributed over the cross-section. In this situation, the dissipated power in units of W/m varies along the length according to

$$P'_{\text{electrode}} = (I_z^{\text{RMS}}(z))^2 R' = \left( V_{\text{RF}} \omega_{\text{RF}} \frac{\epsilon_r \epsilon_0 (W + \delta)}{\sqrt{2} d_0} z \right)^2 \frac{\rho}{Wt} \quad (2.12)$$

where  $R'$  is the electrical resistance per unit length. The heat generation varies quadratically along the length and reaches a maximum at the feed point of the electrode. Examining dissipation in this way is relevant, in that the local temperature of the electrode is typically related to the local heat generation, rather than the integrated dissipation over the entire electrode.

Given the extremely low thermal conductivity of  $\text{SiO}_2$ , the local temperature increase of the electrode occurs almost entirely over the dielectric layer, and the heat disperses rapidly in the much more thermally conductive ground plane and silicon layers. There must be an adequate thermal connection between the chip and its surroundings, or the temperature of the entire chip will rise to drive the heat flux required by the total chip dissipation. For the level of dissipation predicted in these traps, it does not appear that special efforts are required to achieve an adequate path for thermal conduction between the chip and its surroundings.

Another potential source of energy dissipation is due to damping of the vibrating dipole moments in the dielectric. The time average volumetric dissipation due to dipole relaxation is given by

$$P_{\text{dielectric}} = \frac{1}{2} \Re \{ j \omega_{\text{RF}} \epsilon_0 (\epsilon'_r - j \epsilon''_r) \mathbf{E} \cdot \mathbf{E}^* \} \quad (2.13)$$

where  $\epsilon'_r - j \epsilon''_r$  is the complex relative permittivity of the dielectric. A useful and reasonably accurate approximation for heating calculations is that the electric field in the dielectric is

completely uniform between the RF electrode and ground plane with  $|E| = V_{\text{RF}}/d_0$ , and the voltage drop along the RF electrode is negligible.

While the effects of fringing fields will vary with the trap design, this approximation will capture the vast majority of dielectric heating. The total power dissipated in the dielectric therefore reduces to

$$P_{\text{dielectric}} = \frac{1}{2} \omega_{\text{RF}} \epsilon''_r \epsilon_0 \left( \frac{V_{\text{RF}}}{d_0} \right)^2 LW d_0 \quad (2.14)$$

For example, the Gen II trap operating at 60MHz and 150V should dissipate approximately 35mW of energy in the electrodes and dielectric for a loss tangent of 0.01 and aluminum resistivity of  $2.8 \times 10^{-8} \Omega\text{m}$ . The precise value of the loss tangent is not known, but it is likely between 0.001 to 0.01. This should produce less than 1°C of temperature rise between the RF electrode and the silicon chip.

The equations for both dielectric and electrode dissipation indicate that a reduction in electrode width will decrease trap heating for a given RF voltage and frequency. However, a reduction in electrode width also decreases the trap stability parameter  $q$  by shrinking the solid angle subtended by the electrode from the ion position. One method of describing this viewing angle is through a conformal mapping of the planar electrode structure, where a Mobius transformation is used to reframe the electrode width and spacing in terms of ion height  $h$  and an angular parameter  $\theta$  where  $W = 2h \tan \theta$  [8]. For a trap with symmetric rails, the required RF voltage to achieve a specific stability  $q$  can be represented by

$$V_{\text{RF}} = \frac{q\pi h^2}{2 \sin 2\theta} \frac{m\omega_{\text{RF}}^2}{Ze} \quad (2.15)$$

where  $Ze$  and  $m$  are the ion charge and mass respectively. Note that as  $\theta \rightarrow 0$  the required RF voltage to maintain a fixed  $q$  approaches infinity, so excessively narrow electrodes require substantially greater RF voltage and dissipate more energy. An example of this is shown in Figure 2.10 for a Ca ion trapped at a height of 63.2  $\mu\text{m}$  by a 60MHz RF field.

Using this substitution for electrode width and substituting  $V_{\text{RF}}$  for a constant stability parameter  $q$ , the total electrode and dielectric dissipation in watts can be represented via:

$$P_{\text{electrode}} = \frac{\rho}{12t} \left( \frac{\pi q m \epsilon_r \epsilon_0}{2Ze d_0} \right)^2 \frac{(2h \tan \theta + \delta)^2}{\tan \theta \sin^2 2\theta} L^3 \omega_{\text{RF}}^6 h^3 \quad (2.16)$$

and

$$P_{\text{dielectric}} = \omega_{\text{RF}} \epsilon''_r \epsilon_0 \left( \frac{\pi h^2 q m \omega_{\text{RF}}^2}{2Ze \sin 2\theta} \right)^2 \frac{Lh \tan \theta}{d_0}. \quad (2.17)$$

The trigonometric terms in these equations have a minimum at  $\theta = \pi/6$  for small capacitive correction factor  $\delta$ . This corresponds to a rail width of approximately 35  $\mu\text{m}$  at an ion height of 63.2  $\mu\text{m}$ . For a given trap stability parameter and ion height, reducing the electrode width below a certain dimension will actually increase heat dissipation. An example is shown in Figure 2.11, for the total heat dissipation in a 1cm long by 1  $\mu\text{m}$  thick aluminum electrode on top of a 10  $\mu\text{m}$  thick layer of  $\text{SiO}_2$  with a loss tangent of 0.01. There are 4  $\mu\text{m}$  gaps between the RF electrode and neighboring DC electrodes (RF ground) that result in an extra capacitive factor  $\delta$  of 19  $\mu\text{m}$ . The ion height and RF frequency are 63.2  $\mu\text{m}$  and 60MHz respectively.



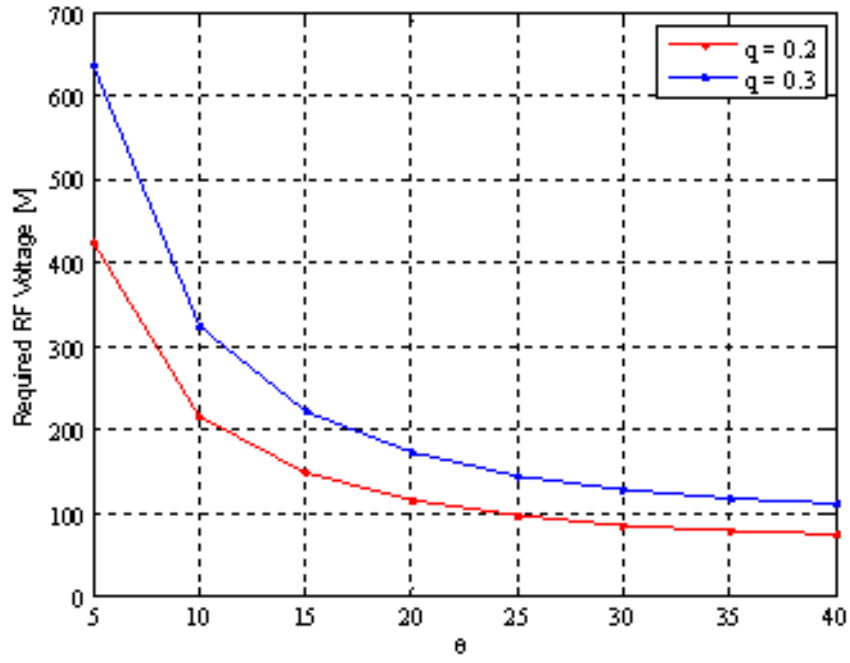


Figure 2.10: RF voltage required to maintain a given trap stability  $q$  as a function of the electrode width parameter  $\theta$  [deg]. The plot represents a calcium ion trapped in a 60MHz field at  $63.2 \mu\text{m}$  above the trap surface.

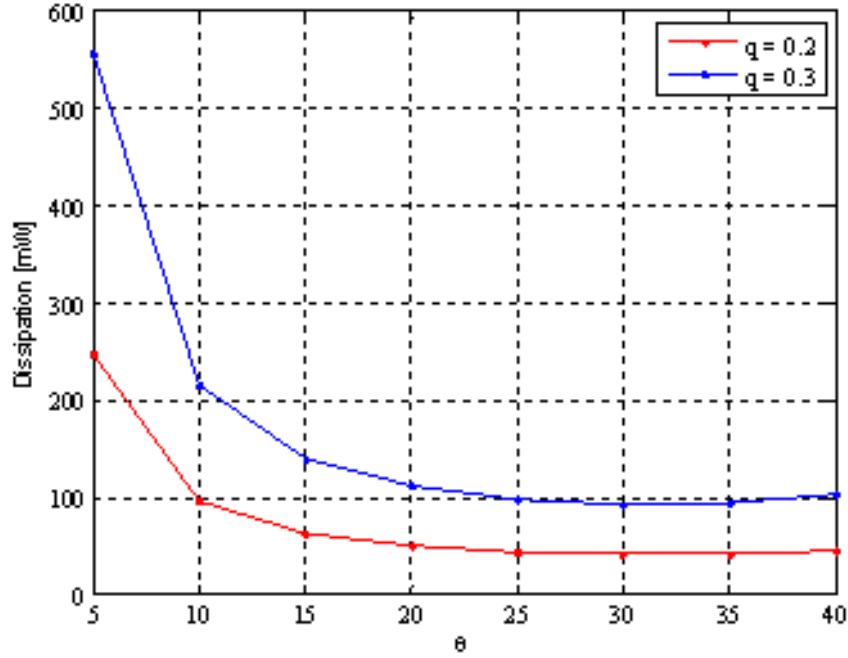


Figure 2.11: Total of electrode and dielectric dissipation in a 1cm long, 1  $\mu\text{m}$  thick aluminum electrode on a 10  $\mu\text{m}$  thick  $\text{SiO}_2$  layer with a loss tangent of 0.01. The ion height is 63.2  $\mu\text{m}$  and RF drive frequency is 60MHz.

As mentioned previously, the expected dissipation and associated temperature rise in the SMIT traps is not problematic, though dissipation must be reevaluated for any future designs involving significantly larger RF structures or different material and operating parameters. In such cases, producing a design that minimizes dissipation may be more important.

## 2.4 Classical ion dynamics

### 2.4.1 Overview

Simulation of ion motion in the trap via direct solution of the Lorentz force law provides insight into ion dynamics and serves as a validation of shuttling behavior due to derived control waveforms. Self-consistent solvers that include ion-ion interactions can also be incorporated directly into the waveform design process to account for Coulomb forces on ion position (as is required for *e.g.* chains of closely spaced ions). GTRI has developed a motion solver that finds the time-dependent particle trajectory due to electric and magnetic fields. The Lorentz force equation to be solved is

$$\mathbf{F} = m \frac{d^2 \mathbf{x}}{dt^2} = q(\mathbf{E} + \mathbf{v} \times \mathbf{B}), \quad (2.18)$$

where time dependence of the position and field quantities is assumed. The electric field arises

from both the fields impressed in the trap due to voltages on the surface electrodes and from ion-ion Coulomb interactions. The trap fields are determined using the electrostatic solver as described in Section 2.2 and are in practice defined over a uniform grid (the particle is allowed to exist anywhere within the grid, with the fields interpolated at the particle position). The Coulomb fields are given by

$$\mathbf{E}(\mathbf{r}_n) = \sum_{m \neq n} \frac{q_m(\mathbf{r}_m - \mathbf{r}_n)}{4\pi\epsilon_0|\mathbf{r}_m - \mathbf{r}_n|^3}. \quad (2.19)$$

In the ion trap development performed under SMIT II, the magnetic field  $\mathbf{B}$  has been assumed negligible compared to the RF trapping fields and Coulomb interactions between ions, though the code used to solve the force equation includes this term for future capability.

Solution of (2.18) is performed by taking its discrete form as central differences and marching the velocity ( $\mathbf{v} = d\mathbf{x}/dt$ ) and position through time. The central difference method is in general second order (that is, the error is  $O(\Delta t^2)$ , where  $\Delta t$  is the time step); it has the advantage of being computationally-efficient (discussed below), which allows the time steps to be taken small compared to the time scale of interest (in our case, the RF drive period). The method suffers compared to adaptive time step and predictor-corrector integrators in that it does not produce an estimate of its own error, and it can become unstable over very long simulations (millions of time steps). For ion shuttling times considered under this program (typically  $\sim 100 \mu s$ ), the finite difference solver has proved to be accurate and robust.

The central difference expression of the Lorentz force law leads to a set of update equations for the velocity and the position:

$$\begin{aligned} v_x^{n+\frac{1}{2}} - v_y^{n+\frac{1}{2}} \left[ \frac{q\Delta t B_z^{n+\frac{1}{2}}}{2m} \right] + v_z^{n+\frac{1}{2}} \left[ \frac{q\Delta t B_y^{n+\frac{1}{2}}}{2m} \right] = \\ v_x^{n-\frac{1}{2}} + \frac{q\Delta t}{m} \left[ E_x^n + \frac{v_y^{n-\frac{1}{2}} B_z^{n-\frac{1}{2}}}{2} - \frac{v_z^{n-\frac{1}{2}} B_y^{n-\frac{1}{2}}}{2} \right]; \end{aligned} \quad (2.20)$$

$$x^{n+1} = x^n + \frac{v^{n+\frac{1}{2}} + v^{n-\frac{1}{2}}}{2} \Delta t. \quad (2.21)$$

Note that if  $\mathbf{B} = 0$ , as is the case in our trap (*i.e.* no externally-applied magnetic fields), then the velocity update equation (2.20) reduces to one add and one multiply (given that  $q\Delta t/m$  is a constant) for each component, or 6 arithmetic operations for the vector update. The position update (2.21) similarly requires 9 arithmetic operations, so the total count to update the particle position is 15. This is a very fast computation; indeed, the computational bottleneck in the motion solver is solution of the electric field due to ion-ion interactions (2.19) and the 3-D interpolation required to determine the field at the ion's location within the grid. But even with these computational burdens, the algorithm requires only  $\sim 10$ s of seconds of computer time to simulate 100's of  $\mu s$  of ion time, which is sufficient to simulate operations such as shuttling through a junction.

## 2.4.2 Cooling

Proper solution of the Lorentz force equation requires knowledge of the initial conditions  $\mathbf{x}(0)$  and  $\mathbf{x}'(0)$ . Ideally, the motion solution should have the following traits:

- Minimum secular motion amplitude in the radial dimension. This constraint minimizes micromotion by holding the ion near the RF null.
- Minimum secular motion amplitude in the axial dimension. This constraint provides for a small position uncertainty of the ion as it moves in the potential well at the axial secular frequency. Having the position effectively fixed over an RF period time scale allows the design of adiabatic waveforms that are time-scale independent.

These requirements dictate that the ion motion amplitude be small and centered around the trap well in all three dimensions. The trap minimum is easily found *a priori* from the fields, which can be used to set  $\mathbf{x}(0)$ , but the initial velocity that leads to minimum excursions is not immediately known (in fact, if the initial velocity is set to zero and the ion is placed at the field null, no motion will result).

A numerical approach that is functionally-equivalent to cooling the ion through laser excitation of the cycling transition (though it is in no way *physically* meaningful) is to introduce a damping force  $\mathbf{F} = -c\mathbf{v}$  into the harmonic oscillator that describes motion in the well:

$$m\frac{d^2x}{dt^2} + c\frac{dx}{dt} + m\omega_s^2 = 0, \quad (2.22)$$

where the solution is assumed to have homogeneous harmonic motion at a frequency  $\omega_s$  and for simplicity the position vector  $\mathbf{x}$  has been reduced to the scalar  $x$ . Critical damping occurs when the two roots of the characteristic equation for (2.22) are equal, leading to  $c^2 - 4\omega_s^2m^2 = 0$  or  $c = 2m\omega_s$ . For an ideal quadrupole field with ion and RF drive frequency chosen for a stable trap,  $\omega_s \approx \omega_{RF}/10$ , so  $c \approx m\omega_{RF}/5$ . Finally, this force can be included into the general Lorentz driving term  $q\mathbf{E}$  to give a modified cooling  $\mathbf{E}^c = \mathbf{E} - \frac{m\omega_{RF}}{5q}\mathbf{v}$ . Numerically, the constant  $c$  is on the order of 10 for Ca ions in a surface electrode trap with RF drive frequency of 30 MHz. In the motion solver, the user can choose to weight this number by a damping factor; typically it is set  $< 1$  to provide weakly-underdamped cooling and also to account for the fact that the field is not the ideal quadrupole assumed in deriving the factor. Furthermore, the user chooses the time duration of cooling; typically the first couple of secular frequency cycles is enough to cool the ion to near its minimum amplitude excursions.

Figure 2.12 shows the effect of cooling on the amplitude of the ion motion along the axial direction of the trap, and Figure 2.13 shows damping in the transverse dimension. In both cases the damping force is turned on at the beginning of the simulation at  $t = 0$  and persists for  $0.4 \mu\text{s}$ .

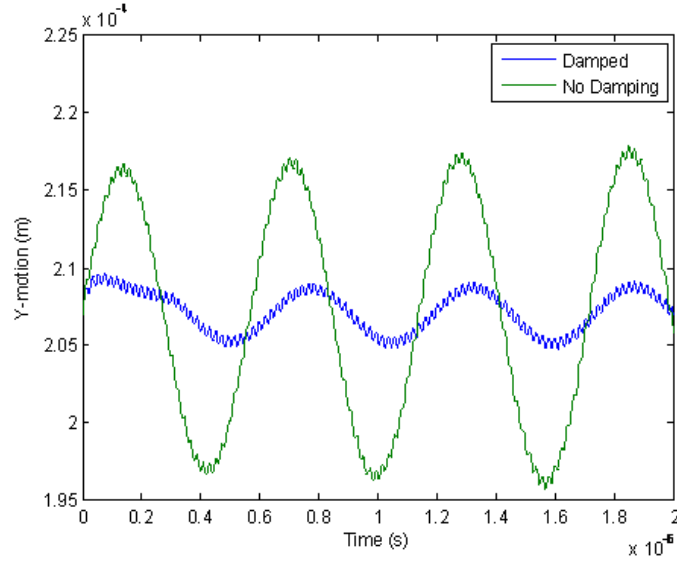


Figure 2.12: Amplitude of ion motion in the axial dimension for the damped and undamped cases. The cooling force is on from  $t = 0$  to  $t = 0.4 \mu\text{s}$ .

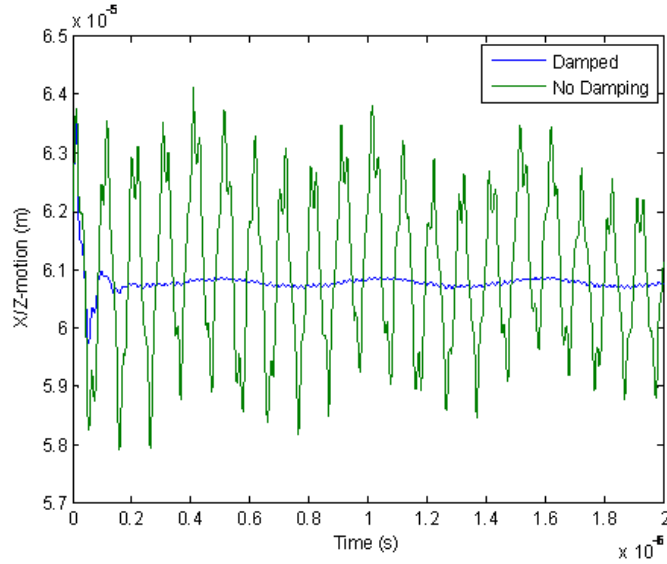


Figure 2.13: Amplitude of ion motion in the transverse dimension for the damped and undamped cases. The cooling force is on from  $t = 0$  to  $t = 0.4 \mu\text{s}$ .

## 2.5 Electrode design

### 2.5.1 Analytic design of linear RF electrodes

#### 2.5.1.1 Fields for surface electrodes.

Consider a surface (planar) trap with electrodes covering the entire surface, neglecting the gaps between them. The electrostatic (or quasi-static) fields for a given set of voltages can be obtained by using a Green's function approach [9]. For a given electrode set to a nonzero potential with the rest of the plane set to zero potential, one gets a formula for the electric field that is almost exactly the same as the formula for the magnetic field of a current on a wire that sits on the boundary of the electrode.

$$\mathbf{E}(\mathbf{x}) = \frac{V}{2\pi} \oint_C \frac{d\mathbf{s}' \times (\mathbf{x} - \mathbf{x}')}{|\mathbf{x} - \mathbf{x}'|^3}, \quad (2.23)$$

where  $d\mathbf{s}'$  is the line element along the boundary  $C$  of the electrode. As opposed to the magnetic field case where the direction of integration is determined by the current, the direction of integration in (2.23) is determined by the normal to the plane pointing towards the evaluation point  $\mathbf{x}$  via the right hand rule. This gives an electric field that is symmetric with respect to the electrode plane, as opposed to the magnetic field. The electrostatic potential is proportional to the solid angle the electrode spans when viewed from the evaluation point  $\mathbf{x}$ .

**Rectangular electrodes.** We obtain the field of a rectangular electrode at a point above the electrode plane by performing the integral in (2.23) along a boundary that consists of four pieces: (1)  $x = x_1$ ,  $z_1 < z < z_2$ , (2)  $x = x_2$ ,  $z_1 < z < z_2$ , (3)  $z = z_1$ ,  $x_1 < x < x_2$ , (4)  $z = z_2$ ,  $x_1 < x < x_2$ .

$$E_z = \frac{V}{2\pi} \left[ - \frac{y \left( \frac{x_2 - x}{\sqrt{(x_2 - x)^2 + y^2 + (z - z_1)^2}} - \frac{x_1 - x}{\sqrt{(x_1 - x)^2 + y^2 + (z - z_1)^2}} \right)}{y^2 + (z - z_1)^2} \right] \quad (2.24)$$

$$+ \frac{y \left( \frac{x_2 - x}{\sqrt{(x_2 - x)^2 + y^2 + (z - z_2)^2}} - \frac{x_1 - x}{\sqrt{(x_1 - x)^2 + y^2 + (z - z_2)^2}} \right)}{y^2 + (z - z_2)^2} \right] \quad (2.25)$$

$$E_x = \frac{V}{2\pi} \left[ - \frac{y \left( \frac{z_2 - z}{\sqrt{(x - x_1)^2 + y^2 + (z_2 - z)^2}} - \frac{z_1 - z}{\sqrt{(x - x_1)^2 + y^2 + (z_1 - z)^2}} \right)}{(x - x_1)^2 + y^2} \right] \quad (2.26)$$

$$+ \frac{y \left( \frac{z_2 - z}{\sqrt{(x - x_2)^2 + y^2 + (z_2 - z)^2}} - \frac{z_1 - z}{\sqrt{(x - x_2)^2 + y^2 + (z_1 - z)^2}} \right)}{(x - x_2)^2 + y^2} \right] \quad (2.27)$$

$$E_y = \frac{V}{2\pi} \left[ - \frac{(x_1-x) \left( \frac{z_2-z}{\sqrt{(x-x_1)^2+y^2+(z_2-z)^2}} - \frac{z_1-z}{\sqrt{(x-x_1)^2+y^2+(z_1-z)^2}} \right)}{(x-x_1)^2+y^2} \right] \quad (2.28)$$

$$+ \frac{(x_2-x) \left( \frac{z_2-z}{\sqrt{(x-x_2)^2+y^2+(z_2-z)^2}} - \frac{z_1-z}{\sqrt{(x-x_2)^2+y^2+(z_1-z)^2}} \right)}{(x-x_2)^2+y^2} \quad (2.29)$$

$$+ \frac{\left( \frac{x_2-x}{\sqrt{(x_2-x)^2+y^2+(z-z_1)^2}} - \frac{x_1-x}{\sqrt{(x_1-x)^2+y^2+(z-z_1)^2}} \right) (z-z_1)}{y^2+(z-z_1)^2} \quad (2.30)$$

$$- \frac{\left( \frac{x_2-x}{\sqrt{(x_2-x)^2+y^2+(z-z_2)^2}} - \frac{x_1-x}{\sqrt{(x_1-x)^2+y^2+(z-z_2)^2}} \right) (z-z_2)}{y^2+(z-z_2)^2} \Bigg]. \quad (2.31)$$

The same results can be obtained by first calculating a Fourier decomposition of the appropriate Green's function for the potential [10], and differentiating. Equations 2.24-2.28 will form our workhorse in the semi-analytic optimizations of the DC electrodes.

### 2.5.1.2 Infinite strips.

If we send  $z_1 \rightarrow -\infty$  and  $z_2 \rightarrow \infty$ , the fields become,

$$E_x = \frac{Vy}{\pi} \left[ - \frac{1}{(x-x_1)^2+y^2} + \frac{1}{(x-x_2)^2+y^2} \right] \quad (2.32)$$

$$E_y = \frac{V}{\pi} \left[ - \frac{(x_1-x)}{(x-x_1)^2+y^2} + \frac{(x_2-x)}{(x-x_2)^2+y^2} \right]. \quad (2.33)$$

The potential for this case is given in [10] as ,

$$\phi(x, y, z) = \frac{V}{\pi} \left[ \arctan \left( \frac{x_2-x}{y} \right) - \arctan \left( \frac{x_1-x}{y} \right) \right], \quad (2.34)$$

and it is easily checked that this is consistent with Eqs. 2.32 and 2.33.

### 2.5.1.3 Conformal mapping techniques for infinite strips.

Infinite strip electrodes can be treated as a two-dimensional problem due to translational symmetry, and one can investigate such problems by using conformal mapping techniques. It is possible to solve for the electric fields directly by this method, however, we will instead use these techniques to find electrode configurations that result in fields with prescribed properties [8].

An appropriate Mobius (rational) map<sup>1</sup> sends the half-space above the electrode into a disc, while mapping the electrode plane to the circle bounding the disc (see Figure 2.14). The two boundary value problems (those of planar electrodes and electrodes on the circle) are related by the Mobius transformation have solutions that are also related by the same

---

<sup>1</sup>A Mobius map is a map of the complex plane of the form  $z \rightarrow \frac{az+b}{cz+d}$ .

transformation, since the Laplace equation and the boundary conditions are preserved under conformal mappings. Moreover, the zeros of the gradient of the potential are also preserved under a conformal mapping.<sup>2</sup>

If we pick a Mobius map that fixes the chosen center of the circle, one can easily find configurations of pairs (or groups) of planar electrodes that place a zero of the electric field at a prescribed location. Namely, by placing arcs of electrodes around the circle in a uniform way and setting them to the same voltage, one gets a zero of the field at the center of the circle due to symmetry. A conformal map that fixes the center then sends these arcs to the desired planar electrodes will result in a zero electric field at the same location. By holding the arcs that represent the electrodes fixed and rotating the disc, it is possible to generate a set of asymmetric RF electrode widths that correspond to the same ion height.

Figure 2.14 gives a geometric description of the action of the relevant Mobius map on the electrode plane. In order to find the points on the circle that correspond to the points on the electrode plane (line), one draws tangents from electrode end points on the circle to the electrode end points on the line. For more details, see [8].

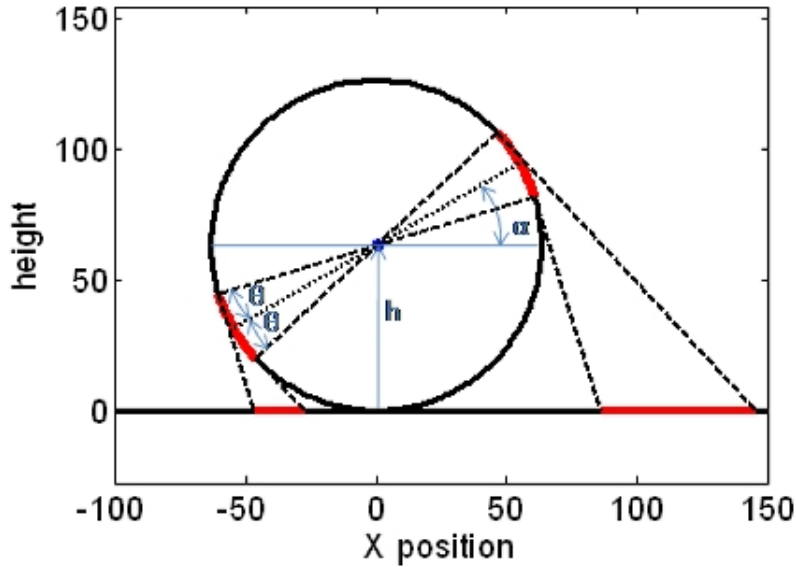


Figure 2.14: A conformal (Mobius) mapping of the planar electrode structure (shown in blue, red and green lines along the  $x$ -axis) to the circle bounding the disc that forms the range of the Mobius map.

#### 2.5.1.4 Application to RF electrodes

Given two infinite strips of RF electrodes, one can obtain the fields either directly through 2.32 or via the conformal mapping techniques described above. The main issues of interest are the location of the zero of the electric field (trap axis), the curvature of the pseudopotential (which gives the  $q$  parameter that determines the stability of the Mathieu equation), and

<sup>2</sup>See, e.g., [11] for a discussion of the applications of conformal mappings to electrostatic problems.



the trap depth, i.e., the pseudopotential difference between the trap axis and the nearest “escape point”. See [8, 10] for more details. Some of the relevant results are summarized below.

We will focus on the relatively simple case of two infinite strips of electrodes of equal widths  $b$ , separated by a distance  $a$ , driven by the same RF voltage with frequency  $\omega_{RF}$  and amplitude  $V_{RF}$ . We will assume that the rest of the plane is grounded. The zero of the total electric field is then at a height,

$$h = \frac{\sqrt{2ab + a^2}}{2}. \quad (2.35)$$

Due to symmetry, there is a single  $q$  value instead of a matrix  $Q$  as discussed above, given by

$$q = \frac{4ZeV_{RF}}{m\omega_{RF}^2} \frac{1}{\pi} \left[ \frac{4b}{(a+b)^2 \sqrt{2ab + a^2}} \right]. \quad (2.36)$$

The trap depth is

$$\Delta U = \frac{(Ze)^2 V_{RF}^2}{\pi^2 m \omega_{RF}^2} \left[ \frac{b}{(a+b)^2 + (a+b)\sqrt{2ab + a^2}} \right]^2. \quad (2.37)$$

Instead of  $a$  and  $b$ , these quantities can also be given in terms of the angles spanned by the arcs describing the electrodes after a Mobius transformation. One has, for example,

$$\text{Gap width} = a = 2h(1 - \sin \theta) / \cos \theta \quad (2.38)$$

$$\text{Electrode width} = b = 2h \tan \theta \quad (2.39)$$

$$\text{Total width} = 2a + b = 2h(1 + \sin \theta) / \cos \theta \quad (2.40)$$

We will utilize the Mobius approach below in specifying the nominal rail width for rails surrounding integrated mirrors.

## 2.5.2 RF electrode design with the genetic algorithm

The well-defined trapping potential due to a pair of parallel RF electrodes can become highly-perturbed in regions where the electrode width or spacing varies. Such discontinuities occur at intersections and in regions where other trap features such as embedded mirrors and loading slots distort the nominal geometry. Under the SMIT II program, GTRI developed and implemented a Genetic Algorithm (GA) electrode shape optimizer that maintains RF pseudopotential well properties in the region of electrode discontinuities. This approach has been successfully applied to designing RF electrodes in 90° crosses and in the vicinity of integrated spherical mirrors.

The genetic algorithm is in principle a global technique that begins a search process with a set of  $N$  random geometries that are representative of all possible trap geometries. The performance of each of these geometries is determined based on some metric and the population ranked from best to worst. Pairs of this generation are collected into *parents* from which a population of *children* are formed. The next population then consists for the best  $N/2$  parents and their  $N/2$  children. The process continues until one or more members

of the population have a metric that meets the design goal. The following section provides details on applying the method to shaping the RF electrodes in a junction.

Wesenberg showed [12] that the intersection of two linear traps results in a weakening of the trapping potential in the junction region, with the trapping potential completely failing in the limit of a  $90^\circ$  intersection angle. Wesenberg’s analysis was for ideal linear sections, which offers the possibility that a cross junction trap might maintain a trapping potential if the trap geometry is perturbed from that ideal case. We implemented a genetic design algorithm to optimize the shape of the RF rails in the junction region to form a trapping potential without an escape route. With hindsight, we see that trapping in a  $90^\circ$  cross is possible through two principal geometric changes: 1) The introduction of long ‘fingers’ of RF rail that extend into the junction and remove the large, symmetric ground electrode that would otherwise be present; and 2) The perturbations of the electrode shape in the transition from the linear regions to the junction that taper the fields into the intersection.

In the case of optimized surface electrode trap geometries, the GA population is composed of RF rail configurations where the shape of the rail is parametrically described by a set of lengths that give the distance from the outer edge of the rail to the inner. As shown in Figure 2.15, the outer edge is fixed and the inner edge is allowed to vary. This choice of geometry was inspired by previous work [13] that showed improvement in junction performance by allowing the inner edge of the rail to intrude into the center of the junction. Each member of the population is thus defined by a set of numbers  $[w_1, w_2 \dots w_n]$ , where  $n$  is the total number of RF rail width parameters. Each of the lengths is constrained to a set of numbers, typically uniformly spaced values between  $w_{min}$  and  $w_{max}$ , where  $w_{min}$  is the minimum line width achievable in fabrication and  $w_{max}$  is chosen to prevent the *center* conductor from becoming too thin.

Note that the ability to efficiently exercise the optimization algorithm requires evaluation of a large population of trap geometries for many generations. To do so requires a means for rapidly determining the metric for each trap; in our case, this means having a fast electrostatics solver for determining the trap fields along the trap axis of interest. This requirements is particularly stressing for large geometries such as the junction

A number of metrics can be used to qualify trap performances; early designs used the single metric of maintaining a constant ion trap height. Figure 2.16 shows the first successful  $90^\circ$  cross designed at GTRI using the genetic algorithm optimization. Overall the shape of the rails is well-behaved and the pseudopotential height is fixed along the arms, with a lowering of the trap axis in the center of the intersection. Despite the pseudopotential axis height change, the pseudopotential contours show that that trapping depth remains sufficient (as evidenced by the closed contours) throughout the trap. Figure 2.17 confirms the trapping performance of the geometry by showing the trajectory of an ion shuttled through the junction using waveforms designed by the particle swarm optimization (see Section 2.7.2).

Over the course of the program, GTRI added a number of improvements and innovations to the GA design of RF electrodes. In the early design of Figure 2.16, the rail excursions are sharp because the drawing algorithm simply put straight line segments between each point in space defined by the length  $w$ . To meet fabrication tolerances and to decrease the chance of arcing due to sharp points, the geometry of the traps was refined to include fillets joining segments along the rail length. The geometry was also generalized to not require a

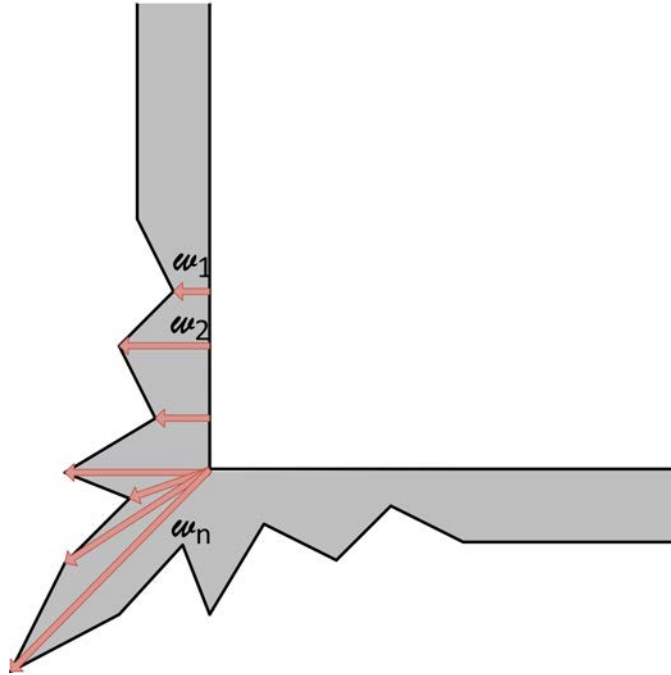


Figure 2.15: Perturbations to the RF rail width are parameterized by distances from the outer edge of the rail ( $w_1, w_2, \dots w_n$ ). The genetic algorithm varies these lengths to form an RF trap that meets constraints imposed by the designer, such as constant ion height, constant secular frequency, and minimum ion heating.

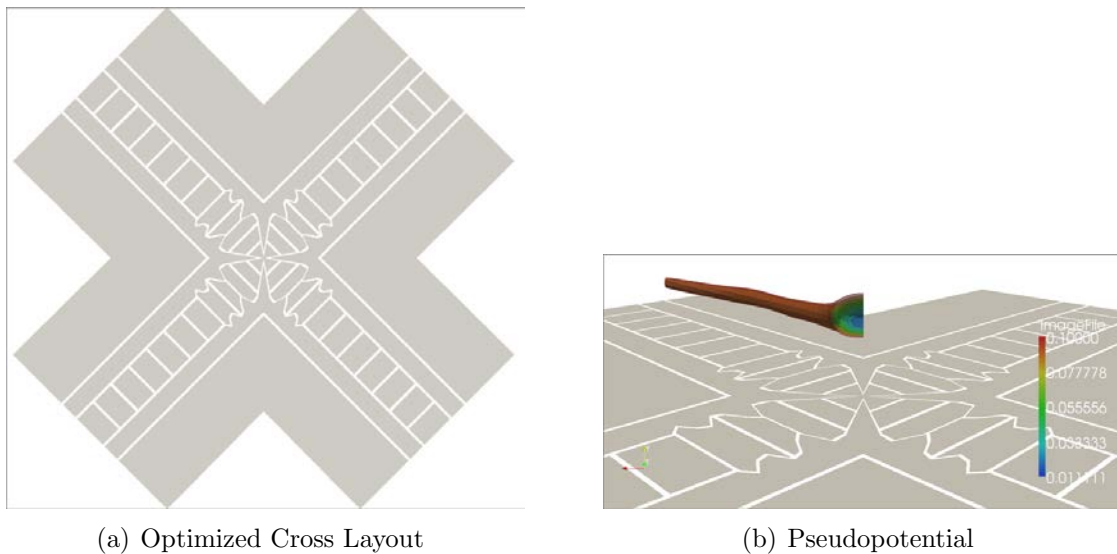


Figure 2.16: An early  $90^\circ$  cross junction with RF rails and center conductor shaped using the genetic algorithm design. The geometry of the trap is seen to be well-behaved (i.e. no rapid spatial excursions of the electrodes) and the resulting pseudopotential has a smooth taper going from the linear to the intersecting region with no evident escape route long lines normal to the trap surface. The fitness metric used to constrain trap design is constant ion height.

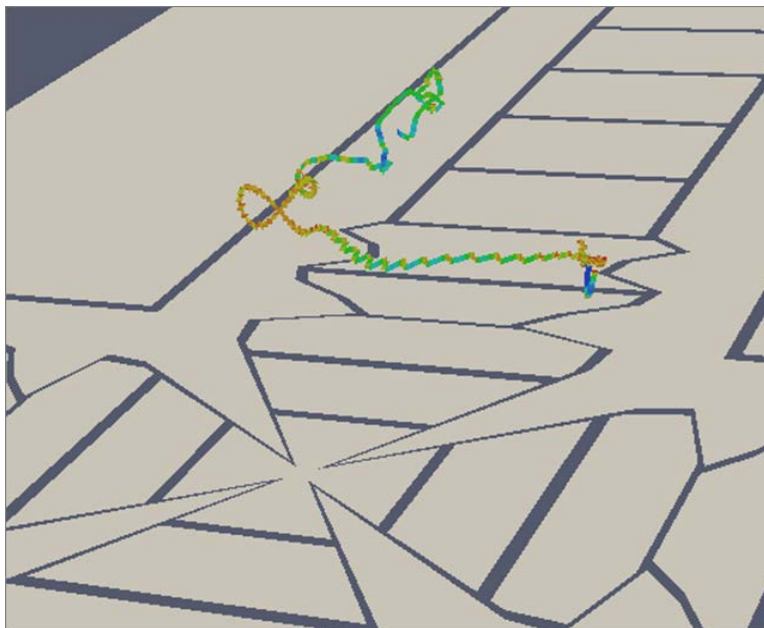


Figure 2.17: Trajectory of an ion in the first cross trap of Figure 2.16 As expected from the pseudopotential picture, the ion does not escape from the top of the trapping region in the center of the intersection (as would be expected with an unadulterated linear section join).

connected center conductor.

To fully account for ion behavior in the trap, the metrics were expanded from requiring constant height to a multi-objective fitness function that ranked trap performance based on the pseudopotential minimum, the shape of the pseudopotential tube, and the change in the electric field along the trap axis (proportional to trap heating). The terms of the multi-objective fitness function are given in (2.41), with descriptions provided in Table 2.5.2.

$$P = \frac{qV_{RF}^2}{4m\omega_{RF}}(E_x^2 + E_y^2 + E_z^2) \quad (2.41a)$$

$$F_1 = \int_0^{l_{max}} P(y|_{P_{min}}, l) dl \quad (2.41b)$$

$$F_2 = P_{max}(y|_{P_{min}}, l) \in [0, l_{max}] \quad (2.41c)$$

$$F_3 = \sqrt{\frac{1}{N_l} \sum_l ((y|_{P=10meV} - y|_{P_{min}}) - 6.5\mu m)^2} \quad (2.41d)$$

$$F_4 = \int_0^{l_{max}} \left( \frac{\partial |\mathbf{E} \cdot \hat{l}|}{\partial l} \right) dl \quad (2.41e)$$

Table 2.2: Description of the multi-objective fitness parameter expressions given in Equation (2.41)

Parameter	Description
$P$	Pseudopotential
$F_1$	The average of the pseudopotential along the trap axis (the pseudopotential minimum)
$F_2$	Maximum value of the pseudopotential excursion along the trap axis
$F_3$	Radial distance from the trap axis to the 10 meV contour – a measure of trapping potential shape and secular frequency compared to the linear region
$F_4$	Average slope of the electric field along the trap axis – a measure of heating

Based on these new design techniques, GTRI explored a number of cross junction designs that culminated in a 90° cross that was fabricated at Georgia Tech. The final design was shown previously in Section 2.2.5 and is shown again in Figure 2.18. The parameters of the multi-objective fitness function for the final design are shown in Figure 2.19 and 2.20

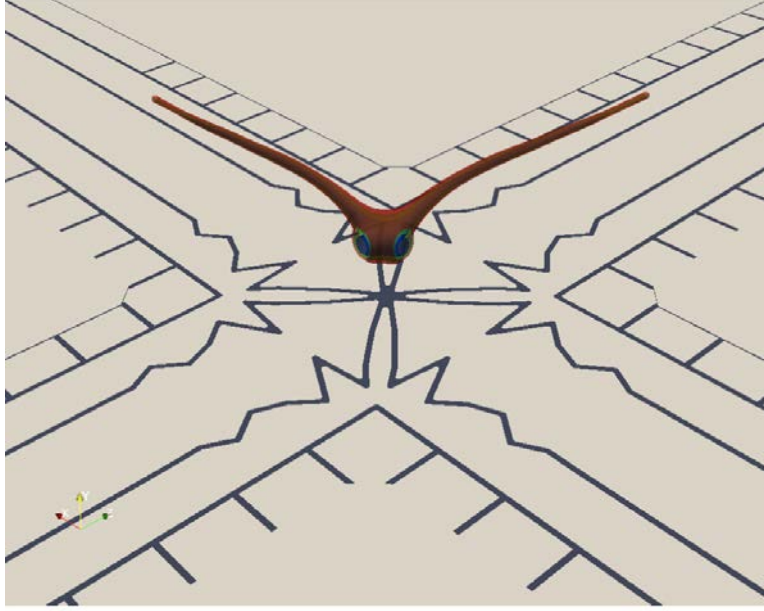


Figure 2.18: CAD rendering of the fabricated cross junction ion trap designed using the multi-objective fitness function in (2.41). The pseudopotential contours showing the RF trapping region are above the surface. Top ground electrodes provide shielding and help to define the extent of the DC electrodes.

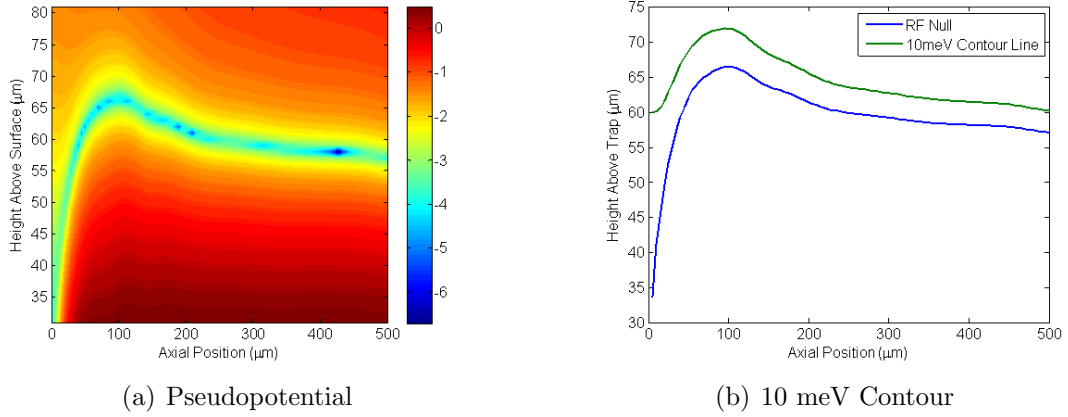


Figure 2.19: The pseudopotential minimum (trap null) has its average value and maximum value minimized under the multi-objective fitness function; for the fabricated cross trap, the value along the axis is  $< 100 \mu\text{eV}$ . The RF pseudopotential tube diameter is held constant until the location is  $100 \mu\text{m}$  from the trap center, at which point it starts to expand. In both plots the axial distance is measured from the center of the junction.

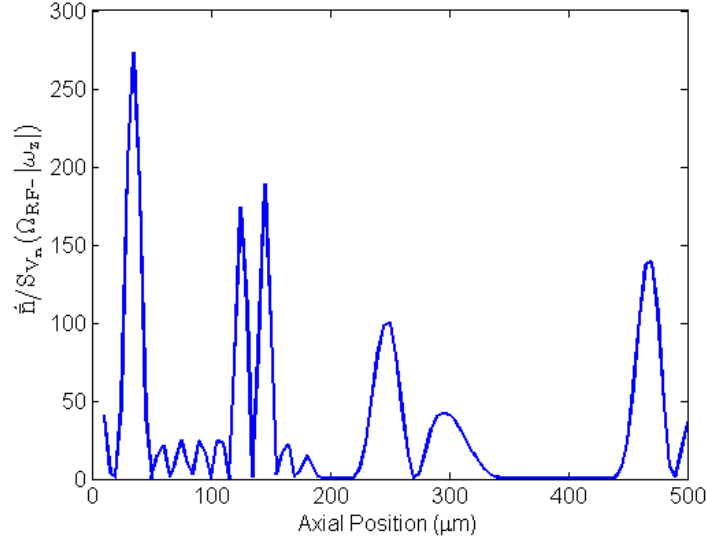


Figure 2.20: The heating rate as a function of axial position for the cross junction designed with the multi-objective fitness function. The heating rate is highest near the intersection, where axial fields due to the perpendicular arm leak into the trapping region.

## 2.6 Integrated mirror design

The development of sophisticated optical systems for detection of ions in ion trap quantum information research experiments becomes increasingly important as the size and fidelity of experiments increases. Because of interest in entanglement of larger numbers of ions, the field is approaching a threshold beyond which many current optical systems will no longer be adequate. For example, the high NA objectives used in most systems have extremely limited field of view, typically less than 1 mm for NA=0.3 and 0.1 mm for NA = 0.45. Because these objectives typically have apertures of one to two inches, they cannot be arrayed to increase the field-of-view (FOV) in any manner on scale with trap features. Lenses can be scaled to larger sizes to achieve greater FOV, however, the expense and optomechanical overhead will become substantial obstacles even on the scale of current traps, and will never be scalable in the quantum systems sense. In any case, these large lens systems are fundamentally inefficient since only a tiny portion of the FOV is of interest for light collection, i.e., the few locations in the FOV containing ions.

A more accessible approach is to scale the objective to a smaller size, such that the FOV of a single objective is well-matched to a single ion location and individual objectives can be arrayed to access many individual ions distributed around the trap. Such an approach has been undertaken by another research group in the case of purely refractive microscale optics [14]. The difficulty inherent with this approach is the optomechanical alignment of the focus of the micro-lens with the ion location in a UHV environment which must survive bakeout to 200°C and possibly cryogenic temperatures.

The approach taken at GTRI is to integrate a micromirror into the center electrode between the RF rails. The micromirror collects a large NA cone of light from the ion,

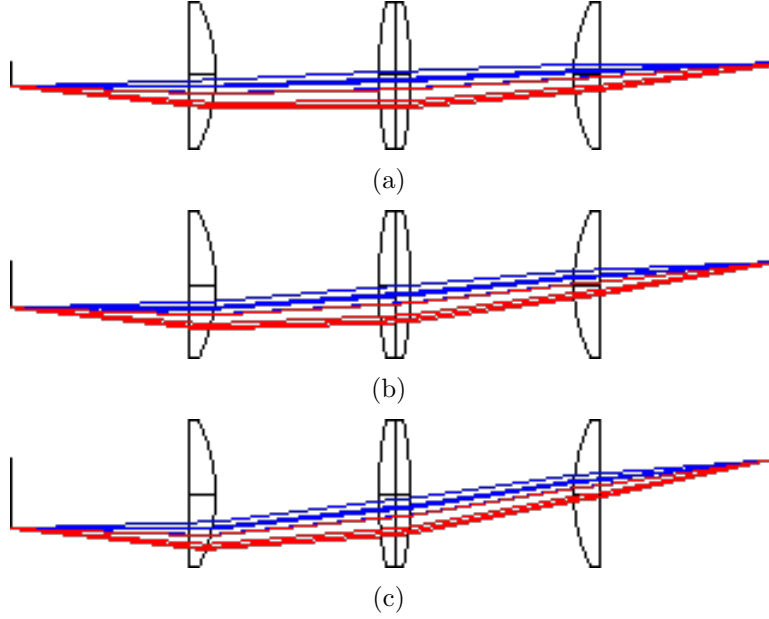


Figure 2.21: Illustrations of light cones produced by spherical micromirrors ( $50\ \mu\text{m}$  ROC) located off-axis relative to the collection lens. The blue rays are for a centered ion and the red rays are for an ion decentered by  $5\ \mu\text{m}$ . a) 4 mm off axis; b) 8 mm off axis defocus; c) 12 mm off axis.

which is then relayed to a detector using a single, large optical system. The same large optical system is capable of relaying light from many individual micromirrors to independent detectors. This approach is referred to as the “multi-scale” optical system. With this approach, the alignment of the optical focus and the ion is entirely the product of design and microfabrication of the trap and is not sensitive to thermomechanical misalignment.

### 2.6.1 Design and tolerancing of the multi-scale optical system

The multi-scale optical system was developed and toleranced under a separate program (ARMY/AMCOM W31P4Q05CR077-6156A) and is detailed in the final report for that program. The optical system is capable of collecting light from many micromirrors distributed across a 16 mm diameter trap surface. The system is highly insensitive to the figure of the mirror and misalignment of the ion from the mirror focus by up to 10% of the radius-of-curvature (ROC) of the mirror. No adaptive positioning of the detectors is required to compensate for micromirror figure or ion alignment errors within these ranges. An example of the alignment tolerance is shown in Figure 2.21 for three positions on the trap surface. The images clearly show that 100% of the light is collected in all cases.

### 2.6.2 Design of the ion trap incorporating a micromirror

It is critical to have an integrated design of the ion trap and the micromirror so that the two are compatible. In particular, the RF rails must be designed to place the ion at the correct



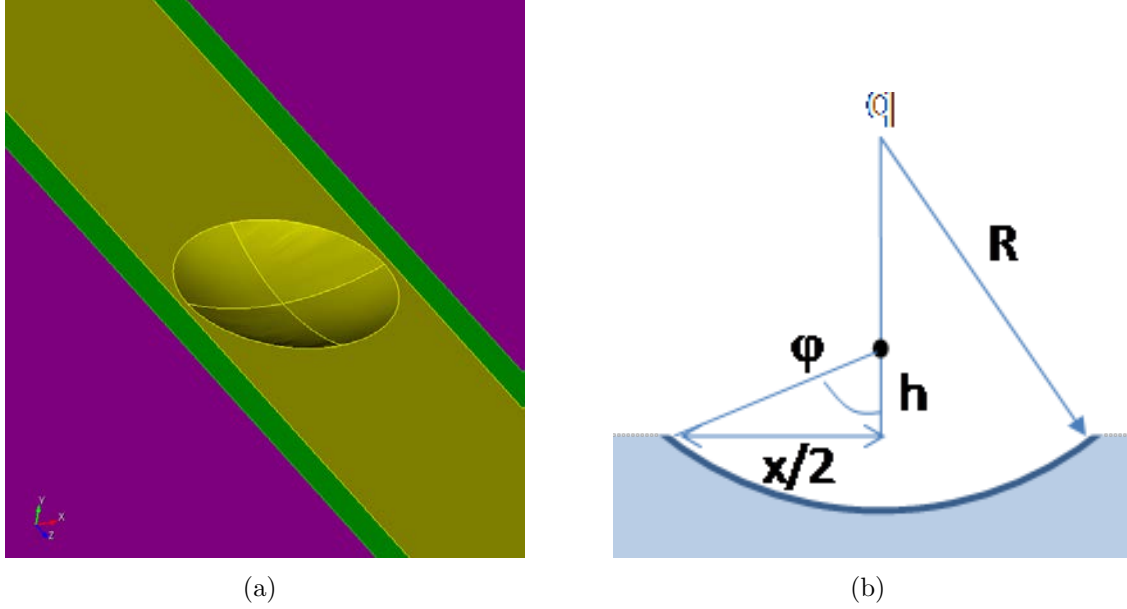


Figure 2.22: Illustration of the geometry of the trap and micromirror.

height and smooth the transition between the linear trapping region and the mirror. We started from a simple analytic model of the trap and then developed relationships among the critical parameters, including mirror curvature, ion height, and RF rail size and location for the design of simple mirror/trap combinations. These combinations are evaluated using GTRI's Method of Moments (MOM) electrostatics code, which is then used in conjunction with a genetic optimization algorithm to obtain a candidate trap design for fabrication.

Using the ground-plane analytic approximation, [8], the width,  $x$ , between two symmetric RF rails is found from:

$$x = \frac{2h(1 - \sin \theta)}{\cos \theta}, \quad (2.42)$$

where  $h$  is the ion height above the ground plane and  $\theta$  is the angular width of the rail seen from the ion (note that this angle is twice the angle used in [8]). The width of the RF electrode is found from

$$w = 2h \tan \theta. \quad (2.43)$$

For simplicity, we substitute  $\psi = (1 - \sin \theta)/\cos \theta$  at many points in this derivation. Also, the angle  $\alpha = (90 - \theta)/2$  is used to change the form over to  $\psi = \tan \alpha$ .

We now insert a micromirror tangent to the RF rails and calculate the relationship among the variables  $R$ ,  $h$ ,  $x$ , and  $\theta$  and the acceptance angle,  $\phi$ , illustrated in Figure 2.22.

Since the mirror radius is restricted to certain values by established fabrication processes, and the RF rail size is governed by electrostatic and fabrication constraints, we wish to calculate  $h$ ,  $x$ , and  $\phi$  as a function of  $R$  and  $\theta$ . First, there are two ways to calculate the sag of the mirror from the figure:

1. Add up the segments along the vertical axis of the figure to get  $\text{sag} = R/2 - h$ ;
2. Use the sag equation for a spherical mirror (slightly modified to account for using  $x/2$ ):  
 $\text{sag} = x^2/8R$ .

These two equations give us a second equation relating  $x$  and  $h$ :

$$x^2 = 4R^2 - 8hR; \quad (2.44)$$

Substitution of  $x$  from (2.42) gives

$$h^2\psi^2 + 2hR - R^2 = 0, \quad (2.45)$$

which can be solved for  $h$ :

$$h = \frac{R}{\psi^2} \left[ \sqrt{1 + \psi^2} - 1 \right].$$

This form can be simplified:

$$h = \frac{R}{\sec \alpha + 1}. \quad (2.46)$$

Note that  $h/R$  is a function only of the RF electrode angle. Therefore, the acceptance angle is independent of the radius of the mirror:

$$\phi = \frac{90 - \theta}{2} \quad (2.47)$$

The upper bound for the mirror acceptance angle,  $\phi = 45^\circ$ , is found when  $\theta = 0$  (NA = 0.71, 15% collection efficiency), which corresponds to a vanishing RF rail width. To complete the analysis, we choose a reasonable, but small, rail angle of  $\theta = 8^\circ$ ,  $\phi = 41^\circ$  (NA = 0.66, 12% collection efficiency).

Table 2.3 is a summary of results for a range of mirror curvatures using  $\theta = 8^\circ$ . All values are in  $\mu\text{m}$ .

Table 2.3: Ion height ( $h$ ), mirror aperture ( $x$ ), sag, and rail width ( $w$ ) for a range of mirror radii. All values are in  $\mu\text{m}$ .

$R$	$h$	$x$	sag	$w$
50	21.5	37.4	3.5	6.0
75	32.3	56.1	5.2	9.1
100	43.0	74.8	7.0	12.1
125	53.8	93.5	8.7	15.1
150	64.5	112.2	10.5	18.1
200	86.0	149.6	14.0	24.2

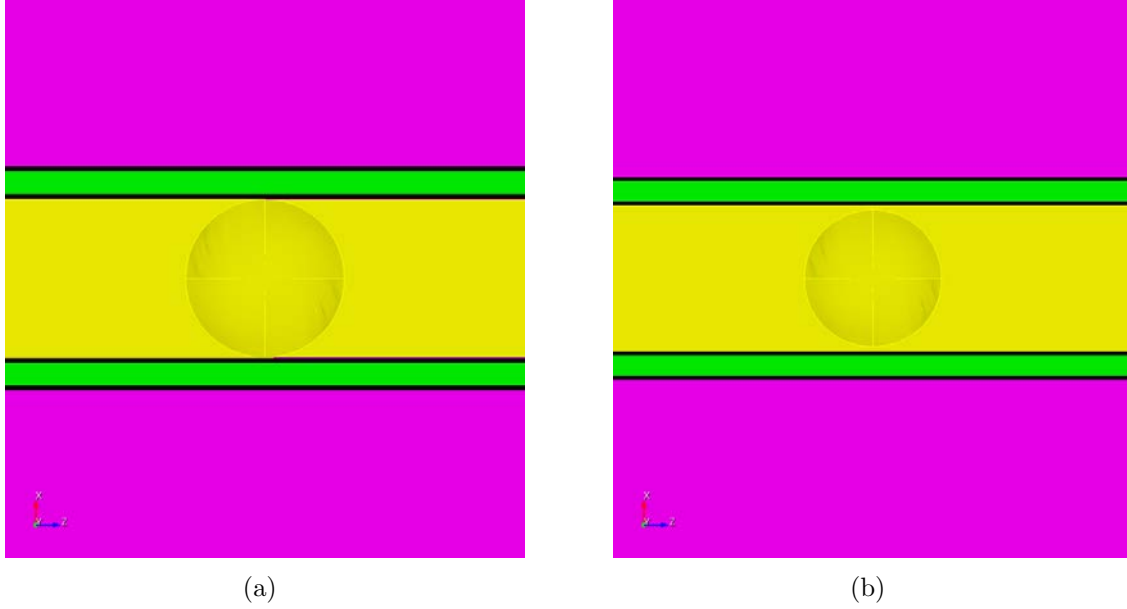


Figure 2.23: Geometry of a linear ion trap with  $4\ \mu\text{m}$  gaps between RF electrodes and grounds. The same geometry including a  $4\ \mu\text{m}$  shelf around the mirror.

These analytic results neglect the effect of the micromirror depression on the fields. The inclusion of the micromirror will lower the ion height and is therefore expected to somewhat improve the result.

**Surface ring trap** A similar analysis can be performed for a dimple tangent to a ring RF electrode. Once again, we neglect gaps between electrodes. The inner radius is given by [8]

$$r_1 = h \left[ 0.75 \sin^{-2}(\pi/6 - \theta) - 1 \right]^{1/2}$$

The form  $\phi = \arctan \sqrt{2} + \theta \sqrt{3/2}$  is very accurate near  $\theta = 0$  and is good to within  $1.5^\circ$  over the full range. The upper bound ( $\theta = 0$ ) gives  $\phi = 54.7^\circ$  (NA = 0.82, 21% collection efficiency). For a reasonable, but small rail angle,  $\theta = 8^\circ$ ,  $\phi = 45^\circ$  (NA = 0.70, 14% collection efficiency).

**Inclusion of gaps between electrodes** Now we wish to reexamine the linear ion trap derivation with the insertion of a gap of width  $g$  between the mirror and RF rail. This gap allows both for the addition of a flat ground electrode around the mirror (a “shelf” for allowance of fabrication misalignment; see Figure 2.23) and for gaps between the RF and ground electrodes (in the infinite ground-plane approximation, the electrodes are assumed to extend to the center of the gap, so the simulated gap is  $1/2$  of the real gap).

The ion height predicted by electrostatics is now given by

$$x + 2g = 2h\psi. \quad (2.48)$$

Table 2.4: Effects of gap size on trap parameters.

gap	$h$	$x$	sag	$w$	$\phi$	collection
0	43.01	74.8	7.0	12.1	41.0	12.3 %
2	43.58	71.8	6.4	12.2	39.5	11.4 %
4	44.17	68.8	5.8	12.4	37.9	10.6 %
6	44.76	65.8	5.2	12.6	36.3	9.7 %
8	45.38	62.9	4.6	12.8	34.7	8.9 %
10	46.00	60.0	4.0	12.9	33.1	8.1 %

Note that  $x$  is taken to be the diameter of the mirror, but is no longer the distance between the RF electrodes. This is combined with (2.44) to get

$$h^2\psi^2 + 2h(R - \psi g) - R^2 = 0, \quad (2.49)$$

where some terms have been dropped under the assumption that the gap is much narrower than half the spacing between the RF rails ( $h\psi \gg g$ ).

As before, this results in a quadratic solution for  $h$ :

$$h = \frac{-(R - \psi g) + \sqrt{(R - \psi g)^2 + \psi^2 R^2}}{\psi^2}. \quad (2.50)$$

This form can be simplified using Taylor expansions assuming  $R \gg \psi g$ :

$$h = \frac{R - \psi g}{\psi^2} \left[ 0.0607 + 0.3536\psi^2 \left( 1 + \frac{2\psi g}{R} \right) \right]. \quad (2.51)$$

The collection angle is given by

$$\tan \phi = \frac{1 - \sin \theta}{\cos \theta} - \frac{g}{h}. \quad (2.52)$$

The ion height still roughly scales proportional to  $R$ . The collection efficiency will improve slowly as the mirror radius increases. Table 2.4 shows the effect of varying gap size for  $R = 100 \mu\text{m}$ ,  $\theta = 8^\circ$ .

**Ion height scaling** When modeling a trap and mirror combination, there will be some discrepancy between the electrostatic null height and the focus of the mirror. The simplest approach to removing this discrepancy is to change the width of the RF rail ( $\theta$ ) while holding the mirror radius fixed. In our analysis, this is equivalent to holding the spacing between the rails ( $x$ ) fixed. This causes the mirror focus to stay at a fixed height while the electrostatic height changes. Differentiation of (2.42) gives

$$\frac{dh}{h} = \frac{d\psi}{\psi}$$

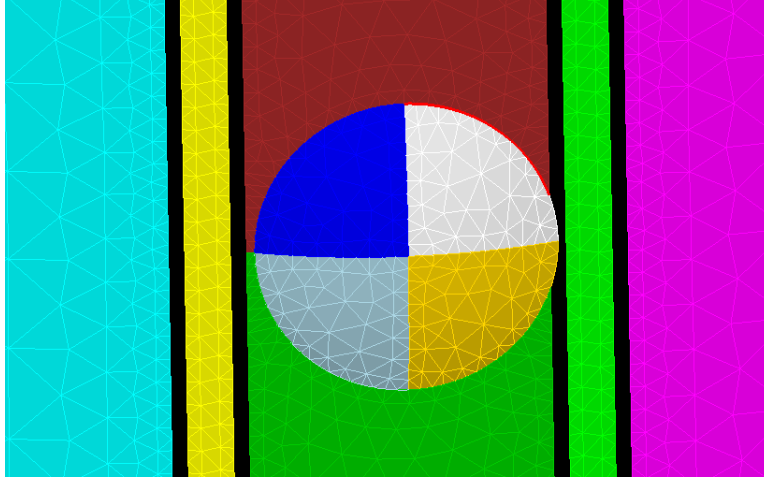


Figure 2.24: Center portion of the simulation geometry showing a  $2\ \mu\text{m}$  lateral shift in the mirror position.

The sign is correct since an increase in  $\psi$  will increase  $h$ . There is a convenient form for the right-hand side:

$$\frac{d\psi}{\psi} = d\theta \frac{\cos \theta}{1 - \sin^2 \theta},$$

where we note that  $d\theta$  is in radians. For any angle  $\theta$  less than 25 degrees, we can simply use

$$\frac{d\psi}{\psi} = d\theta$$

to less than 10% error. The fabrication of a trap with such large RF rails is unlikely considering equation (2.47). Therefore,

$$\frac{dh}{h} = d\theta \tag{2.53}$$

For example, if the physical height of the null is 5% too high, it is possible to decrease the angle of the electrode by 0.05 radians ( $2.9^\circ$ ).

**Simulation with electrostatic MOM code** Electrostatic simulations were used to tolerance the misalignment of the RF rails with the mirror and to refine the design of a trap for fabrication. In these simulations, the mirror shape is modeled as spherical.

First, we simulated the case of  $R = 100\ \mu\text{m}$ ,  $\theta = 8^\circ$  with  $4\ \mu\text{m}$  gaps. The expected ion height with these parameters is  $44.2\ \mu\text{m}$ . The observed height is  $43.4\ \mu\text{m}$ , for which the correction is to increase  $\theta$  to  $9^\circ$ .

Based on preliminary feedback from the fabrication team, the maximum misalignment of the mirror relative to the RF rails is expected to be  $2\ \mu\text{m}$ . A  $2\ \mu\text{m}$  lateral shift in the mirror position was simulated (Figure 2.24). Results show a  $0.12\ \mu\text{m}$  shift in the RF null location, indicating that such misalignments will not impact the functionality of the trap.

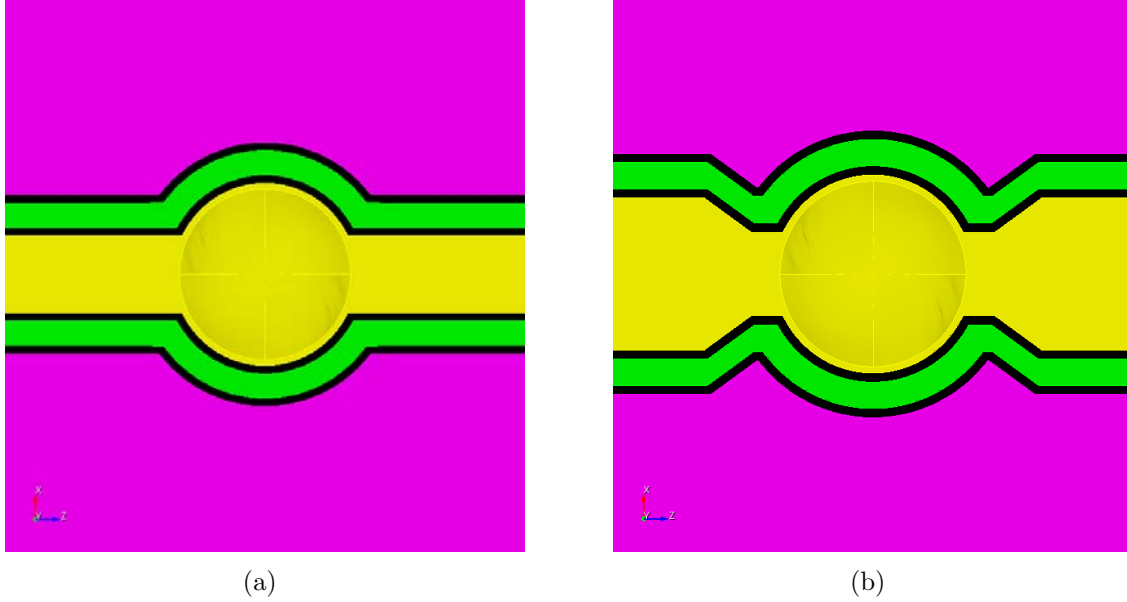


Figure 2.25: (a) A micromirror with wrapped RF rails. (b) The same micromirror with a taper to a linear section.

The fabricated trap will ideally have an ion height of  $63\ \mu\text{m}$ . Using  $\theta = 8^\circ$  with a  $7\ \mu\text{m}$  gap ( $4\ \mu\text{m}$  porch plus  $1/2$  of a  $6\ \mu\text{m}$  electrode spacing), the ideal ROC is  $142\ \mu\text{m}$ . The mirror diameter is  $96\ \mu\text{m}$ , the sag is  $8.1\ \mu\text{m}$ , and the collection efficiency is 10.2%.

For fabrication reasons (to be discussed), a sag of at least  $10\ \mu\text{m}$  was desired and for performance reasons, a greater collection efficiency was desired. Therefore, the size and ROC of the mirror were increased and the RF rails were allowed to wrap around the mirror (see Figure 2.25(a)). As before, slight adjustments of the RF rail widths are used to bring the RF null into alignment with the mirror focus. Note that the appearance of the mirror is something much closer to the mirror tangent to a ring RF electrode, which achieves slightly better collection efficiency.

This trap is The final trap parameters are  $R = 150\ \mu\text{m}$ ,  $x = 120\ \mu\text{m}$ ,  $h = 63\ \mu\text{m}$ , sag =  $12.5\ \mu\text{m}$ ,  $w = 17\ \mu\text{m}$ , geometric collection efficiency = 14%. The gaps around the RF rails are  $6\ \mu\text{m}$ . It is desirable to have the ion height over the mirror section match the ion height in the linear section. To accomplish this, a taper is added between the mirror and the linear section (Figure 2.25(b)). In the linear section, the RF rails are spaced by  $111.5\ \mu\text{m}$  (including gaps) for an ion height of  $62\ \mu\text{m}$ .

**Optimization of RF electrodes** The mirror trap is divided into three design regions based on the behavior of the RF rails: 1) the wrapping region, where the RF rail geometry is defined by the contour of the mirror; 2) the transition region, where the electrode shape can be optimized; and 3) the linear region, where the electrodes are straight. These regions are illustrated in Figure 2.26.

A genetic solver was used to optimize the shape of the RF electrode in the transition region. The objective of the optimization is to reduce the portion of the linear section

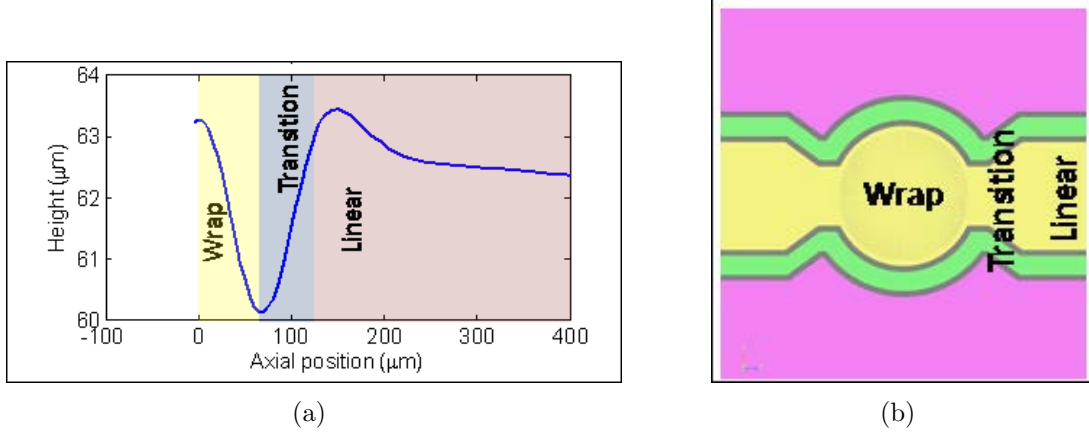


Figure 2.26: Illustration of the three design regions for the mirror trap. (a) plot of the height of the pseudopotential minimum for the geometry illustrated in (b).

which has too much micromotion to perform logical operations on ions while maintaining the alignment of the RF null and the mirror focus. The actual figure of merit is the distance from the mirror center to the last position where the axial pseudopotential is greater than some threshold.

The design resulting from this process is shown in Figure 2.28. Note the cross-axis misalignment of the mirror by approximately  $2\text{ }\mu\text{m}$ . The final trap design incorporating 21 segmented electrodes and a  $300\text{ }\mu\text{m}$ -long loading slot is shown in Figure 2.29. The entire center rail is grounded except for the narrow segment to the right of the mirror. The gaps between DC electrodes are  $4\text{ }\mu\text{m}$ . This trap uses the unsegmented top-level ground as in the Gen II linear trap. The fabrication process for these traps is described in Section 3.

**Characterization of micromirror figure** During process development, an effort was made to characterize the figure of the micromirrors. Two instruments were used. The first is a WYKO NT4400 phase-shifting profilometer. Because of the limited NA of its objective lens, the WYKO is capable of measuring only up to an NA of 0.38 (substantially smaller than the 0.7 NA of the fabricated mirror). The raw data for a mirror of nominal ROC  $150\text{ }\mu\text{m}$  is shown in Figure 2.30(a). Figure 2.30(c) shows both a spherical and parabolic fit to the raw data. Note that there is no difference between the two mirror figures over the measured NA. The residual P-V difference is  $0.5\text{ }\mu\text{m}$  for the spherical fit, as shown in Figure 2.30b.

The second instrument is the Olympus LEXT confocal microscope. This instrument is capable of measuring the entire surface of the mirror (Figure 2.31(a)), however, only data up to  $\text{NA} = 0.7$  is processed and shown in the figures. The LEXT measurement is very poorly matched to a sphere, but is well-represented by a combination of 2nd and 4th order terms. These results are suspicious because the measurement appears to include several artifacts, including a flat mirror bottom for the first  $8\text{ }\mu\text{m}$  radius, distinct Gibbs phenomenon at both the bottom and top of the mirror, and discontinuities in the height. A height discontinuity near the edge and center flatness can be seen in the residual mirror figure in Figure 2.31(b).

While the Wyko data is somewhat more trustworthy, we reserve final judgment on the

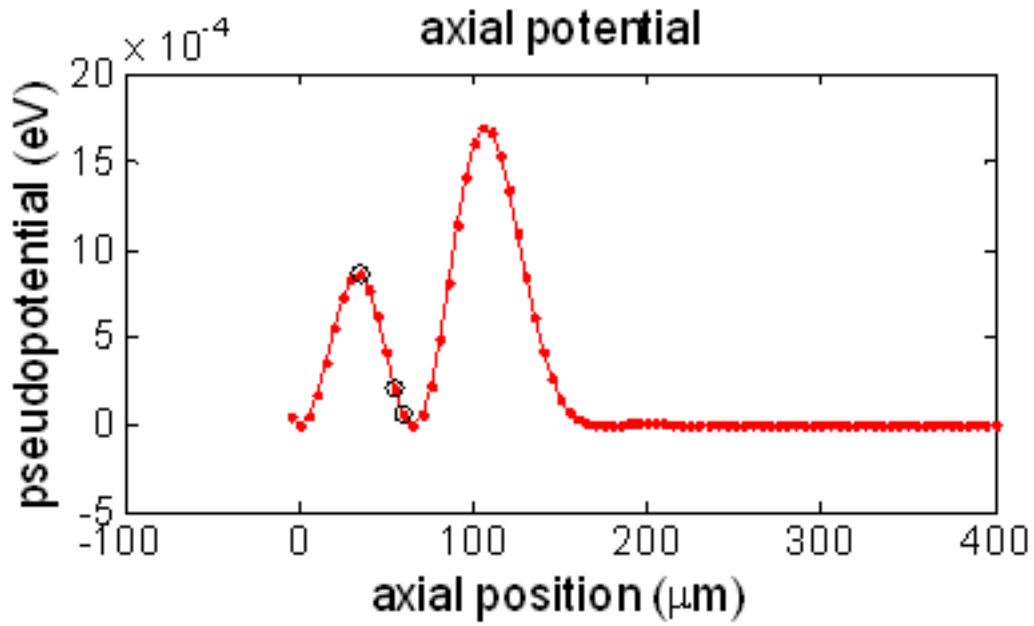


Figure 2.27: Residual pseudopotential along the RF tube for the trap shown in Figure 2.26. The center of the mirror is aligned with the zero of the axial position. There is a third pseudopotential hump centered at  $z = 200 \mu\text{m}$ .

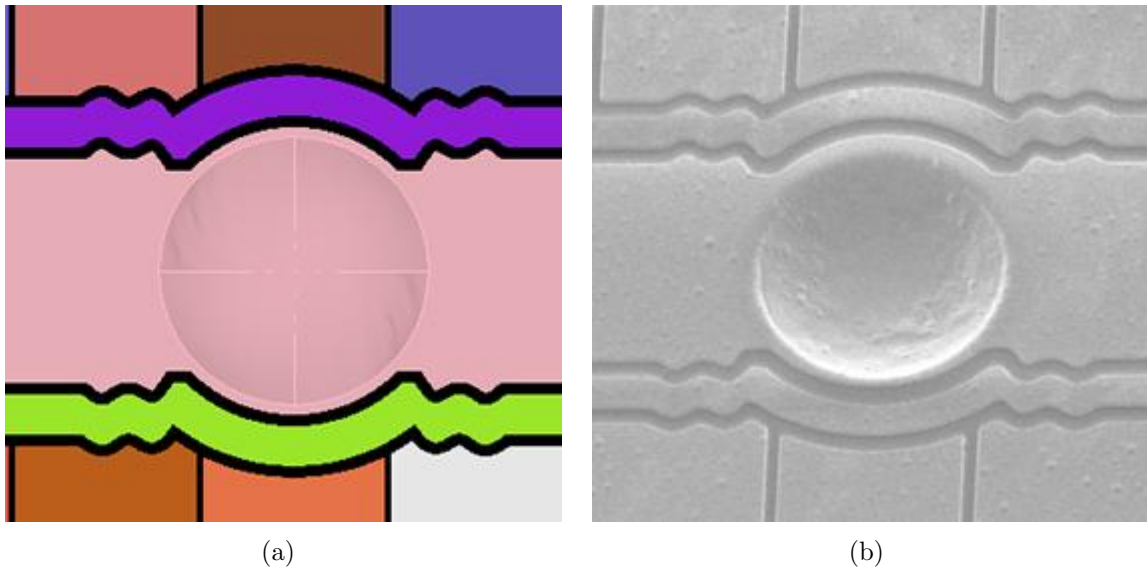


Figure 2.28: (a) Design of the micromirror trap. (b) SEM image of the micromirror trap from the lead wafer. Note that the surface is rough due to incomplete process development; this is corrected in following wafers.



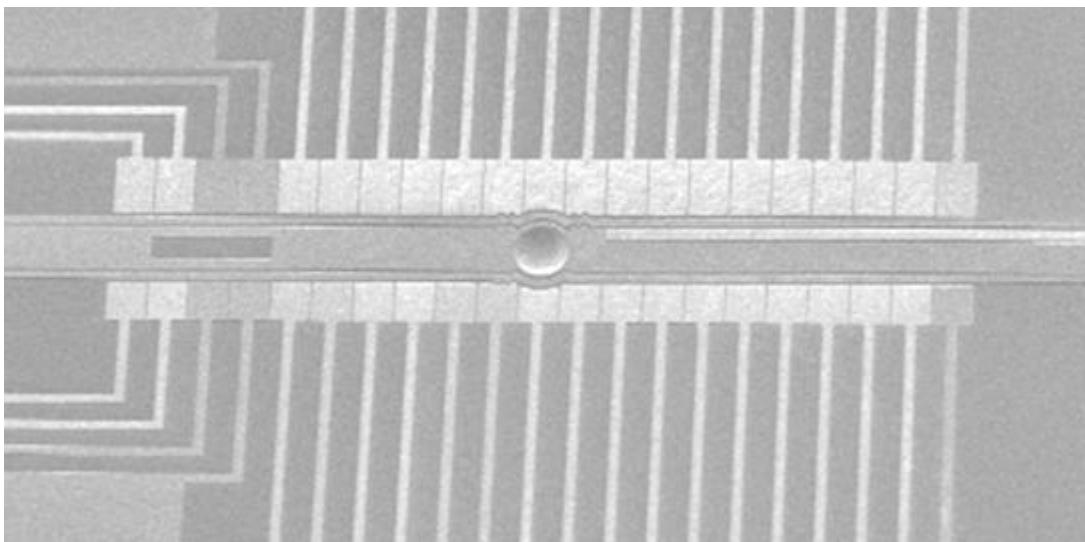


Figure 2.29: The electrode layer from the lead wafer.

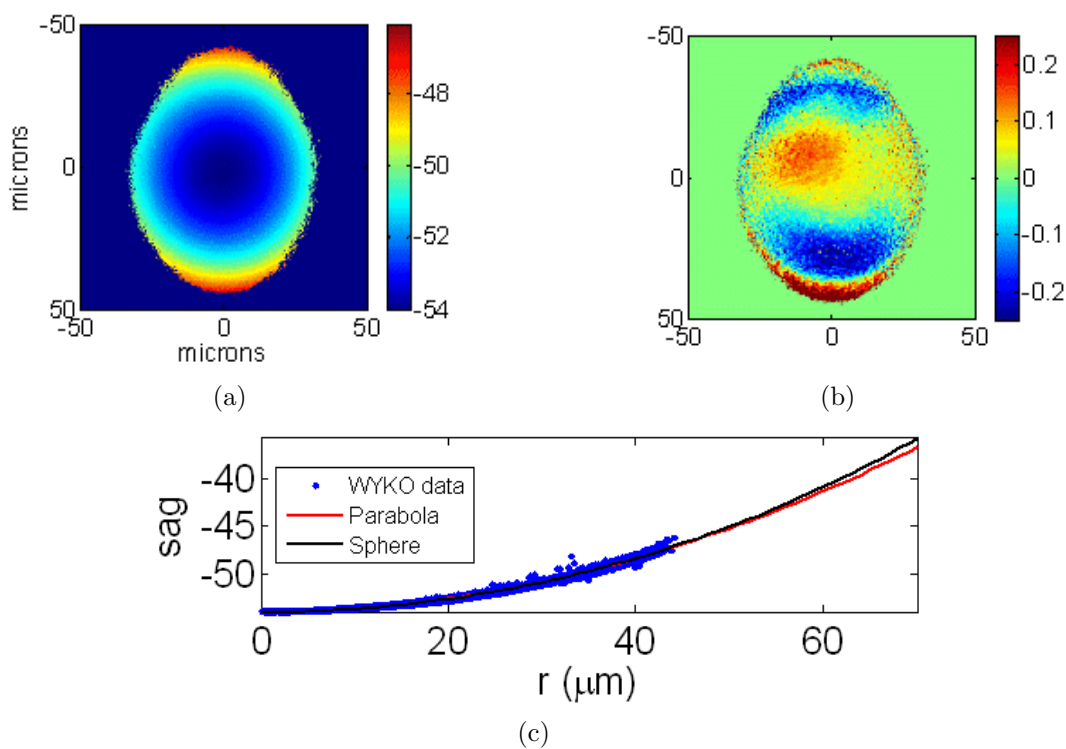


Figure 2.30: Characterization of mirror figure using the WYKO profilometer. (a) raw data; (b) residual to a spherical fit; (c) spherical and parabolic fits.

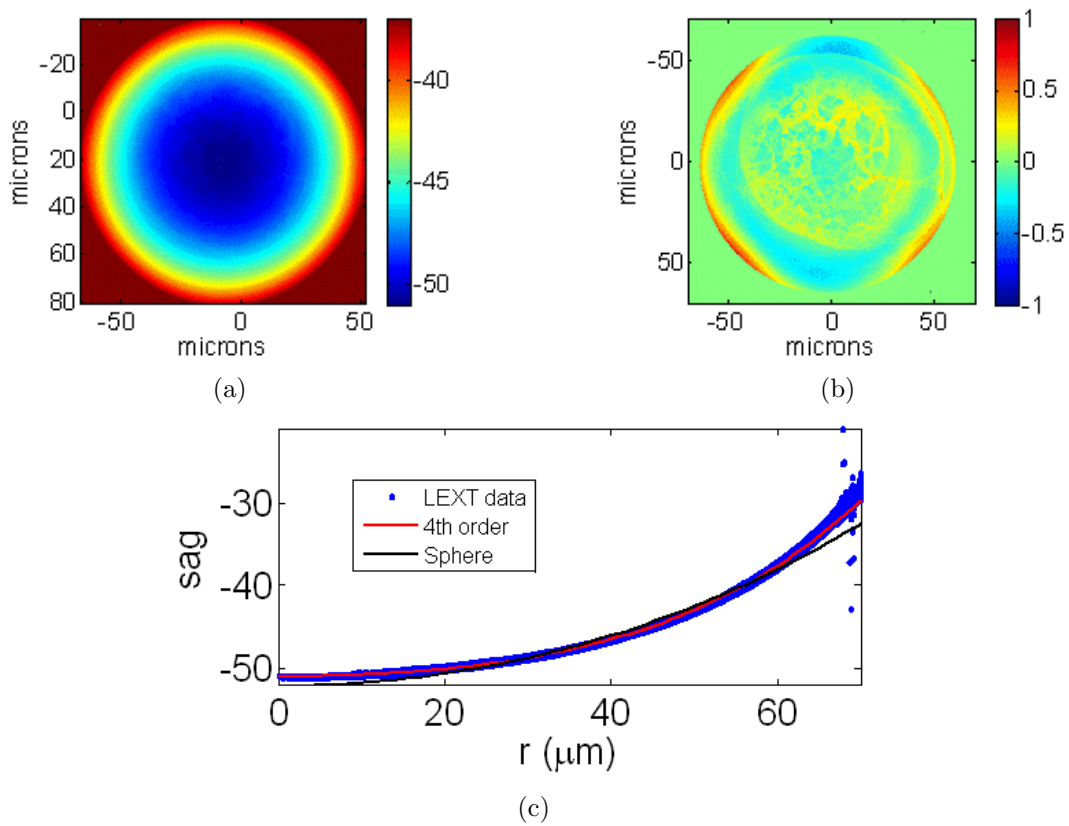


Figure 2.31: Characterization of mirror figure using the LEXT confocal microscope. (a) raw data; (b) residual to a 4th order fit (c) spherical and 4th order fits.

mirror shape until the discrepancies can be accounted for. Optical simulations indicate that neither mirror figure degrades the overall collection efficiency, so the determination of the exact figure is not a prerequisite to success of this trap.

## 2.7 Waveform Design

### 2.7.1 Field fitting waveform design

This approach to waveform design forms an adiabatic solution from an interpolated series of static field solutions. Each individual trapping location is solved independently from the field datacubes with constraints that impose the required location, frequencies, axis rotation, and minimum/maximum voltages. The notion of time is absent from these solutions. Adiabaticity of the final waveform must be adaptively imposed by optimizing the density of solved trapping locations, continuity of the voltages, and speed of the ion.

#### 2.7.1.1 Solving at a single ion location

The process of solving for voltages to form a single potential well begins with calculation of the RF pseudopotential from the electrostatic fields generated by the RF rails. We first define a plane in which the ion is to be trapped, then search for the point within this plane that is both radially confined and has the minimum RF pseudopotential. This point is then selected as the desired location of the ion in the well because the ion will exhibit minimum micromotion at this point.

In the case of uniform width, parallel RF rails, the RF pseudopotential forms an isotropic tube along the axis of the trap (the  $\hat{z}$  direction for this discussion). The plane defined for choice of trapping position is the  $XY$  plane at a given  $z$  location in the trap. Because the tube is isotropic,  $E_z$  is zero everywhere and there is no confinement of the ion in the axial direction (Figure 2.32(b-c)). Furthermore, the pseudopotential in the  $XY$  plane has degenerate principal axes (Figure 2.32(a)).

At the chosen trapping point, we wish to superimpose a DC electric potential on the RF pseudopotential. The sum of these two potentials is referred to as the secular potential. The DC electric potential serves three purposes:

1. confine the ion in the axial direction (create a 3D potential well)
2. position the ion at the location of minimum RF pseudopotential
3. achieve the desired ion secular motional principal axes and frequencies

#### 2.7.1.2 Design constraints

Because the excursion of a doppler-cooled ion in a well-designed trap is extremely small on the scale of field inhomogeneities, we choose to neglect electric field terms higher than linear in the optimization of the DC fields. Furthermore, the Coulomb interaction of ions is small enough to ignore so long as multiple ions are not trapped in a single well. Under this

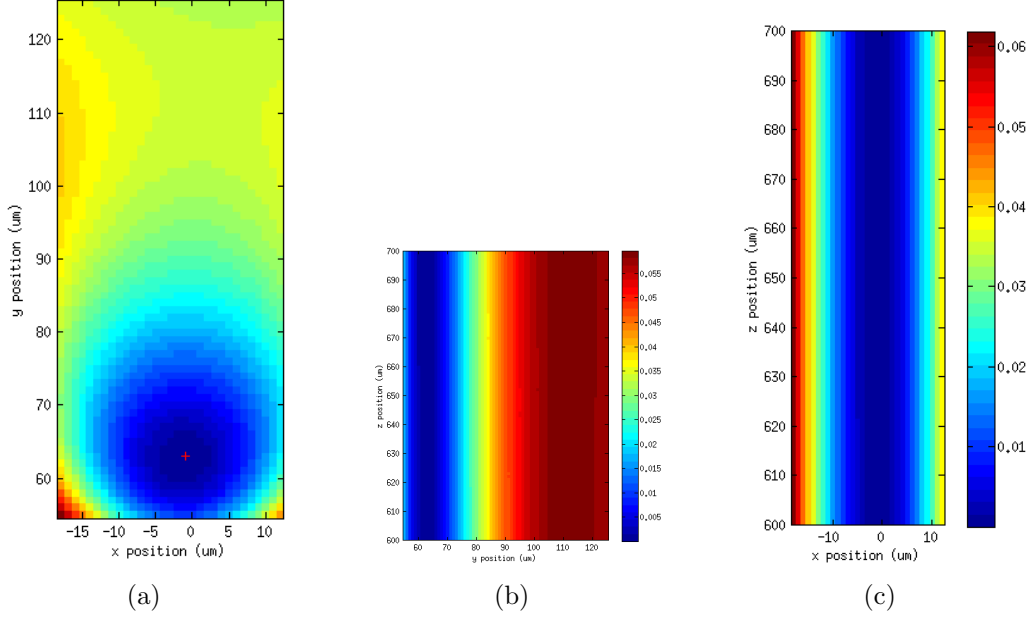


Figure 2.32: Slices of pseudopotential from an isotropic ion trap (SMIT Gen II).

assumption, there are twelve terms that are kept in the optimization (three field values and nine vector field derivatives):

$$\mathbf{E} = \{E_x, E_y, E_z\} \quad (2.54)$$

$$\frac{d\mathbf{E}}{d\mathbf{r}} = \begin{Bmatrix} \partial E_x / \partial x & \partial E_x / \partial y & \partial E_x / \partial z \\ \partial E_y / \partial x & \partial E_y / \partial y & \partial E_y / \partial z \\ \partial E_z / \partial x & \partial E_z / \partial y & \partial E_z / \partial z \end{Bmatrix} \quad (2.55)$$

For static fields in the absence of charge, we can impose constraints using the Maxwell-Faraday equation ( $\nabla \times \mathbf{E} = 0$ ) and Gauss' law ( $\nabla \cdot \mathbf{E} = 0$ ):

$$\begin{aligned} \partial E_x / \partial y &= \partial E_y / \partial x \\ \partial E_x / \partial z &= \partial E_z / \partial x \\ \partial E_y / \partial z &= \partial E_z / \partial y \end{aligned} \quad (2.56)$$

$$\partial E_x / \partial x + \partial E_y / \partial y + \partial E_z / \partial z = 0. \quad (2.57)$$

Therefore, four of the twelve terms are redundant. Since we only require confinement in the  $\hat{z}$  direction, we can neglect both  $\partial E_x / \partial x$  and  $\partial E_y / \partial y$  as long as the two values are not equal (to break the degeneracy of the principal axes). This leaves seven terms, or constraints, in the optimization of the DC potential well.

The geometry of the trap can be used to further reduce the degrees of freedom for a given DC solution. When the DC electrodes are uniformly spaced and of equal size, using DC solutions that are symmetric about the  $XY$  plane imposes three constraints:

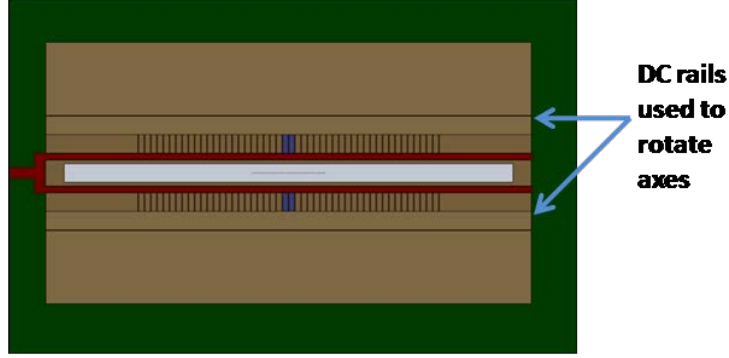


Figure 2.33: The Gen III trap that will be fabricated under the MUSIQC program. The DC rails outside the control electrodes help to rotate the axes.

$$\partial E_z / \partial z = 0; \quad \partial E_z / \partial y = 0 \quad E_z = 0 \quad (2.58)$$

Such symmetries are available when trapping either at the center of a DC electrode or at the center of the gap between two DC electrodes (see Figure 2.42(a), Figure 2.42(b)). In this case, one of the DC principal axes is aligned with the RF tube. This alignment minimizes crosstalk between micromotion and secular motion by eliminating micromotion along the lowest-frequency secular axis, and minimizes coupling between secular modes induced by micromotion. Finally, this arrangement means that the secular principal axes are equivalent to the DC principal axes (recall that the radial RF axes are degenerate).

When using  $z$ -symmetry, we optimize a DC potential well with only four constraints ( $E_x$ ,  $E_y$ ,  $\partial E_y / \partial x$ , and  $\partial E_z / \partial z$ ). The third term induces rotation of the principal axes in the  $XY$  plane. Since Doppler cooling only cools ion motion along the direction of the laser, any secular principal axis perpendicular to the laser will not be cooled. Surface traps that do not allow beams to pass through the chip must be cooled by lasers parallel to the surface of the chip. Therefore, rotation in the  $XY$  plane is required to Doppler cool ions.

Geometric asymmetry in the cross-axis direction ( $\hat{x}$ ) can impose the necessary axis rotation if properly designed. Candidates for good asymmetry include breaking the center DC electrode into two halves (one of which can be grounded), or adding two fixed-potential DC rails outside of the segmented DC electrodes. The SMIT Gen II trap is an example of the former solution. The natural axis rotation is approximately  $25^\circ$ . The Gen III trap (the linear trap that will be fabricated for the MUSIQC program; Figure 2.33) is an example of the latter technique, in which variable axis rotation is achieved by placing equal and opposite potentials on the outside rails.

It is possible to design traps that geometrically constrain both radial compensation terms at selected points, leaving only one constraint on the optimization of DC potentials ( $\partial E_z / \partial z$ ). Such solutions are novelties since, in practice, additional constraints are required to move ions between the select points and experimental compensation of the DC well always requires at least three degrees of freedom.

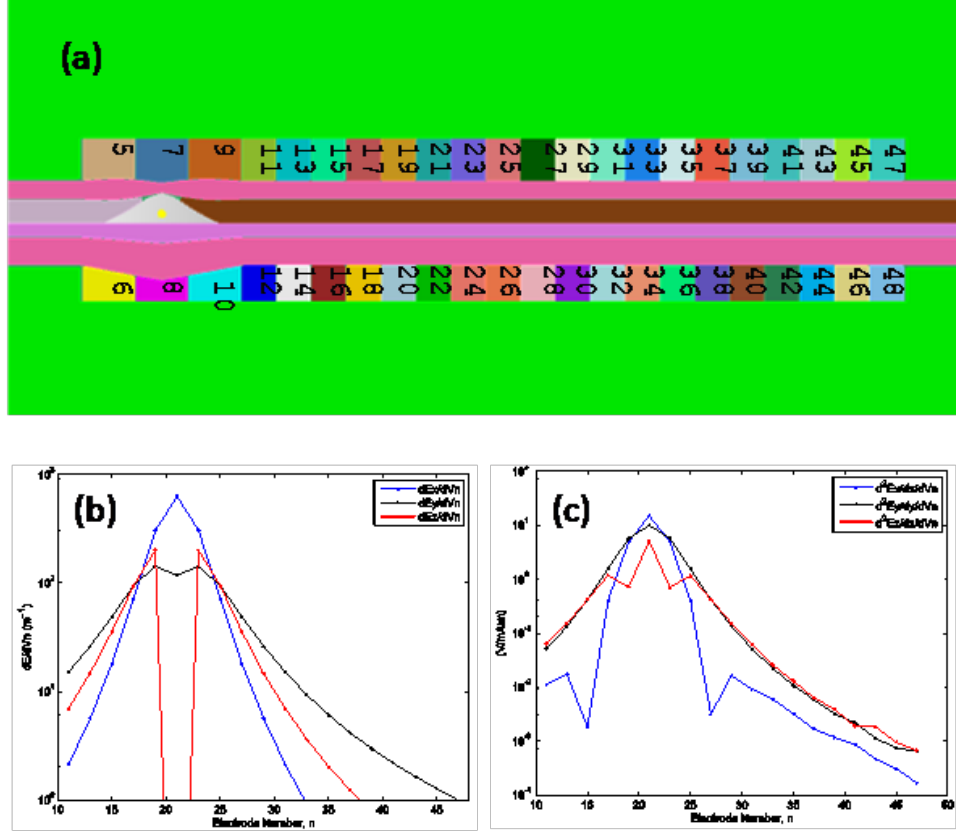


Figure 2.34: (a) Gen II trap. (b) The DC electric field vs. 1V applied to a electrode 17. The evaluation point is at the RF null position in the transverse plane at the middle of electrode 21 in the gen-II ion trap. (c) The derivatives of the DC electric field vs. 1V applied to a given DC electrode. Absolute value of the fields is plotted in both cases.

### 2.7.1.3 Design degrees-of-freedom

Having defined the constraints on the DC potential solution space, it is now important to define the degrees-of-freedom available for satisfying those constraints. We have not performed a thorough study on this subject. However, we know in practice that the potential on an electrode close to the ion represents one degree of freedom. As we move to electrodes further from the ion we eventually reach some point at which their contribution is either too weak (as limited by the maximum allowable voltage) or too redundant (with their immediate neighbor) to be useful. For example, Figure 2.34(a) shows the electric field generated at a single evaluation point by applying 1V of electric field to each electrode along one side of the Gen II ion trap. The fields are observed to drop rapidly moving away from the nearest electrodes (approximately 5, 2.5, and 3 dB/electrode for  $E_x$ ,  $E_y$ , and  $E_z$ , respectively). Such precipitous decline means that applying a voltage to any particular electrode (e.g., 25) has a greater effect than applying a voltage to all electrodes further away than that electrode (27-47). Substantially faster falloff is observed for the field derivatives shown in Figure 2.34c.

In ion traps fabricated under SMIT, the DC electrode axial length is generally chosen to

be within a range of 80% to 133% of the height of the ion. Using this design rule ensures that there is an abundance of degrees-of-freedom available to solve the problem.

A trap can also have an unsegmented DC electrode. Because the RF tube is isotropic, this electrode can act as a useful degree-of-freedom for all positions (simultaneously) along the trap.

In the interest of maintaining high ion density, we wish to design traps so that a single potential well occupies the minimum length of linear section. To date, all traps manufactured under SMIT have two segmented DC rails. For such traps, a well cannot occupy less than three electrode lengths in order to both satisfy the required number of design constraints (3 or 4 including symmetry) and allow shifting of the wells. For the remainder of this section, a “zone” in a trap refers to three consecutive electrode lengths. A zone possesses six segmented electrodes and may share one or more unsegmented DC electrodes with the rest of the linear section. When trapping the ion at the center of the zone using symmetric potentials, a zone possesses four degrees of freedom (plus shared DOF from any unsegmented rails). In a geometrically rotated trap (such as the Gen II trap), this means that at least one degree of freedom is unused. This extra DOF can be used to minimize crosstalk between neighboring zones on the trap.

#### 2.7.1.4 Crosstalk analysis

In an ion trap containing many ions in many wells, the design of waveforms is easiest if sequential wells can be said to exhibit no crosstalk. That is, voltages can be designed to move ions independently of the presence of neighboring ions. In practice, crosstalk is manifested as a change in position, compensation, or secular frequency of one ion when a second ion is moved into the neighboring zone on the linear section. Slight changes in the absolute axial position are irrelevant since there is no measurable error induced by such a shift. Slight changes in secular frequencies are also tolerable as long as multi-qubit gates are not being performed. Therefore, the most important manifestation of crosstalk is induced micromotion due to decompensation of the neighboring ion. As discussed earlier, micromotion is undesirable because it increases secular heating, mixes motional modes, and alters the efficiency of gates, readout, and other single-qubit operations due to induced sidebands on optical transitions.

A simulation demonstrating low crosstalk for a Gen II SMIT II trap is shown in Figure 2.35. A trap is first formed using three contiguous pairs of electrodes along a linear portion of the trap (electrodes 17-22 in Figure 2.36). This results in a very small  $\beta$  [15], where  $\beta$  is a measure of the amount of micromotion at the trapping position. For example, when  $\beta = 1$ , the micromotion induced Doppler shifts are sufficient to noticeably broaden the ion fluorescence spectrum and reduce the laser cooling efficiency. The  $\beta$  value for a single optimized three electrode trap is shown as the yellow triangle in Figure 2.35. The low  $\beta$  value of 0.14 is limited by a lower bound associated with the numerical accuracy of the simulation program ( $\beta < 0.25$  is generally considered acceptable for all but the most complex multicubit gate operations).

Next we consider the case where a second ion is trapped in a nearby potential formed by the next series of three electrodes in the linear chain (Zone 2 in Figure 2.36). We assume that this three electrode combination uses the same trapping voltages as used for the initial

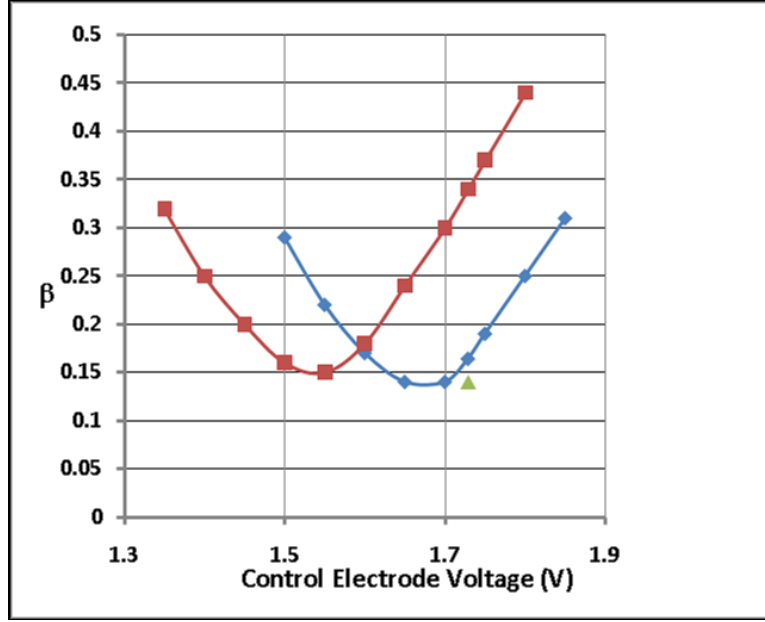


Figure 2.35: Beta as a function of a control electrode voltage for the linear section a Gen II SMIT II trap. The yellow triangle is the low  $\beta$  value obtained by an optimization algorithm. The value of beta has a lower limit of 0.14 due to numerical limits imposed by model fidelity and field interpolation. The trapping voltages are for a series of three electrode pairs. These voltages are then applied to the neighboring three electrodes as if one were trapping an ion in a well next to the initial well. The resulting  $\beta$  values as a function of compensating voltage on two electrodes of the initial trap are shown by the orange points and curve (a guide to the eye). If the neighboring trap is moved one further electrode width away from the initial trap, very small compensating voltages ( $<3\%$ ) are required to restore the initial small  $\beta$  value as shown by the gray points and curve.

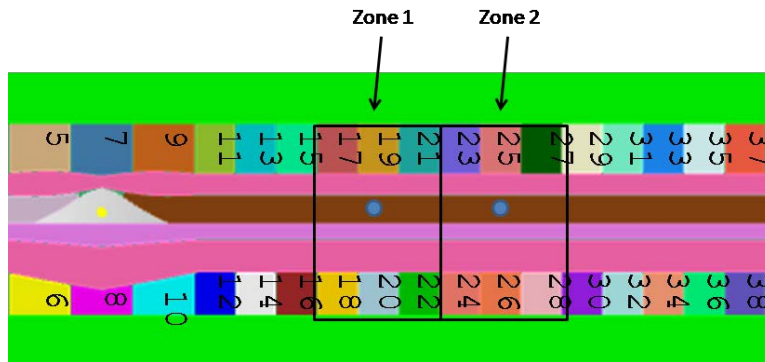


Figure 2.36: The Gen II trap was used for a crosstalk study. An ion was trapped in Zone 1. When a second ion was trapped in Zone 2, the influence on the second ion was measured and compensated by adjusting the voltage on electrodes 17 and 21 (which are the same, by design).



trap. After turning on the voltages to this second trap, we observe that the  $b$  value increases to 0.34 (red square at 1.73V), slightly in excess of the tolerable level.

Now we use the extra degree of freedom to adjust the initial trap to compensate for this increased micromotion. A decrease in the compensating voltage used on electrodes 17 and 21 (their voltages are the same by design) from 1.73 to 1.55 V restores the low  $\beta$  value, a change of  $\sim 10\%$ . The control electrode widths in the Gen II trap are  $80\text{ }\mu\text{m}$ , so that the distance between trapping position in this case is  $240\text{ }\mu\text{m}$ . Moving the neighboring trap position one further electrode away (using electrodes 25-30 to define the trapping zone) from the initial trap results in the gray points and curve in Figure 2.35. Now the fraction change in compensating voltage is less than 3% for an ion separation of  $320\text{ }\mu\text{m}$ . Although we have not compared the simulation to experiment, the agreement between simulation and experiment has been extremely good in SMIT II. It appears that we have essentially met our goal for crosstalk during SMIT II.

#### 2.7.1.5 Static voltage design suite

A MATLAB script was written to solve for DC voltages at single points in the trap as outlined in the previous sections. The code is highly configurable (dozens of optional input parameters and several operational modes) and generates 15 useful plots and large quantities of summary data about the solutions. Therefore, a detailed explanation is beyond the scope of this report. In brief, this code incorporates the following capabilities:

1. specification of each of the 12 optimization constraints, with individual allowances for removing offsets introduced by the RF pseudo-fields
2. least-squares solver generates the solution with the minimum required voltages to satisfy the given problem
3. imposition of electrode symmetry
4. predefined voltage offsets on solved and unsolved electrodes
5. calculates null location, principal axes, secular frequencies, micromotion, sideband parameter ( $\beta$ )
6. deliberate offsets of the DC null from the RF minimum, secular minimum from the RF minimum
7. analysis of axial, radial, and 3D well depth
8. analysis of the RF well anisotropy
9. readily used as a kernel for iterative optimization of voltages

#### 2.7.1.6 Generation of smooth waveforms

Adiabatic waveforms are generated by interpolation of a series of static field solutions. Fast motion of the ion through the trap requires a smooth static voltage profile. In the presence of voltage discontinuities, the ion must be brought to a complete stop to preserve adiabatic motion. Similarly, slope discontinuities in the voltages require acceleration of the ion to maintain adiabaticity. If these discontinuities are removed, the ion is allowed to travel at constant (maximum) velocity limited only by the cutoff frequency of the low-pass DC filters and update rate of the DACs (although deconvolution of the voltages by the update rate and low-pass transfer functions can at least partially overcome this limit).

#### 2.7.1.7 Choice of trapping locations

In order to move the ion, we must first construct a set of cardinal points between which the voltages will be interpolated. General guidance is to select points such that any positive-definite-scaled linear interpolation of the voltages from neighboring points form a trapping location along the RF null between those two points (i.e., neighboring solutions form a convex set in the space of valid trapping solutions between them). In an isotropic linear section, this requirement is generally satisfied by choosing sequential points that are spaced by half of an electrode width. In more complex traps (junctions, loading slots, tapers, etc.), we add the additional constraint that no significant pseudopotential maxima and minima occur between the selected points.

For the linear section of the trap, there are two convenient choices for the initial set of trapping locations based on maximizing symmetries. In the first case, as shown in Figure 2.42(a), we choose three pairs of electrodes and place the ion in the center of the middle pair. For the second case, we may use four pairs of electrodes and choose the location halfway between the inner electrodes. This situation is illustrated in Figure 2.42(b). This choice of trapping points is further useful in that these are the exact locations where electrodes are turned on/off to maintain the three-electrode width of a single well.

#### 2.7.1.8 Linear interpolation

In the first interpolation example, we impose linear interpolation on all electrodes that are either being turned on or off between two initial solve positions. The voltages on remaining electrodes are solved to maintain the compensation of the ion. The first attempt resulted in ragged potentials (Figure 2.37(a)). Close analysis of the result indicates periodicity in the same frequency as the datacube sampling (10  $\mu\text{m}$   $z$  sampling in this case). A sampling size of 1  $\mu\text{m}$  was required to reduce this artifact to an acceptable level (Figure 2.374(b)). This study was the basis for settling on a 1  $\mu\text{m}$  grid size for all future waveform design.

#### 2.7.1.9 Cubic interpolation

The voltages designed using linear interpolation have no discontinuities. However, they exhibit discontinuities in the slope of the voltages that will limit the ion velocity. These slope discontinuities are readily removed by using a piecewise cubic spline interpolation method. (Figure 2.38). The interpolation is applied to all electrodes at each solve point,

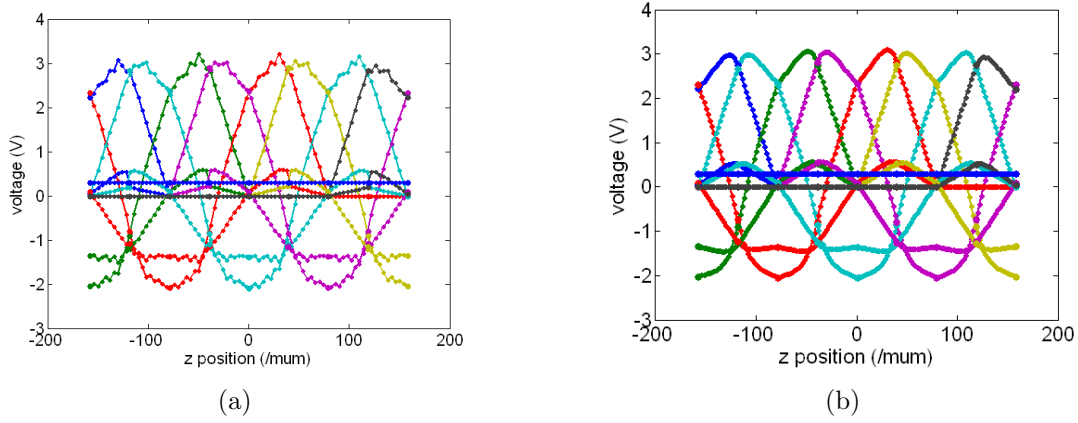


Figure 2.37: Waveforms designed with linear interpolation (Gen II trap). Larger dots indicate initial solve points, small dots indicate interpolated points. (a) inadequate spatial sampling in the datacube. (b) increased sampling. The absolute  $z$  position is different from Gen II results shown elsewhere since this simulation uses a different datacube.

and the voltages on all electrodes are solved (except the center rail, which is held fixed for axis rotation).

Waveforms generated using this approach were successfully evaluated in GTRI’s numerical motion solver and in several ion traps. The results of the numerical simulation are shown in Figure 2.39.

## 2.7.2 Waveform design with the particle swarm optimization

The Particle Swarm Optimization (PSO) method, like the Genetic Algorithm (GA), is an evolutionary optimization technique capable of finding a global minimum in a complex search space. It was developed by Eberhart and Kennedy in 1995 after the pair applied observations of flocking species in search of food sources to mathematical search problems [16]. Hence, the algorithm operates by generating a random population of guesses about the correct answer to a given problem. These guesses (called particles) are evaluated according to a user-defined fitness function which quantifies the quality of the solution in a single or a handful of fitness values. The particles then proceed to “fly” through the search space, evaluating their fitness value at each new point in the search space.

The position of each particle is updated according to

$$\mathbf{x}_{n+1,j} = \mathbf{x}_{n,j} + \Delta t \mathbf{v}_{n,j}, \quad (2.59)$$

where  $n$  is the current iteration number,  $\mathbf{x}_{n,j}$  is the vector of parameter guesses at iteration  $n$  for the  $j^{th}$  particle,  $\Delta t$  is the timestep which is usually just normalized to 1, and  $\mathbf{v}_{n,j}$  is the velocity. The velocity update equation is the cornerstone of the PSO process and controls the ultimate rate of convergence and quality of the final answer. In most PSO implementations, the velocity is given by

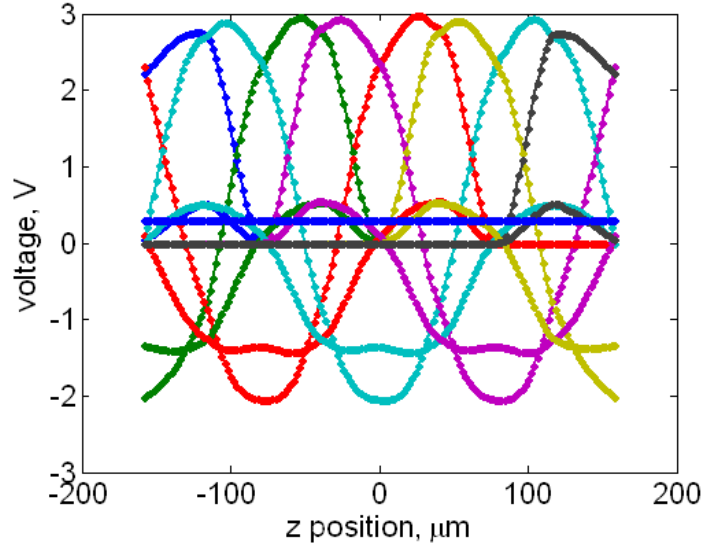


Figure 2.38: Voltage waveforms designed using a piecewise cubic spline interpolation method.

$$\mathbf{v}_{n+1,j} = w_i \mathbf{v}_{n,j} + w_p \text{rand}(0, 1) (\mathbf{x}_n^{\text{best}} - \mathbf{x}_{n,j}) + w_s \text{rand}(0, 1) (\mathbf{g}^{\text{best}} - \mathbf{x}_{n,j}) \quad (2.60)$$

where  $w_i$  is an inertia weighting parameter,  $w_p$  is a personal weight parameter,  $\text{rand}(0, 1)$  is a uniform random number generator,  $w_s$  is a social weight parameter,  $\mathbf{x}_n^{\text{best}}$  is the  $n^{\text{th}}$  particle's personal best-ever parameter set, and  $\mathbf{g}^{\text{best}}$  is the entire population's best-ever parameter set. An example of how a particle might move from one iteration to the next is illustrated in Figure 2.40. The step is decomposed into the vector contribution from each component of the velocity update equation. The presence of the random number generators introduces a “mood” for each particle since at any given time the particle may be heavily influenced by their personal best parameter set and/or the best solution found thus far by the entire population. In any case, the particle will have some inertia governed by the  $w_i$  parameter to encourage the particle to explore a region where it was already intending to go.

After a number of iterations, the population will converge to a common point which may be the globally best solution in the search space. Often though, it helps to invoke a restart mechanism in which the particles are reinitialized to promote further exploration. This is particularly useful for high dimensionality search spaces and problems with many local minima.

For designing waveforms, the particles are taken to be  $N$  basis functions on  $M$  electrodes for a total of  $N \times M$  particles. The basis functions are staggered triangles that represent a voltage waveform on a given electrode; the amplitude of each triangle is the variable parameter in the PSO. For a segment of time, the desired trajectory of the ion is defined and the PSO is used to find the waveform amplitudes that place an ion as close to the desired trajectory as possible. This approach has been successfully used to find waveforms for shuttling an ion in a linear trap with segmented RF rails (where the segments have the dual

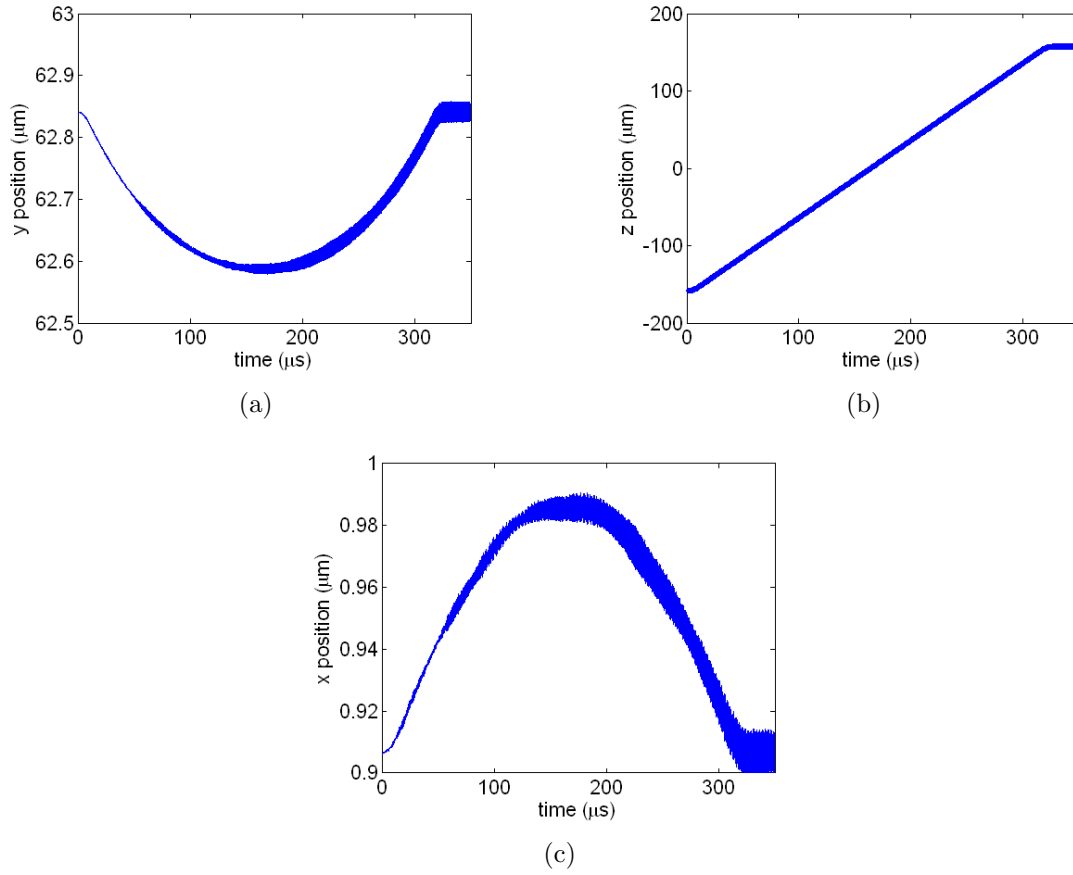


Figure 2.39: Motion predicted by numerical motion simulation model for cubic interpolated voltages. The accumulated secular motion is an artifact of the interpolation technique used by the motion solver.

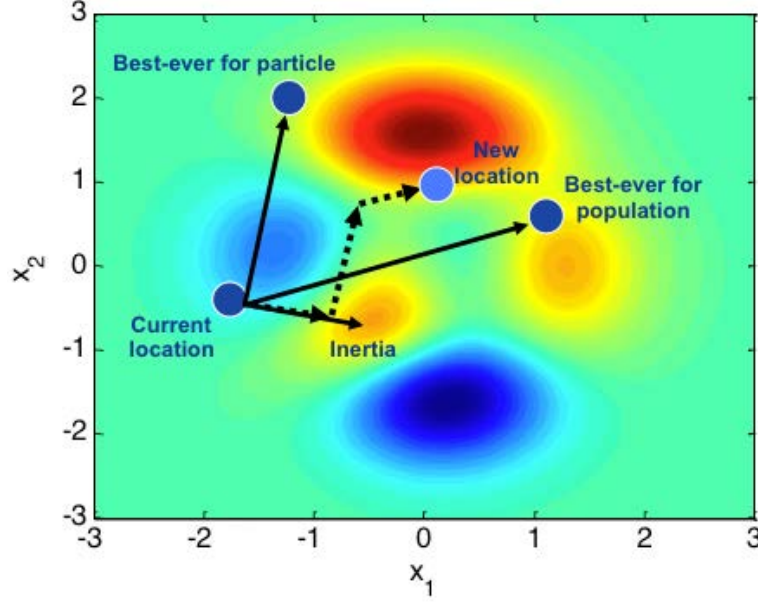


Figure 2.40: The three-component velocity update for the PSO is composed of a weighted inertia term, a randomly weighted personal best term, and a randomly weighted population best term.

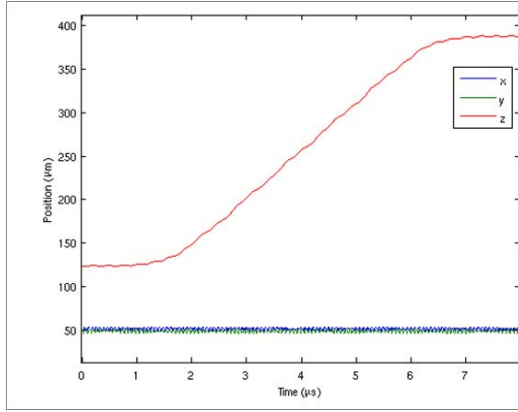
purpose of carrying RF and control voltages) and a cross junction. The cross junction results where given in Figure 2.17 and the linear trap results are given in Figure 2.41. Although the PSO gives valid shuttling waveform solutions, its dependence on the calculation of ion motion for each PSO particle leads to long run times; furthermore, there is no mechanism implemented to test higher-order properties of the ion motion, such as constant secular frequency. In the next section, we discuss an automated waveform generation technique that overcomes these limitations.

## 2.7.3 Waveform design automation

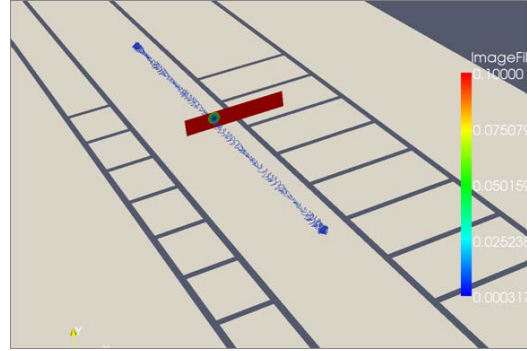
### 2.7.3.1 Choice of trapping locations

The field fitting approach of Section 2.7.1 has been generalized and automated for transport in linear sections and cross junctions. For the linear section of the trap, there are two possibilities for the initial set of trapping locations. In the first case, as shown in Figure 2.42(a), we choose three pairs of electrodes and place the ion in the center of the middle pair. For the second case, we may use four pairs of electrodes and choose the location halfway between the inner electrodes. This situation is illustrated in Figure 2.42(b). These key locations allow us to construct a set of fields with the proper symmetries.

For the fabricated junction that will be considered here, we must also include the corner electrodes in the intersecting region. The layout of the junction is seen in Figure 2.43. We assume a coordinate system with the origin at the center of the junction, a z-axis along the length of the trap and an x-axis running horizontally along the two junction legs. The

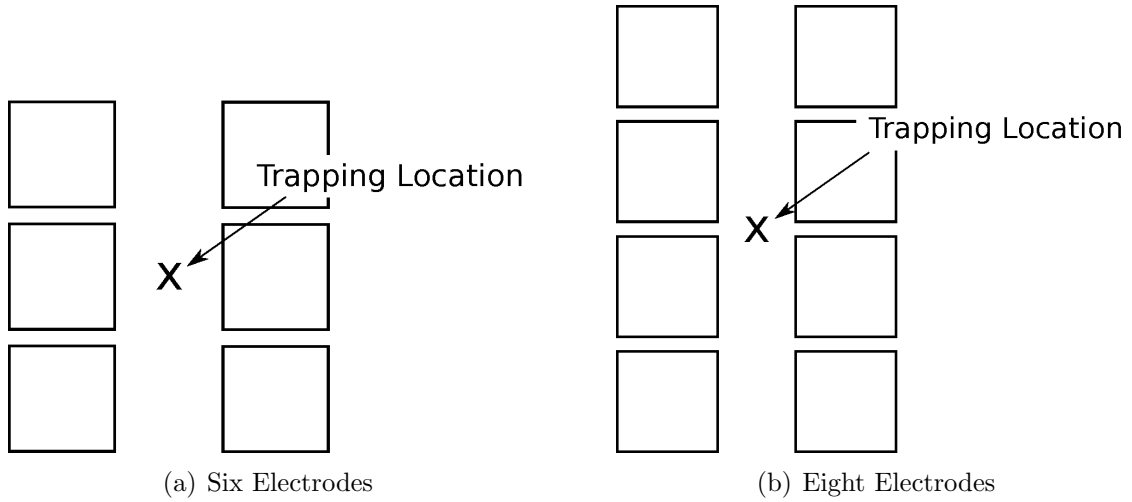


(a) Line Plot



(b) Trajectory

Figure 2.41: The particle swarm optimizer (PSO) generates waveforms that successfully shuttle the ion through a linear section of a segmented RF trap. The line plot shows that the transverse ( $x - y$ ) motion remains constant while the axial  $z$  position of the ion increases. The trajectory shows the ion position progression down the axis of the trap.



(a) Six Electrodes

(b) Eight Electrodes

Figure 2.42: For an ion axially-centered on an electrode, voltages on six electrodes are used to form the potential well. If the ion is between two electrodes, then eight electrodes are used to define the potential well.

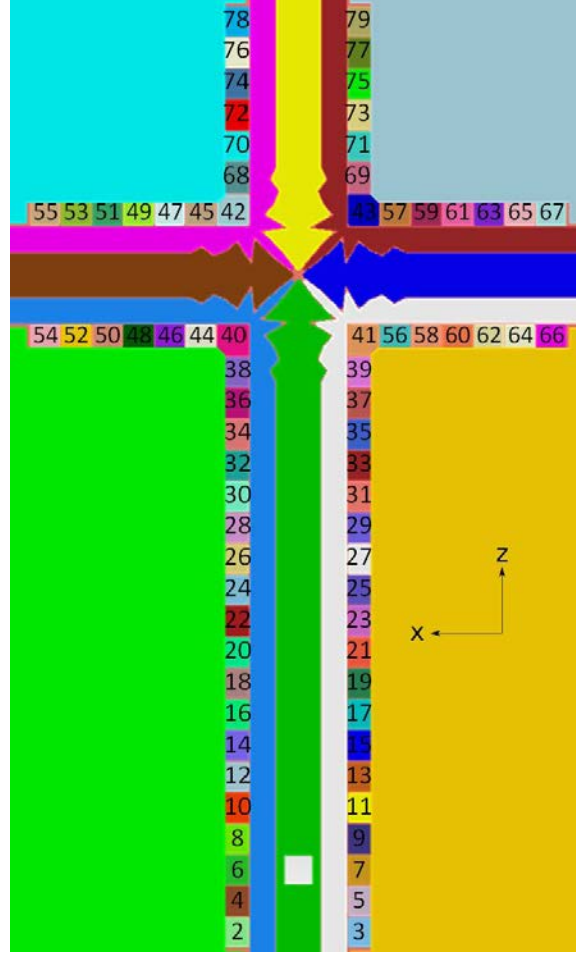


Figure 2.43: Electrode numbering in the junction.

y-axis points vertically out of the trap surface. Our objective is to transport an ion from the loading zone to the center of the junction, turn right, then move along the linear region until we reach the midpoint of electrodes 64 and 65.

Inside the junction, we use the three electrodes on each corner for a total of twelve electrodes. As displayed in Figure 2.44, this junction region includes points between the center of each of the final electrodes along the linear sections. Furthermore, a point was specifically picked to be in the center of the junction. Remaining points were placed approximately  $10\text{ }\mu\text{m}$  apart throughout this interval.

### 2.7.3.2 Forming solutions

Once we have selected the appropriate points and electrode configurations, we may trap at each one of the given locations by forcing the total electric field at that location to zero; we further constrain ion behavior by requiring a specified axial frequency. For the linear section, this axial frequency is 1 MHz. The axial frequency is stepped down gradually as the ion moves into the junction. It reaches 500 kHz in the center and is stepped back up as it



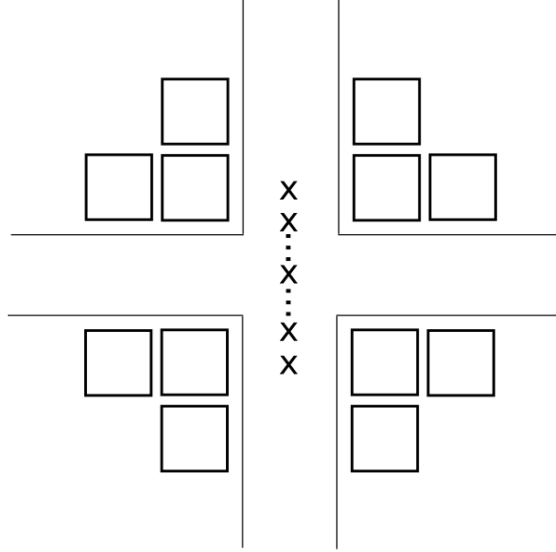


Figure 2.44: For an ion in the intersecting region of the junction, voltages on a total of twelve electrodes are used to create the potential well.

exits into the next linear section.

In the linear sections we impose the additional constraint that the DC electric fields should be rotated to facilitate ion cooling. In general, simply setting the electric field to zero and enforcing the axial frequency produces fields without rotation. As an example, we take a 6 electrode case providing us with 6 unknowns but only 4 constraints (3 field components and the axial frequency). We may solve this underdetermined system via a least squares linear solver and produce one of infinitely many solutions (the one with a minimum norm). Unfortunately, the fields have no rotation as seen in Figure 2.45. Since we have an underdetermined system, we may reduce the number of solutions available by enforcing symmetries in the electrode voltages, as demonstrated in Figures 2.46 and 2.47. Although the initial rotation provided by this technique is slight, we may further enhance the rotation by using the solution as an offset for the least squares solver. First, we may scale the solution to strengthen the fields and increase the angle of rotation (up to the maximum voltages allowed by the DAC cards). Next, we apply this set of voltages as a DC offset while allowing the least squares solver to find new voltages without any symmetries in place. This ensures us that the axial frequency is still being properly enforced while maintaining the proper rotation. Figure 2.48 shows the result of this procedure. Finally, since the linear section is rather uniform, we may form the solution at one location using 6 electrodes and another using 8 electrodes and then reuse those solutions down the length of the trap. The voltages are generally very similar, although not exactly the same. To remedy this, we can simply use these two solutions to seed the least squares solver. This allows us to correct any problems with those solutions.

Inside the junction, rotation is unnecessary and we simply request a particular axial frequency while forcing the electric fields to zero. Aside from the point at the center of the junction, there are no symmetries enforced on the 12 inner electrodes. At the center

location, the four innermost electrodes have the same voltage applied and the eight outermost electrodes are set equal to one another as well. This ensures that the voltages will be continuous when changing directions in the center of the junction since the solution must be symmetric with respect to the x and z axes.

DC potential at DC null position

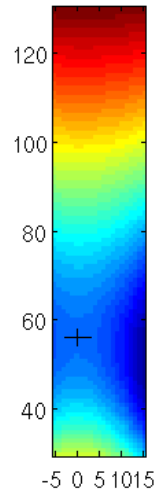


Figure 2.45: Field distribution without rotation.

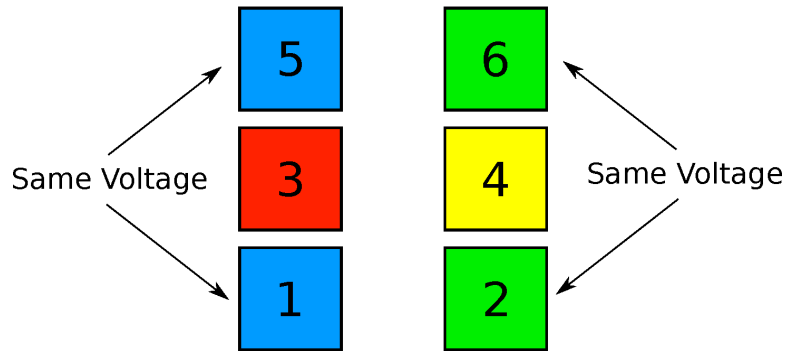


Figure 2.46: Electrode symmetries for choice of 3 electrode pairs.

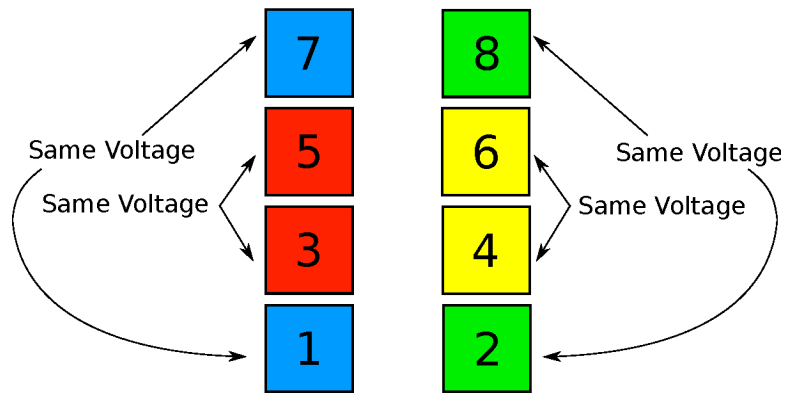


Figure 2.47: Electrode symmetries pairs for choice of 4 electrode pairs.

DC potential at DC null position

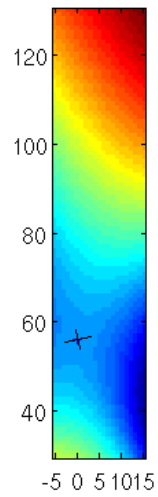


Figure 2.48: Field distribution with rotation.

### 2.7.3.3 Voltage interpolation

Since the locations we pick initially are spaced far apart, there will be relatively large voltage jumps between those points and any waveforms we produce using those points will be jagged. To remove discontinuities and smooth the voltages, we can simply perform cubic spline interpolation on the voltages from the initial points. Again, we must re-solve each of the interpolation points using these interpolated voltages as a seed for the least squares solver to retain zero fields at the trapping point as well as the requested axial frequency. Figure 2.49 demonstrates the effect of this procedure. The waveform is no longer jagged and varies smoothly with ion position.

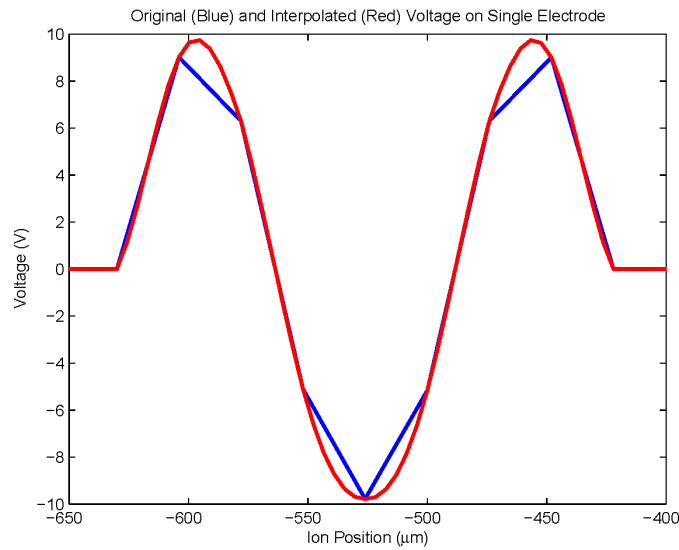


Figure 2.49: Cubic interpolation is applied between initial trapping points to smooth voltages.

### 2.7.3.4 Final Solution

Once we have solved for enough locations along the ion's path, we may construct a time-domain solution that allows us to transport the ion. If we let  $\Delta x$  be the distance between two adjacent trapping points, we may determine a time step between the points via the equation  $\Delta t = \Delta x/v$ . For our solution, we chose  $v = 2$  m/s in the linear section and  $v = 1$  m/s inside the junction. Applying these timesteps, we produce the desired waveforms as seen in Figure 2.50. Figure 2.51 provides a closer look at the voltages used inside the junction. Along the linear sections, the waveforms for the electrodes along a particular side of the trap have the same basic shape. Figures 2.52 and 2.53 show the waveforms for electrodes 26 and 27, respectively.

In the experimental setup, the waveforms pass through a 150 kHz low-pass filter. In order to see how this will affect the shape of the waveforms, we can use a Fourier transform and remove all frequency content above 150 kHz. This operation results in voltage waveforms that are indistinguishable from those shown in Figure 2.50.

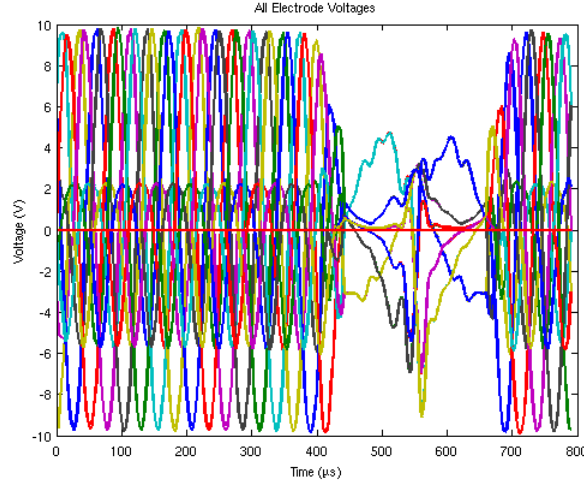


Figure 2.50: Voltages on all electrodes.

### 2.7.3.5 Numerical verification of solution accuracy

The actual path of the ion due to our waveforms can be traced out by running the motion solver (Section 2.4). Figure 2.54 shows the ion's position along the x-axis versus time for the given waveforms. Similarly, Figures 2.55 and 2.56 show the position along the x and y axes, respectively. As the ion enters the junction at  $\approx 425 \mu\text{s}$ , it slows down to half its speed along the linear section, as can be seen by the noticeable change in slope in Figure 2.56. At  $\approx 550 \mu\text{s}$ , the ion reaches the center of the junction, makes a right turn, and begins to move along the x axis. Figure 2.54 shows a noticeable increase in slope at  $\approx 650 \mu\text{s}$  where the ion exits the junction and resumes its original velocity. Also, note that the RF tube changes dramatically in the junction region as seen in Figure 2.55. Figure 2.57 plots the path along both x and z so that the junction turn may be seen more clearly.

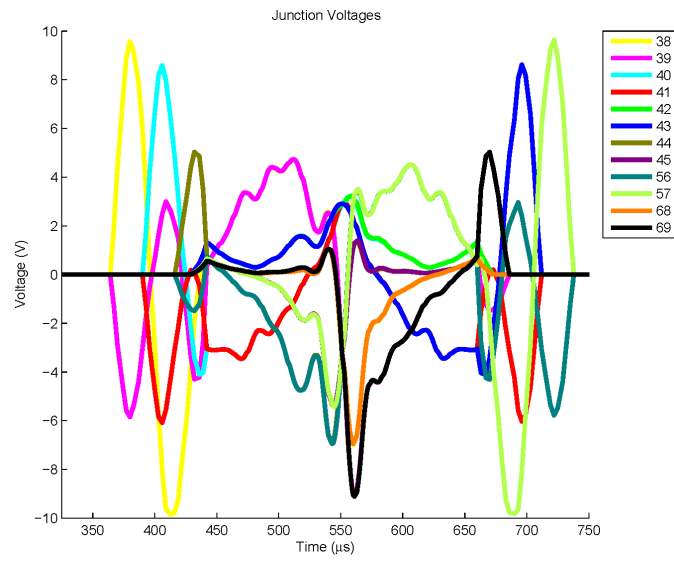


Figure 2.51: Voltages used inside junction.

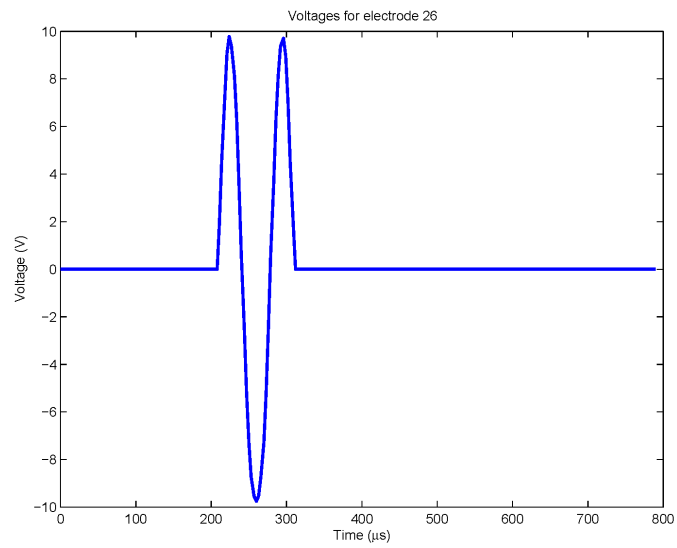


Figure 2.52: Voltages for electrode 26 in the linear region.

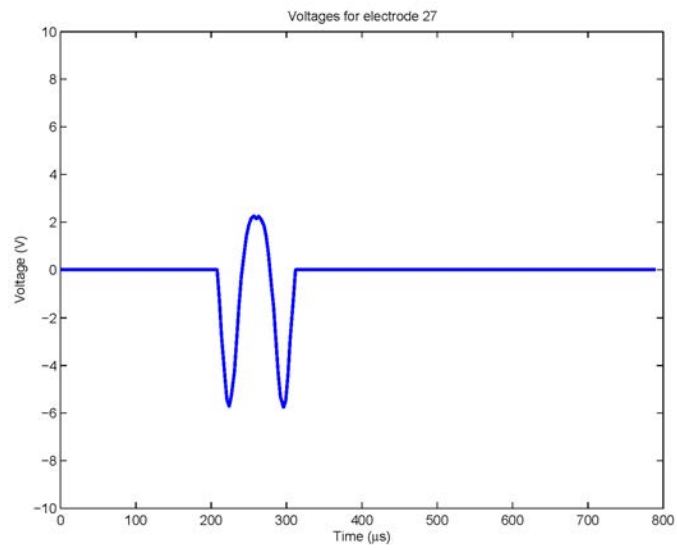


Figure 2.53: Voltages for electrode 27 in the linear region.

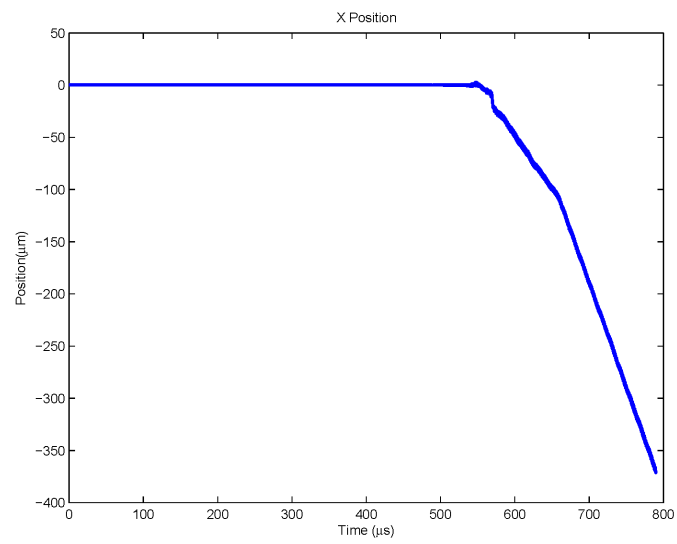


Figure 2.54: Position of ion along x-axis.

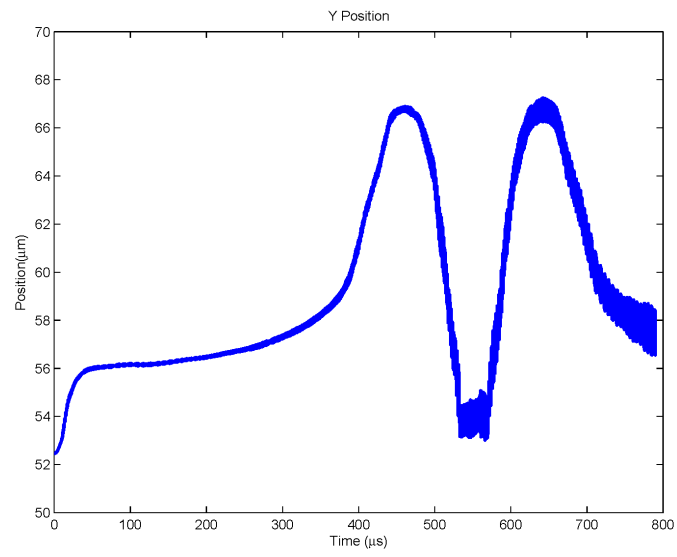


Figure 2.55: Position of ion along y-axis.

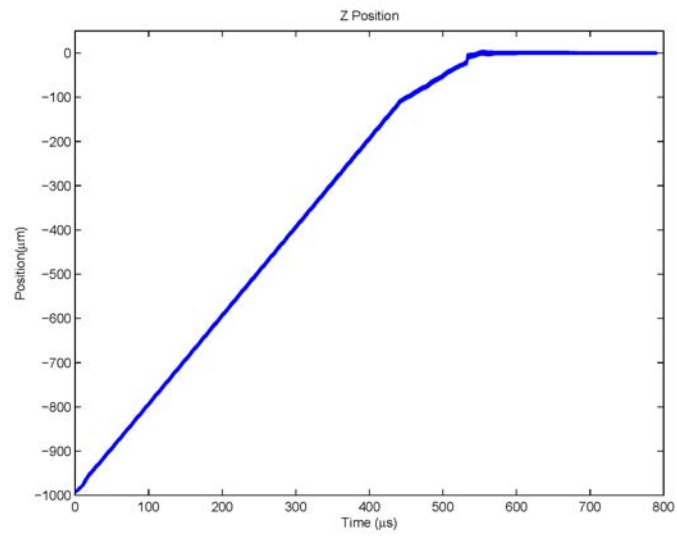


Figure 2.56: Position of ion along z-axis.



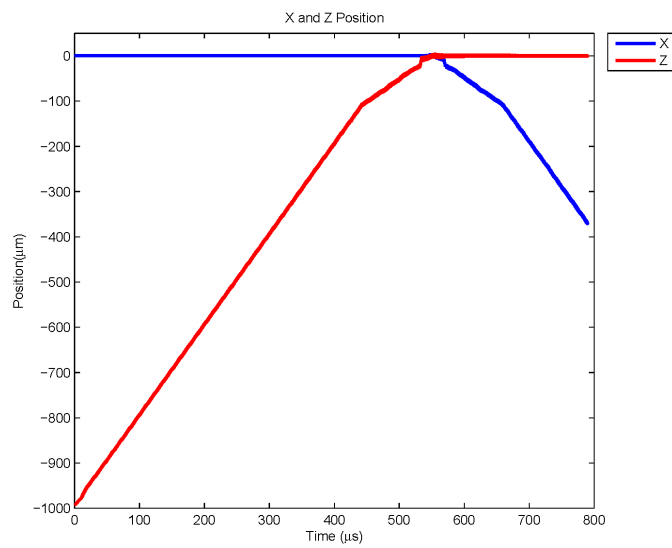


Figure 2.57: Position along x and z axes demonstrating turn in junction.

## 2.8 File handling

Under the SMIT II program, GTRI developed a number of process improvements to handle the exchange of data between codes and to provide error-free transfer of trap geometries between numerical simulation and mask layout.

### 2.8.1 HDF5: data sharing file format

Portability of data between the various simulation programs is streamlined through the use of the HDF5 (Hierarchical Data Format) file format. HDF5 has a number of attributes that make it attractive as a data storage format for sharing trap potentials and fields:

1. It is an open standard currently supported by the HDF Group, which supplies libraries and APIs for manipulating HDF5 files in Fortran 90 and C++.
2. The HDF format is completely extensible and allows any data type to be stored in a hierarchical, directory-tree-like structure. The creator of the file is free to name the data structures, providing easy retrieval of datasets within the file through reference to the attribute name.
3. Data are stored in a compact binary format, with metadata (such as data dimensions) available to high level calling routines without interrogating the actual data. The raw binary format provides a  $\times 10$  reduction in file size over the ASCII counterpart, and further compression is available. This is a critical feature for storing and transferring the datacubes that hold the trap field data; for large traps such as the full cross junction, data file size can exceed 1 GB.
4. A number of support programs used in the design and modeling effort – such as Matlab and the data visualizer Paraview – support the HDF5 data format.

All of the codes described here – StaticMoM, the motion solver, and the waveform generator – have adopted the HDF5 file format, and it has proved to be an efficient and reliable standard for data exchange.

### 2.8.2 Modeling and fabrication CAD interchange

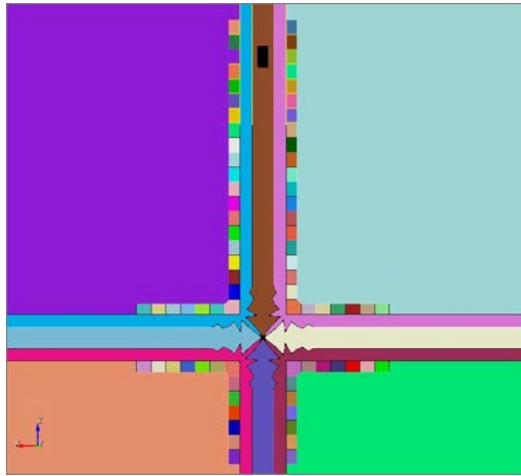
A persistent challenge across many disciplines is the incompatibility between CAD models used to design and simulate structures, and the CAD formats used in fabrication. The source of the difficulty is need: CAD formats for physics models (EM, thermal, etc.) tend to use numerically-attractive discretizations of the geometry, such as triangles or uniform cubical grids, that are amenable to the numerical solution of integral and differential equations. Fabrication on the other hand requires coordinates, such as the location of elements with respect to a common origin or absolute position of some quantity (typically element end-points), to control a machine positioning system. Translating between the two formats is often problematic and requires human intervention.

GTRI developed a robust method for translating between modeling and fabrication file formats that minimizes errors and reduces the amount of people time required. As discussed

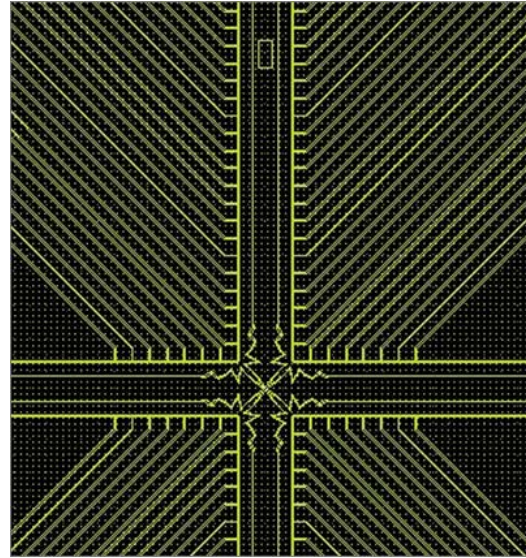
above in the context of MoM simulations, the simulation of surface electrode ion traps requires discretization of the geometry into a set of triangles. GTRI uses the government-funded (through Sandia National Laboratories) program CUBIT to mesh a given electrode shape into triangles; this code also forms a facet file, which is a standard geometry format that consists of the minimum number of triangles needed to represent an arbitrary geometry. This minimum number does not include interior triangles, so the outline of any shape can be found by tracing the outer boundary of adjacent triangles. GTRI developed a Matlab script that performs this operation and writes the perimeter as a set of coordinates in a comma-separated variables (CSV) file.

On the fabrication side of the process, the standard file format is GDSII. GTRI uses the commercially-available program LayoutEditor to read the CSV file generated from the geometry mesh and export it as a GDSII file. Via this process, the mesh files used for designing and simulating traps are quickly translated into GDSII files that lead directly to mask layout. The method is generally applicable regardless of electrode complexity, though the tracing algorithm is unable to correctly identify interior holes, such as those in the center conductor at the loading slot. In this case, the loading slot must be manually added to the mask layout. Figure 2.58 shows the mesh file for the cross trap as generated by CUBIT, and the GDSII file the results from translating the CUBIT file to a mask file.

Once the mask layout is complete – including the addition of leads, bond pads, and integrated capacitor plates – the layout can be exported to a Drawing Exchange Format (DXF) file (a ubiquitous, open-standard ASCII format available for export from most commercial drawing software). GTRI developed a DXF grabber GUI that allows a portion of the DXF file (such as the active trap electrodes) to be captured as a CUBIT file. Figure 2.59 shows a screen shot of the DXF grabber, where a linear trap DXF file generated from a mask is ready to be exported into a CUBIT file. In this way, a direct feedback loop between model and measurement exists: numerical files can be translated to mask files, and those mask files can be re-converted to numerical files to confirm that no errors occurred during the mask layout. This process has been successfully used to design, fabricate, and test both linear and cross traps under the SMIT II program.



(a) CUBIT



(b) GDS

Figure 2.58: Traps are designed and simulated using geometries defined by the CUBIT mesher language. GTRI developed codes for converting the CUBIT files into GDS, the standard geometry description language used for mask layout.

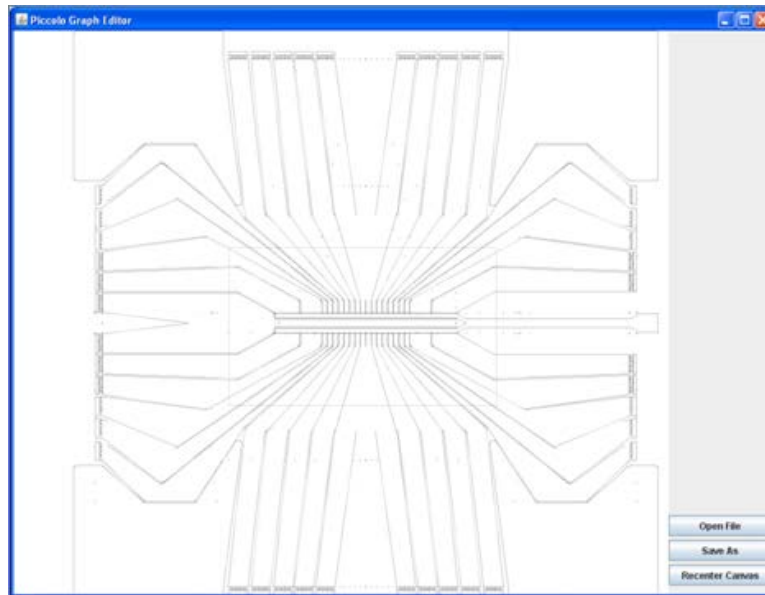


Figure 2.59: GTRI developed a GUI interface that allows DXF files to be imported from mask layouts into the CUBIT language for simulation. The GUI allows portions of the geometry to be selected to ignore extraneous layout features such as leads and bond pads that would make the simulated geometry prohibitively large.

# Chapter 3

## Ion Trap Fabrication

Fabrication of advanced ion traps at Georgia Tech began with a transfer of existing process flows and material sets developed at Bell Labs for the SMIT I project to the Nanotechnology Research Center (NRC) at Georgia Tech. This work was undertaken over the first 6 months of the SMIT II project and culminated with the production of a first generation ion trap wafer in December of 2008. Subsequent work has focused on improving the quality and reliability of each process step, adding additional process modules to increase ion trap design flexibility, and producing multiple generations of ion trap chips for testing at GTRI and throughout the ion trapping community. This section will describe each aspect of the fabrication process undertaken as a part of the SMIT II program.

### 3.1 Introduction

A schematic drawing of the first generation SMIT II linear trap is shown in Figure 3.1. The trap electrodes are fabricated using deposited Aluminum metal layers, Metal 1 (M1) through Metal 4 (M4). The control electrodes are segmented in the direction out of the plane of the cross section shown in Figure 3.1 and biased sequences of these control electrodes provide axial confinement for the ions. Radial confinement is provided by RF voltages with frequencies in the range from 30 to 100 MHz applied to the RF electrodes. In this design, the M1 layer is the bottom ground, the M4 layer forms the DC and RF control electrodes, and the M3 layer provides a capacitor for grounding RF potential on the control electrodes. In the second generation linear trap, the symmetric cross trap, and the trap with an integrated micromirror, the ground M3 layer was moved to the top in order to define the shape of the control electrodes and eliminate unwanted stray fields due to the leads. This architecture is shown in Figure 3.2.

### 3.2 Process development at NRC

The following sections describe the processes we used at the NRC to create ion traps as of July 2010. Each of these processes was developed during the course of the SMIT II program. Additional details of the development of these processes, alternative processes, and unsuitable processes investigated throughout this project are also included when applicable.

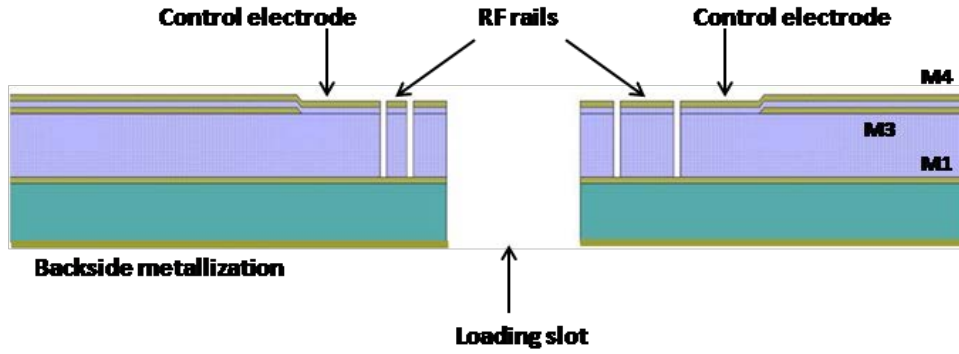


Figure 3.1: Figure 1. Schematic drawing in cross section of an initial design for a SMIT surface ion trap. The green area is a cross section of a highly doped silicon substrate. The yellow areas are deposited Al metal and the purple areas are thick silicon oxide. The ion is trapped approximately 60 to 70  $\mu\text{m}$  above the surface electrodes. The slot through the silicon wafer can be positioned for loading the ions from the rear of the silicon chip in order to avoid deposition on the top electrodes. The M3 layer provides a capacitor for grounding RF potential on the control electrodes.

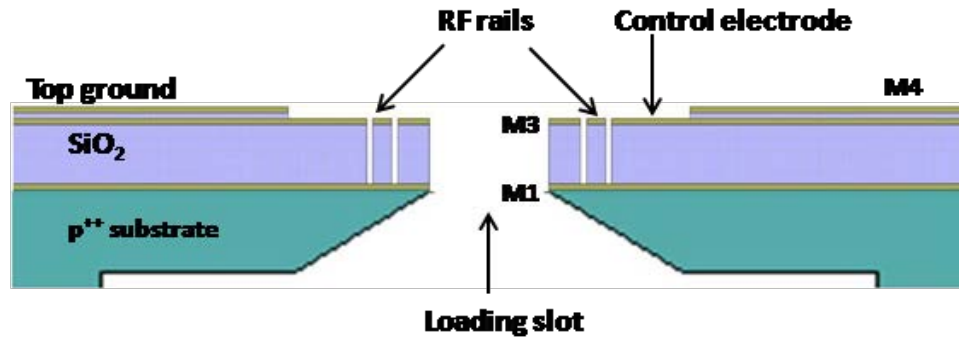


Figure 3.2: Schematic drawing in cross section of the later design for a SMIT surface ion trap. Note that the ground layer that provides capacitance for grounding RF potentials on the control electrodes has been moved to the top layer. Here it has the added benefit of defining the shape of the control electrodes and protecting the trap surface.

### 3.2.1 Wafer cleaning

Prior to any processing, all wafers are cleaned with a 10 min, 120°C Piranha etch ( $\text{H}_2\text{SO}_4$ ,  $\text{H}_2\text{O}_2$ , and  $\text{H}_2\text{O}$ ) followed by a deionized (DI) water rinse and a 20 s buffered oxide etch (BOE) followed by a DI water rinse. The Piranha etch removes any organic contamination on the wafer surface and the BOE removes native oxides that form on the silicon surface enabling electrical contact between the silicon wafer and the first deposited metal layer. Throughout the wafer buildup process, a number of cleaning steps are required to remove surface layers and contamination. Each lithography step, for instance, leaves a photoresist layer that must be removed prior to further processing and the method for removal depends on the prior treatments to the surface. If a resist has not been subjected to any plasma treatment it can be removed with a 5 minute acetone dip followed by a final rinse in isopropyl alcohol (IPA). Once a resist has been used during a plasma treatment it is typically harder to remove, in this case a 5 minute ultrasonic agitation treatment in acetone followed by an IPA final rinse is often used. Dry etching of resist can also be used when ultrasonic acetone is not appropriate; this is true if any cantilever type structure is present that could break during ultrasonic treatment. The Gasonics asher provides a heated downstream oxygen plasma environment for efficient stripping of photoresists without any damage to the underlying surface. The Gasonics asher typically requires two 60 second etching treatments to fully remove up to 2  $\mu\text{m}$  of photoresist from a surface. It is also necessary following metal etch steps to remove any conductive metal residue that remains on the surface. This is achieved with an ethylene glycol and BOE mixture (EG-BOE) that protects the bulk metal surface while removing a thin layer of surface oxide containing any metal residue. The EGBOE mixture used in this project contains 76 ml water, 75 ml ethylene glycol, and 24 ml 6:1 BOE solution. Typical treatment time is 30 seconds (at room temperature), which removes up to 2,000 Å of surface oxide. Finally, it is also necessary to remove any oxide layers that may form on metal and silicon surfaces prior to backside metallization and wirebonding. The Vision reactive ion etcher (RIE) tool in the NRC has the capability of removing these oxide layers with an argon plasma treatment (80 sccm Ar, 350 W RF power, 12 mTorr process pressure) that removes oxides at a rate of 25 Å/min.

### 3.2.2 Metal deposition

Metal deposition is a key process in building planar ion traps. The metal layers need to have uniform thickness, high conductivity, strong adhesion to underlying layers, the ability to provide good step coverage, and smooth surfaces following subsequent processing and bakeout (up to 250°C). Sputter deposited aluminum with 1% silicon was chosen, as it meets each of these requirements when combined with a thin layer of titanium for adhesion. The tool best suited to this deposition in the NRC is the Unifilm Sputterer, which has the capability of depositing films with uniform thickness ( $\pm 1\%$ ) across a four inch wafer. Initial work with aluminum films found that the standard deposition conditions of 400 Å/min deposition rate with a target thickness of 1 micron at room temperature produced metal films with rough surfaces (RMS roughness of 70 nm). The multilevel process required to build ion traps utilizes three metal depositions, each rough deposition adds to the roughness of the underlying layers, creating top surfaces with roughness on the order of 170 nm. These

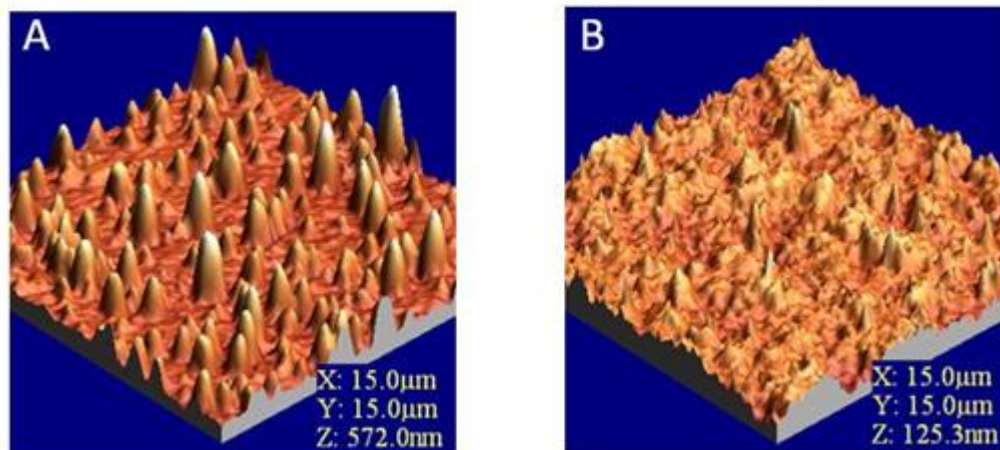


Figure 3.3: A) Metal deposited at 400 Å/min (RMS =70.4 nm), B) Metal deposited at 300 Å/min (RMS = 11.4 nm).

surfaces appear ‘foggy’ to the eye and it was believed that they would produce high levels of laser scatter, though no scatter measurements were taken. As the result of directed maintenance on the equipment and the development of new recipes, the roughness of metal after the initial deposition was reduced to 11 nm with a top surface roughness of 30 nm. Figure 3.3 shows AFM images of an as-deposited metal layer using the original deposition conditions (A) and the improved deposition conditions (B). The current recipe utilizes a peak deposition rate of 300 Å/min (nominal deposition rate 50 Å /min) to a target thickness of 1 μm. Additional deposition conditions include: deposition occurs at room temperature, starting chamber pressure is less than  $1 \times 10^{-6}$  Torr, operating pressure is  $5.10 \times 10^{-3}$  Torr, sputter gas is Ar with a flowrate of 90 sccm, target is 3 inches in diameter made of aluminum with 1% silicon, sputtering current is typically 0.100 A and voltage is 120 V. In order to promote adhesion between the aluminum and underlying materials, a 300 Å thick layer of titanium is deposited immediately before the aluminum. The deposition conditions are identical to those for aluminum except for peak deposition rate (100 Å/min) and voltage (132 V).

In addition to frontside aluminum deposition, the backside of ion traps must also be metalized. Backside metallization does not require step coverage, but strong adhesion and electrical contact between the ion trap and spacer is critical. In this project, solder is used to provide adhesion and electrical contact between the ceramic spacer and the back of the ion trap chip. In order to promote adhesion between each of these surfaces and the solder, each surface must be coated in gold (gold reacts with the solder to form a strongly adherent alloy between the chip and spacer). The gold/solder/gold interface performs well at room temperature, cryogenic temperatures, and is compatible with ultra high vacuum (UHV) systems. In this application 300 Å of titanium is deposited at 20 Å/s followed by 3000 Å of gold deposited at 30 Å/s in a CVC electron beam evaporator (typical starting chamber pressure is  $1 \times 10^{-6}$  Torr).



	Photoresist	SC 1827	SC 1827	AZ 4620	AZ 4620
	Material Being Etched	Metal	Nitride	Oxide	Silicon
Spreading	Speed (rpm)	1000	1000	1000	N/A
	Ramp Rate (rpm/s)	500	500	500	N/A
	Time (s)	10	10	10	N/A
Final Spin	Speed (rpm)	3000	3000	1500	500
	Ramp Rate (rpm/s)	1000	1000	1000	250
	Time (s)	40	40	40	30
	Soft Bake	5 min @115 C	5 min @115 C	3 m 20 s @ 110 C	20 min @ 105 C
	Exposure Dose (mJ/cm <sup>2</sup> )	500	800	500	750 (365 nm)
	Develop Time (m)	1-3	1-4	3-5	3-6
	Develop Chemistry	MF 319	MF 319	AZ 400k	AZ 400k
	Hard Bake	10-20 min @ 115 C	10-20 min @ 115 C	30 min @ 115 C	30 min @ 115 C
	Thickness (um)	2.3-2.8	2.3-2.8	8-10	25-30

Figure 3.4: Lithography process details.

### 3.2.2.1 Lithography

Lithography is performed in the NRC with two photoresists, Shipley SC 1827 and AZ Electronic Materials 4620. Details of the application conditions for each resist are shown in Figure 3.4, including the materials being etched for each photoresist.

### 3.2.2.2 Metal patterning

Metal patterning in microelectronics fabrication processes can occur in a number of ways. Lift-off processes, wet-chemical etching, and dry etching in plasmas are the three most common ways of creating a pattern on a metal surface. Lift-off and wet-chemical etching both proved to be incompatible with our metal materials and deposition techniques and were not utilized during the SMIT II project. Dry etching can etch aluminum with 1% silicon and the underlying titanium layer with a single etch chemistry, and it was chosen for all metal patterning in this program. In the NRC there are multiple tools available for this etching, we have chosen to use the Plasma-Therm SLR Reactive Ion Etcher (PT-SLR RIE), which is dedicated to metal etching. The recipe developed for etching 1  $\mu\text{m}$  aluminum with 1% silicon and 300 Å titanium utilizes 16 sccm  $\text{Cl}_2$ , 32 sccm  $\text{BCl}_3$ , 2 sccm  $\text{H}_2$ , pressure of 20 mTorr, power of 150 W, DC voltage of 330 V for 12-15 minutes. Typical results using this etch recipe for Gen II and Symmetric Cross ion traps are shown in Figure 3.5.

It is important in the metal etch process to ensure that the photoresist is properly cured in order to maintain sharp feature edges. A 5 minute softbake at 115°C and a 20 minute hardbake at 115°C are necessary to ensure proper curing with SC 1827 photoresist. Tests also indicate that placement of the sample on the PT-SLR RIE chuck can affect the rate and uniformity of the etch process. Samples are held at the center of the chuck with glass slides in order to ensure even, repeatable etching. Immediately following etching, samples must be rinsed in DI water for 3 minutes in order to remove any residual chlorine on the line edges. If the chlorine is not removed, corrosion will occur on line edges, distorting the desired etch pattern. Finally the photoresist can be stripped via acetone, ultrasonic agitation in acetone, Gasonics ashing, or a combination of these treatments. Typically ultrasonic acetone is used

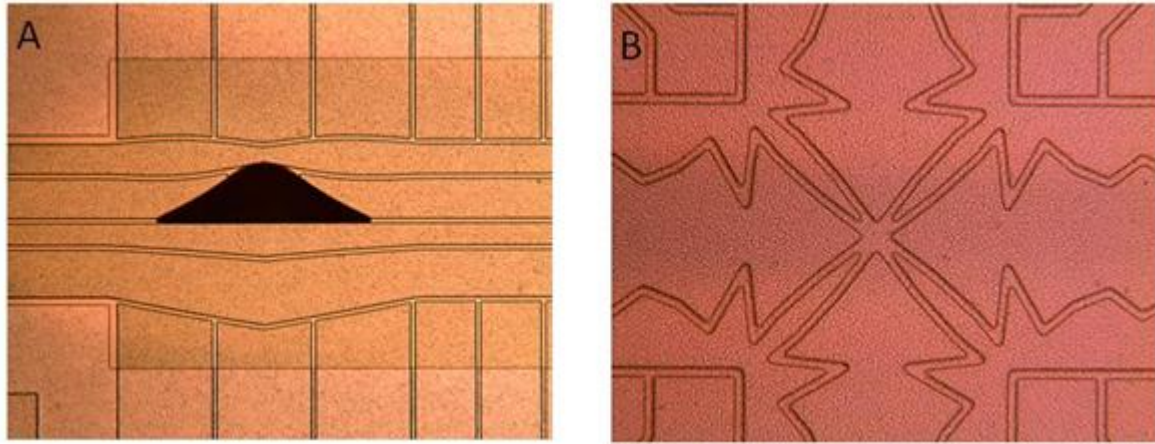


Figure 3.5: Metal etch results for A) Gen II Ion Trap, B) Cross Ion Trap.

for stripping resist after a Metal 1 etch because any overetch into silicon during the etch process can leave a residue on the surface that cannot be removed purely with an ashing treatment. Gasonics ashing treatments are used to remove resist following Metal 3 and Metal 4 etch as there is no silicon residue produced during these etch steps.

### 3.2.2.3 Oxide deposition

Oxides are required on the ion trap chips to electrically insulate different layers of control electrodes from each other and from ground layers. In order to minimize capacitance between the RF and ground and maintain structural integrity at both room temperature and cryogenic temperatures, a low stress oxide layer up to 10  $\mu\text{m}$  thick is needed. Oxide deposition must also be compatible with other process materials, such as the metals used to create ground and control layers. Aluminum has a melting point of 660°C and begins to form hillocks and other surface features at temperatures over 300°C. Oxide deposition therefore must not occur at temperatures over 660°C and ideally would occur well below 300°C in order to minimize the risk of developing unwanted surface features. This eliminates the possibility of using thermal oxides, which require temperatures of 800 – 1200°C and restricts the range of other oxide deposition techniques. In this project, oxides are deposited via plasma enhanced chemical vapor deposition (PECVD) at a temperature of 250°C. The NRC has a number of tools capable of depositing oxides in this manner; a Unaxis PECVD was chosen for this work since it had been previously used to deposit low stress oxides. The Unaxis can also process up to 4 wafers at a time, helping to maximize throughput efficiency. The recipe developed for the Unaxis in the NRC utilizes 900 sccm  $\text{N}_2\text{O}$ , 400 sccm  $\text{SiH}_4$  (5% in He), pressure of 900 mTorr, RF power of 25 W, and sample chuck temperature of 250°C to deposit oxide at a rate of 550 Å/min. Oxide films deposited with this recipe have low stress, on the order of 20 MPa for a 10  $\mu\text{m}$  thick layer, and thickness uniformity across a 4 inch wafer of  $\pm 2\%$ . In order to ensure uniform film quality and deposition conditions for each PECVD process, step oxide layers are deposited in steps of no more than 2  $\mu\text{m}$  at a time. The chamber must also be cleaned for at least one hour prior to processing, with a 5 minute seasoning run

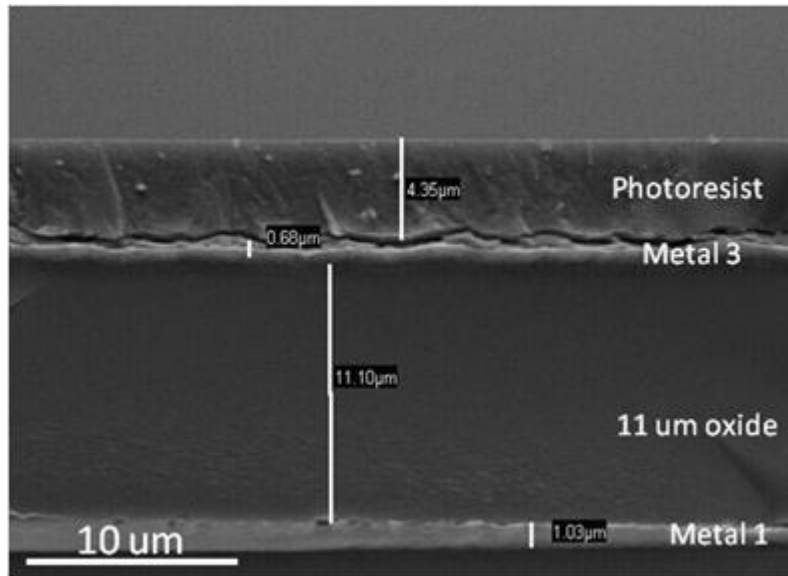


Figure 3.6: Cross section SEM image of a metal-oxide-metal stack with protective photoresist.

(same deposition conditions as the oxide process) following the cleaning. Once the seasoning run is complete, deposition can begin. Figure 3.6 is a SEM image of the cross section of a metal-oxide-metal stack demonstrating the uniformity of the 11  $\mu\text{m}$  PECVD oxide film.

#### 3.2.2.4 Oxide etch

Oxide etching is required in our process to open the loading slot area, open vias for metal contact, open bondpads for contact to underlying metals, and remove exposed oxide to reduce charging. Oxide etching must produce vertical sidewall profiles, high selectivity to the masking material, and high selectivity to underlying metal or silicon layers. Plasma etching of oxides meets each of these requirements and recipes have been developed for the SMIT II project using both photoresist and aluminum as masking layers. The two pieces of equipment best suited for oxide etching in the NRC are the STS Advanced Oxide Etcher (AOE) and the Plasma-Therm Inductively Coupled Plasma (ICP) tool. The recipes used in the AOE and ICP tools are shown in Figure 3.7. The ICP produces the most consistent results due to uniform temperature control on the wafer. The AOE, on the other hand, has a six inch chuck and four inch wafers must be mounted on a carrier wafer to be used in this tool. This hinders temperature control on the wafer, leading to inconsistent results from test to test.

#### 3.2.2.5 Silicon etching

Silicon etching is used to create through-wafer ion loading slots. In the NRC we utilize a Bosch etch process in the Plasma-Therm ICP tool. The Bosch etch has three process steps, a thin polymer deposition to protect sidewalls from etching, followed by two etching steps

	Plasma Therm ICP	Plasma Therm ICP	STS AOE	STS AOE	STS AOE
	Resist Mask	Aluminum Mask	Al Mask	Al Mask w/O <sub>2</sub>	Resist Mask
Ar (sccm)					
CF <sub>4</sub> (sccm)	45	45	40	40	22
O <sub>2</sub> (sccm)		10		10	
H <sub>2</sub> (sccm)					
He (sccm)			150	150	55
C <sub>4</sub> F <sub>8</sub> (sccm)	15				25 (x5)
Press (mTorr)	5	8			4
RF1 (W)	20	5	40	30	200
RF2 (W)	800	800	1100	2000	1100
Heat Ex Temp	60	60			
substrate Temp	16	16			5 Below
DC (V)	~-66 V	~-30 V	~-22 V	~-6 V	212 (pp~590)
Oxide etch	1840 A/min	1100 A/min	~ 1300 A/min	~ 1100 A/min	~ 6000 A/min
PR etch	1200 A/min		~ 270 A/min	~ 270 A/min	
Al etch	10 A/min	~ 0 A/min	~ 25 A/min	~ 0 A/min	~ 230 A/min

Figure 3.7: Oxide etch recipe details.

designed to break through the polymer layer on the base of the feature and etch silicon. These steps are repeated up to 850 times with 0.65  $\mu\text{m}$  of silicon etched during each cycle. The detailed process steps are shown in Figure 3.8.

### 3.3 Additional process module development

In addition to the standard processes used to fabricate ion traps at the NRC, a number of additional process modules have been developed in order to increase design flexibility and ion trap performance for future ion trap designs. These include integrated micromirrors to enhance photon collection efficiency, recessed bondpads to increase laser access across the trap surface, and backside angled slots to enable through wafer laser access. Each of these processes is described in detail in this section.

#### 3.3.1 Fabrication of integrated micromirrors

Fast quantum state detection requires efficient fluorescence collection optics. We have developed a process to build high quality spherical micromirrors in silicon. This structure is ideally suited for integrated collection optics in planar ion traps.

##### 3.3.1.1 Isotropic wet etching of silicon

Here we present a method for fabricating spherical micromirrors in silicon through an isotropic wet etch process. We use a solution of hydrofluoric, nitric, and acetic acids (HNA) as an etchant solution. During the etching,  $\text{HNO}_3$  oxidizes the exposed silicon substrate; the oxide is then subsequently removed by HF. The overall etch rate and final surface morphology are highly dependent on the concentrations of each of the etchant components and

	ICP Bosch		
	Deposition	Etch A	Etch B
CF4 (sccm)	70	0.5	0.5
SF6 (sccm)	0	50	100
Ar (sccm)	40	40	40
Press (mTorr)	15	15	15
RF1 (W)	1	9	12
RF2 (W)	800	800	800
Time (sec)	4	2	16
Si etch	~ 0.65 um/cycle		

Figure 3.8: Silicon slot etching recipe on PT ICP.

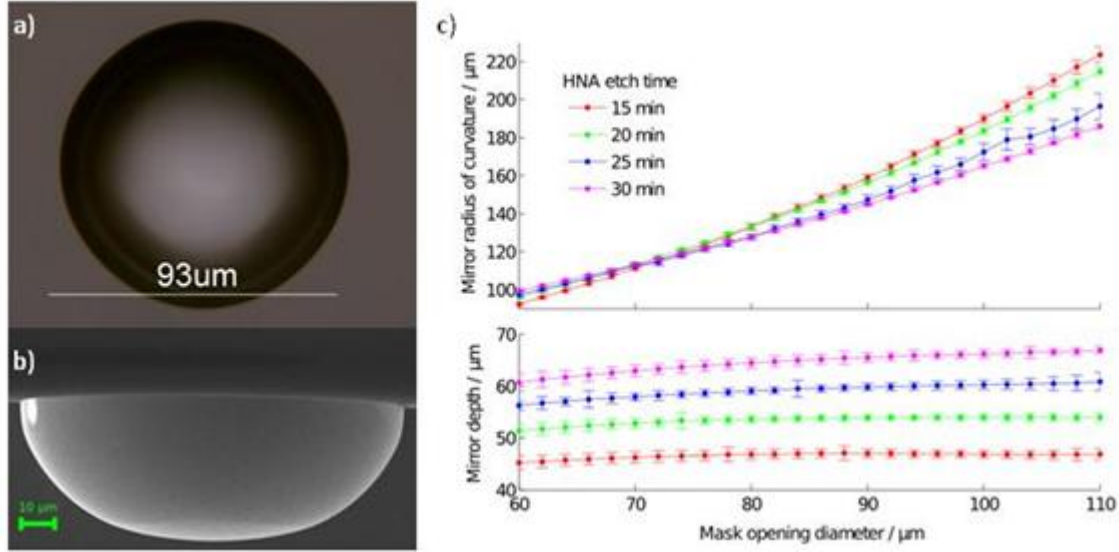


Figure 3.9: a) An optical image of an unpolished mirror. b) Scanning electron micrograph image of an unpolished mirror cleaved near the mirror diameter. c) Mirror radius of curvature and depth as a function of mask aperture opening diameter and etch time. The surface profile of each mirror was measured by an optical profilometer and fitted to a sphere using a least-squares method. Error bars are the standard deviations of 125 individual mirrors.

must be carefully optimized to provide a smooth controllable etch. Precise control of these factors gives us repeatable mirror profiles in silicon. We have selected a 1 HF : 8 HNO<sub>3</sub> : 1 CH<sub>3</sub>COOH (by vol.) solution for a highly isotropic etch with low occurrence of surface defects.

The HNA etchant is highly aggressive; a 3000 Å low-stress LPCVD silicon nitride film is used as a protective mask during the wet processing. Circular apertures between 60 and 175 μm in diameter patterned in the mask define regions on the surface where mirrors are to be fabricated. The wafer is immersed in a room temperature HNA bath without agitation for fifteen to forty minutes. Following HNA etching, the remaining nitride mask is removed by a HF bath. Typical mirrors produced by this process are illustrated in Figure 3.9(a) and (b). The size and shape of the spherical cavities can be tightly controlled by choosing the appropriate mask opening size and HNA etch time. In Figure 3.9(c) the mirror radius of curvature and depth is plotted as a function of aperture opening and etch time for a large set of mirrors.

### 3.3.1.2 Chemical mechanical polishing

We find that we can reliably machine microscopic cavities of a given radius or width, however it is difficult to independently control the mirror depth in a single step process; the isotropic HNA etch consistently yields cavities with depths comparable to the mirror radius. To find application in our planar ion trap designs, these mirrors must have a much shallower depth of approximately 12 μm in order to efficiently collect scattered photons. Mirrors produced



by the HNA process can be thinned using a combination of lapping and silicon chemical mechanical polishing (CMP), typically removing around 40  $\mu\text{m}$  of silicon from the patterned frontside of the wafer. We protect the mirrors during CMP processing by first depositing a thick 15  $\mu\text{m}$  layer of PECVD oxide. This layer prevents the surface of the mirrors from coming into contact with any abrasives or corrosives used in the CMP process. The grind and polishing is performed by a CMP sub-contractor (Aptek Industries, San Jose CA). Following polishing, the protective oxide is cleaned and stripped off using a buffered oxide etch (BOE). The CMP process can thin mirrors to within three to five microns of a target depth; we expect this can be further improved with the use of more specialized polishing techniques.

### 3.3.1.3 Optical performance of micromirrors

Efficient simultaneous fluorescence detection of multiple point-like sources can be achieved with a multi-scale optics system utilizing micromirrors. An experiment performed at Duke University demonstrated high collection efficiency ( $26 \pm 3$  %) from microscale polystyrene beads over a  $10 \times 10$  mm imaging area. A polished micromirror with a 100  $\mu\text{m}$  radius of curvature and a depth of 15.6  $\mu\text{m}$  was used to refocus scattered laser light from a fluorescent bead onto a conventional imaging system. With the micromirror removed, the maximum point source collection efficiency of the system was 1.5%.

### 3.3.1.4 Mirror fabrication process

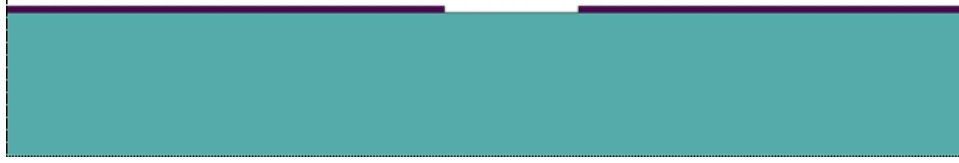
**Step 1 – Clean:** Silicon substrates are cleaned in a 120°C Piranha bath for ten minutes, followed by a short dip in buffered oxide etch to remove native oxide.



**Step 2 – Deposit 3000 Å LPCVD Nitride:** A silicon nitride film is deposited using a low pressure CVD furnace with 100 sccm dichlorosilane and 17 sccm  $\text{NH}_3$  at a pressure of 130 mtorr and a temperature of 835°C. The deposition rate is 40 Å/min.



**Step 3 – Pattern Circular Mask Openings:** Circular apertures are plasma etched through the nitride film using SC1827 photoresist as a dry etch mask. We use a Vision RIE system with 45 sccm  $\text{CHF}_3$  and 5 sccm  $\text{O}_2$  at a pressure of 40 mtorr and temperature of 25°C. The RF power is set to 270 watts. The etch rate is 314 Å/min.



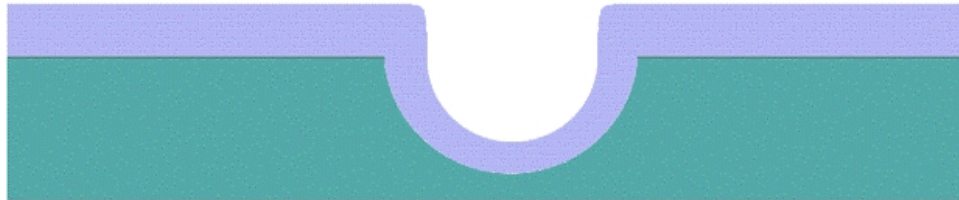
**Step 4 – HNA Wet Etch:** Mirrors are patterned using a 1:8:1 HNA acid etch. Fresh etchant solution is prepared for each wafer. During the isotropic etch, the HNA undercuts beneath the nitride mask forming a spherical cavity.



**Step 5 – Nitride Mask Strip:** LPCVD nitride mask is stripped of in 49% HF solution. The wet etch rate of our nitride is slow ( $\sim 53 \text{ \AA/min}$ ), however bare silicon is an effective etch stop. The nitride film can be removed without roughening the mirror surface.



**Step 6 – Deposition of  $15 \text{ }\mu\text{m}$  Oxide:** The same processing conditions as described in Step 4 of the Gen I ion trap section are used to deposit a total of  $15 \text{ }\mu\text{m}$  of PECVD oxide.



**Step 7 – Chemical Mechanical Polishing:** A combination of lapping and CMP with silica based slurries prepares mirrors with a well controlled depth. The polishing process removes the oxide layer and a portion of silicon substrate, however the oxide deposited inside the mirror cavity survives.



**Step 8 – Oxide Strip:** After polishing, the oxide is stripped in buffered oxide etchant (BOE), the mirror properties are characterized, and the wafer is prepared for further processing.





### 3.3.2 Recessed bondpads

As the number of controllable electrodes increases on ion trap chips, it becomes more difficult to accommodate laser access across the trap surface. One solution is to shrink the size of the bondpads, though the wirebonds must still connect to a carrier with unchanged spacing, so this solution is non-ideal. Another is to bring the bondpad surface down below the bulk surface of the trap. In this case, the wirebond loop will stay below the surface and lasers can access any part of the trap. The process for building recessed bondpads is explained in the following schematics.

**Step 1 – Nitride Deposition:** A 6000 Å thick silicon nitride film is deposited using a low pressure CVD furnace with 100 sccm dichlorosilane and 17 sccm  $\text{NH}_3$  at a pressure of 130 mtorr and a temperature of 835°C. The deposition rate is 40 Å/min.



**Step 2 – Pattern Recessed Bondpads:** Rectangular patterns are plasma etched through the nitride film using SC1827 photoresist as a dry etch mask. We use a Vision RIE system with 45 sccm  $\text{CHF}_3$  and 5 sccm  $\text{O}_2$  at a pressure of 40 mtorr and temperature of 25°C. The RF power is set to 270 watts. The etch rate is 314 Å/min.



**Step 3 – Etch Recess Bondpads:** Recessed bondpads are etched into the silicon substrate using a 25% KOH solution at a temperature of 60-80 C. Etch rate ranges between 0.5 and 1  $\mu\text{m}$ /minute depending on the process temperature used.



**Step 4 – Nitride Mask Strip:** The LPCVD nitride mask is stripped of in 49% HF solution. The wet etch rate of our nitride is slow ( $\sim 53$  Å/min), however bare silicon is an effective etch stop. Periodic agitation of the wafer is required during this nitride strip in order to remove bubbles that form on the wafer surface.



**Step 5 – Complete Wafer Buildup:** Once the recessed bondpads are created, wafer buildup can continue as normal. One exception is that spincoating does not work with deep recesses ( $>40$   $\mu\text{m}$  deep), lithography steps must be performed using a spraycoater to evenly spread resist across the wafer surface.



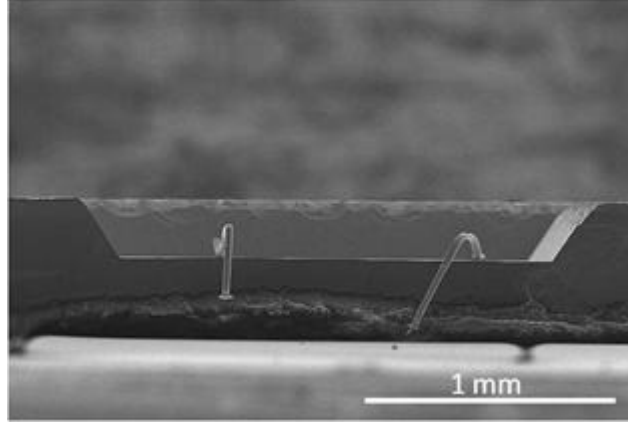


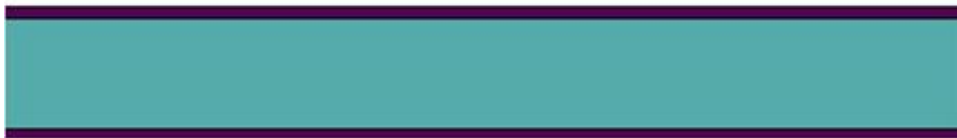
Figure 3.10: Completed recessed bondpad with attached wire bonds.

The process of creating bondpads has been demonstrated experimentally and is available as a process module for future ion trap designs. Ion trap build up on top of recessed bondpads, however, is more complicated than traditional processing due to the fact that spincoating photoresist over deep recesses produces uneven coating and poor lithography results. In order to overcome these difficulties a spraycoater has been installed in the NRC and will be available for this process in the near future. Once this tool is operational, buildup on recessed bondpads can become a standard process available for all ion trap designs. An SEM image of a test bondpad with wire bond is shown in Figure 3.10.

### 3.3.3 Through-wafer angled slots

An additional application for KOH etching of silicon is in the creation of through-wafer angled slots for increased laser access through the wafer. In this process, nitride is deposited under the same conditions as for the recessed bondpads and a slot is etched into the wafer from the backside leaving an  $80\text{ }\mu\text{m}$  thick layer of silicon to provide mechanical stability through the remainder of the buildup process. This process has been fully tested at the NRC and is available as a process module for all future ion trap designs. Figure 3.11 is a representative SEM image of a slot that is KOH etched into silicon showing the repeatable angle of the sidewalls ( $54.7^\circ$ ), which is determined by the silicon crystal structure and etch chemistry.

**Step 1 – Nitride Deposition:** A  $6000\text{ }\text{\AA}$  thick silicon nitride film is deposited using a low pressure CVD furnace with  $100\text{ sccm}$  dichlorosilane and  $17\text{ sccm}$   $\text{NH}_3$  at a pressure of  $130\text{ mtorr}$  and a temperature of  $835^\circ\text{C}$ . The deposition rate is  $40\text{ }\text{\AA}/\text{min}$ .



**Step 2 – Pattern Slot for KOH Etching:** Rectangular patterns are plasma etched

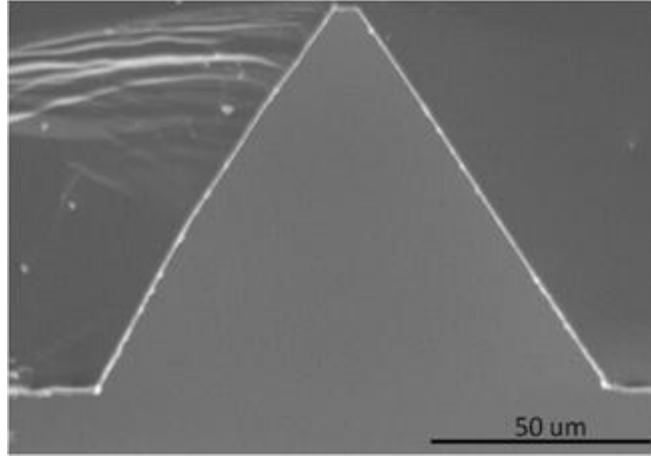


Figure 3.11: KOH etched angled slot

through the nitride film using SC1827 photoresist as a dry etch mask. We use a Vision RIE system with 45 sccm  $\text{CHF}_3$  and 5 sccm  $\text{O}_2$  at a pressure of 40 mtorr and temperature of  $25^\circ\text{C}$ . The RF power is set to 270 watts. The etch rate is  $314 \text{ \AA}/\text{min}$ .



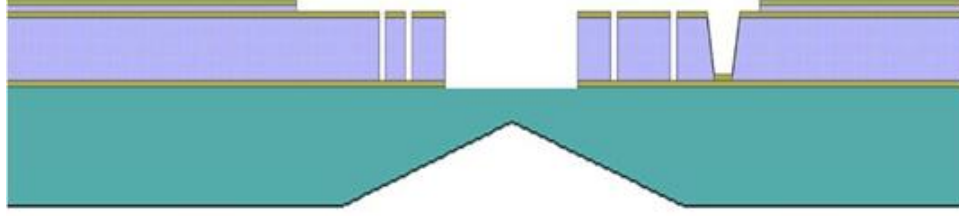
**Step 3 – Etch Slot:** The loading slot is etched into the silicon substrate using a 25% KOH solution at a temperature of  $60 - 80^\circ\text{C}$ . Etch rate ranges between  $0.5$  and  $1 \text{ μm}/\text{minute}$  depending on the process temperature used.



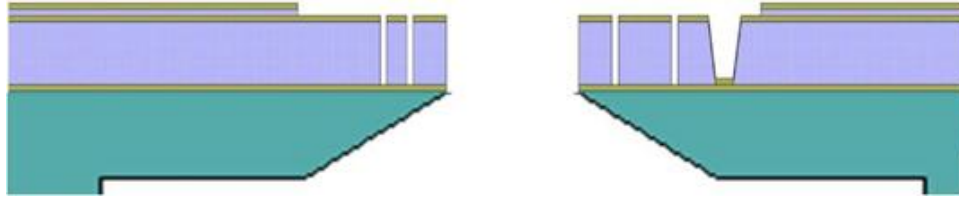
**Step 4 – Nitride Mask Strip:** The LPCVD nitride mask is stripped of in 49% HF solution. The wet etch rate of our nitride is slow ( $\sim 53 \text{ \AA}/\text{min}$ ), however bare silicon is an effective etch stop. Periodic agitation of the wafer is required during this nitride strip in order to remove bubbles that form on the wafer surface.



**Step 5 – Complete Wafer Buildup:** Once the loading slot is created, wafer buildup can continue as normal.



**Step 6 – Complete Slot Etch:** Following the completion of wafer buildup the loading slot etch is finished with a Bosch dry etching process to open the silicon through the wafer. Depending on the application the angled slot can also be metalized to reduce charging on the silicon surface.



## 3.4 Ion trap fabrication

### 3.4.1 Gen I wafers

The first generation of ion traps developed under the SMIT program contains three metal layers, a 10  $\mu\text{m}$  oxide layer, a 1  $\mu\text{m}$  oxide layer, a through wafer loading slot, 43 independently controllable DC electrodes, and on-chip capacitive filters for each DC electrode. This structure is fabricated using the general process flow described in the following cross sectional schematics. In each of these schematics the green layer is the silicon substrate, gold layers are metals, and blue layers are silicon dioxide.

**Step 1 – Clean and Label:** The silicon substrate is labeled, cleaned in a Piranha bath for 10 minutes to remove contaminants from the surface, and dipped in buffered oxide etchant to remove any surface oxide.



**Step 2 – Deposit Metal 1:** Deposit 300 Å titanium at a deposition rate of 100 Å/min followed by 1  $\mu\text{m}$  aluminum with 1% silicon at a deposition rate of 300 Å/min. Sheet resistance of the deposited metal film is measured using a four point probe and is typically 0.04 to 0.06  $\Omega/\text{square}$  for a 1  $\mu\text{m}$  thick layer.

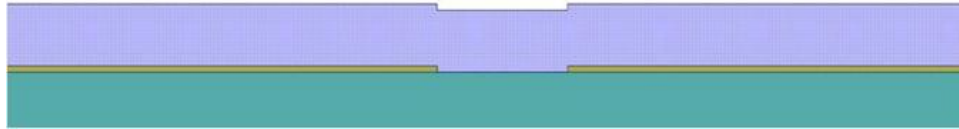


**Step 3 – Pattern Metal 1:** Lithography is performed using Shipley Microposit 1827 producing a coating that is 2.5  $\mu\text{m}$  thick following hard bake with openings for alignment

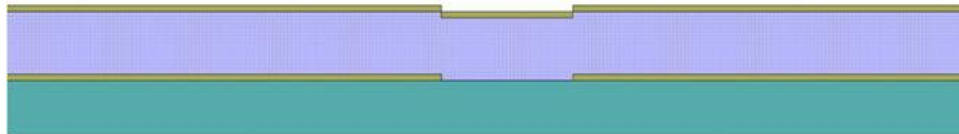
marks and the loading slot. Additional process details can be found for each wafer at the end of this section in the wafer process results tables. Once lithography is completed the exposed metal is etched in a Plasmatherm SLR RIE with  $\text{Cl}_2$  and  $\text{BCl}_3$  process gases. This process etches through the aluminum and titanium layers and slightly roughens the underlying silicon. Samples are immediately rinsed in deionized water for 3 minutes to remove any residual chlorine that can cause corrosion along feature edges. Resist is stripped with a 5 min ultrasonic acetone treatment followed by a rinse with isopropyl alcohol and a final 60 s oxygen ashing in a Gasonics asher.



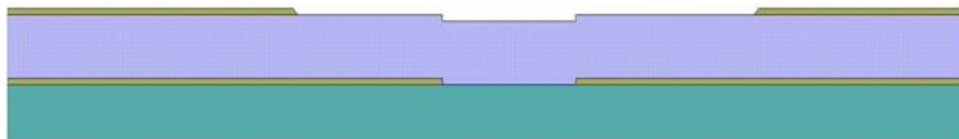
**Step 4 – Deposit 10  $\mu\text{m}$  PECVD oxide:** Oxide is deposited in a Unaxis PECVD with 400 sccm  $\text{SiH}_4$  (5% in He) and 900 sccm  $\text{N}_2\text{O}$ , a pressure of 900 mTorr, RF power of 25 W, and a deposition temperature of  $250^\circ\text{C}$ . The deposition rate is  $550 \text{ \AA}/\text{min}$  and oxide is deposited in 2  $\mu\text{m}$  increments. Immediately prior to each deposition the PECVD chamber is cleaned for 1 hour and a 5 min seasoning recipe (same conditions as oxide deposition) is run in order to prepare the chamber and ensure consistent deposition results.



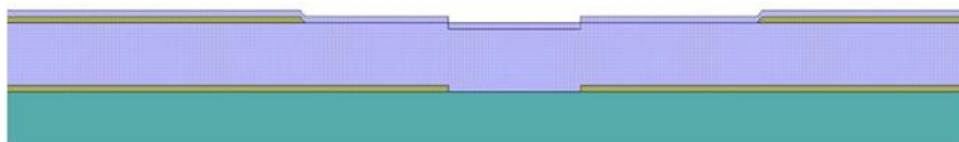
**Step 5 – Deposit Metal 3:** Deposit  $300 \text{ \AA}$  titanium followed by 1  $\mu\text{m}$  aluminum with 1% silicon under the same conditions as described in Step 2.



**Step 6 – Pattern Metal 3:** Metal 3 is patterned using the process described in Step 3. The pattern for Metal 3 defines the ground layer that lays 1  $\mu\text{m}$  beneath the final DC electrode layer (Figure 3.12). This ground provides the capacitive filter for each DC electrode and is removed around the RF rail in order to minimize capacitance between the RF and ground.



**Step 7 – Deposit 1  $\mu\text{m}$  PECVD oxide:** The same conditions as described in Step 4 are used during this process step.



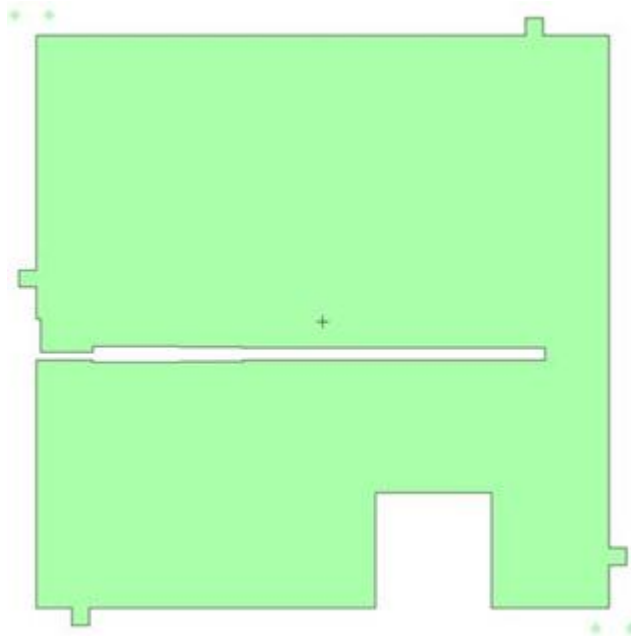
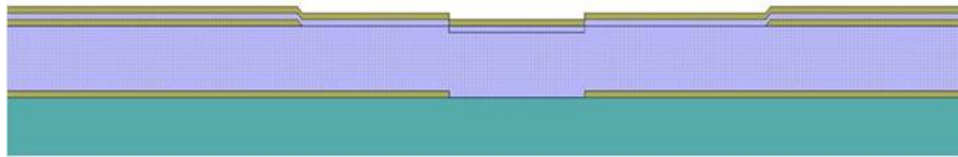
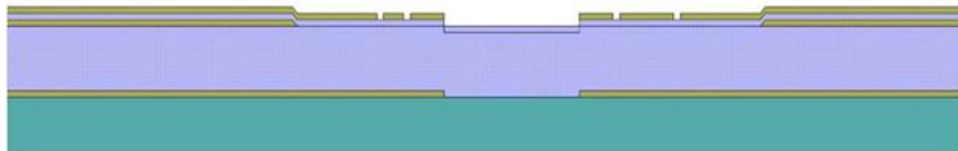


Figure 3.12: Ground layer pattern for M3.

**Step 8 – Deposit Metal 4:** Deposit 300 Å titanium followed by 1  $\mu\text{m}$  aluminum with 1% silicon under the same conditions described in Step 2.



**Step 9 – Pattern Metal 4:** Metal 4 is patterned using the process described in Step 3 with the DC and RF electrode pattern shown in Figure 3.13. This pattern defines all the DC and RF electrode geometries, routing each electrode to an independent bondpad for electrical connections to the carrier. Spacing between electrodes is 4  $\mu\text{m}$  around the trapping zone and expands to 10  $\mu\text{m}$  during the fanout of the electrodes to the bondpads.



**Step 10 – Etch Oxide:** A Surface Technology Systems (STS) Advanced Oxide Etcher or Plasma-Therm Inductively Coupled Plasma (PT ICP) is used to etch up to 11  $\mu\text{m}$  of oxide using the patterned Metal 4 layer as an etch mask. The initial process flow for this wafer etched 2  $\mu\text{m}$  of oxide with Metal 4 as a mask followed by 9  $\mu\text{m}$  of oxide with a photoresist mask that covered the entire wafer surface except the loading slot and Metal 1 bondpad

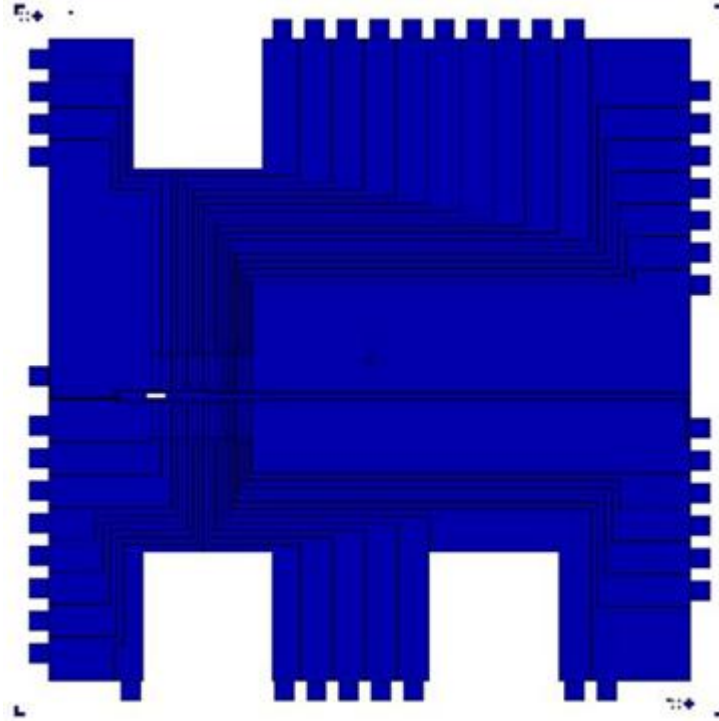
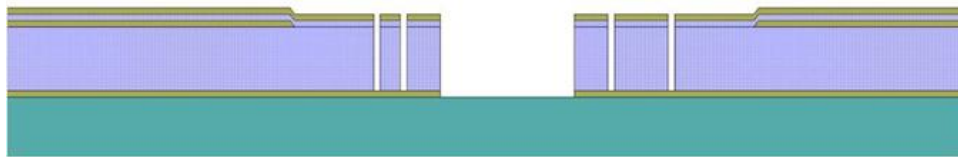


Figure 3.13: DC and RF electrode pattern for M4.

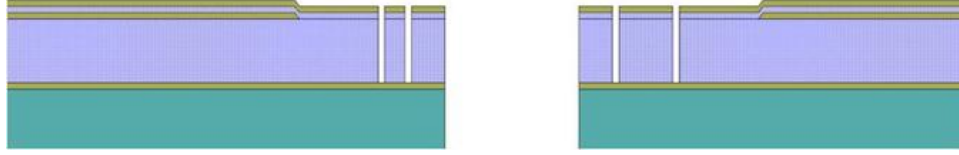
areas. In order to etch  $9\text{ }\mu\text{m}$  of oxide with a resist mask, AZ 4620 photoresist (made by AZ Electronics Materials) is used to create a  $10\text{ }\mu\text{m}$  thick photoresist layer. The oxide etch recipe with a resist mask etched oxide at a rate of  $3600\text{ }\text{\AA}/\text{min}$  with a selectivity to resist etching of 1.2-2:1. Any remaining resist on the surface following the etch process is removed with an ultrasonic acetone cleaning followed by a final rinse with isopropyl alcohol. Wafers SMIT 7 and SMIT 15 used this process while GT 22 used a modified process with Metal 4 as the mask for the entire  $11\text{ }\mu\text{m}$  oxide etch. This change was made in order to remove oxide in the spaces between electrodes. The oxide etch recipe with a metal mask etched oxide at a rate of  $1100\text{-}1300\text{ }\text{\AA}/\text{min}$  with a selectivity of 50-100:1.



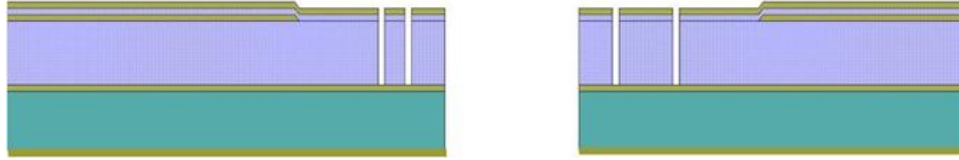
**Step 11 – Etch Loading Slot:** A through-wafer loading slot is etched into the wafer from the backside using a thick photoresist as the etch mask. The front of the wafer is protected with a coating of AZ 4620 resist before any processing on the backside of the wafer begins. Backside processing begins with applying an AZ 4620 photoresist layer that is  $20\text{ }\mu\text{m}$  thick, silicon is then etched using a Plasma-Therm Inductively Coupled Plasma system with a Bosch etch process. The Bosch etch has multiple process steps, a thin polymer deposition to protect sidewalls from etching, followed by two etching steps to break through the polymer



layer on the base of the feature and etch the silicon. These steps are repeated up to 850 times with  $0.65\ \mu\text{m}$  of silicon etched during each cycle. The final result is a through wafer slot with vertical sidewalls that is well-aligned to the frontside features on the wafer.



**Step 12 – Backside Metallization:** The backside of the wafer is coated with  $300\ \text{\AA}$  of titanium deposited at  $20\ \text{\AA}/\text{s}$  followed by  $3000\ \text{\AA}$  of gold deposited at  $30\ \text{\AA}/\text{s}$ . This deposition occurs in an electron beam evaporator and the loading slots are covered with Kapton tape to keep the Au from reaching any frontside features on the wafer.



The full mask set with 4 layers is shown in Figure 3.14. The four layers are used to create the patterns for etching the loading slot metal (red), the ground layer (green), the DC and RF electrodes (blue), and the loading slot silicon from the backside of the wafer (same as loading slot). The large openings in the mask are designed to allow for handling of the wafer during the mounting process and for possible attachment of a heat sink at cryogenic temperatures. A zoomed-in image of the trapping zone shows the configuration of the RF rails, the individual DC electrodes, and the loading slot design (Figure 3.15). This design has 21 DC electrodes on each side of the RF rails, a center DC electrode between the RF rails, two trapping zones with different separations of the RF rails ( $120\ \mu\text{m}$  and  $90\ \mu\text{m}$ ) and corresponding DC electrode widths ( $80\ \mu\text{m}$  and  $60\ \mu\text{m}$ ).

Utilizing this process flow, a number of wafers were produced with the Gen I ion trap design, including the traps used to first trap ions at GTRI (wafer SMIT 15), and traps that have been used to gather data at GTRI and MIT (wafer GT 22). Figure 3.16 shows SEM images of the GT 22 wafer at the completion of processing. Figure 3.16(a) shows a wide range SEM image of the trapping zone, Figure 3.16(b) shows the area around the splitting of the RF rail with the RF rail highlighted by charging during the imaging, Figure 3.16(c) shows the thin RF rail with dimensions and is a good representation of the vertical sidewalls achieved with the  $11\ \mu\text{m}$  oxide etch, and Figure 3.16(d) shows the loading zone and associated dimensions.

Specific results from each process step, including the date of process, for each of the completed Gen I wafers are shown in Figure 3.17 – Figure 3.19. The first wafer, SMIT 7, was completed in May 2009 and sent to MIT for our first ion trap tests, though no ions were trapped. The second wafer, SMIT 15, was completed in August 2009 and resulted in our first trapped ions under the SMIT II program in October 2009. The third wafer, GT 22, was completed in December 2009 and resulted in numerous trapped ions, ion chains, and ion shuttling beginning in January 2010.



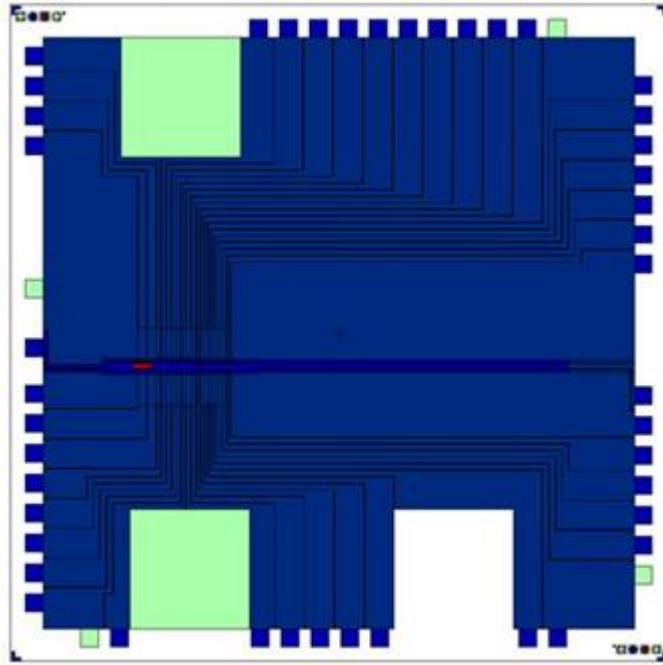


Figure 3.14: Gen I complete mask set.

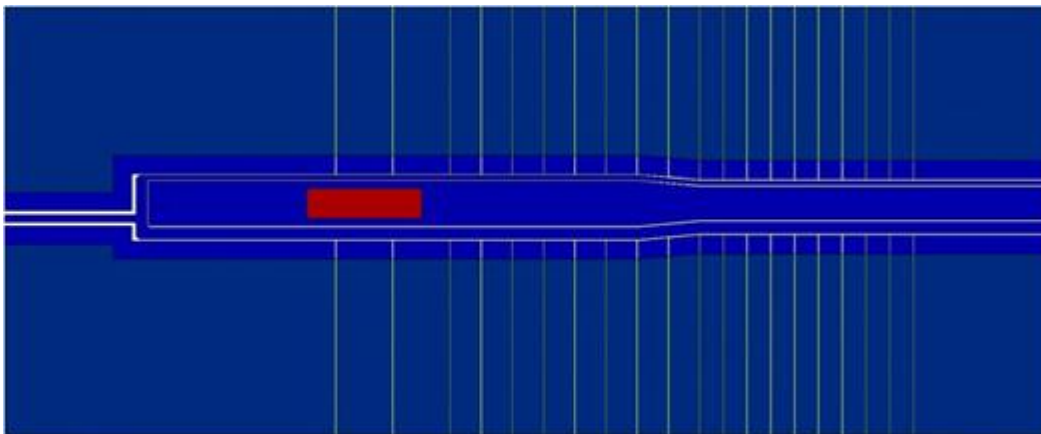


Figure 3.15: Gen I trapping region.

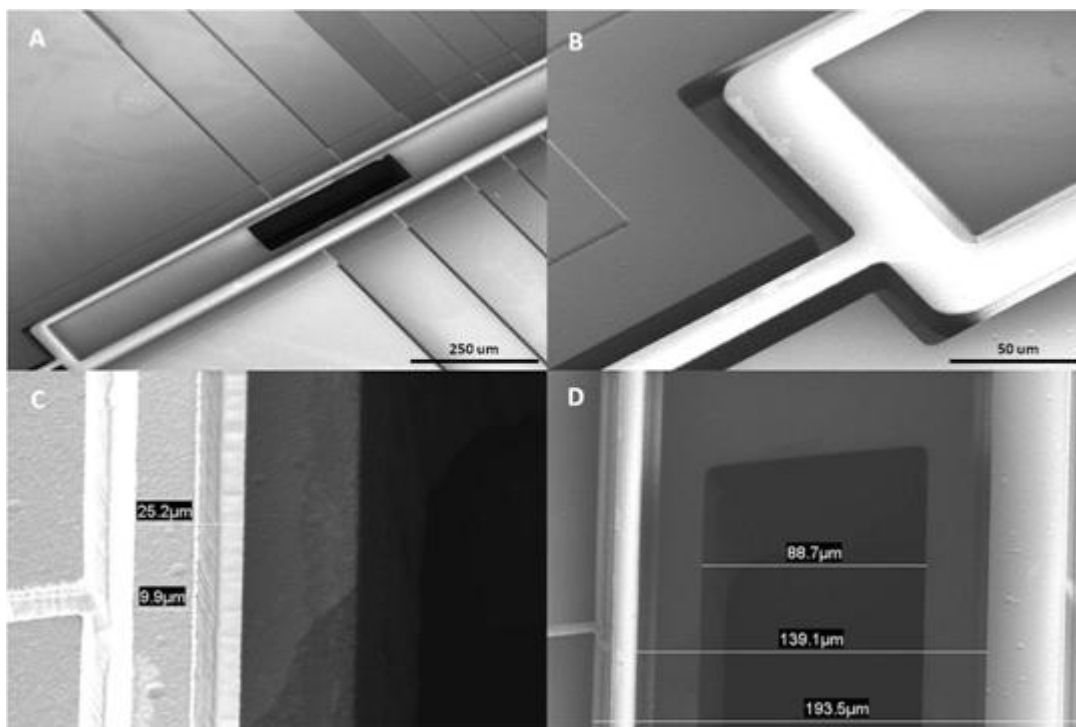


Figure 3.16: A) SEM of Trapping Region, B) RF Rail Split, C) Thin RF Rail With Vertical Sidewall Profile, D) Loading Slot Area.

	Process Step Name	Process Details	Date of Process
1	wafer ID	SMIT 7	
2	Measure curvature	3900 A Curvature	1/28/2009
3	clean wafer	10 min @120C	1/27/2009
4	clean wafer	15 s	1/27/2009
5	Deposit M1	Planet 3: Al/Si 1% Calibration B	1/28/2009
6	measure sheet Rs	4.43 *10 <sup>-2</sup> ohms/sq	1/29/2009
7	Measure curvature	1.5 um, -41 Mpa compressive	2/6/2009
8	Deposit D1 Oxide	10 um deposited in 4 steps 3:3:1:3	2/6, 2/13, 2/17/2009
9	measure oxide thickness	10.1 um	2/17/2009
10	Measure curvature	11.73 um, -25.4MPa	3/6/2009
11	Deposit M3	Al/Si 1% 300A Ti @100A/min; 10000A Al/Si @400 A/min Calibration B	4/8/2009
12	measure sheet Rs	.0585 ohms/sq	4/8/2009
13	Measure Curvature	9.53 um, -22.7 Mpa	4/8/2009
14	Litho M3	SPR 1827, 1000/500/10 + 4000/1000/40: 60 s @115 C; 150MJ/cm2 exposure: 3 min develop: 15 min @ 115C: resist 2.6 um thick	4/8/2009
15	Etch M3	2 runs of 3.5 minutes	4/8/2009
16	Strip PR	Acetone/Methanol + Plasma Therm RIE Descum 0:30/4:30	4/8/2009
17	Measure Metal Thickness	0.8 um	4/8/2009
18	Deposit D3 Oxide	1.00 um deposited in 1 step	4/9/2009
19	measure oxide thickness	1.00 um	4/9/2009
20	Deposit M4	Al/Si 1% 300A Ti @100A/min; 11000A Al/Si @400 A/min Calibration B	4/9/2009
21	measure sheet Rs	.062-.085 ohms/sq	4/10/2009
22	Litho M4	SPR 1827, 1000/500/10 + 4000/1000/40: 60 s @115 C; 180MJ/cm2 exposure: 3 min develop: 15 min @ 115C: resist height = 2.2 um	4/10/2009
23	Etch M4	2 runs of 3.5 minutes	4/10/2009
24	Strip PR	Acetone/Methanol + Plasma Therm RIE Descum 0:30/4:30	4/10/2009
25	Measure Metal Thickness	1.00-1.05 um	4/10/2009
26	Remove Residue	100 ml 30:1 BOE + 75 ml EG 1 min etch	4/13/2009
27	Etch Oxide	ICP recipe PT2C4F6R 7 min metal 4 aluminum as mask	4/13/2009
28	Litho Slot	AZ4620: 1000/100/10 + 4000/1000/45: 3 min @110C; 440 MJ/cm2 exposure: 4.5 min develop in 4:1 DIWater:AZ400k: 15 min @ 110C: resist 7 um thick	4/13/2009
29	Oxide Etch	STS AOE 12 + 12 + 5 DGOxide	4/13/2009
30	Deposit Backside Ti/Au	500 A Ti + 3000 A Au	4/14/2009
31	Dice	11 mm die	4/15/2009

Figure 3.17: Process results summary for SMIT 7 wafer (Tested at MIT, no ions trapped).

	Process Step Name	Process Details	Date of Process
1	wafer ID	SMIT 15	4/9/2009
2	Measure curvature	2.53 um	4/9/2009
3	clean wafer	10 min @120C	4/9/2009
4	clean wafer	15 s	4/9/2009
5	Deposit M1	300 A Ti @ 100 A/min; 10000 S Al/Si 1% @300 A/min cal B	5/18/2009
6	measure sheet Rs	0.069 ohms/sq	5/18/2009
7	Measure curvature		
8	Deposit D1 Oxide	Deposited in 5 steps 2 um per step	5/19/2009 - 5/28/2009
9	measure oxide thickness		
10	Measure curvature		
11	Deposit M3	300 A Ti @ 100 A/min; 10000 S Al/Si 1% @300 A/min cal B	5/29/2009
12	measure sheet Rs	0.064 ohms/sq	5/29/2009
13	Measure Curvature		
14	Litho M3	SPR 1827, 1000/500/10 + 4000/1000/40: 60 s @ 115 C: 180MJ/cm2 exposure: 13 min develop: 15 min @ 115C: resist 2.5 um thick	5/29/2009
15	Etch M3	SLR DKB_Al etch 4 minutes	5/29/2009
16	Strip PR	5 min Acetone Ultrasonic and 3:30 PT RIE Descum	5/29/2009
17	Measure Metal Thickness	0.90 um	5/29/2009
18	Deposit D3 Oxide	1 um deposited in 1 step	5/29/2009
19	measure oxide thickness	1.04 um	5/29/2009
20	Deposit M4	300 A Ti @ 100 A/min; 10000 S Al/Si 1% @300 A/min cal B	5/29/2009
21	measure sheet Rs	0.065 ohms/sq	6/1/2009
22	Litho M4	SPR 1827, 1000/500/10 + 4000/1000/40: 60 s @ 115 C: 180MJ/cm2 exposure: 7 min develop: 15 min @ 115C: resist 2.3 um thick	6/2/2009
23	Etch M4	SLR DKB_Al etch 7 minutes	6/2/2009
24	Strip PR	5 min Acetone Ultrasonic and 3:30 PT RIE Descum	6/2/2009
25	Measure Metal Thickness		
26	Remove Residue	N/A	
27	Etch Oxide	ICP recipe STD_OX for 12 min metal 4 aluminum as mask	6/2/2009
28	Litho Slot	AZ4620: 1000/500/10 + 1500/1000/45: 3:20 min @110C: 480 MJ/cm2 exposure: 4.5 min develop in 4:1 DIWater:AZ400k: 15 min @ 110C: resist 10 um thick	6/4/2009
29	Oxide Etch	STS AOE 12 + 12 + 1 min DGOxide	6/10/2009
36	Litho Backside Slot	AZ4620: 500/100/10 + 700/300/45 + 1500/3000/1: 3 min @120C: 1800MJ/cm2 exposure: 6 min develop in 4:1 DIWater:AZ400k: 20 min @ 110C: resist 20.2 um thick	6/17/2009
37	Cavity etch	850 cycles etched through resist (only 400 um Si etch)	6/22/2009
38	Etch M1 from Backside	SLR DKB_Al etch 8 minutes	Chip Level
39	Clean Backside Contact	Acetone/Methanol + Plasma Therm RIE Descum 0:30/4:30	Chip Level
40	Deposit Backside Ti/Au	Ti 1.5 A/sec + Au 3.0 A/sec	Chip Level
41	Dice	11 mm die	6/23/2009

Figure 3.18: Process results summary for SMIT 15 (first ions trapped in SMIT II, 10/2009).



	Process Step Name	Process Details	Date of Process
1	wafer ID	GT 22	10/15/2009
2	clean wafer	10 min @120C	10/15/2009
3	clean wafer	15 s	10/29/2009
4	Deposit M1	300 A Ti @ 100 A/min; 10000 S Al/Si 1% @300 A/min cal B	10/29/2009
5	Litho M1	SPR 1827, 1000/500/10 + 4000/1000/40: 60 s @115 C: 190MJ/cm2 exposure: 3 min develop: 15 min @ 115C: resist 2.6 um thick	11/3/2009
6	Etch M1	SLR DKB_AI etch 8 minutes	11/4/2009
7	Strip PR	Acetone/Methanol + Plasma Therm RIE Descum 0:30/4:30	11/4/2009
8	Deposit D1 Oxide	10 um deposited in 5 steps	11/5-11/9/2009
9	measure oxide thickness	10.0 um	11/9/2009
10	Deposit M3	300 A Ti @ 100 A/min; 10000 S Al/Si 1% @300 A/min cal B	11/10/2009
11	measure sheet Rs	.051 ohms/sq	11/11/2009
12	Litho M3	SPR 1827, 1000/500/10 + 4000/1000/40: 60 s @115 C: 150MJ/cm2 exposure: 3 min develop: 15 min @ 115C: resist 2.6 um thick	11/11/2009
13	Etch M3	SLR DKB_AI etch 15 minutes	11/11/2009
14	Strip PR	Acetone/Methanol + Plasma Therm RIE Descum 0:30/4:30	11/11/2009
15	Deposit D3 Oxide	1 um deposited in 1 step	11/12/2009
16	measure oxide thickness	0.99 um	11/12/2009
17	Deposit M4	300 A Ti @ 100 A/min; 11000 S Al/Si 1% @300 A/min cal B	11/12/2009
18	Litho M4	SPR 1827, 1000/500/10 + 4000/1000/40: 60 s @115 C: 180MJ/cm2 exposure: 7 min develop: 15 min @ 115C: resist 2.3 um thick	11/17/2009
19	Etch M4	SLR DKB_AI etch 20 minutes + 12 min SF6 in Vision RIE	11/17/2009
20	Strip PR	Acetone/Methanol + Plasma Therm RIE Descum 0:30/4:30	11/17/2009
21	Remove Residue	60 s EG-BOE clean	11/24/2009
22	Etch Oxide	STS AOE 105 min DG-Oxide to etch 11 um	11/23 + 12/1/2009
23	Frontside Silicon Etch	50 cycles of Boschsmi recipe on PT ICP	12/7/2009
24	Litho Backside Slot	AZ4620: 500/250/30 + 1500/3000/1: 20 min @105C: 1500MJ/cm2 exposure (365 nm): 2:15 min develop in 4:1 DIWater:AZ400k: 20 min @ 105C: resist 21 um	12/7/2009
25	Cavity etch	940 cycles of Boschsmi recipe on PT ICP	12/7 + 12/8/2009
26	Strip PR	Acetone, IPA, and Plasma Therm RIE Descum 0:30/4:30	12/8/2009
27	Clean Backside Contact	5 min SMITDS + 2 min SMITAR in PT RIE	12/14/2009
28	Deposit Backside Ti/Au	300 A Ti @ 1.5 A/sec + 3000 A Au @ 3.0 A/sec	12/14/2009
29	Dice	11 mm die	12/16/2009

Figure 3.19: Process results summary for GT 22 (used to trap and shuttle ions).

### 3.4.2 Gen II wafers

The second generation of SMIT II ion traps incorporated a number of changes in trap design, wafer cross section, and process flow. The design changes included:

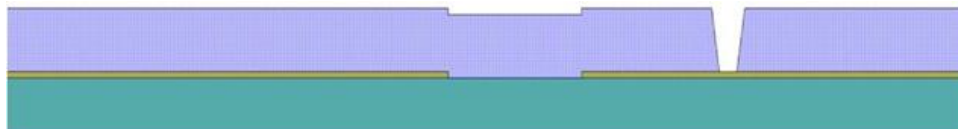
1. A new loading slot design
2. RF and DC rails contoured around the loading slot
3. Two interior electrodes (between RF rails), one ground and one DC
4. A top level ground layer that protects the bulk of the surface from physical contact and controls the effective length of the DC electrodes without via and fanout layers
5. Equal area ( $1 \text{ mm}^2$ ), built-in capacitors for each DC electrode for ease of characterization
6. Via connections for the center ground electrode

The following figures illustrate the new design features for the Gen II ion traps. Figure 3.20 is an overview of the entire ion trap chip, with the trap located left of center on the chip. This view highlights the equal area capacitors, the top level ground (green layer), and the laser access paths along the trap axis, as well as from 45 and 90 degrees. In each figure red areas indicate a negative image of the Metal 1 pattern (Metal 1 is present everywhere but the loading slot as a ground layer), the blue layer is a positive image of the Metal 3 pattern and the green layer is a positive image of the Metal 4 pattern. Figure 3.21 illustrates the trapping region with the top layer ground setting the edge of the DC electrode. This trap design includes 22 DC electrodes on each side of the trap as well as one DC and one ground electrode inside the RF rails for a total of 45 DC electrodes. Figure 3.22 is a close-up image of the new loading slot design showing the contoured RF rails and center electrodes around the loading slot.

The process flow for Gen II wafers is slightly different than that for Gen I wafers due to the addition of vias and the change in placement of the ground layer. The change involves adding a new process step, Step 5, with a via lithography and etch as described below.

**Steps 1-4 – Initial Processing:** Same processes as described for Gen I ion traps.

**Step 5 – Via Etch:** Lithography is performed using AZ Electronic Materials 4620 photoresist, applied with the conditions for oxide etching shown in Figure 2 to produce an 8-10  $\mu\text{m}$  thick layer. This photoresist is used as the etch mask for 10  $\mu\text{m}$  of oxide etching. The oxide etch is processed in either the Plasma-Therm ICP or STS AOE using the plasma conditions described in Figure 5. Resist is stripped with a 5 minute ultrasonic acetone treatment followed by a rinse with isopropyl alcohol and a 60 second oxygen ashing in a Gasonics asher. The exposed Metal 1 layer is cleaned with a final 5 min argon descum in the Vision RIE in order to remove any oxide layer on the surface and enable electrical contact with the subsequently deposited Metal 3 layer.



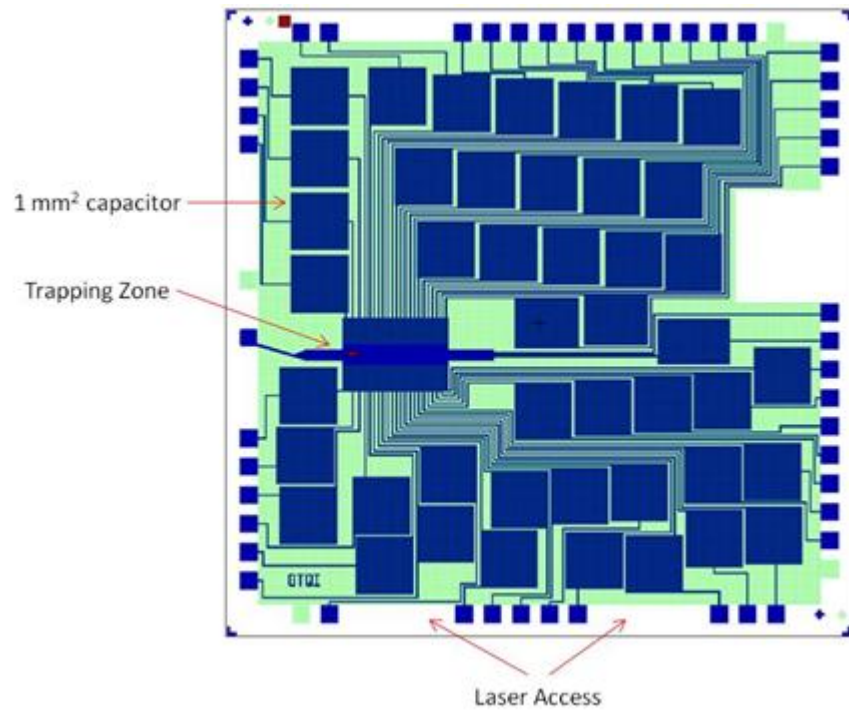


Figure 3.20: Gen II Ion Trap design.

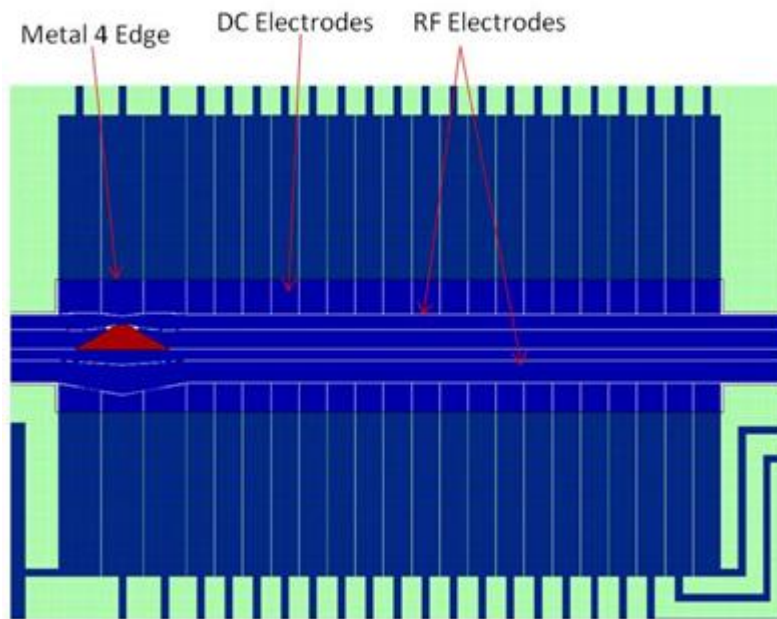


Figure 3.21: Gen II trapping region.

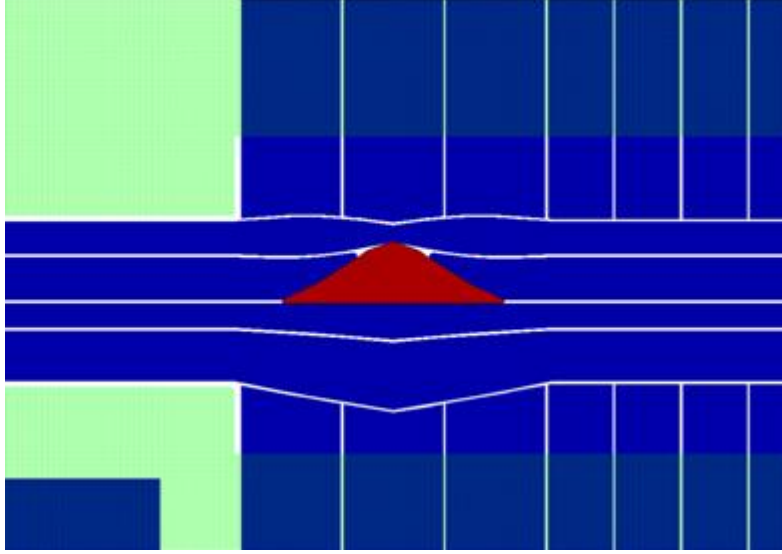
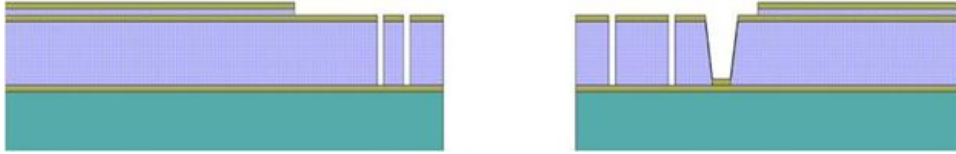


Figure 3.22: Gen II loading slot region.

**Step 6-13 – Continued Buildup.** The remainder of the process flow is identical to the Gen I process, with only a difference in the patterns defined on the Metal 3 and Metal 4 layers as shown in Figure 3.23. This produces the final cross section shown below, illustrating via connections and the top level ground structure.



A number of ion traps have been fabricated using this process flow and trapping has been demonstrated with this design. Figure 3.24 shows a series of images from completed Gen II ion traps, included a SEM image of the trapping region (Figure 3.24(a)), a close-up SEM image of the new loading slot design (Figure 3.24(b)), and images of the via connections on the center ground from an optical microscope (Figure 3.24(c)) and SEM (Figure 3.24(d)). The detailed process flows and results for each completed wafer are shown in Figure 3.25 and Figure 3.26.

### 3.4.3 Cross wafers

The third type of ion trap fabricated at Georgia Tech during the SMIT II program was the cross junction. The junction design utilizes the same process flow and cross section as the Gen II ion traps with added complexity due to the number of electrodes required. The junction contains 78 DC electrodes, four center ground electrodes connected to the Metal 1 layer with vias, and the RF rail. Figure 3.27 and Figure 3.28 show the mask patterns used to create the Metal 3 and Metal 4 layers on the cross junctions.



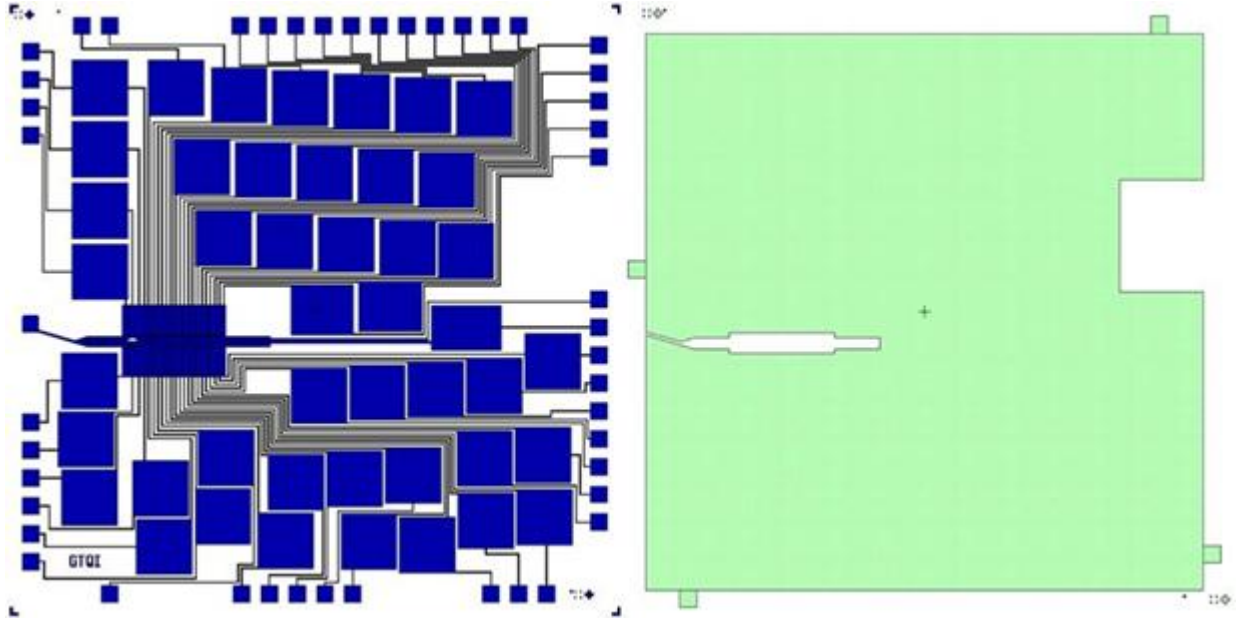


Figure 3.23: M3 mask layer (blue) and M4 mask layer (green).

Cross wafers were fabricated during the SMIT II project utilizing the process flow described for the Gen II ion traps. Figure 3.29 shows a series of images of completed cross junction ion traps. A detailed process results summary for the initial cross wafer (GT 35) is presented in Figure 3.30.

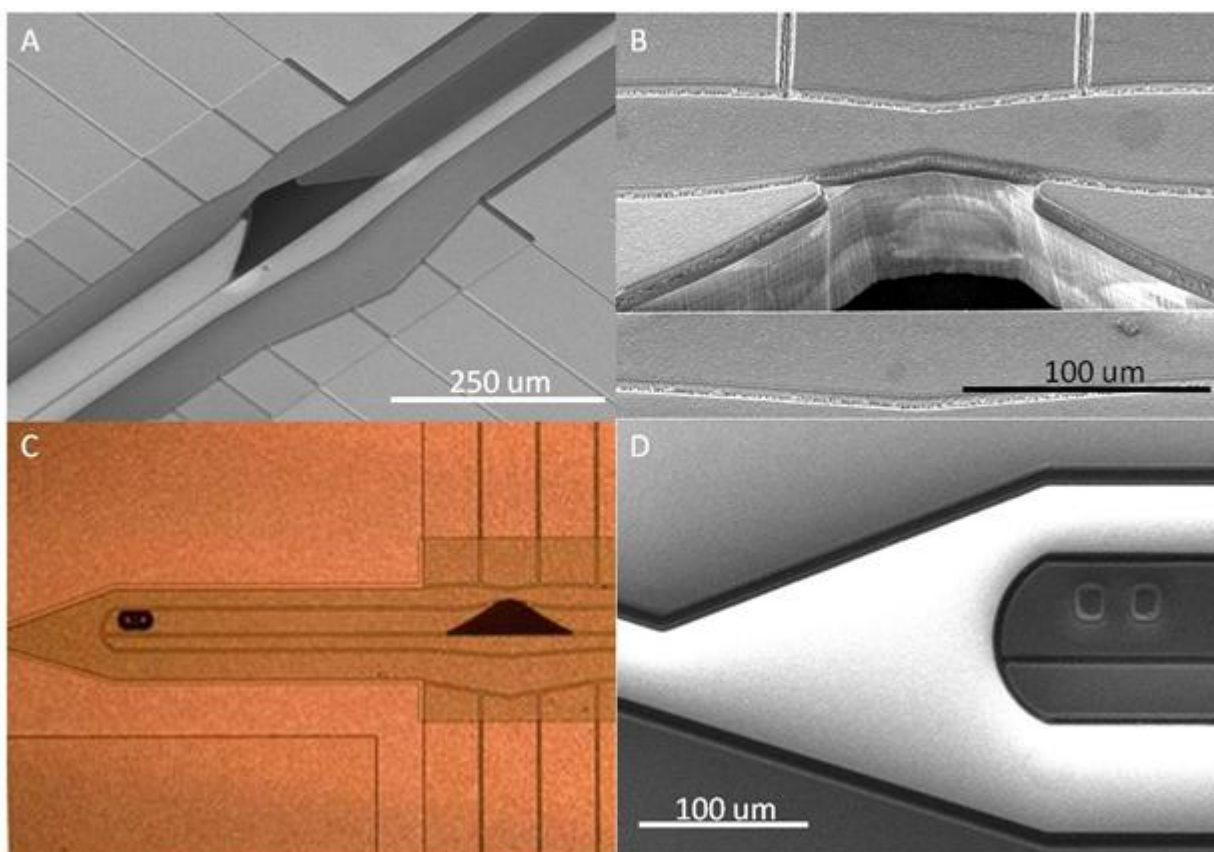


Figure 3.24: (a) SEM image of the loading zone, (b) SEM image of the loading slot showing the silicon etch profile, (c) Optical microscope image of the loading zone and center ground via connection, (d) SEM image of the center ground via connections with RF rail brightened by charging in the SEM.

	Process Step Name	Process Details	Data
1	wafer ID	GT 34	
2	clean wafer	10 min @120C	1/27/2009
3	clean wafer	15 s	1/27/2009
4	Deposit M1	Planet 3: Al/Si 1% Calibration B	1/28/2009
5	measure sheet Rs	0.056 ohms/sq	1/5/2010
6	Litho M1	SPR 1827, 1000/500/10 + 4000/1000/40: 60 s @115 C: 150MJ/cm2 exposure: 2 min develop: 10 min @ 115C	1/12/2010
7	Etch M1	12 minutes SMITDKB recipe in PT SLR RIE	1/12/2010
8	Strip PR	5 min ultrasonic acetone + 5 min PT RIE SMITDS descum	1/12/2010
9	Deposit D1 Oxide	10 um deposited in 5 steps	1/15-1/20/2010
10	measure oxide thickness	9.99 um	1/20/2010
11	Litho Via	AZ4620: 1000/100/10 + 1500/1000/40: 3:20 min @110C: 480 MJ/cm2 exposure: 3 min develop in 4:1 DiWater:AZ400k: 15 min @ 110C	1/20/2010
12	Etch Via Oxide	12 + 12 + 8 + 8 min DG-Oxide recipe STS AOE	1/20/2010
13	Strip PR	TCE + 5 min Acetone Ultrasonic + IPA + 10 min SMITDS in PTRE + 30 s Gasonics ashing	1/20/2010
14	Clean Via Contact	10 min SMITDS in PTRE + 5 min SMITAR in PTRE	1/21/2010
15	Deposit M3	Planet 1: Al/Si 1% Calibration B	1/21/2010
16	measure sheet Rs	0.058 ohms/sq	4/8/2009
17	Litho M3	SPR 1827, 1000/500/10 + 3000/1000/40: 60 s @115 C: 180MJ/cm2 exposure: 4 min develop: 10 min @ 115C	1/21/2010
18	Etch M3	12 minutes SMITDKB recipe in PT SLR RIE	1/28/2010
19	Strip PR	3 X 8 min SMITDS in PTRE + 60 s Gasonics Ashing	1/28/2010
20	Remove Metal Residue	30 s EGBOE dip	2/2/2010
21	Electrical Test	Tested Via Connections (~30 ohms), M3 connected pads (~7-35 ohms) and 12 nearest neighbors (no shorts)	2/2/2010
22	Deposit D3 Oxide	Deposit 1 um oxide in 1 step	2/2/2010
23	measure oxide thickness	1.01 um on M3, 10.85 um on M1	2/2/2010
24	Deposit M4	300 A Ti @ 100 A/min + 12000 A Al/Si 1% @ 300 A/min: Al/Si 1% Calibration B	2/2/2010
25	measure sheet Rs	0.058 ohms/sq	2/3/2010
26	Litho M4	SPR 1827, 1000/500/10 + 3000/1000/40: 60 s @115 C: 180MJ/cm2 exposure: 2:30 min develop: 10 min @ 115C	2/3/2010
27	Etch M4	12 minutes SMITDKB recipe in PT SLR RIE	2/3/2010
28	Strip PR	5 min ultrasonic acetone + 2 X 60 s Gasonics Ashing	2/3/2010
29	Etch Oxide	STS AOE 90 s DG-OX350 + 12 + 24 + 24 min DG- OXO70	2/5/2010
30	Frontside Slot Etch	100 cycles Boschsmi recipe on PT ICP	2/9/2010
31	Litho Backside Slot	AZ4620: 500/250/30: 20 min @ 105C: 800 MJ/cm2 exposure (365 nm): 13 min develop in 4:1 DiWater:AZ400k: 30 min @ 105C	2/10/2010
32	Cavity etch	200 + 100 + 300 + 50 cycles boschsmi recipe on PTICP	2/10-2/11/2010
33	Strip PR	TCE + Acetone + IPA + 60 s Gasonics Ashing	2/11/2010
34	Clean Backside Contact	Cleaned on chip level	
35	Deposit Backside Ti/Au	Deposited on chip level	
36	Dice	11 mm die	2/22/2010

Figure 3.25: Process results summary for GT 34 (used to trap ions).

	Process Step Name	Process Details
1	wafer ID	GT 50
2	clean wafer	10 min @120C
3	clean wafer	15 s
4	Deposit M1	Planet 5: Al/Si 1% Calibration B
5	measure sheet Rs	0.054 ohms/sq
6	Litho M1	SPR 1827, 1000/500/10 + 4000/1000/40: 60 s @ 115 C: 180mJ/cm2 exposure:110 s develop: 10 min @ 115C
7	Etch M1	12 minutes SMITDKB recipe in PT SLR RIE
8	Strip PR	5 min Acetone Ultrasonic + IPA + 60 s Gasonics Ashing
9	Deposit D1 Oxide	10 um deposited in 5 steps
10	measure oxide thickness	10.01 um
11	Litho Via	AZ4620: 1000/500/10 + 1500/1000/40: 3:20 min @ 110C: 500 MJ/cm2 exposure (365 nm): 4 min develop in 4:1 DiWater:AZ400k: 30 min @ 115C: resist height 9.07 um
12	Etch Via Oxide	PT ICP SMITOXHB recipe for 16 + 16 + 16 + 6 + 10 + 9 min (73 total)
13	Strip PR	5 min Acetone Ultrasonic + IPA
14	Clean Via Contact	5 min Ar Descum recipe in Vision RIE
15	Deposit M3	Planet 3: Al/Si 1% Calibration B
16	measure sheet Rs	0.052 ohms/sq
17	Litho M3	S 1827, 1000/500/10 + 3000/1000/40: 5 min @ 115 C: 500 mJ/cm2 exposure: 60 s develop: 10 min @ 115C: resist height 2.7 um
18	Etch M3	12 minutes SMITDKB recipe in PT SLR RIE
19	Strip PR	5 min Acetone Ultrasonic + IPA + 60 s Gasonics Ashing
20	Remove Metal Residue	30 s EGBOE dip
21	Electrical Tests	Via connections good (~20 Ohms) some shorts (kOhm)
22	Remove Metal Residue	30 s EGBOE dip
23	Electrical Tests	Previous kOhm shorts gone, only 1 short measured (chip E-5)
24	Deposit D3 Oxide	Deposit 1 um oxide in 1 step
25	measure oxide thickness	1.02 um
26	Deposit M4	300 A Ti @ 100 A/min + 8000 A Al/Si 1% @ 300 A/min: Al Calibration A: Planet 5
27	measure sheet Rs	0.069 ohms/sq
28	Litho M4	S 1827, 1000/500/10 + 3000/1000/40: 5 min @ 115 C: 500 mJ/cm2 exposure: 60 s develop: 20 min @ 115C
29	Etch M4	15 minutes SMITDKB recipe in PT SLR RIE
30	Strip PR	2 X 60 s Gasonics Ashing + Acetone + IPA + 30 s EGBOE
31	Etch Oxide	STS AOE DG OXLBO 15 min + 2 min Dgoxide + 30 min DGOXLBO + 45 min DGOXLBO
32	Frontside Slot Etch	20 + 30 cycles Boschsmi recipe on PT ICP
33	Litho Backside Slot	AZ4620: 500/250/30: 20 min @ 110C: 900 MJ/cm2 exposure (365 nm): 4 min develop in 4:1 DiWater:AZ400k: 30 min @ 115C: resist height 25.4 um
34	Cavity etch	250 + 250 + 100 + 50 cycles boschsmi recipe on PTICP
35	Strip PR	TCE + Acetone + IPA + 2 X 60 s Gasonics Ashing
36	Clean Backside Contact	3 min SMITDS + 3 min SMITAr in PT RIE + 3 min Ar Descum in Vision
37	Deposit Backside Ti/Au	300 A Ti @ 1.5 A/sec + 3000 A Au @ 3.0 A/sec
38	Dice	11 mm die

Figure 3.26: Process results summary for GT 50.



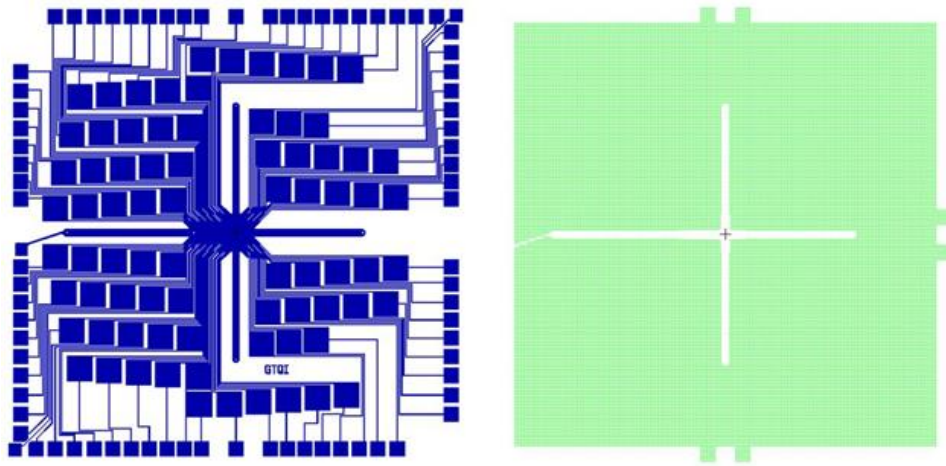


Figure 3.27: Metal 3 (Blue) and Metal 4 (Green) mask patterns.

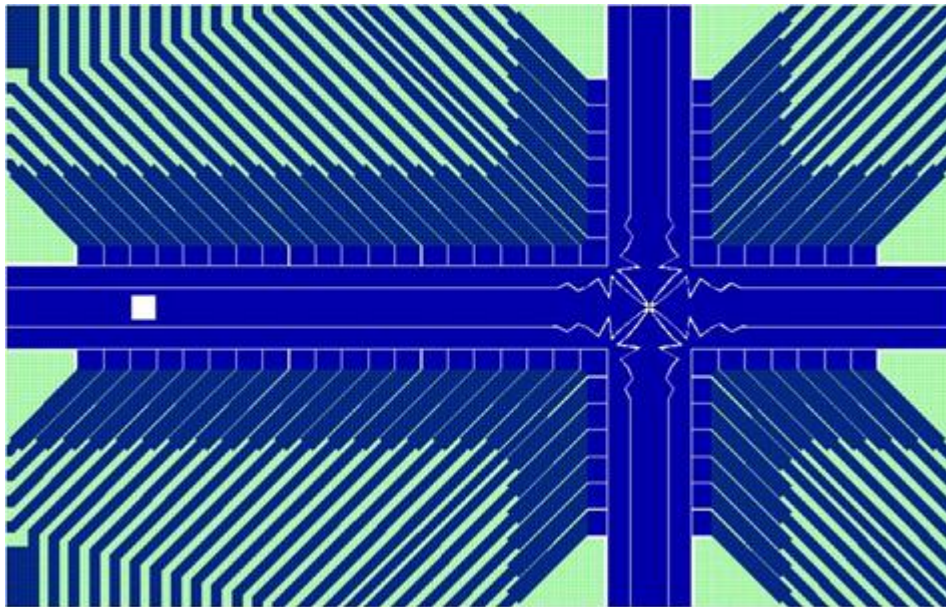


Figure 3.28: Zoomed image of cross junction pattern showing Metal 3 (blue) and Metal 4 (green) layers.

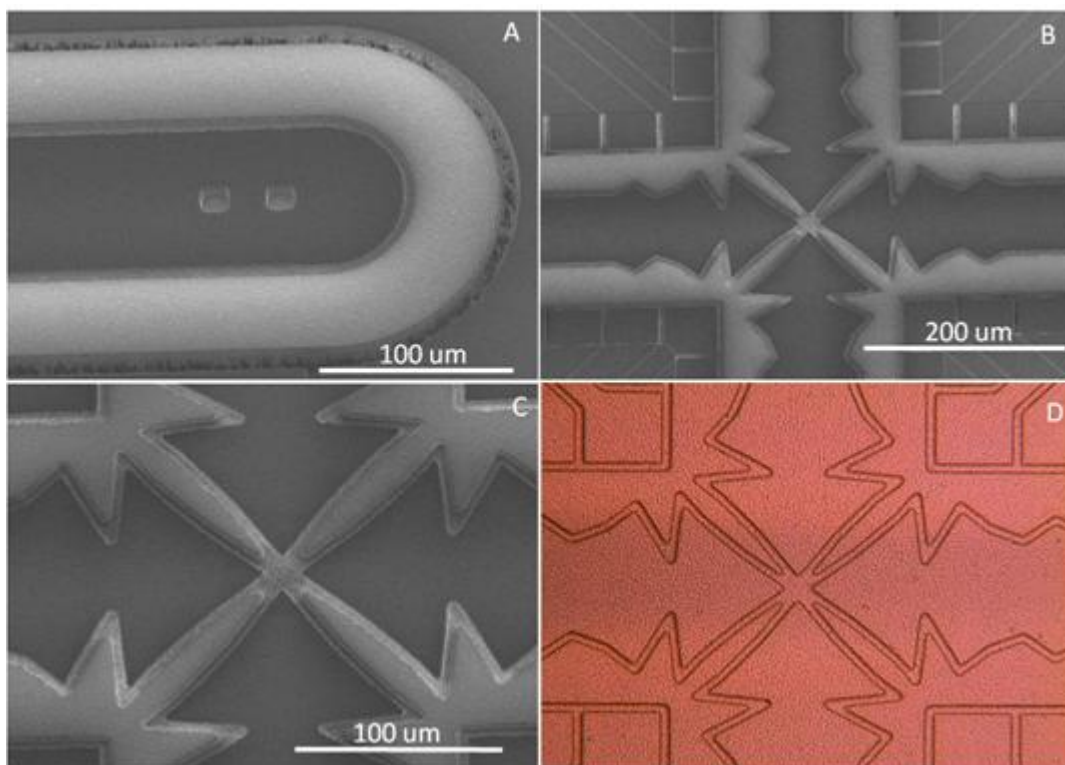


Figure 3.29: Images of a completed cross wafer: (a) SEM image of center ground via connections, (b) SEM image of the junction center, (c) SEM image of RF fingers at the center of the junction, (d) Optical microscope image of junction center.

	Process Step Name	Process Details	Data
1	wafer ID	GT 35	
2	clean wafer	10 min @120C	1/5/2010
3	clean wafer	15 s	1/5/2010
4	Deposit M1	Planet 5: Al/Si 1% Calibration A	1/5/2010
5	measure sheet Rs	0.042 ohms/sq	1/5/2010
6	Litho M1	SPR 1827, 1000/500/10 + 4000/1000/40: 60 s @115 C: 180mJ/cm2 exposure:90 s develop: 10 min @ 115C	3/15/2010
7	Etch M1	12 minutes SMITDKB recipe in PT SLR RIE	3/15/2010
8	Strip PR	2 X 60 s Gasonics Ashing + Acetone + IPA	3/15/2010
9	Deposit D1 Oxide	10 um deposited in 5 steps	3/16-3/23/2010
10	measure oxide thickness	9.99 um	3/23/2010
11	Litho Via	AZ4620: 1000/500/10 + 1200/1000/40: 3:20 min @ 110C: 480 MJ/cm2 exposure (365 nm): 4 min develop in 4:1 DiWater:AZ400k: 15 min @ 110C: resist height 9.74 um	3/25/2010
12	Etch Via Oxide	STS AOE DG-Oxide 12 + 6 + 6 min	3/25/2010
13	Strip PR	5 min Acetone Ultrasonic + IPA + 60 s Gasonics Ashing	3/25/2010
14	Clean Via Contact	5 min Ar Descum recipe in Vision RIE	3/30/2010
15	Deposit M3	Planet 3: Al/Si 1% Calibration A	3/30/2010
16	measure sheet Rs	0.059-0.072 ohms/sq	3/30/2010
17	Litho M3	S 1827, 1000/500/10 + 3000/1000/40: 5 min @ 115 C: 500 mJ/cm2 exposure: 60 s develop: 10 min @ 115C	3/30/2010
18	Etch M3	12 minutes SMITDKB recipe in PT SLR RIE	4/1/2010
19	Strip PR	2 X 60 s Gasonics Ashing + 10 min O2 Descum in Vision RIE + 5 min Acetone Ultrasonic + IPA	4/1/2010
20	Deposit D3 Oxide	Deposit 1 um oxide in 1 step	4/6/2010
21	measure oxide thickness	0.99 um	4/6/2010
22	Deposit M4	300 A Ti @ 100 A/min + 12000 A Al/Si 1% @ 300 A/min: Al Calibration A	4/12/2010
23	measure sheet Rs	0.064 ohms/sq	4/12/2010
24	Litho M4	S 1827, 1000/500/10 + 3000/1000/40: 5 min @ 115 C: 500 mJ/cm2 exposure: 60 s develop: 10 min @ 115C	4/15/2010
25	Etch M4	15 minutes SMITDKB recipe in PT SLR RIE	4/15/2010
26	Strip PR	2 X 60 s Gasonics Ashing + Acetone + IPA + 30 s EGBOE	4/15/2010
27	Etch Oxide	PT ICP SMITOXHB 3 + 6 + 6 + 30 s EG-BOE + 3 + 6 + 12 + 12 + 12 + 12 + 6 + 3 min (81 total)	4/15 + 4/20/2010
28	Frontside Slot Etch	30 cycles Boschsmi recipe on PT ICP	5/11/2010
29	Litho Backside Slot	AZ4620: 500/250/30: 20 min @ 105C: 900 MJ/cm2 exposure (365 nm): 5:30 min develop in 4:1 DiWater:AZ400k: 30 min @ 105C	5/14/2010
30	Cavity etch	400 + 200 + 100 + 50 cycles boschsmi recipe on PTICP	5/17-5/19/2010
31	Strip PR	TCE + Acetone + IPA + 2 X 60 s Gasonics Ashing	6/17/2010
32	Clean Backside Contact	3 min SMITAr in PT RIE	6/18/2010
33	Deposit Backside Ti/Au	300 A Ti @ 1.5 A/sec + 3000 A Au @ 3.0 A/sec	6/18/2010
34	Dice	11 mm die	6/30/2010

Figure 3.30: Process results summary for GT 35 cross wafer.

# Chapter 4

## Trap Packaging and Characterization

Under the SMIT program, the GTRI Quantum Information Systems group developed a comprehensive, tightly-coupled modeling, design, fabrication, and testing capability that has allowed us to develop, demonstrate, and deliver novel ion traps. The GTRI QIS laboratory was built and equipped using internal GTRI funds at the beginning of the SMIT program. Most of the testing and characterization techniques described in this section were developed at GTRI using SMIT traps under the SMIT program.

### 4.1 Packaging

Packaging capabilities have all been moved in-house to improve control and reliability, and to allow for process development for special applications. Capabilities now include:

1. Mounting of trap chips to spacer and carrier with AuSn solder as shown in Figure 4.1. This bonding method forms rigid, conducting, high temperature (270°C) connections.
2. Wirebonding between chip and package connections with 1 mil Al wires on a Palomar 2470 wedge bonder. GTRI's investment in the Palomar bonder has given us the ability to reliably bond 100s of connections per chip. The bonder's deep access ability will also be invaluable for future projects where multiple devices are packaged to the same in-vacuum substrate and where multiple tiers of connections need to be made between devices.
3. Testing for shorts and measuring capacitances.

### 4.2 Vacuum Chambers

Two vacuum chambers provide rapid turnaround and efficient use of the trap testing station.  
*Chamber 1:*

1. Name: Neo
2. Connections: 98-pins into four 25-pin D connectors.



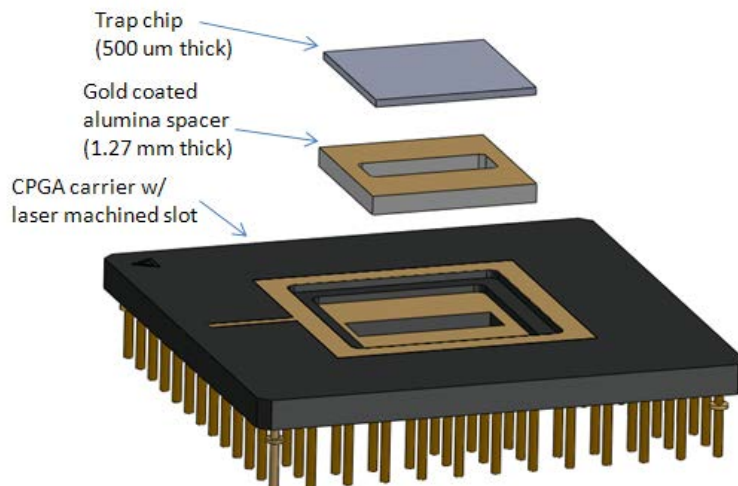


Figure 4.1: Drawings of the carrier assembly with trap, spacer, and carrier mounted with AuSn solder.

3. Vacuum: 40 l/s ion pump, Ti sublimation pump, nude ion gauge.

*Chamber 2:*

1. Name: Morpheus
2. Connections: 50-pins into two 25-pin D connectors
3. Vacuum: 40 l/s ion pump.

#### 4.2.1 In-vacuum sockets

The sockets are fabricated from PEEK and, in newer designs, glass-filled PEEK on a stainless steel frame. Individual pin receptacles are sandwiched between PEEK plates screwed to the frame (Figure 4.2). The receptacles are crimped to Kapton coated wires which are then bundled and terminated in commercial in-vacuum 25-pin D connectors.

To reduce thermal stresses during the bakeout (see below), the original PEEK socket assemblies were replaced with glass-filled PEEK, which exhibits a lower thermal expansion coefficient, closer to the expansion of the stainless steel.

#### 4.2.2 Ca oven

The Calcium ovens that supply fluxes of neutral Calcium consist of a packed formed folded SS sheet that encompasses the Calcium filings. Stainless steel wire, spot welded to the package provide a current path and the bulk of the resistive heating. These ovens require roughly 3-4 A and 2 V to operate. After the chamber bakeout (see below), the ovens seem to need a high temperature step (4-5 A for a few minutes) to begin the evaporation. This is only needed once after the oven has been at air.

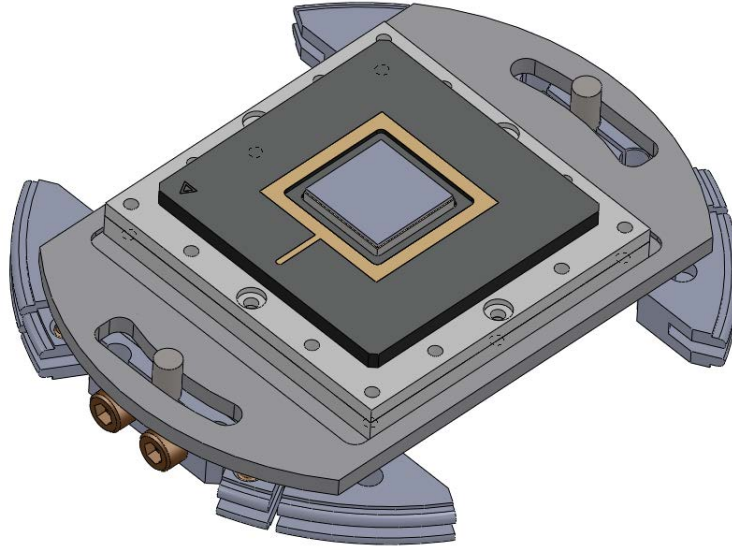


Figure 4.2: Drawing of a socket and chip carrier mounted to two Kimball Physics groove grabbers. The groove grabbers lock to the inside of a 4.5" spherical octagon (also Kimball Physics).

### 4.2.3 Ground shield

To reduce the effects of charging of insulating surfaces (such as the main viewport), the traps had a grounded screen installed 2 mm above the trapping surface. Two types of shield assembly were used: a machined stainless steel assembly with a clamped steel screen and a snap-on sheet metal shield with a spot welded screen. Both are shown in Figure 4.3. The screen was a 100 line-per-inch woven stainless steel cloth with 80% light throughput.

The snap-on shields were water-jet cut from 0.020" thick 316 stainless steel sheet and hand formed to shape. The screen and cover were spot welded into place. A wire was crimped onto the shield to make an electrical connection. The accuracy of the forming process could be increased in the future by using a press and forms. These shields are inexpensive and can be supplied with each trap and will provide an additional layer of physical protection to the trap during transport and installation.

In addition to providing shielding against charging, the shield is also used in the trap characterization process as part of the 'tickle' measurements for the mode frequencies. For this purpose, the connection to the shield passes through a port and is grounded through a bias-tee. The DC input of the bias-tee is shorted to ground while the RF input is connected to the 'tickle' RF source. The bias-tee removes any DC component from the applied RF that would effectively act as a stray field while passing the RF onto the shield. The tickle measurements are described in more detail in the Frequency Control section (4.4.3) and the Gen I trap testing section (4.5.1).

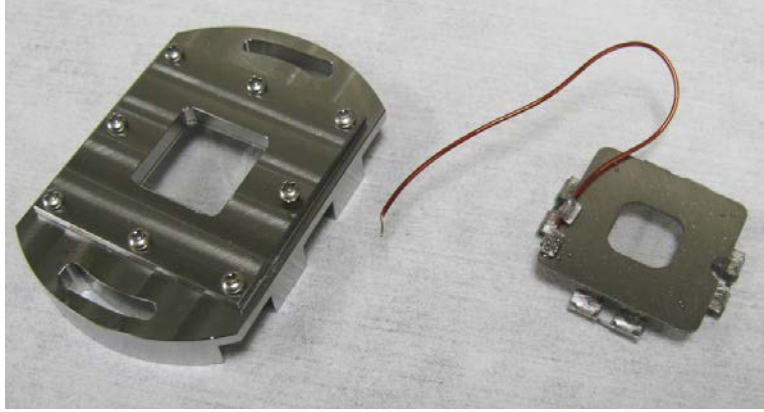


Figure 4.3: Machined shield (left) and snap-on shield (right).

### 4.3 Bakeout

To achieve the  $< 10^{-11}$  torr vacuums needed for long ion lifetimes, the vacuum chamber is baked at  $240^{\circ}\text{C}$  for several days connected to a turbo molecular pump. A programmable oven large enough to enclose the vacuum chamber provides the controlled temperature ramp to prevent damage to the vacuum components from thermal gradients. Once the pressure at the turbo has stabilized, the temperature is reduced to  $200^{\circ}\text{C}$ , the ion pump is connected and turned on, and the pump out continues for several more days until the pressure again bottoms in the low  $10^{-8}$  torr range. During the bake out process, various components in the vacuum system are degassed, e.g. the Ti-sublimation pump and the Ca oven.

## 4.4 Trap characterization

To characterize the packaged traps, we developed a comprehensive testing and characterization platform supported by a flexible data acquisition system. The testing platform has a number of subsystems described here.

### 4.4.1 Laser farm and frequency lock

The laser farm contains the following diode lasers set to the various  $^{40}\text{Ca}^{+}$  transitions:

1. 397 nm – Fluorescence
2. 423 nm (doubled) – Photoionization
3. 377 nm – Photoionization
4. 866 nm – Repump
5. 854 nm – Repump
6. 729 nm – Qubit transition



Rough laser frequencies are measured with a Toptica WS7 wavemeter. However, drifts in the wavemeter were too large for reliable trap characterization. For more consistent locking, we implemented a cavity lock referenced to a commercial stabilized HeNe laser. The cavity is routinely calibrated against scans of the ion fluorescence through the data server (see below).

### 4.4.2 Optical control

The optical control subsystem modulates the amplitude and frequency of the 397 nm fluorescence laser and provides an overlapped fixed-frequency far-detuned beam for loading and cooling very hot ions and a variable frequency beam used for the fluorescence scans and the majority of the cooling. A switched RF source (see Frequency Control, below) for the variable frequency beam permits a single measurement cycle to switch rapidly between two different detunings in addition to the far detuned beam.

### 4.4.3 Data acquisition

The data acquisition system we developed for characterizing traps provides comprehensive diagnostics of trap performance. Much of the characterization process is automated so that complete test sequences can be performed in sufficient detail to determine trends and with sufficient statistics to base reliable conclusions. Also, by automating the sequences, the resulting data sets are generated consistently from trap to trap.

The data acquisition is comprised of four subsystems that are controlled by a custom interface based on the Wavemetrics' IGOR Pro data acquisition and analysis package supplemented with custom extensions written in C++. Automation was developed using IGOR Pro scripting language.

The four subsystems in the data acquisition system are: the pulse control, frequency control, waveform generators, and data server.

#### 4.4.3.1 Pulse control

Each experiment cycle is controlled by a custom FPGA based timing system. The timing system takes a byte code program and expands it into a timing sequence (the control process in the figure below). The timing sequence is then parsed on a precise schedule based on an external clock. The result is a complex sequence of digital signals (currently 24 channels) for controlling experimental parameters (laser intensity, frequency, tickle sources, etc.) and counters for acquiring photomultiplier counts that measure the ion fluorescence. Each experiment cycle is repeated (usually 100 to 800 times) to acquire sufficient statistics for that single data point.

The control code is written in VHDL (one of two standard languages for FPGA programming) and runs on an inexpensive XILINX Spartan 3 FPGA. The code is modular so that changes and extensions are straightforward. Examples of such changes could be additional control busses for DDS frequency control and external memory for more complex pulse sequences.

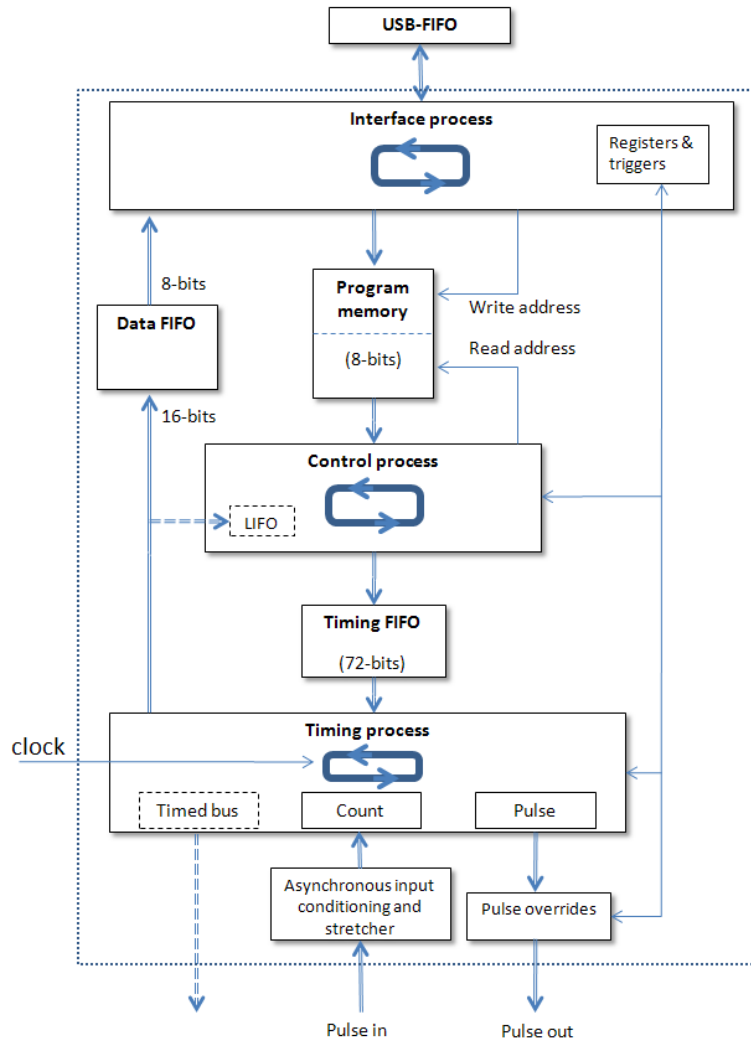


Figure 4.5: Schematic of the VHDL code that provides the control signals for the experimental control. Dashed lines indicate components that are still in development.

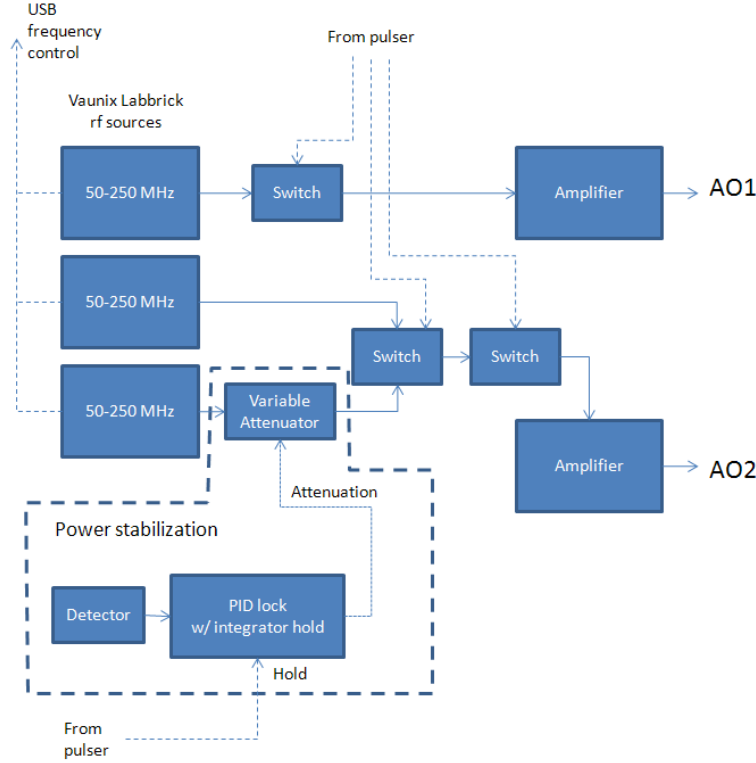


Figure 4.6: Schematic of the laser pulsed frequency control. Through two AO's and switched RF sources, each cycle of the pulse control program can generate up to three different laser frequencies. One of the frequencies is power stabilized using a variable attenuated adjusted by a PID lock. This reduces fluctuations in ion fluorescence during the various trap characterization measurements.

#### 4.4.3.2 Frequency control

During an experiment cycle, multiple laser frequencies may be needed to manipulate the ions and generate fluorescent light for detection. The current version of the laser frequency control uses several USB controlled sources (Vaunix Labbricks) that are fed through high isolation switches to the two AO's used for the frequency control. By using multiple, switched RF sources, we can perturb a trapped ion with one frequency and then cool it with another, permitting measurements that would be unstable with a single frequency due to heating of the ion by the laser.

The frequencies and amplitudes of these sources are set through USB by the data acquisition computer. Since they have to be set by USB, they can only be changed slowly over the course of a scan and within a single experiment cycle. In the future, the pulse control system can be readily expanded to control direct digital synthesis (DDS) modules to provide rapid frequency shifting during a single cycle.

In addition to the laser frequency control, there is a second system for applying 'tickle' perturbations to the ions to measure the mode frequencies and stray fields. There are two tickle methods: DC tickle and RF tickle. DC tickles have the perturbing RF applied to

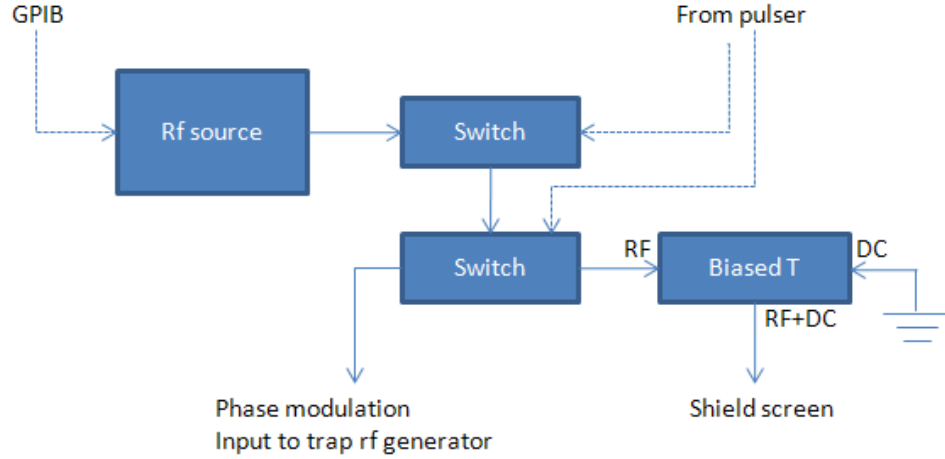


Figure 4.7: Schematic of the frequency ‘tickle’ source. A pulsed RF frequency near or on resonant with a secular motional mode of the trapped ion can be excited by either applying an oscillatory electric field (RF applied to the shield screen) or by creating side.

the shield screen (or, in most labs, to a control electrode on the trap itself). When the RF potential is on or near a secular motional frequency, the ion motion will be excited and then detected with the corresponding change in fluorescence due to the Doppler shifts. With this method, we measure the radial and axial mode frequencies of the ion. For RF tickle, the RF frequency is applied to the phase modulation input of the trap RF source generating an amplitude modulation in the pseudopotential strength at the modulation frequency. If the ion is at the micromotion null, the amplitude modulation will not affect the ion. However, if there are any stray fields that push the ion off the pseudopotential minimum, the modulation of the pseudopotential strength will cause a corresponding modulation of the ion position (as the balance between the stray field and the pseudopotential shifts) that can excite secular motion. Since the RF tickle is dependent on the stray fields, this technique can be used to measure and null the stray fields at the ion location. The RF tickle method has the benefit of detecting stray fields in both radial directions. However, it only detects stray fields and not any micromotion that might remain after the stray fields are nulled. A simpler and faster technique based on laser fluorescence (discussed later) will only detect the stray fields along one radial direction (orientation depends on the trap geometry) but is sensitive to any remnant micromotion remaining after stray fields are nulled. A full trap characterization would use both techniques.

#### 4.4.3.3 Waveform generators

The waveform system provides control voltages for holding and transporting single and multiple ions. The system consists of 96 channels from 16 National Instruments 6733 DAC cards clocked by the pulse control system. By controlling the DACs with the pulse control system, ion transport and control perturbations can be interspersed with measurement processes within a single experiment cycle. This capability allows complex processes where an ion can





Figure 4.8: Example of transports interspersed within a single experiment cycle.

be transported to a particular region of the trap, perturbed by, for example, a tickle (see Mode Frequency Measurements below), and then transported back for detection, all within one measurement cycle that can then be repeated automatically by the FPGA pulser to generate statistics.

#### 4.4.3.4 Data servers

To facilitate transfer of parameters and data between various applications and between computers running those applications, the data servers provide network services for key computers. The servers can be configured to read particular information, such as data returned from the camera software or laser frequency measurements, or provide a buffer between applications on separate computers, such as laser lock corrections after an ion fluorescence scan.

## 4.5 Traps tested under the SMIT program

### 4.5.1 Gen I Trap

The bulk of the trap testing facility was developed with the GTRI SMIT Gen I traps. Cryogenic testing at MIT was also performed on this generation of trap.

1. Backside loading slot reduces the possibility of shorting by the neutral atom flux and deposition of Ca on the front surface electrodes.
2. Asymmetric RF rails.
3. Two ion regions with different ion heights for relative heating measurements (the narrow portion of this region was not experimentally characterized).

Ions were loaded into three Gen I traps. A number of traps were tested, but the trap SMIT15 C9 was the first trap to load ions. All the subsequent traps also loaded ions. Most of characterization system was being developed as these traps were brought on line so only the third trap has close to a full data set. A summary of each of the Gen I traps follows:

#### Chip ID: SMIT15 C9

*Description:* This trap was the first to load an ion. This trap required a metallization patch to the backside of the load zone to correct for a fabrication error that etched the metallization on the underside of the cantilevered oxide. Because of the slot, this backside metal layer significantly affected the RF potential near the loading region. While we were able

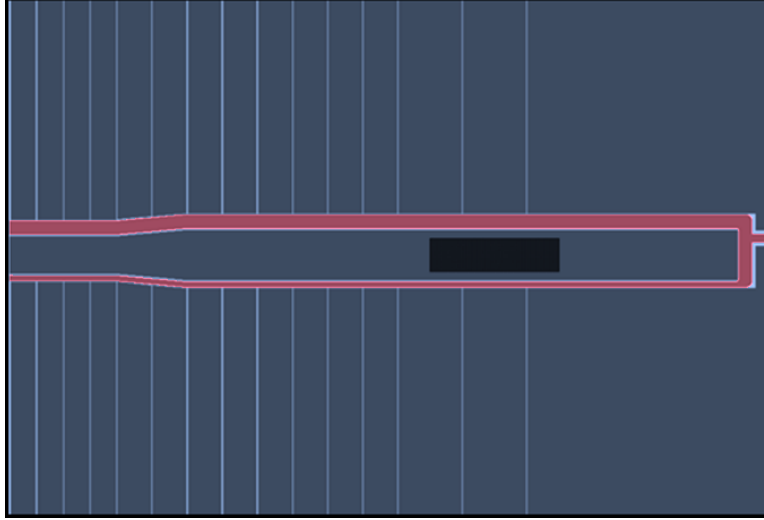


Figure 4.9: Gen I ion trap. The RF rails are highlighted in red and are functionally divided into two regions with different rail spacing. We characterized these traps only in the region with the wider spacing because of time constraints.

to load ions in this trap, we determined later that there was a floated control electrode due to a wire bond that became disconnected during bakeout. This electrode became charged, probably by photoelectric emission from the RF rail, and generated large stray fields at the load zone. This required large corrections to the calculated trapping potentials to load ions. Because of this wire bonding problem, we investigated new methods and equipment for bonding the trap. The resulting packaging changes resulted in stronger, more reliable bonds.

*Summary of testing:* We were able to load in this trap, but the potentials required had to be initially hand tuned since the potential on the floating electrode was not known. The characterization system was still very basic at this time.

Chip ID: GT22 C4

*Description:* This trap has been the workhorse for our testing and characterization development and was also tested at cryogenic temperatures at MIT (discussed later). The issue that resulted in etching of the backside metallization of the loading slot was fixed so this trap did not require any loading slot patch. A new wirebonder provided stronger, more reliable connections between the chip and carrier. This trap has worked reliably and the comparison between the models and trap characterization measurements have been very good (see later for a description of these the measurements). This trap has been the gold-standard for our development work.

*Summary of testing:* This trap worked reliably both at room temperature and at cryogenic temperature. This trap loaded ions on the first attempt and with calculated potentials. We demonstrated a thousand  $600\ \mu\text{m}$  transports from the load zone without loss. Ion lifetimes in the dark exceeded a minute (the lifetime measurement is described later along with the results for this trap) and lifetime with cooling was several hours and possibly limited by frequency drift in the cooling laser. Most of the trap characterization used an RF frequency

of 58 MHz, an axial frequency of 1 MHz, and radial frequencies around 5 MHz.

Chip ID: GT22 C1

*Description:* Same wafer as the GT22 C4 chip. This trap was installed in our then-new 100-pin chamber. We later determined that a region of the carrier behind the trap chip was floating. This region became biased and generated stray fields in the load zone. This trap performed very well once we determined the bias and applied a correction to the models. Unfortunately, the bias shifted twice during the characterization of this trap, preventing a complete characterization data set. The problems with this trap led us to improve the mounting and packaging of the traps.

*Summary of testing:* The trap loaded reliably. However, the trap exhibited a large stray field in the load zone. Detailed mapping of the deviation of the ion position during transport indicated that something behind the trap had charged (see Figure 4.10). We were able to model corrections and obtain reliable transport out of the load zone and along the first few hundred microns outside the load zone. A sudden change in the stray field in the load zone curtailed our characterization and we decided to switch to a Gen II trap (see later) which had become available. After the trap was pulled from the vacuum chamber, it was found that a portion of the carrier behind the chip was electrically floating. Ion lifetimes in the load zone were shorter than the GT22 C4 chip (see the Lifetime Measurement section below) probably due to the stray fields perturbing the trap depth. We did not get a chance to measure the lifetimes or mode frequencies outside the load zone. We did obtain detailed mode frequency measurements as a function of applied bias fields (see the Compensation section below). Most of the trap characterization used an RF frequency of 46 MHz (new chamber had higher capacitance, driving the frequency down from the 58 MHz of the GT22 C4 trap), an axial frequency of 1 MHz, and radial frequencies around 5 MHz.

#### 4.5.1.1 Ion loading

Ions were loaded reliably and quickly using resonant assisted photoionization over the load zone in all three of the Gen I traps, though the SMIT15 C9 trap needed a correction to compensate for the floating electrode. There did not seem to be any special trap RF amplitudes needed to load single ions and we generally set the RF amplitude to give us a radial frequency of about 5 MHz. For an unknown reason, only single ions would load at this RF amplitude. Reducing the RF amplitude by about 30% resulted in loading chains of up to five ions (the number depended on the axial trapping strength) even though it would seem that a tighter radial well would improve loading.

#### 4.5.1.2 Ion transport

We demonstrated fast ion transport over 600  $\mu\text{m}$  using the calculated waveforms without any experimental tweaking. Each of the following round trip transports was repeated 1000 times without ion loss in the GT22 C4 trap:

1. 10 ms transport time w/ cooling laser at the loading zone ( $z=0\mu\text{m}$ ) and at the final transport zone ( $z=600\mu\text{m}$ ). Ion pauses 0.2sec at either end of the transport.
2. Same as 1 except the transport time was reduced to 1ms.

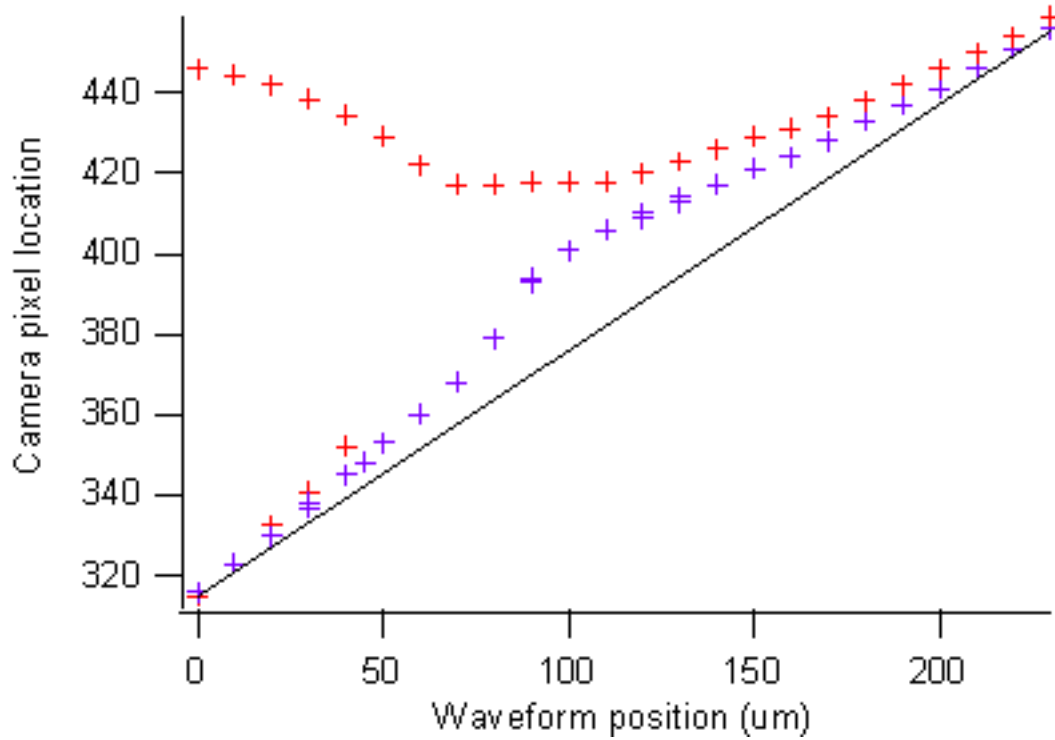


Figure 4.10: Ion displacement (in pixels) vs. calculated position. The displacement was expected to be a straight line corresponding to a fixed number of pixels per micron but stray fields in the loading slot generated displacements near the edge of the slot (slot is centered at  $0\text{ }\mu\text{m}$  and the slot edges are at  $\pm 150\text{ }\mu\text{m}$ ). The jump in the red crosses is due to a double well forming at the edge of the slot which generates a hysteresis in the ion position between transport out of the slot (blue) and the return (red).

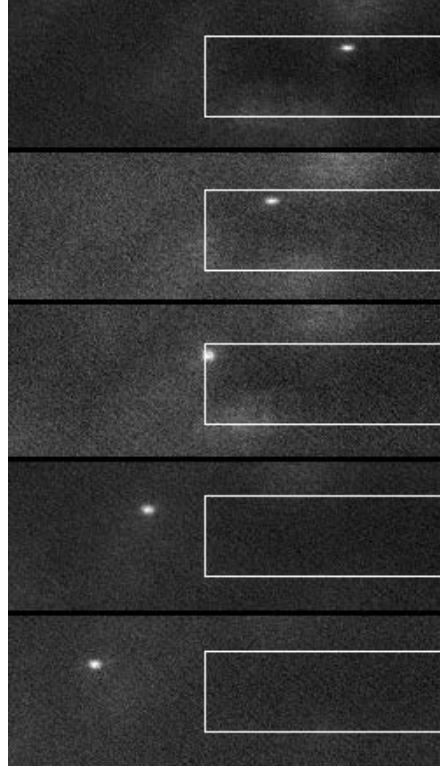


Figure 4.11: Example of a single ion transport from the load zone to about  $100\ \mu\text{m}$  beyond the load zone. Overall transport distance is  $250\ \mu\text{m}$ . The overlaid outline indicates the extent of the loading zone. The cooling laser beam was manually adjusted to track the ion position.

3. Same as 2 except the  $z=600\ \mu\text{m}$  cooling beam was blocked. Ion now sits in the dark at  $z=600\ \mu\text{m}$  for 0.2 sec before returning to the load zone.

Figure 4.11 demonstrates (in GT22 C4) a slow transport from the load zone to a point about  $100\ \mu\text{m}$  beyond the load zone, stopping at various locations to record an image of the ion location. Figure 4.12 shows two ions simultaneously held in the trap, one at the load zone and the other at  $600\ \mu\text{m}$  from the first. The ion at  $600\ \mu\text{m}$  was loaded first, and then transported out to the shown location. The trapping potentials were then modified to recreate the load zone potential well while not affecting the transported ion. The second ion was then loaded.

#### 4.5.1.3 Ion chains

We demonstrated short ion chains in harmonic axial wells. We normally trapped with radial frequencies around 5 MHz, but it was necessary to reduce the RF potential by 30% before chains would load. In addition to reducing the RF potential, we also had to scale the axial potential by a factor of 70% (corresponding to a single ion frequency of 0.5 MHz) to load the longer chains. The need to weaken the axial well is understood from the basic stability

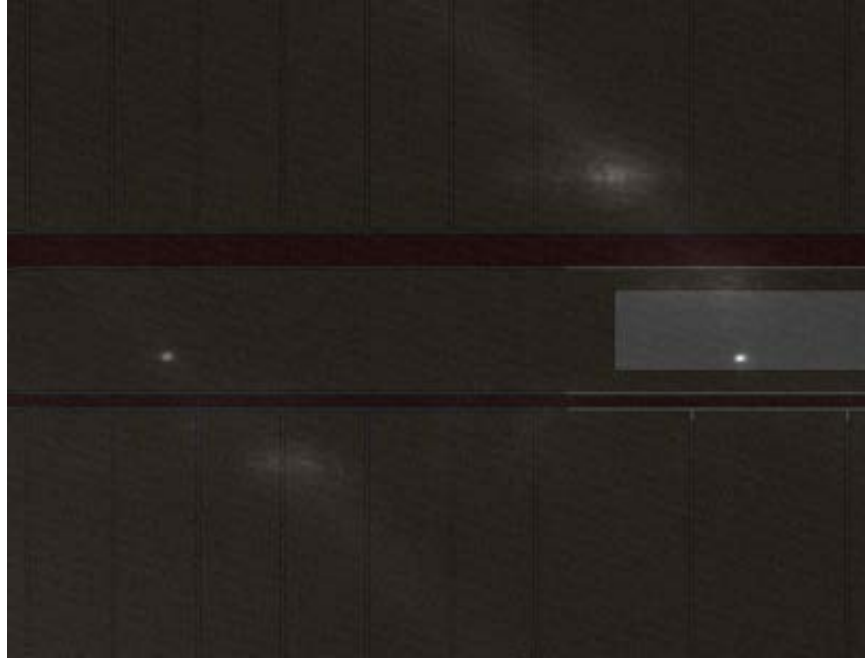


Figure 4.12: Example of two ions simultaneously held in separate wells  $600\text{ }\mu\text{m}$  apart. The ion on the left was loaded first and transported out of the loading zone. A second ion was then loaded while keeping the first in its well. A rendering of the trap surface has been overlaid to show the trap structure. Each ion has a cooling laser beam centered on it to keep it trapped and to cause it to fluoresce for this image.

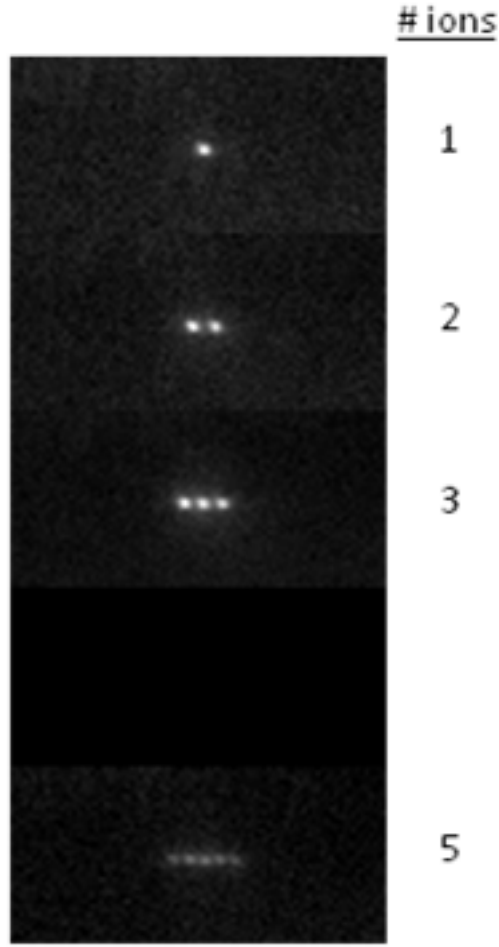


Figure 4.13: Example of short ion chains in a Gen I trap. The axial trap potential is harmonic and is the same for all cases.

requirement that the axial potential be weaker than the radial potential to prevent zig-zag chains (i.e. not a simple line of ions) from forming. We have not seen zig-zag chains when we increase the axial trapping potential which implies that they were unstable for the settings we used.

We have not studied chains in detail beyond simply loading demonstration chains and rough lifetime measurements in the early stages of the Gen I trap testing. The lifetimes were fairly short (seconds for longer chains and minutes for few ion chains) but given that the neutral flux oven was on during those measurements and the potentials were not optimized for chain stability, the short lifetimes are not unexpected. More recent observations in the Gen II trap (described in a later section) have shown much longer lifetimes.

#### 4.5.1.4 Single ion lifetimes

Single ion lifetimes were measured in both the GT22 C4 (with and without cooling) and GT22 C1 traps (without cooling). Generating lifetime measurements with good statistics

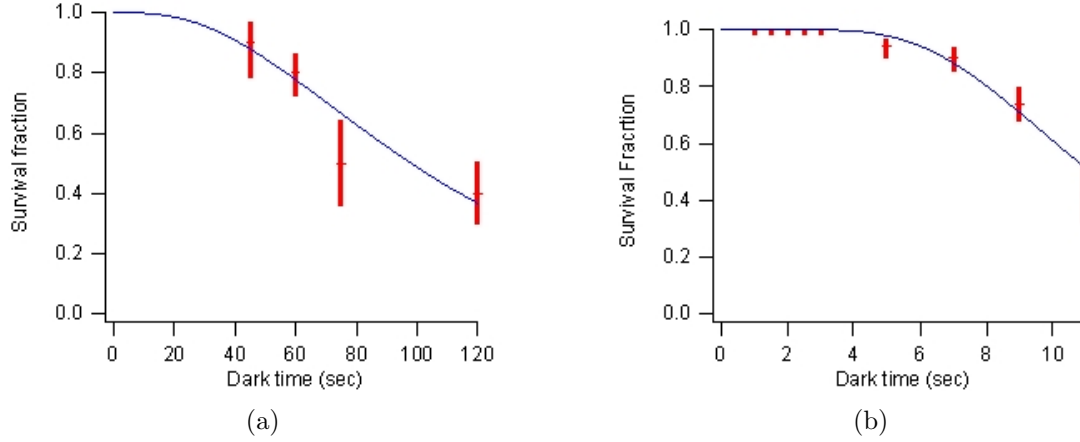


Figure 4.14: Dark lifetime measurement in the GT22 C4 trap (left) and GT22 C1 trap (right) over the load zone. The fit is a simple multiple collision loss model and is provided only to aid the eye. The actual dominant loss mechanism has not been determined yet.

is time consuming as the lifetime can be hours with laser cooling and tens to hundreds of seconds in the dark.

For the GT22 C4 trap and cooled lifetimes, we wrote an automated routine to monitor ion fluorescence and automatically reload when the ion was lost. After eight hours of data acquisition, we found a cooled lifetime of around two hours. At this time, the laser frequency locks were unstable, which might have reduced the ion lifetime by momentarily heating the ions. The laser lock has since been stabilized, but we have not repeated this measurement.

Similarly, for the dark lifetimes, an ion would be loaded (the neutral source was turned off after every load and a delay added to let the chamber pressure drop) and then a shutter in the cooling beam was closed for a given period. The cooling beam was then unshuttered and the ion fluorescence showed whether the ion survived or not. If not, then the ion was reloaded. This cycle was repeated to obtain statistics at various dark (cooling shuttered) times. Figure 4.14 shows results for the GT22 C4 trap. For the GT22 C1 trap, an automation script was able to take more data for better statistics. These results are also shown in Figure 4.14.

From the data, it seems clear that a simple model of ion loss that has an exponential time decay does not fit. The effective lifetime at less than a few seconds in the dark is much longer than the average lifetime. To aid the eye, we used a basic multiple collision model to create a fit curve. There are other possible models that might create a similar shape. More study would be needed to determine the loss mechanism.

The dark lifetimes for the GT22 C1 trap are considerably shorter than for the preceding trap. This might be due to the observed stray field from behind the load zone affecting the trap depth. However, for the short periods over which an experiment is performed and during which the ion is likely to remain in the dark, the sharp drop off in the survival rate at five seconds should not be an issue. The Gen II trap discussed later demonstrates a  $>1$  minute dark lifetime, so we believe that the short GT22 C1 dark lifetime is an aberration.

The long effective dark lifetimes for periods of under a few seconds implies that at least



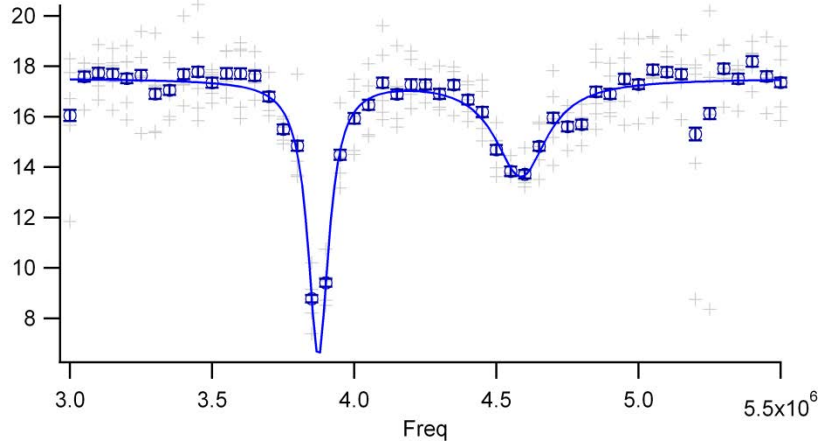


Figure 4.15: Example of a mode frequency measurement showing the two radial modes. The vertical axis is the ion fluorescence and the horizontal axis the applied DC tickle frequency. The unfit peak on the right is a glitch caused by ion heating or momentary shelving of the ion state.

dark lifetime will not be problematic for quantum information experiments since most experiments last much less than a second and are interspersed with ion cooling. However, whatever mechanism is causing the eventual loss might have an effect on an experiment (e.g. heating or decoherence) and needs to be studied in more detail. The surface traps have lower well depths than the 4-rod Paul trap devices and so the lifetimes are expected to be lower in the surface traps. Further studies of the loss mechanisms might allow for longer lifetimes. Also, since lifetimes of chains tend to be considerably shorter than for single ions, these studies will become particularly important for quantum information experiments using long ion chains.

#### 4.5.1.5 Mode frequency measurements

Mode frequencies are measured by exciting the motional modes with a perturbing RF potential applied to the grounding screen (see the Frequency Control section above for a description of RF and DC tickles). When the potential is on resonance with one of the modes, the motion is excited and the ion fluorescence decreases. Figure 4.15 shows a sample radial frequency measurement with a fit to measure the two radial mode frequencies. The splitting in the radial modes is generated by the applied electrostatic trapping potentials and, in theory, can be adjusted within the range of Mathieu equation stability requirements.

Detailed mode frequency scans versus perturbations to the applied potentials will be discussed later. Such scans provide information on the trapping potentials and stray fields.

#### 4.5.1.6 Compensation

There are several methods to measuring stray fields at the ion location. We have mainly used fluorescence side band measurements (this will be described shortly) but have partially

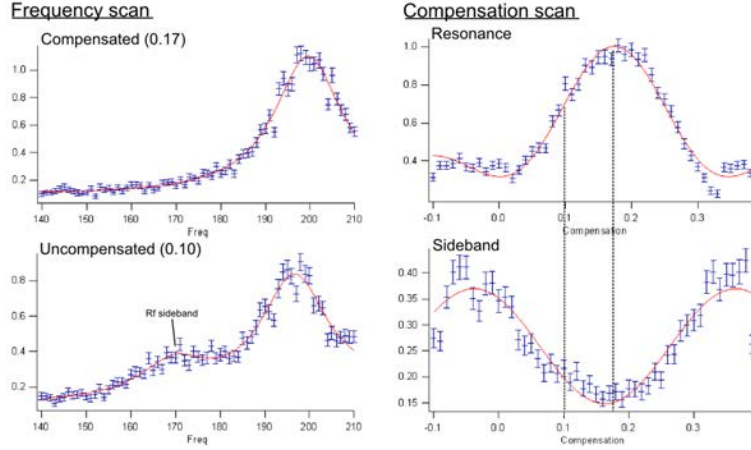


Figure 4.16: Example of micromotion measurement using the RF sidebands on the fluorescence profile. At a compensation of 0.17 (this is the potential in volts applied to a set of control electrodes), the frequency scan shows the Lorentzian profile characteristic of a 2-level transition. The right hand figures show the ion fluorescence as function of the applied compensation when the fluorescence laser is tuned to be on resonance (top figure) and to be on the micromotion side band (bottom figure).

set up an RF tickle system (described in the Frequency Control section above).

The fluorescence side band technique measures the component of the ion’s micromotion that lies along the laser beam propagation direction. If the ion has micromotion with a component parallel to the probing laser, the laser in the ion’s frame will exhibit sidebands at the trap RF frequency, as shown in the uncompensated frequency scan in the Figure 4.16. Scanning the compensation, the fluorescence of a probe on resonance with the atomic transition will exhibit a maximum while a probe detuned to the RF sideband will exhibit a minimum as shown in Figure 4.16. This only nulls the component of the micromotion along the laser beam.

The height of the sideband is parameterized by the modulation coefficient  $\beta$  which is proportional to the stray electric field. The sideband is maximized for  $\beta=1.8$  and corresponds to roughly 300 V/m for the parameters we used for our measurements. We expect to be able to null to a few percent of this field corresponding to a loss in on-resonance fluorescence of better than 0.5%.

#### 4.5.1.7 Cryogenic Ion Trap Testing at MIT

In July 2010, we took the GT22 C4 trap to Prof. Isaac Chuang’s group at MIT for testing at cryogenic temperatures. Within one week, the trap was loading reliably and we were characterizing the ion trap by its mode frequencies and heating rate.

1. One week turnaround for testing dominated by two chamber cooldowns (the oven had to be reposition after the first cooldown).

2. Heating rate roughly  $58 \pm 12$  q/s at  $\sim 4$ K ( $68 \mu\text{m}$  ion-trap distance, 0.8 MHz trap mode frequency). See Figure 4.19 for the data and Figure 4.20 for a comparison to other traps.
3. Mode measurements (2 radial and 1 axial) match calculations to within 2%. Only one unknown, the RF amplitude, was used in the calculations.
4. Single dark lifetime measurement showed the ion surviving at  $>1$  min. Ion was lost at 90 sec in the dark. We are not sure why the lifetime wasn't much longer. One possibility is that the trap did not get very cold. The quantity of cryogen limited the experiment to only a handful of ion loads.

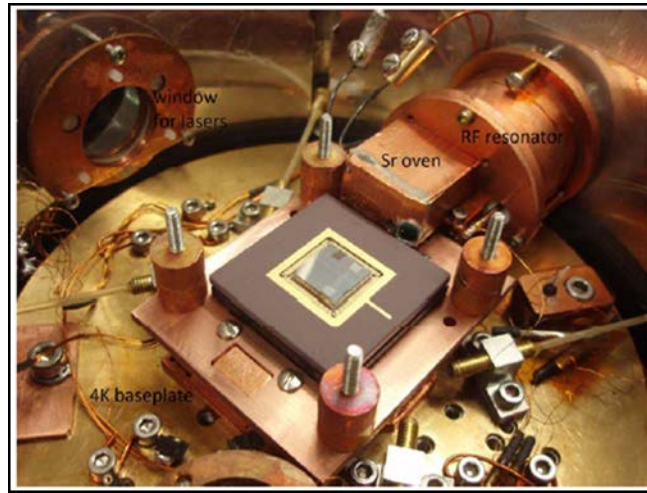


Figure 4.17: Photograph of the inside of the MIT cryogenic system with the GTRI trap installed (courtesy S. Wang and C. Chuang). Trap was cooled through the carrier but because there was no temperature sensor attached to the trap, final trap temperature is unknown.

### 4.5.2 Gen II trap

The GTRI Gen II trap design was developed from the experience we gained from modeling, testing, and fabricating the Gen I trap. Its key features are:

1. Shaped backside loading slot to reduce RF barriers and keep ion height constant across the loading slot and non-loading slot regions.
2. Wider asymmetric RF rails than the Gen I to reduce the required RF potential and consequently reduce the possibility of arcing and reduce the power consumption.
3. 22 zones to allow for multiple wells and ion chains.

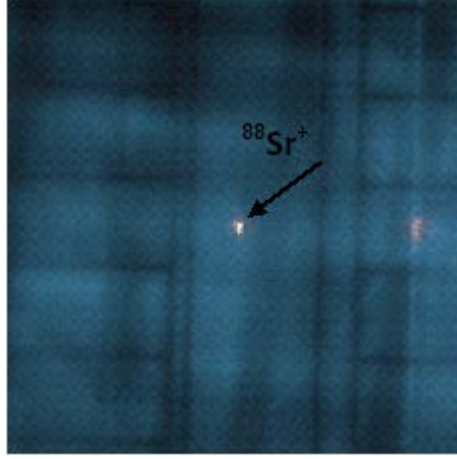


Figure 4.18: Composite image of an  $^{88}\text{Sr}^+$  ion loaded in the GTRI trap at cryogenic temperatures.

4. Top layer ground localizes the control pads and decreases the possibility of shorts due to dust and scratches.

A single Gen II trap (GT34 F2) was tested before the end of the SMIT program. As with the Gen I traps, loading is reliable without tweaking the control potentials. During this period, we demonstrated:

1. Reliable ion loading in the shaped loading slot (see Figure 4.22).
2. Transport along the 1.5 mm region.
3. Dark lifetimes  $> 1$  minute as shown in Figure 4.23. The loss versus time has a similar profile as to that seen in the GT22 C4 chip.
4. Loading of simple ion chains in a harmonic well as shown in Figure 4.24.

## 4.6 Comparison between model and measured trap parameters

The trap testing facility provides feedback on the accuracy of the numerical models and on aspects of the trap fabrication that can affect the trapping properties. We quantify the match between model and fabricated trap using the following experimental parameters:

1. Ion axial position
2. Secular frequencies
3. Micromotion compensation

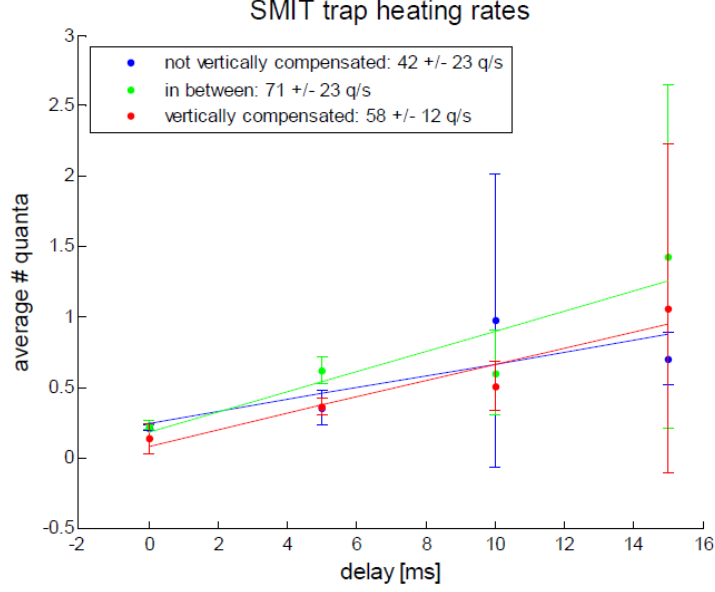


Figure 4.19: Heating rates at cryogenic temperature (courtesy S. Wang and C. Chuang).

The ion position can be measured relative to trap features using a CCD camera. The secular frequencies are measured by applying an RF excitation to the ground shield above the trap in a method called ‘DC tickle’ (see the Frequency Control section above for a more detailed description of DC and RF tickles). When the RF frequency matches a trap secular frequency, the ion motion is excited and the detected fluorescence is reduced. Micromotion can be measured in several ways. We are currently using changes in the ions fluorescence profile vs. laser frequency induced by the micromotion parallel to the laser direction. This gives a sensitivity of a few volts per meter which corresponds to less than a percent loss in ion fluorescence due to the micromotion. For traps with slots through the wafer, two fluorescence beams can be used to null in both radial directions. The laser fluorescence technique can also detect intrinsic micromotion due to pseudopotential barriers that might be caused by a particular RF structure (e.g. in a junction) or due to phase shifts in the RF rails.

The second method, using sidebands injected onto the trap RF (‘RF tickle’), is still in development but would measure the micromotion in both radial directions with a single fluorescence laser. For surface traps, the large anharmonic terms in the RF potentials make RF tickle difficult as the mode frequencies will depend on the stray fields and the RF tickle depends on knowing the mode frequencies in advance. To deal with this issue, we plan to use a combination of DC and RF tickle to both measure the mode frequencies and subsequently the micromotion as compensation voltages are varied. We do not know yet the sensitivity we will be able to achieve, though we expect it to be sufficient for diagnosing trap performance. Unless one is using a trap for systems such as ion clocks where the second order Doppler shift is an issue, the micromotion perpendicular to the laser direction does not couple into the trap operations so the requirements for the sensitivity to this micromotion are relaxed. When trapping ions, we apply a given trap RF power and control potentials. Ideally, only the

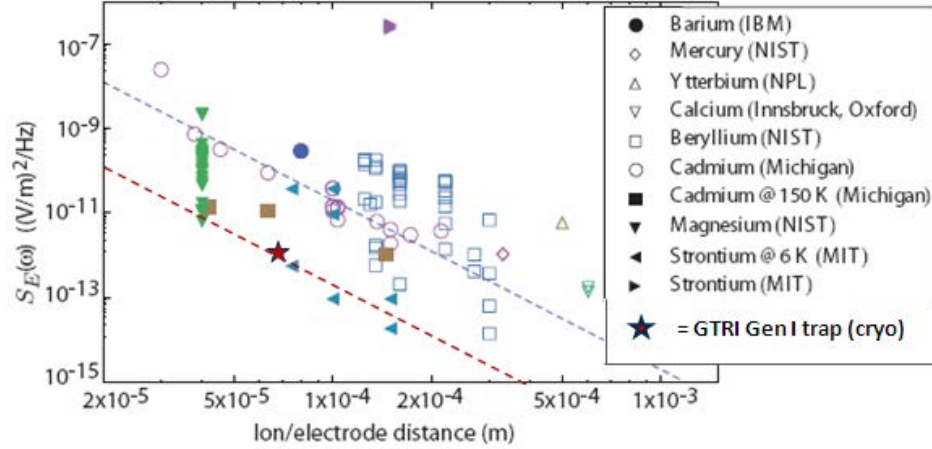


Figure 4.20: GTRI Gen I heating rate at cryogenic temperatures compared to other traps. The vertical scale is the square of the electric field noise density. The electric field noise is dependent on frequency. In this case, the relevant frequency is the trap secular frequency which varies between the various measurements plotted.

conversion between the RF power and actual peak voltage on the RF rails would be a variable in matching the model to the experimental data. However, there is a more extensive set of parameters that we need to be able measure:

1. RF amplitude,
2. stray electric fields,
3. modeling uncertainties, and
4. fabrication variances.

All of these parameters are to some extent entangled. The modeling uncertainties arise from numerical uncertainties and approximations made during the field calculations, such as zero thickness metal, planarization of surfaces that due have a micron of variance in the fabricated trap, and the lack of dielectrics in the gaps between the electrodes. Fabrication variances are the micron level variations in the electrode shapes that are due to fabrication limitations. In general, the current set of trap characterization data matches the models to a couple percent and we believe both of the modeling uncertainties and fabrication variances are well under control; however, in future programs, we will continue to accumulate characterization data and further refine the models and the processes. This type of characterization and model comparison is needed to convince experimental groups that the devices we produce will work for them and will perform to the specifications they provide. The characterization technique that we will demonstrate here is a mapping of the mode frequencies under a sequence of perturbations to the control voltages. We use a basis of two perturbations that nominally generate an orthogonal set of radial fields. These two perturbations are parameterized by the potentials Comp1 and Comp2. Comp1 nominally parameterizes a



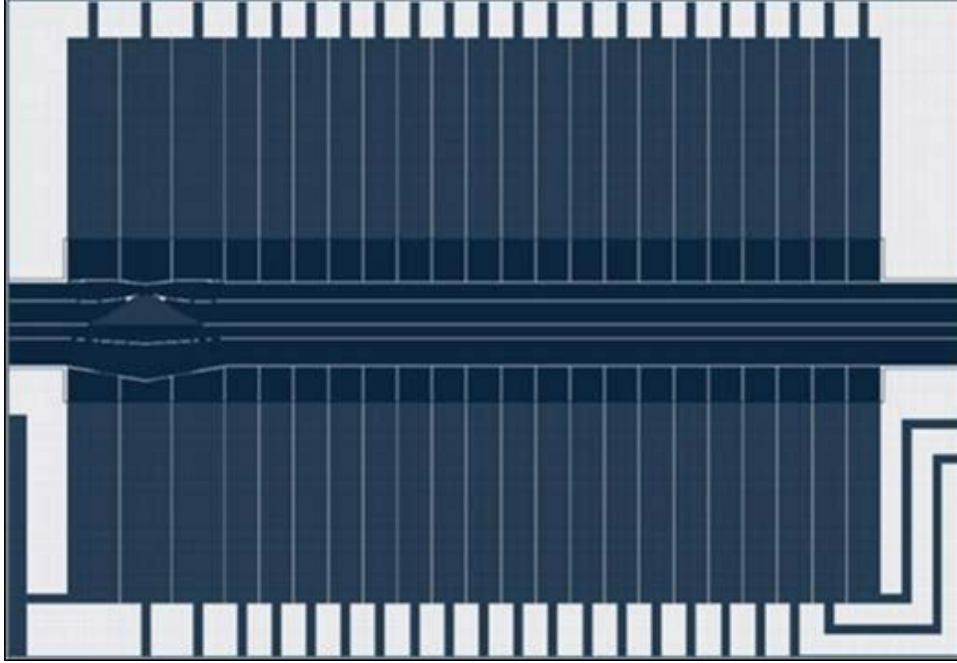


Figure 4.21: Active region of a Gen II ion trap. The shaped loading zone is on the left. The bulk of the control electrodes are shielded by a ground plane except for the regions adjacent to the RF.

field parallel to the trap surface and Comp2 a field perpendicular to the surface and both are specified in terms of the voltage applied to a particular sets of electrodes.

The first set of measurements find the Comp1 potential needed to remove the component of the micromotion along the laser propagation direction. Any micromotion parallel to the laser changes the laser fluorescence profile as shown in the top right of Figure 4.16. This measurement of Comp1 is repeated for a range of Comp2 values. Figure 4.25 is a comparison of the experimental results (open circles) in the GT22 C1 trap with the model results assuming no stray fields except for a compensation applied to correct for the carrier ground plane bias that was independently measured by mapping the measured ion position vs calculated position (see the description of the GT22 C1 trap above). In essence, Figure 4.25 provides a map of the appropriate compensations needed to keep one component of the micromotion zero (the component along the laser propagation direction) while applying a field that modulates the perpendicular component. At some combination of Comp1 and Comp2, both components of the micromotion are nulled. As we don't have the RF tickle working yet, we have to infer the values for the null from this compensation map and the mode measurements described below. But even with the RF tickle, these types of scans provide detailed information for comparison with models of the trap fields.

There is a uniform offset of about 50 mV, implying that the component of the stray field parallel to the trap surface is nonzero but small ( $<200$  V/m). Given that the GT22 C1 trap had a floating ground plane under the chip, the measured stray field is expected given that the only correction was made from a rough independent measurement (again see

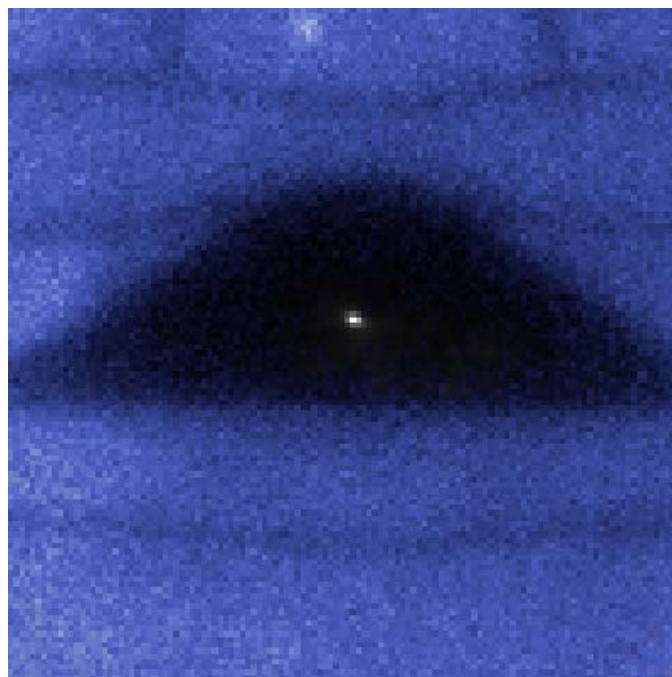


Figure 4.22: Composite image of a  $^{40}\text{Ca}^+$  ion loaded in the GTRI Gen II trap GT34 F2. An image of the loading slot has been superimposed on the ion image. The ion is within a few microns of the expected position.

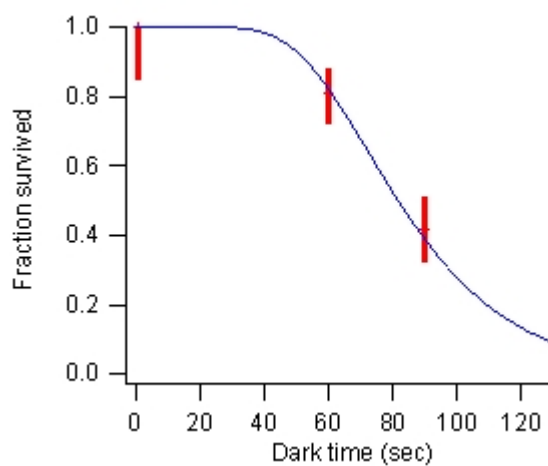


Figure 4.23: Dark lifetime in the Gen II GT34 F2 trap. The statistics for each point are fairly low. However, a lifetime of  $> 1$  minute is clear. The fit is a simple multiple collision loss model.



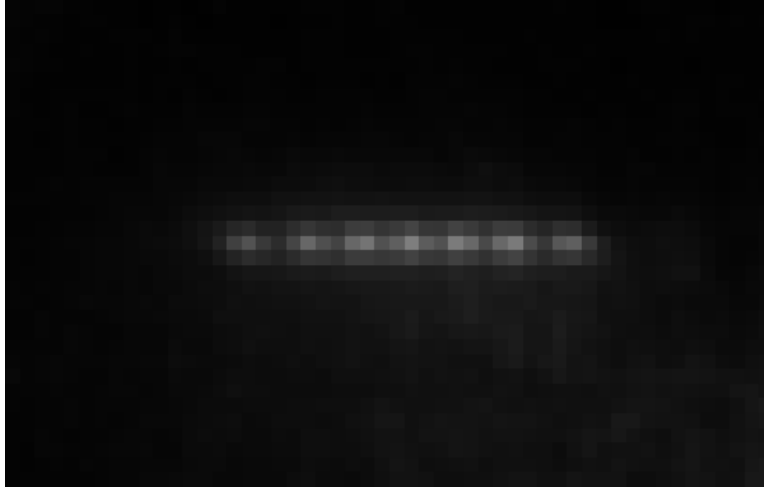


Figure 4.24: Example of a seven ion chain over the load zone in the Gen II trap GT34 F2. The axial trapping potential is quadratic.

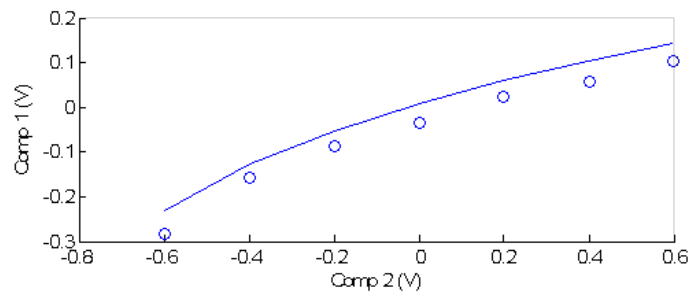


Figure 4.25: Scan of the Comp1 potential versus the Comp2 potential in the GT22 C1 trap load zone (o = experiment, line = model).

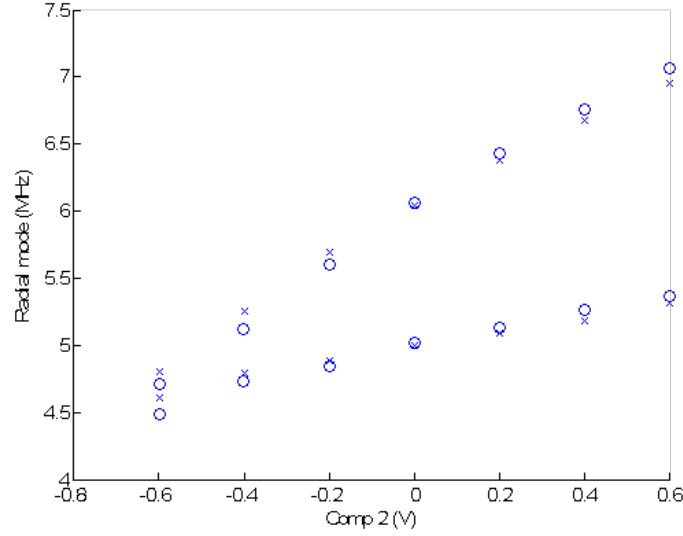


Figure 4.26: Radial mode frequencies as a function of the Comp2 potential (and, simultaneously, the corresponding Comp1 potential). (o = experiment, x = model)

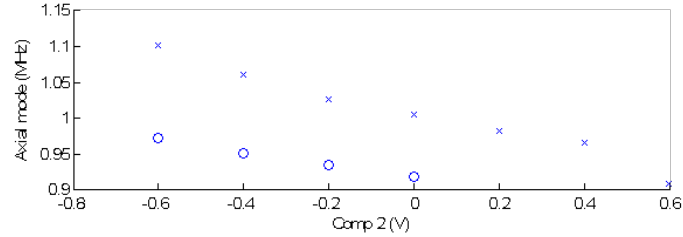


Figure 4.27: Axial mode frequencies as a function of the Comp2 potential (and, simultaneously, the corresponding Comp1 potential). (o = experiment, x = model)

the description of GT22 C1 in section on Gen I traps earlier). For each pair of Comp1 and Comp2 in Figure 4.25, we measure the radial and axial modes. We then compare the measurements to the model values with a single parameter, the RF voltage, adjusted to give the overall scale as shown in Figure 4.26 and Figure 4.27.

The close match between the sets of curves implies that the remaining parameters, i.e. stray fields and modeling uncertainties, and fabrication variances, are fairly small. Assuming only stray fields, we have two more parameters to adjust. A rough adjustment, around 200 V/m, gives the results in Figure 4.28, Figure 4.29, and Figure 4.30.

There are still some deviations that need to be investigated, for example the 10% deviation of the axial modes. Some of the variations in the shape of the curves in Figure 4.29 might be due to slow variations in the trap RF power, possibly from temperature changes affecting the resonator. Monitoring of the applied trap voltage during the scans should eliminate that effect and hopefully further reduce the deviations.

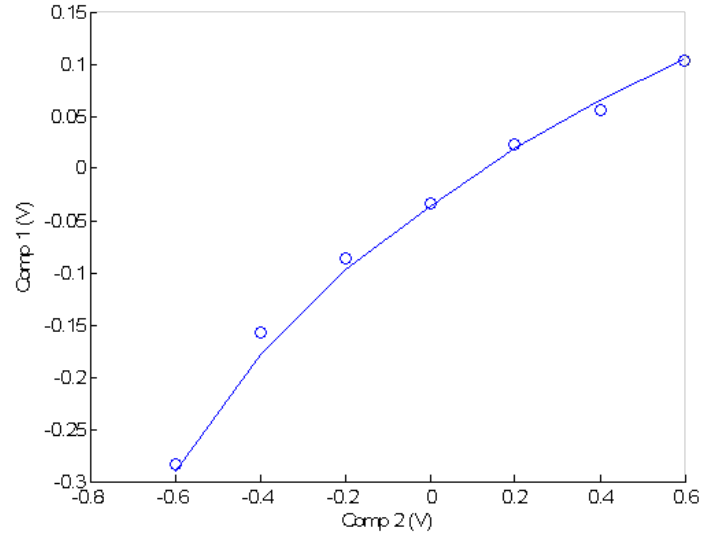


Figure 4.28: Comp1 vs Comp2 after correcting for a  $\sim 200$  V/m stray field. (o = experiment, line = model)

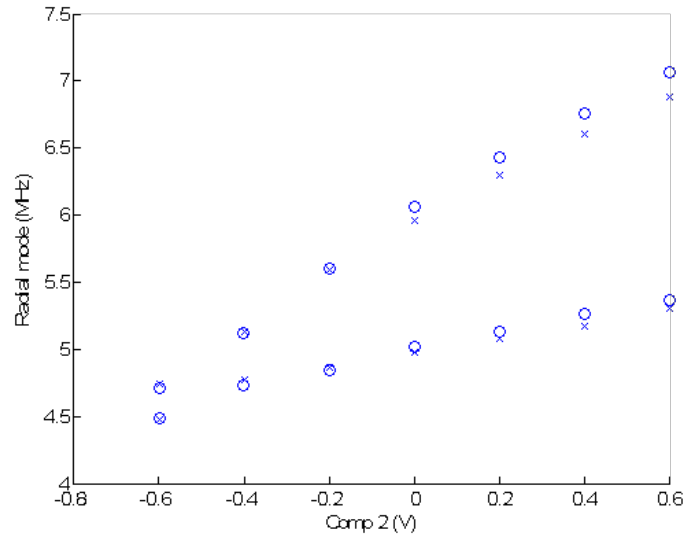


Figure 4.29: Radial mode frequencies after correcting for a  $\sim 200$  V/m stray field. (o = experiment, x = model). Some of the remaining deviation might be due to drift in the trap RF power during the scan. The scan system now tracks RF power drift.

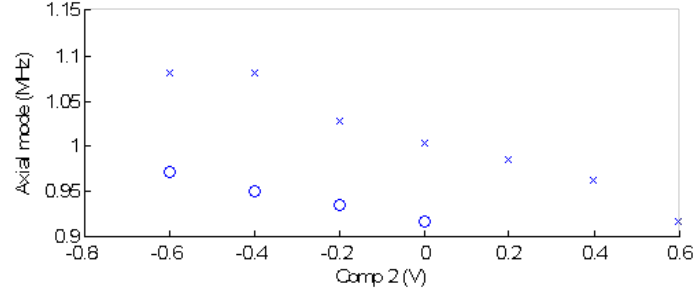


Figure 4.30: Axial mode frequencies after correcting for a  $\sim 200$  V/m stray field. (o = experiment, x = model)

Mode frequency scans such as those described above, repeated at multiple axial positions and between multiple traps, provide detailed profiling of trap parameters, modeling uncertainties, and trap variances. A large part of the effort in developing the trap testing facilities has been and continues to be directed towards generating test and measurement capabilities that allow for complete and consistent measurement sets. These complete data sets, with all control parameters monitored and stabilized, provide clean comparison of the performance and characteristics of different traps and even between different measurements of the same trap.

# Chapter 5

## Integrated Optics

*Jungsang Kim, Duke University*

### 5.1 Project Objectives and Goals

The integrated optics portion of SMIT II program started with three major integration goals as described in this section.

**Optical integration goal A** on The first technology development goal focused on **efficient and scalable collection of scattered photons from the ions during the state detection process**. In current experiments, the detection speed and field of view are limited by the use of bulky collection optics and inefficient detectors. This research effort was intended to integrate micro-optical elements with the surface trap architectures for efficient collection of photons scattered from the ions during the state detection process.

**Optical integration goal B**

Efficient collection of photons for remote entanglement of ion pairs by photon coupling is qualitatively similar to the collection of photons for state detection (as in goal A). However, this task requires the photon emitted by the ion to be collected by a single optical mode in order to ensure that the photons from two ions are indistinguishable, a crucial condition for quantum interference. In the current experiments, the collection efficiency of a photon emitted by an ion into a single mode fiber is on the order of  $4 \times 10^{-3}$ : one can dramatically improve this efficiency by placing the ion in an optical cavity with a very small mode volume, so that the dipole coupling to the cavity mode is substantially enhanced. The goal of this research effort was to **construct a high quality micro-cavity with a small mirror and a fiber tip, and integrate this optical structure with the ion trap**. The trapping and heating issues arising from a close coupling between the optical element and the ions has to be explored.

**Optical integration goal C**

In most current ion trap experiments, the laser beams addressing the ions are fixed and cannot be shifted dynamically during the experiment. While reducing the mechanical vibration between the laser source and the ion is important for high fidelity gate operations, the flexibility to address multiple ion trap zones with a single manipulation beams seems to be a critical functionality in scalable ion trap quantum information processors (QIPs). The

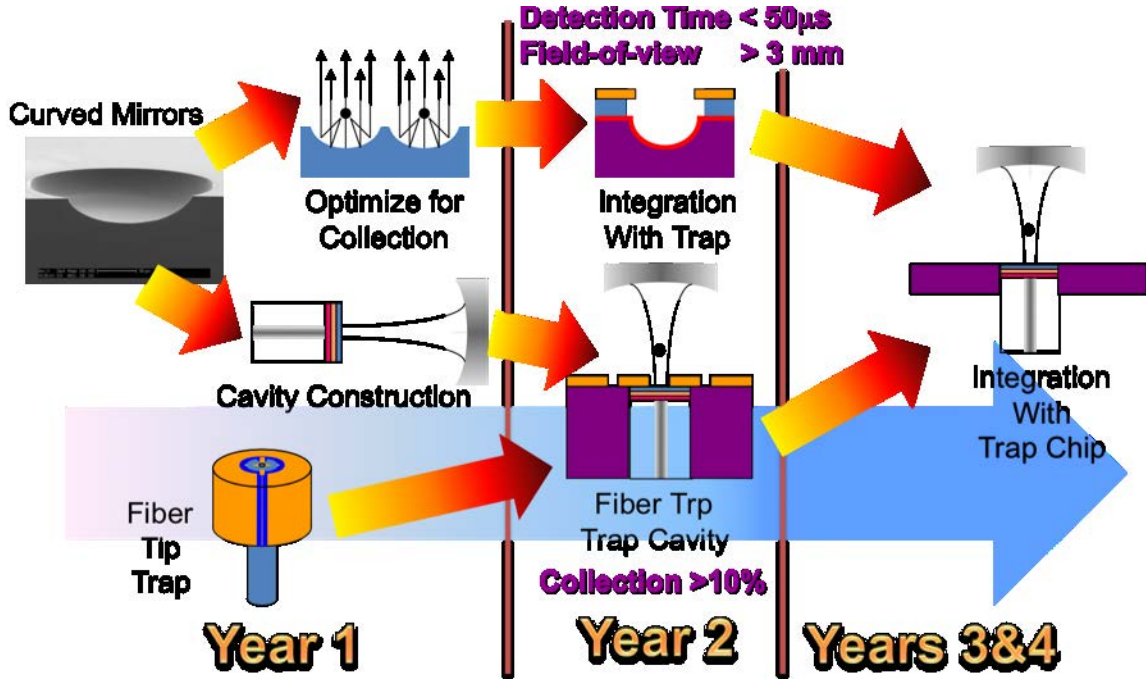


Figure 5.1: Graphical illustration of the integrated optics tasks in SMIT II program.

goal of this task was to explore the feasibility of utilizing high-speed micro-electromechanical systems (MEMS) devices for addressing multiple ions in a complex ion trap, and **design a compact optical system where the mechanical vibration between the delivery beam and the trapped ion is eliminated to enhance the logic gate fidelity, while securing the flexibility in multiplexed beam delivery.**

#### Optical integration metrics/goals summary

The measurable metrics and goals for optical integration are outlined in Table 5.1. Figure 5.1 shows the project tasks and milestones in a graphical form. As outlined in the table, we concentrated on Goals A and B in the first two years and left Goal C for exploration in subsequent years.

## 5.2 Research Results from Integrated optics

In this section, we summarize the research results and progress achieved in the first two years of SMIT II program. The research activities on integrated optics was performed in close collaboration between the GTRI, Duke and MIT teams, as evidenced by the exchange of personnel, technology, sample devices and joint publications.

### 5.2.1 Goal A: Scalable approach to qubit state detection

It was determined early on that the use of reflective optics could lead to a much higher light collection efficiency for the state detection, compared to any refractive optics. Furthermore, we concluded that the integration of these reflective surfaces is compatible with surface

Table 5.1: Summary of integrated optics metrics and goals.

Goal	Metric	Present Value	Project Goal	Year	Comments
A	# of Measurement locations for high speed detection	1	8	2	
A	Measurement time	$\sim 200 \mu s$	$< 100 \mu s$	2	
A	Measurement fidelity	$> 99\%$	$> 99\%$	2	
A	Field-of-view	0.5 mm	$> 3\text{mm}$	2	
B	Coating reflectance on micromirrors	$\sim 90\%$	99.9%	1	Single wavelength between 300-400 nm
B	curved mirror surface roughness	N/A	$< 1 \text{ nm RMS}$	1	
B	Cavity mode beam waist	$\sim 54 \mu m$	$< 2 \mu m$	2	Mundt et al., PRL 89, 103001 (2002)
B	Cooperativity factor	$< 0.1$	$> 2$	3	<i>ibid</i>
B	Atom-photon coupling/atomic decay ( $g/\Gamma$ )	$< 0.05$	$> 10$	3	<i>ibid</i>
B	Collection efficiency of photon into fiber	$< 0.005$	$> 0.1$	4	Moehring et al, Nature 449, 68 (2007)
B	Integration of micro-cavity with ion trap chip	N/A	Demonstrate	4	
C	Multiplexed beam locations	1	$> 5$	2	
C	Intensity fluctuation-induced gate error (geometric phase gate)	3%	$< 0.5\%$	4	

traps to be fabricated in the SMIT II program, as long as the mirrors can be fabricated in silicon substrates. During the first two years of the program, we 1) developed an optimized fabrication process for creating concave mirrors on silicon substrates for high-NA reflective optics (Duke); 2) transferred the basic fabrication process to GTRI, where scalability of the fabrication process to a 4" wafer was established (GTRI and Duke); 3) improved the ability of this approach to dramatically improve the collection efficiency of the scattered photons was demonstrated (Duke); 4) completed an integrated design for ion traps that located the ion at the location with respect to the micromirror to guarantee optimal light collection (GTRI); and 5) worked on establishing trap fabrication processes that are consistent with the mirror integration (GTRI and Duke).

### 5.2.1.1 Micromirror fabrication process

The fabrication process for the micromirror was initially developed at Duke University. The fabrication process consists of depositing silicon nitride film on <100> silicon wafers using low-pressure chemical vapor deposition (LPCVD) process, to be used as an etch mask. An array of mask openings with diameter of 5-80  $\mu\text{m}$  is etched on the LPCVD nitride film using reactive ion etching (RIE) process. The wafer is etched in a 1:8:1 hydrofluoric, nitric and acetic acid (HNA) etching solution for 10-20 minutes, to isotropically etch the exposed silicon underneath. The resulting silicon etch results in a close-to-spherical etch with smooth surface (RMS roughness of better than 0.5nm), and a reasonable etch rate (of about 4.5  $\mu\text{m}/\text{min}$ ), as shown in Figure 5.2(a) and (b). Some of the key findings through the process optimization include:

1. Low stress, LPCVD nitride is a crucial requirement to serve as an etch mask. Plasma-enhanced chemical vapor deposition (PECVD) nitrides have been tested, but did not protect the silicon surface underneath due to porosity of the film.
2. The ratio of HNA mixture was crucial in achieving a smooth and isotropic surface. The etching process involves the oxidation of silicon surface via the nitric acid, followed by removal of resulting oxide with hydrofluoric acid. When the etching process is oxidation-limited (i.e., low nitric acid concentration compared to hydrofluoric acid concentration), it results in very smooth surfaces.
3. Our etching process does not involve any stirring of the solution or the sample during the etching process. This ensured that the center of the resulting concave surface is not displaced from the center of the mask opening by more than  $\pm 2\mu\text{m}$ , resulting in accurate prediction of the center of the mirror (Figure 5.2(c)).

### 5.2.1.2 Transfer of mirror fabrication process to GTRI

The mirror fabrication process developed at Duke University was performed on small pieces of silicon roughly 20mm on a side. In order for this process to be compatible with the SMIT II trap fabrication process, we needed to port this process to a standard 4" wafer and confirm its uniformity across the wafer. The mirror etching process was first transferred to GTRI, as



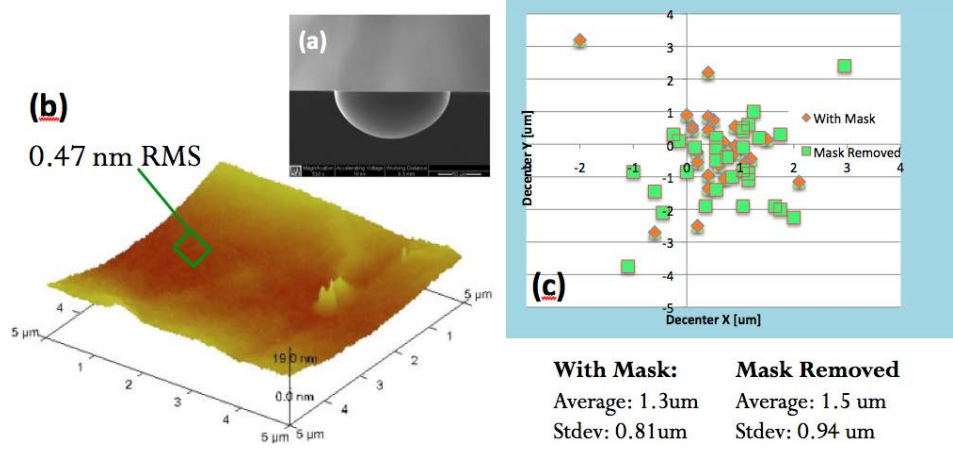


Figure 5.2: (a) SEM cross-section and (b) surface roughness of the concave surface etched using 1:8:1 HNA process. (c) Measurement on the center of the etched surface with respect to the mask opening.

two researchers spent two days on Duke University’s campus to get trained on the process. Then, the uniformity of the process was further improved by expanding the approach to a 4” wafer, and establishing automated characterization processes to measure the statistical variation of the etch parameters across the full wafer. The 4” process established at GTRI is fully compatible with integration of SMIT II trap structures.

### 5.2.1.3 Measurement of light collection capability for micromirrors

While the mirrors were being integrated with the ion traps, the Duke University team explored ways to verify the enhanced light collection from a point source using this approach. Instead of an atomic ion, we used a small polystyrene fluorescent microbead ( $\sim 15 \mu\text{m}$  in diameter) as the point source. The experimental setup is shown in Figure 5.3: the microbead is glued to a tip of a micro-pipette that is mounted on an xyz stage for precise control of the bead location, and pumped with a 407nm laser diode. The fluorescence is collected using a macroscopic imaging system with  $F/2$  and an effective focal length of 90mm, near 500nm through a band-pass filter. The collected fluorescence is detected using an electron-multiplying charge-coupled device (EMCCD). An iris located before the imaging optics can control the collection solid angle of the imaging system, providing a calibration of the absolute collection efficiency for the system. The measured collection efficiency of the fluorescence is consistent with a simple prediction estimated from the collection solid angle (Figure 5.4(a) and (b)). Then, a micromirror was placed behind the microbead, in such a way that the microbead is located at the focal point of the concave micromirror. The collected light at the EMCCD is dramatically enhanced (Figure 5.4(c)): it is estimated that over 30% of the light scattered from the microbead could reach the detector, dramatically enhancing the potential for fast and accurate detection of the qubit states. We simulated the situation of simultaneous state detection using multiple micromirrors each positioned behind the ion to be measured, by shifting the point source-micromirror pair with respect to the imaging

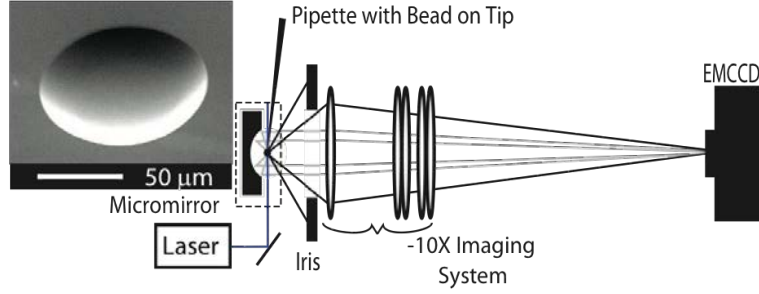


Figure 5.3: Experimental setup with macroscopic F/2 imaging system and a large NA micromirror (inset), using a fluorescent microbead as a point source.

optics. The result is shown in Figure 5.4(d): we see that the collection efficiency does not degrade substantially over  $\sim 10\text{mm}$  field of view for the macroscopic imaging system. This experimental situation is carefully simulated using a ray-tracing optical modeling tool (Zemax), and a close agreement between the simulation and experimental results have been obtained to validate the conclusions.

#### 5.2.1.4 Design of mirror-integrated ion traps

It is critical to have an integrated design of the ion trap and the micromirror so that the two are compatible. A full description of this design process is provided in Chapter 2).

**Establishing trap fabrication process** Developing the fabrication process for integrating the micromirrors with the SMIT II traps poses several challenges. The GTRI and Duke teams have been collaborating to address these challenges in the second year of the SMIT II program. Some of the challenges, solutions, and remaining issues are described here.

- a. The first challenge was to establish alignment marks for the mirror fabrication process, so subsequent trap fabrication processes could be aligned to the mirror. Since the mirror etch is highly isotropic, the etching process itself cannot be used to fabricate alignment marks that require micron-type accuracy. The team developed deep reactive ion etching (DRIE) process to create alignment marks on the silicon substrate. In our approach, a deep trench alignment mark ( $\sim 40\text{mm}$ ) is etched into the substrate first (Figure 5.5), and the silicon nitride etch mask is deposited. The nitride mask protects the alignment mark during the HNA mirror etching process and retains the sharp features for subsequent mask alignment.
- b. The micromirror as etched using the HNA process is not adequate for direct integration of SMIT II ion traps, since the mirror sag is much more than what would be desired. We need to reduce the mirror sag from about  $50\text{ }\mu\text{m}$  to about  $15\text{ }\mu\text{m}$  without compromising the mirror shape or surface roughness. GTRI developed a process where a  $10\text{ }\mu\text{m}$ -thick oxide is grown on top of the mirror substrate protecting both the mirror and the alignment marks, and then the wafers are sent to an outside vendor

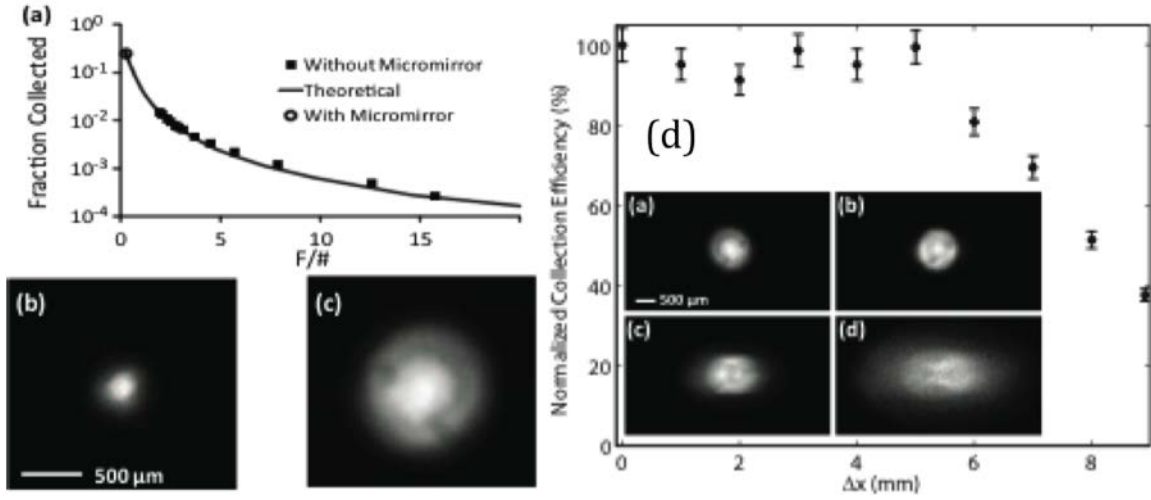


Figure 5.4: (a) Collection efficiency of the fluorescence from the microbead. The closed squares and (b) show the collection efficiency and the image seen by the camera without the micromirror, as the  $F/\#$  of the collection optics is controlled by adjusting the iris opening. The open circle and (c) show the collection efficiency and the image when the micromirror is placed behind the point source. (d) Collection efficiency as the point source-micromirror pair is displaced from the center of the imaging system, normalized by the value at the center. The insets show the detected image as the pair is shifted 0mm, 3mm, 5mm and 7mm from the center of the imaging optics, respectively.

(Aptek) for grind/polish to the adequate thickness. The process optimization took several iterations, but has finally been stabilized to be a reliable process. Once the polished wafers are returned to GTRI, the protection oxide can be stripped in HF and the wafer is ready for SMIT II standard trap fabrication. We confirmed that neither mirror shape nor surface roughness is affected by this polishing process.

- c. The team confirmed that the SMIT II standard trap fabrication process is compatible with the mirror-integrated substrate. Figure 5.6 shows an example of micromirror integrated with the first metal layer of SMIT II fabrication process. Integration of subsequent layers is currently under way at GTRI, with a target completion date of November 2010.
- d. One remaining challenge is to establish an acceptable surface roughness of the mirror surface for high reflectance. Figure 5.7 shows the relationship between the RMS surface roughness and the Rayleigh scattering that results from reflecting off the surface at a wavelength of 370nm, which will be seen effectively as a loss. In order to keep the optical loss from a rough surface to below a few percent, one needs to ensure that the RMS roughness of the surface be maintained below 10nm in the worst case, preferably below 5nm. The Al metal films in SMIT II are sputtered aluminum with  $\sim 1\%$  silicon intended for thermally stable electrodes, and turns out to be much more rough compared to these requirements (Figure 5.8). These metal layers were not originally intended for optical reflectors, but now there is a need to improve the quality of the metal for reflectors. We have attempted to smooth out the roughness of the 10  $\mu\text{m}$  oxide deposited as an insulator between the RF electrodes and the RF ground by illumination of CO2 laser (reflow technique), but the PECVD oxide used in this process has sufficient levels of incorporated impurities that they do not flow nicely to form smooth surfaces. Process development is under way to strip the rough films (metal and oxide) from the mirror region after the completion of the trap fabrication process, so that a thin, smooth metal film could be deposited to achieve high quality reflector.

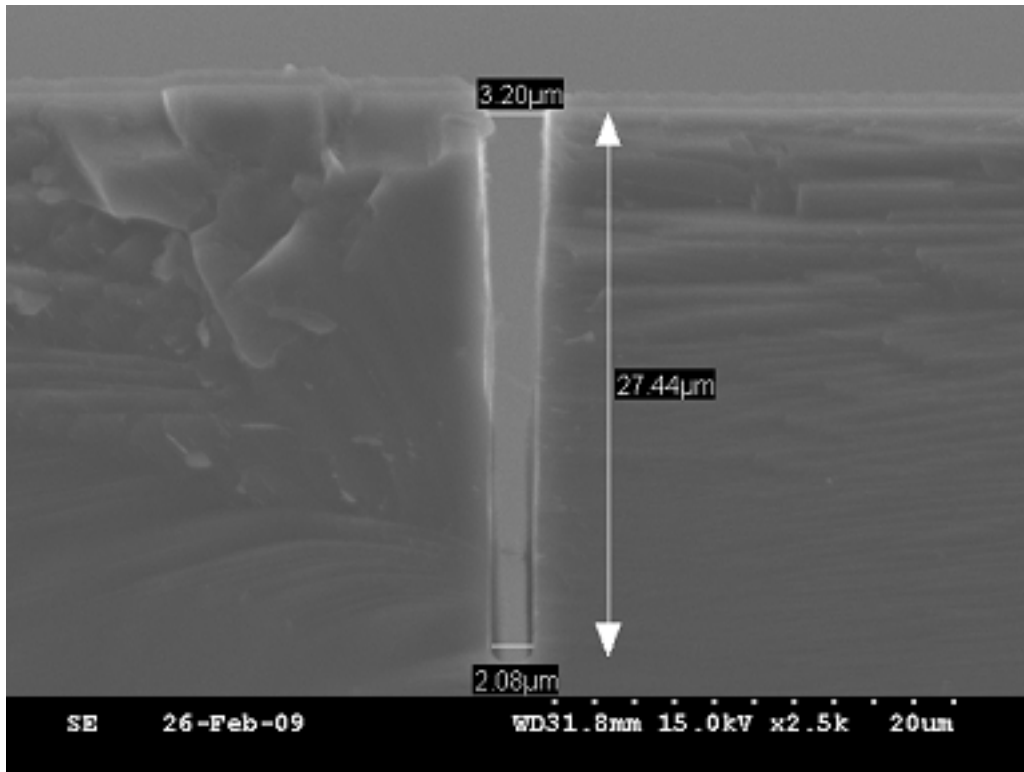


Figure 5.5: Deep reactive ion etching (DRIE) of silicon to implement alignment marks for the HNA etching process.

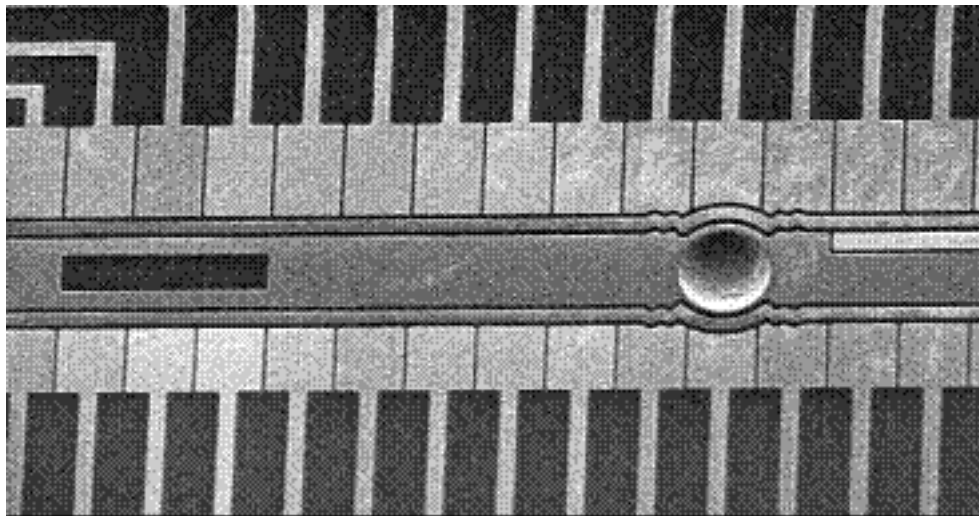


Figure 5.6: Micromirror integrated with the first layer of metal in the SMIT II process.

RMS (nm)	Scatter (ppm)	Scatter (%)
50	944336	94.43
10	109112	10.91
5	28426	2.84
1	1154	0.115
0.5	289	0.0329
0.2	46	0.005
0.1	12	0.001

Figure 5.7: Fraction of scattered light as a function of the RMS roughness as a result of Rayleigh scattering.

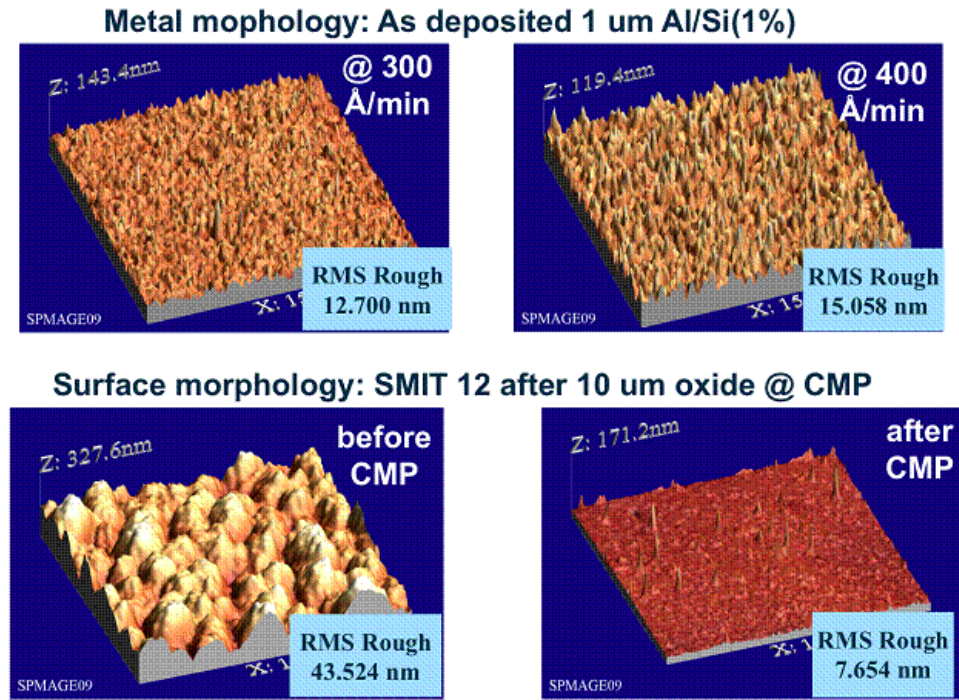


Figure 5.8: Surface roughness of as-deposited metal layers on SMIT II traps. These metalization processes have been developed for thermally stable electrodes and not for optical reflectors, and we need a process improvement to achieve acceptable mirror performance.

### 5.2.1.5 Conclusions

While the final mirror-integrated trap fabrication is yet to be completed, we have verified several critical project milestones through independent experiments. Most importantly,

1. We demonstrated a parallel detection approach where the field-of-view over which the micromirror integrated ion trap would effectively operate is over 10mm. This was confirmed using a fluorescent microbead as a point source, and performing light collection experiment with the micromirror and a conventional macroscopic imaging system. The number of independent micromirrors that could be distinguished within this field of view constitutes the maximum number of ions that could be measured simultaneously, and a simple analysis shows that many thousand micromirrors could fit in this field. This indirectly demonstrates the possibility of parallel state detection in our approach.
2. While we have not tested the integrated mirror with an actual atomic ion qubit, we have independently verified the ability of our approach to dramatically increase the collection efficiency of the photons scattered by a single ion. Our first mirror-integrated ion trap design should allow us to collect light from about 15% of the solid angle (slight reduction expected from the finite reflectance of the mirror surfaces), which is a factor of 3 improvement from the current state-of-the-art experimental situation. This is expected to reduce the integration time of the measurement by a factor of 3, and increase the measurement fidelity where the probability of measurement error is determined by the off-resonant scattering of photons. In the Yb case, the enhanced collection efficiency should lead to theoretical measurement fidelity of over 99.9% [17].
3. We anticipate the completion of the first mirror-integrated trap fabrication run to complete in November 2010. While there is some more process optimization to be done to improve the mirror reflectance, we anticipate that these traps could be used to provide quantitative projections on the performance enhancement of this approach for scalable ion state detection.

## 5.2.2 Goal B: Micro-optical cavities for efficient collection of scattered photons

### 5.2.2.1 Conditions for collecting spontaneous emission into the cavity mode

Entanglement between two ions in separate traps (or even separate vacuum chambers) can be generated using photons as intermediaries. In this scheme, the ions are first entangled with photons, and then the entanglement is swapped between the photons using Bell state detection (photon interference). If this process can be performed efficiently, it provides an important means to scale trapped ion quantum computing by enabling photonic channels through which multiple sections of trapped ions could be connected. The success probability of this process crucially depends on the ability to collect the single photon emitted by the ion into a single optical mode, so that the interfering photons are indistinguishable from each other.



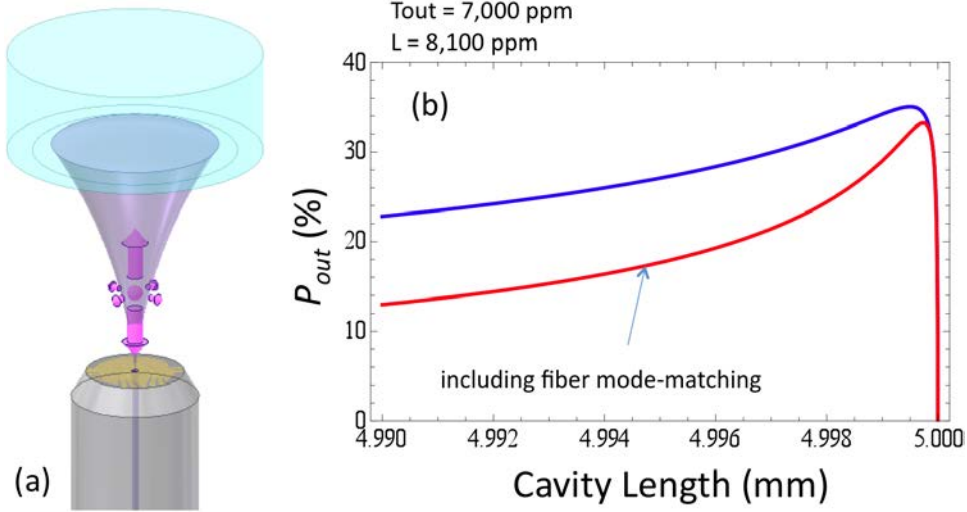


Figure 5.9: (a) Schematic of our approach to cavity-trap integration. The cavity is a plano-convex cavity, with the cavity waist located at and matched with the core of a single-mode optical fiber. (b) Expected collection efficiency of the single photons when ion is located at the optimal location in the cavity mode. Red line includes the mode-matching with the single mode fiber, and should indicate the probability of capturing the photon in the single mode fiber.

Such efficient photon collection can be achieved by utilizing the Purcell effect, where the spontaneous emission from a single atom is coupled strongly to a single mode of electromagnetic field with small mode volume. In this scheme, the atom is put inside a tight optical cavity with small mode volume. In order for the collected photons to interfere to swap entanglement, one needs to ensure that the photons are collected into a single spatial mode (single mode fiber), and their frequency, shape of photon wavepacket and arrival time at the beam splitter are all carefully matched.

For a dipole radiation source (atomic ions in our case) positioned inside an optical cavity, the probability of getting the photon out into the cavity mode is given by

$$P_{out} = \frac{2C}{1 + 2C} \frac{\kappa}{\kappa + \gamma} \frac{T_{out}}{L} \quad (5.1)$$

where  $C = g^2/2\kappa\gamma$  is the cooperativity and the dipole-cavity coupling rate, cavity field decay rate, and atomic polarization decay rate are denoted by  $g$ ,  $\kappa$ , and  $\gamma$ , respectively;  $T_{out}$  is the transmission of the out-coupling mirror for the cavity, and  $L$  is the total loss of the optical cavity. The coupling rate  $g$  is inversely proportional to the square root of the cavity mode volume, and therefore a cavity with a small mode volume is desired for higher collection efficiency.

Figure 5.9(a) shows our approach to achieving the cavity-trap integration. The optical cavity is formed between the tip of a fiber (planar mirror) and a concave mirror. The cavity is aligned to be close to half of a concentric cavity, so that the waist of the cavity mode is positioned at the core of the optical fiber. A cavity mode with a narrow waist (and thus



small mode volume) can be achieved with this approach. When the ion is located about 50  $\mu\text{m}$  from the tip of the fiber, one can calculate the coupling rate  $g$  by calculating the electric field strength due to a single photon in the cavity at the location of the ion. Figure 5.9(b) shows the resulting photon collection probability into the cavity mode (blue) and out to the single mode fiber (red) in this experimental configuration, when the cavity parameters are designed so that the total optical loss in the cavity is 8,100ppm with 7,000ppm accounting for the transmission of the out-coupling mirror (on the fiber tip). The transmission of the out-coupling mirror is designed to achieve critical damping of the cavity. The optical coating requirement of this cavity is fairly relaxed such that the finesse of the cavity is a modest value of  $<1,000$ , which is easy to achieve in the UV wavelength of interest. We anticipate that collection efficiency of 15-20% is feasible for the emitted photons into a single mode fiber. This efficiency is an improvement over current experimental status by a factor of 50, which is expected to improve the success probability of the remote entanglement protocol by a factor of  $\sim 50^2 = 2,500$ .

### 5.2.2.2 New approach to cavity-trap integration

In the original proposal, we planned to utilize the structure of the fiber itself and the natural dimensions of the fiber ferrule to create a surface point Paul trap to integrate the cavity and the ion trap. However, we concluded that successful fabrication of such trap poses many technical challenges, including (a) electrical contact to the ground plane realized by metalizing the fiber, (b) electrical isolation between the center ground electrode (fiber) and the RF electrode (metalized ferrule), (c) high reflectance coating of the fiber tip, and subsequent insertion into the fiber ferrule (and eventually through the UHV chamber), (d) reliability of the fabrication and integration process, (e) expected ion height of  $\sim 100 \mu\text{m}$  determined by the dimensions of the center ground plane (fiber) and the RF electrode (ferrule), which decreases the coupling rate, and (f) integration challenges with longer ion chains.

We have decided to pursue a more monolithic process for fabricating the trap on the fiber tip, to enhance the success probability of the fabrication process. Figure 5.10(a) shows the schematic of this approach. First, the fiber is assembled into a fiber ferrule. The tip of the fiber ferrule provides  $\sim 4 \text{ mm}^2$  of real estate to process the traps. This provides sufficient area for fabricating a multi-segment ion trap using a single-step lithography process. Once the trap is fabricated, the fiber ferrule is mounted in a standard ceramic package by using a custom-fabricated submount that includes on-chip RC low-pass filters (Figure 5.10(b)). Figure 5.10(c) shows an experimental setup where a multi-segment ion trap is fabricated on a small fused silica substrate and mounted on the submount: this system will be tested for the quality of the trap and any charging/drift arising from the dielectric substrate used in this approach.

The new approach provides several advantages, but also brings about new challenges that must be addressed. The inherent advantages include:

1. Simple monolithic fabrication process, compared to metallization and manual assembly of the fibers into the ferrule with the additional complication of the high reflectance (HR) coating. Here, the fabrication process can proceed once the fiber-ferrule is assembled and the HR coating has been applied.

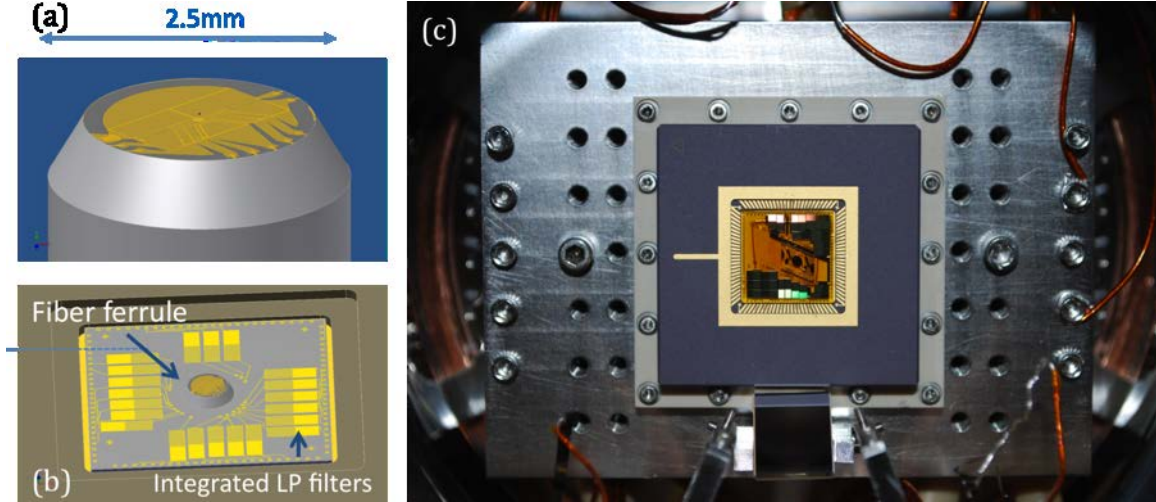


Figure 5.10: New approach to fiber tip trap fabrication. (a) A linear trap is fabricated on the tip of the optical fiber and ferrule using a single-step lithography process, after the fiber tip-ferrule assembly is properly polished for high quality optical surface and high reflectance coating is applied. (b) The fabricated fiber tip trap is mounted in a standard ceramic package through a submount. The submount is fabricated on a fused quartz (or fused silica) substrate, and RC low-pass filters are fabricated on it. (c) Experimental setup with a fabricated submount and a linear trap fabricated on a small fused quartz substrate.

2. The height of the ion is not determined by the natural dimensions of the fibers, but can be controlled by the design of the electrodes. This allows us to bring the ion closer to the fiber tip to position it near the waist of the cavity mode, leading to enhanced coupling rate.
3. More complex ion traps can be fabricated compared to a simple point Paul trap, including a quartic trap capable of trapping long linear ion chains.

On the other hand, the new approach poses several technical challenges that must be addressed. Here we summarize some of the challenges and how we have addressed/plan to address them.

1. In order to achieve low-loss HR coatings, the fiber-ferrule assembly has to be baked at high temperatures ( $\sim 400^\circ\text{C}$ ) after the coatings have been applied. We found out that in order for the assembly to survive this process, the coefficient of thermal expansion for the fiber and ferrule has to match. This means that we cannot use commercial zirconia ferrules widely used for fiber connectors. We have custom-fabricated fused quartz ferrules and identified an adequate epoxy to assemble the fiber into the ferrule, and confirmed that the assembly will endure the necessary bake temperature without mechanical degradation.
2. In order to reduce the Rayleigh scattering loss to manageable levels for the cavity ( $<250\text{ppm}$ ), the RMS surface roughness of the fiber tip has to be reduced to below

0.5nm (5Å). This requirement is much more stringent than a typical polishing requirement for optical connectors. Furthermore, the polishing process for optical connectors lead to substantial radius of curvature for the ferrule, which poses a substantial challenge for the microfabrication process on the fiber tip. We developed a custom polishing process that can routinely achieve the necessary RMS roughness, while eliminating the curvature of the surface to acceptable levels (RoC > 200mm) for microfabrication process. We have also developed a CO2 laser smoothing technique that could potentially reduce the surface roughness to about 0.5Å levels, although further fine-tuning of the process is necessary before we can apply that to the fiber-ferrule assembly.

3. Performing standard lithography on a fiber-ferrule tip is challenging in several aspects. First, it is very difficult to coat the small tip with uniform layers of photoresist since the standard spinning coating technique cannot be applied. We are developing a novel stamping process to coat the fiber tip with a uniform photoresist film adequate for further processing. Second, the standard lithography tools are set up for printing patterns on a flat substrate, and do not accommodate long fiber ferrules with extensions of fiber attached to it. We constructed a custom lithography tool using a standard microscope, CCD camera and a UV light emitting diode. This tool has been successfully used to pattern fine features on a small fused silica substrate. Once the stamping process can successfully coat photoresist on the fiber-ferrule tip, we expect to be able to apply this new tool for lithography on the fiber-ferrule tip.
4. Fiber feedthrough for UHV chambers is a non-trivial task, especially since the extreme vacuum requirement ( $< 10^{-11}$  Torr) for ion trapping experiments. We have successfully adopted an existing fiber feedthrough technology [18] and demonstrated its applicability to the vacuum levels necessary for ion trapping experiments by establishing a high-temperature baking procedure.

### 5.2.2.3 Preliminary tests on cavities constructed using fiber tip and a concave mirror

In the first year of the project, the Duke University team coated some fiber tips and small radius-of-curvature (RoC,  $\sim 5$ mm) mirrors from a vendor with high reflectance coating. The fiber was carefully cleaved to create a flat surface, and the 5mm RoC mirror was standard-polished by the vendor. Figure 5.11 shows the experimental measurement of the cavity alignment setup and the measurement of cavity reflectance using these optical components. We realized a cavity with finesse of about 800, but the maximum transmittance of the cavity on resonance was only about 1.1% (should expect close to 100% for a high quality cavity). From these measurements, we concluded that the transmission of the coatings on the mirrors was about 400ppm, while the scatter and absorption loss were about 3,500ppm. We concluded that the surface quality responsible for scatter losses and optical coating quality responsible for the absorption must be substantially improved.

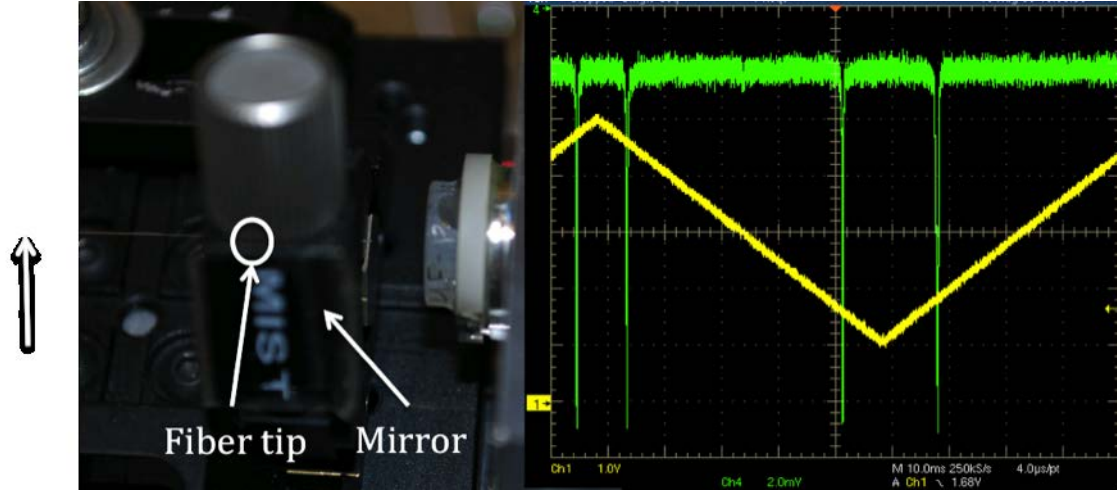


Figure 5.11: Left: Experimental setup to characterize an optical cavity formed between a fiber tip and a small RoC mirror (RoC=5mm). Right: Cavity reflectance (green) measured as a function of cavity length (scanned using a piezoelectric actuator, the control voltage is shown in yellow).

#### 5.2.2.4 Developing high quality surfaces and optical coatings for micro-cavity mirrors

We have since developed various means to measure surface roughness using both an optical non-contact profilometer and atomic force microscopes to assess the quality of optical surfaces before they are sent out for coating. Also, the polishing process for fiber tips was developed, as discussed in the previous section. We have since identified sources for super-polished optical substrates with adequate surface roughness qualities ( $<100\text{ppm}$  scatter losses), which have been sent to Advanced Thin Films for ion-beam sputtering process, which is known to produce absorption losses on the order of  $250\text{ppm}$  at these UV wavelength of interest. We expect to receive these mirrors in December 2010 and will be testing them.

#### 5.2.2.5 Test of point Paul trap

The Duke University and MIT team have collaborated on realizing the first generation point Paul traps using Rogers circuit board material. The point Paul trap was designed and fabricated at MIT while Duke's postdoctoral fellow was working in the MIT group for the first summer to stimulate collaboration. Figure 5.12(a) shows the fabricated point Paul trap mounted in a standard ceramic package. The package was mounted inside a UHV chamber (Figure 5.12(b)). This experiment required completion of all laser systems for photoionization, trapping and cooling of  $174\text{Yb}^+$  ions, including  $399\text{nm}$  for photoionization,  $369.5\text{nm}$  for cooling,  $935\text{nm}$  for repumping out of the D-levels, and another  $372\text{nm}$  to assist with photoionization. All laser wavelengths were stabilized to about  $1\text{MHz}$  using a reference to a wavemeter. With these infrastructure, the Duke University team was able to successfully trap  $174\text{Yb}^+$  ions as shown in Figure 5.12(c).

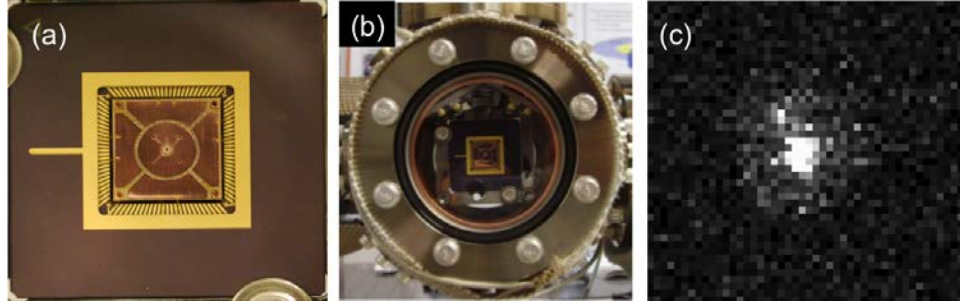


Figure 5.12: Testing point Paul trap at Duke University. (a) Picture of the point Paul trap fabricated on Rogers circuit board material and mounted on a ceramic chip carrier. (b) UHV chamber in which the packaged trap is mounted. (c) image of a single ion trapped in the point Paul trap.

#### 5.2.2.6 Conclusions and future activities

The following milestones as originally described in the proposal has been achieved:

1. As for mirror coating, we worked with a vendor to achieve about 99.6% reflectance on our mirrors and fiber tips. However, the coating had substantial amount of scatter and absorption loss, and was deemed unusable for the cavity QED experiments. We have established polishing and characterization processes to achieve high quality surfaces where the scatter loss can be reduced to below 250ppm. We also discovered that ion-beam sputtering (IBS) process is necessary to get the high quality optical where the absorption loss is minimized. Both absorption and scatter losses become much more substantial in the UV wavelength of interest (370nm) compared to the near infrared where neutral atom cavity QED experiments are performed (at 780nm, the absorption and scatter losses can be reduced to below 10ppm). Currently, the high quality substrates have been prepared and sent to an adequate vendor capable of performing low-loss IBS coating, and we expect to receive the high performance mirrors by December 2010.
2. For the surface roughness, we identified an adequate specification necessary to achieve our cavity QED goals. In order to suppress the scatter losses to below 250ppm (comparable to absorption losses intrinsic to the coating material at these UV wavelengths), we need to reduce the RMS roughness of the surface to below 5nm. We have three processes where we could achieve that: 1) a careful fiber polishing process that will lead to 5nm RMS roughness; 2) HNA etching of silicon substrates that will lead to 0.5nm RMS roughness; and 3) CO<sub>2</sub> laser reflow process that will lead to as low as 0.05nm RMS roughness. Also, commercial vendors can provide super-polished surfaces with RMS roughness as low as 0.02nm. We are currently getting several of these substrates coated with high performance IBS coating, and will be testing the performance in early 2011.
3. For the cavity mode volume, we have successfully demonstrated the alignment and characterization of fiber-tip cavities (no ion traps yet) with finesse as high as 800. This

cavity mode is expected to have a beam waist of about 1.5mm, matching the core size of the single mode fiber. We will align a cavity with similar dimensions once the components with higher quality coatings become available.

The third and fourth years of this project were scheduled to produce cavity-integrated traps where the photon collection efficiency of over 10% would be achieved. The experimental progress we have made and improvements on the course of research should put us on a good path to achieve these goals in the next two years.

## 5.2.3 Goal C: Multiplexed delivery of manipulation beams

### 5.2.3.1 Progress in flexible beam delivery

The Duke University team has been developing MEMS-based beam steering system with adequate performance for individual atom addressing in an array of trapped atoms. The technology development effort over the past several years achieved the following specifications crucial for low cross-talk individual atom addressing:

1. The steering speed between two sites in the lattice has been reduced to below 5 ms. This is an improvement of about three orders of magnitude compared to other analog beam steering systems based on MEMS technology.
2. The quality of optical beams has been optimized, so that the residual intensity of laser beam on adjacent lattice site is suppressed by more than four orders of magnitude. Further improvement can be achieved using single crystal mirrors, and a process development to achieve this goal is currently under way.
3. The power handling capability of MEMS mirrors used in this application has been fully characterized. We anticipate that with adequate reflector coating and optimal packaging environment, the MEMS beam steering system can handle over 1W of optical power without degrading the quality of the steered beam.

Using these advances, the Duke University team has demonstrated individual addressing of Rb atoms in an optical lattice, in collaboration with Prof. Mark Saffman's group at University of Wisconsin at Madison [19]. Application of a similar technology to trapped atomic ions poses some challenges in MEMS device design, but also provides improved system performance (larger addressing range) due to its shorter wavelength of operation. Most importantly, the MEMS mirrors fabricated using standard foundry processes are made of polycrystalline silicon, which might have grain sizes larger than ideal, leading to rough surfaces causing Rayleigh scattering. This would not be of concern for neutral atoms since the operating wavelength is in the infrared and the Rayleigh scattering is much less. We have established a polishing process after the MEMS devices are returned from the foundry, and verified that the extra loss due to Rayleigh scattering is maintained to below 2%. With this modification, we are in a good position to construct MEMS-based optical beam steering system operating at 369nm wavelength for Yb.

#### **5.2.3.2 Future activities**

We plan to construct MEMS-based beam steering system and demonstrate stable addressing of multiple ions in a linear chain. However, this was outside the scope of the first two years of the SMIT II program, and was not pursued here.

# Appendix A

## Ion Motion Stability in Surface Ion Traps

### A.1 Introduction

Paul traps confine ions by a combination of static and oscillating electric fields that share a common null. In the most common setting, the static and oscillating potentials are well-approximated by quadratic functions with coincident principal axes. The static field pulls the ion towards the null along certain directions, and pushes it away in others. The rapidly oscillating potential -in a certain regime of parameters- behaves like a static pseudopotential that pulls the ion back towards the null in all three directions. Roughly speaking, the equilibrium location is stable when the total effective pull towards the null wins over the push.

When the principal axes of the static and oscillating potentials overlap, the equations of motion become particularly simple, and one ends up with separate (decoupled) equations for  $x$ ,  $y$ , and  $z$  directions. All three of these equations have the form of the Mathieu equation, whose so-called  $q$  and  $a$  parameters are given in terms of various physical parameters characterising the ion trap, such as the voltages on the electrodes, the parameters that describe the geometry of the electrodes, etc. A detailed analysis of the stability problem of the Mathieu equation gives regions in the  $q$ - $a$  space for which the motion is stable. Relating these regions of  $q$  and  $a$  to regions of trap parameters, one can then look for trap designs or voltages for which the ion motion is stable in all three directions. This is how the parameters of the classical Paul traps are picked.

Surface electrode Paul traps are a recent development in the design of ion traps for quantum information processing. Many of the designs that are being considered have asymmetry built into their geometries. The asymmetry helps rotate the trap axes to angles with respect to the electrode surface, which is required to cool the ion when the cooling laser is parallel to the trap surface. On the other hand, the asymmetry introduces a relative angle between the principal axes of the RF and DC fields. This invalidates the classical stability analysis used in the symmetric case. When there is a nonzero relative angle between the RF and DC axes, the motion is described by a coupled, multi-dimensional version of the Mathieu equation, whose regimes of stability are not readily available in the literature. The knowledge of these



regimes is crucial for the optimization of the electrode voltages and the design of the trap itself.

We obtain the stability diagram of asymmetric surface traps via Floquet analysis—by obtaining a basis set of numerical solutions, and extracting the eigenvalues of the matrix that evolves the system by one period. We demonstrate that the development of the instabilities as the parameters change is due to the “collisions” of the eigenvalues of the relevant matrix on the unit circle.

While useful, this approach requires a full numerical solution of the system for the particular geometry (or the relative angle between RF/DC axes) under consideration. In order to have a rough, quick estimate of the stability boundaries, we resort to multiple scale perturbation theory, and using some hints from the numerical Floquet analysis, obtain approximate formulas for the boundaries of the primary stability region. We check these formulas against the numerics, and show that the formulas give a conservative estimate of the size of the primary stability region, and thus can be trusted as first estimates during the trap design process.

As a third check, we attack the problem by using an “infinite determinant” method by expanding the solution to a Fourier series and obtaining a set of linear equations for the coefficients. We show that the method is capable of giving the “simple” stability boundaries, i.e., the boundaries whose analogues exist in the decoupled case, as well.

## A.2 Equations of motion.

Let us assume that the oscillating (RF) and the static (DC) electric fields have a coincident zero (or “null”) at the origin,  $O$ . We work in the quasi-static approximation, so in order to calculate the motion of charged particles in these fields, it will be sufficient to know the instantaneous electrostatic potentials  $V^{\text{RF}}$  and  $V^{\text{DC}}$ . Since the electric fields vanish at  $O$ , the first order terms in the Taylor expansions of  $V^{\text{RF}}$  and  $V^{\text{DC}}$  around  $O$  vanish. Denoting the potential energy of an ion by  $U = eV$  where  $e$  is the ion charge, and shifting the zero of  $U$  so that  $U(O) = 0$ , we have,

$$U(x, y, z) = U^{\text{RF}} + U^{\text{DC}} \quad (\text{A.1})$$

$$= \frac{1}{2} \sum_{ij} x_i x_j U_{ij}^{\text{RF}} \cos(\omega t) + \frac{1}{2} \sum_{ij} x_i x_j U_{ij}^{\text{DC}}, \quad (\text{A.2})$$

where  $x_1, x_2, x_3$  stand for  $x, y, z$ , respectively, and the  $U_{ij}^{\text{DC/RF}}$  are the matrices of second derivatives (Hessians) of the RF and DC potential energies.

The equations of motion are given as,

$$m \frac{d^2 x_i}{dt^2} = - \frac{\partial U}{\partial x_i} \quad (\text{A.3})$$

$$= - \sum_j U_{ij}^{\text{RF}} x_j \cos(\omega t) - \sum_j U_{ij}^{\text{DC}} x_j. \quad (\text{A.4})$$

Defining a new time variable  $\tau$  by  $\omega t = 2\tau$  and denoting the derivatives with respect to  $\tau$  by dots, we get,

$$\ddot{x}_i + \sum_j A_{ij} \dot{x}_j + 2 \sum_j Q_{ij} x_j \cos 2\tau = 0, \quad (\text{A.5})$$

where,

$$A_{ij} = 4U_{ij}^{\text{DC}}/m\omega^2, \quad Q_{ij} = 2U_{ij}^{\text{RF}}/m\omega^2, \quad (\text{A.6})$$

are the multi-variable analogues of the  $a$  and  $q$  parameters of the single-variable Mathieu equation, which we discuss below. The main aim of this paper is to explore the stability properties of (A.5) for the two dimensional case. Note that Gauss's law enforces the matrices  $A_{ij}$  and  $Q_{ij}$  to be traceless,

$$\sum_i A_{ii} = 0, \quad \sum_i Q_{ii} = 0. \quad (\text{A.7})$$

**The decoupled case.** One can diagonalize  $U_{ij}^{\text{DC}}$  by an orthogonal transformation,

$$x_i = \sum_j S_{ij} \tilde{x}_j, \quad (\text{A.8})$$

and obtain,

$$U^{\text{DC}} = \frac{1}{2} \left( \tilde{U}_{11}^{\text{DC}} \tilde{x}_1^2 + \tilde{U}_{22}^{\text{DC}} \tilde{x}_2^2 + \tilde{U}_{33}^{\text{DC}} \tilde{x}_3^2 \right), \quad (\text{A.9})$$

where the diagonal matrix  $\tilde{U}_{ij}$  is given by  $\tilde{U}_{ij} = \sum_{kl} S_{ik} S_{jl} U_{kl}$ . If the RF and DC principal axes coincide, the same transformation (A.8) also diagonalizes  $U_{ij}^{\text{RF}}$ , and we get (dropping the tildes),

$$U = \frac{1}{2} \left( U_{11}^{\text{RF}} x_1^2 + U_{22}^{\text{RF}} x_2^2 + U_{33}^{\text{RF}} x_3^2 \right) \cos(\omega t) + \frac{1}{2} \left( U_{11}^{\text{DC}} x_1^2 + U_{22}^{\text{DC}} x_2^2 + U_{33}^{\text{DC}} x_3^2 \right).$$

This is the classical case of a symmetric Paul trap. The equations of motion resulting from this potential are decoupled; after transforming the time variable by  $\omega t = 2\tau$  as above, one gets,

$$\ddot{x}_i + (a_i + 2q_i \cos 2\tau) x_i = 0, \quad (\text{A.10})$$

where,

$$a_i = 4U_{ii}^{\text{DC}}/m\omega^2, \quad q_i = 2U_{ii}^{\text{RF}}/m\omega^2. \quad (\text{A.11})$$

Equation (A.10) is known as the single-variable Mathieu equation, and one can apply the classical stability analysis of this equation to each component and obtain the regions of joint stability. This gives the standard  $a - q$  stability plots for Paul traps.

### A.3 Stability of periodic Hamiltonian systems

We will discuss various approaches to the stability analysis of the two dimensional version of the system (A.5). The main aim is to find conditions on the entries of the matrices  $A$  and  $Q$  that would ensure all solutions to (A.5) are bounded. If some solutions are bounded while others are not, it is still in principle possible to fine-tune the initial conditions so that only the bounded solutions contribute. However, in reality, small errors in the initial conditions and small perturbations (as well as nonlinearities) will make the system pick up the unbounded solution, and result in instability.

**Equivalent first order system.** By defining,

$$\mathbf{u} = \begin{bmatrix} \mathbf{x} \\ \dot{\mathbf{x}} \end{bmatrix}, \quad (\text{A.12})$$

we obtain the equivalent first order system,

$$\dot{\mathbf{u}} = \mathbf{G}(\tau)\mathbf{u}, \quad (\text{A.13})$$

where,

$$\mathbf{G}(\tau) = \begin{pmatrix} \mathbf{0} & \mathbf{I} \\ -2\mathbf{Q}\cos 2\tau - \mathbf{A} & \mathbf{0} \end{pmatrix}, \quad (\text{A.14})$$

is periodic in time with period  $T = \pi$  ( $\mathbf{I}$  denotes the  $n \times n$  identity matrix, where  $n$  is the number of spatial directions under consideration). Although our primary interest is in the case of  $n = 2$ , where  $\mathbf{u}$  is a 4-dimensional vector, much of what we say below will be valid for a general periodic system of the form (A.13) with a  $2n$ -dimensional  $\mathbf{u}$ .

**Fundamental solution matrix.** In order to explore the long-time stability properties of the solutions to (A.13), we first obtain a set of fundamental solutions,  $\mathbf{u}_i$ , that form a basis to the space of all solutions. We take the initial value of  $\mathbf{u}_i(0)$  to be the  $i$ th column of the  $2n \times 2n$ -dimensional identity matrix. In other words, we take the  $i$ th component of  $\mathbf{u}_i(0)$  to be 1, all the other components to be 0. Since the system (A.13) is linear, a solution with arbitrary initial conditions  $\mathbf{u}(0) = \mathbf{u}_0$  can be obtained as an appropriate linear combination of the fundamental solutions,

$$\mathbf{u}(t) = \sum_i u_{0i} \mathbf{u}_i. \quad (\text{A.15})$$

We combine the column vectors  $\mathbf{u}_i$  into a  $2n \times 2n$  “fundamental solution matrix”,  $\mathbf{U}(t)$ , with,

$$\mathbf{U}(t) = [\mathbf{u}_1(t) \dots \mathbf{u}_{2n}(t)]. \quad (\text{A.16})$$

Then, the general solution (A.15) can be expressed as,

$$\mathbf{u}(t) = \mathbf{U}(t)\mathbf{u}_0. \quad (\text{A.17})$$

The fundamental matrix satisfies the equation,

$$\dot{\mathbf{U}} = \mathbf{G}(t)\mathbf{U}, \quad (\text{A.18})$$

with the initial condition,

$$\mathbf{U}(0) = I. \quad (\text{A.19})$$

If the system (A.13) were autonomous, i.e., if  $\mathbf{G}(\tau)$  were independent of time, it would be possible to treat  $\mathbf{U}(\Delta\tau)$  as a “time translation operator”, giving the solution at time  $\tau_0 + \Delta\tau$  when applied to an initial condition at  $\tau_0$ . Since the system under consideration is not autonomous, this is not generally the case;  $\mathbf{U}$  only gives time translations from the moment  $\tau = 0$ .

**Mapping at a period.** Although the system (A.13) is not invariant under arbitrary time translations, it is invariant under translations by one period,  $T$  ( $= \pi$ ). Using this, it is possible to prove that  $\mathbf{U}(T)$  translates the system from an arbitrary integer multiple  $mT$  of  $T$  by an amount  $T$ ,

$$\mathbf{U}(T)\mathbf{u}(mT) = \mathbf{u}((m+1)T). \quad (\text{A.20})$$

Using  $\mathbf{u}(mT) = \mathbf{U}(mT)\mathbf{u}_0$ , we get,

$$[\mathbf{U}(T)]^m = \mathbf{U}(mT). \quad (\text{A.21})$$

Thus, the matrix  $\mathbf{U}(T)$ , called the matrix for the “mapping at a period”, contains relevant information about the long time behavior of the system (A.13). In particular, it can be shown that the equilibrium solution of (A.13),  $\mathbf{u}(t) = \mathbf{0}$ , is stable if and only if it is stable under successive applications of  $\mathbf{U}(T)$  [20, 21]. If there is a vector  $\mathbf{v}$  such that  $[\mathbf{U}(T)]^m \mathbf{v}$ ,  $m = 1, 2, \dots$  is an unbounded sequence of vectors then there will be an (arbitrarily small) initial condition of the system for which the solution will grow unboundedly.

This connection with the stability under successive applications of the mapping at a period opens the door to testing for stability of (A.13) by investigating the eigenvalue/eigenvector (or more generally, Jordan) decomposition of the matrix  $\mathbf{U}(T)$ . In particular, the equilibrium is unstable if  $\mathbf{U}(T)$  has an eigenvalue  $\lambda$  with  $|\lambda| > 1$ . If the eigenvalues of  $\mathbf{G}(T)$  are not repeated, and all have magnitudes less than or equal to 1, then the equilibrium is stable.<sup>1</sup>

**Some properties of the eigenvalue spectrum of a symplectic map.** The mathematical theory of classical mechanics imposes certain conditions on the eigenvalues of  $\mathbf{U}(T)$ , which we will denote by  $\mathbf{T}$  for convenience. The fact that the time evolution map in a Hamiltonian system is a canonical transformation is reflected by the condition that [20],

$$\mathbf{T}^T \mathbf{J} \mathbf{T} = \mathbf{J}, \quad (\text{A.22})$$

where  $\mathbf{J}$  is the “canonical symplectic form”, an antisymmetric matrix given in terms of the identity matrix  $\mathbf{I}$  as,

$$\mathbf{J} = \begin{bmatrix} \mathbf{0} & -\mathbf{I} \\ \mathbf{I} & \mathbf{0} \end{bmatrix}. \quad (\text{A.23})$$

Using (A.22), it is possible to show that if  $\lambda$  is an eigenvalue of the matrix  $\mathbf{T}$ , then, so is  $\frac{1}{\lambda}$ . Since the coefficients of the characteristic polynomial of  $\mathbf{T}$  are all real, we see that  $\bar{\lambda}$ , the complex conjugate of  $\lambda$ , is also an eigenvalue. This proves that the eigenvalues of  $\mathbf{T}$  come in four kinds of groups ( $\Im\lambda$  denotes the imaginary part of  $\lambda$ ),

---

<sup>1</sup>For repeated eigenvalues, one has to look at the relevant Jordan block. If an  $m$ -fold repeated eigenvalue  $\lambda$  with  $|\lambda| \leq 1$  has  $m$  distinct eigenvectors, then the subspace spanned by these eigenvectors is still stable.

- 4-tuples  $\lambda, \bar{\lambda}, 1/\lambda, \frac{1}{\bar{\lambda}}$  with  $\Im\lambda \neq 0, |\lambda| \neq 1$ .
- Real pairs,  $\lambda, \frac{1}{\lambda}$ , where  $\lambda = \bar{\lambda}, |\lambda| \neq 1$
- Pairs on the unit circle,  $\lambda, \bar{\lambda}$ , where  $\frac{1}{\lambda} = \bar{\lambda}$
- Single eigenvalue,  $\lambda = 1$ .

The multiplicities of a 4-tuple (or a pair in the real or unit length cases) are the same.

It follows from this list of possibilities that the origin  $\mathbf{u} = 0$  is stable under successive applications of  $\mathbf{T}$  only if all the eigenvalues of  $\mathbf{T}$  are on the unit circle. If, in addition to being of unit magnitude, all the eigenvalues are distinct, then the system is necessarily stable.<sup>2</sup>

As we change the parameters of the system (A.13), i.e., if we change the entries of the matrices  $\mathbf{Q}$  and  $\mathbf{A}$ , the eigenvalues of  $\mathbf{T}$  change. Suppose we start with a set of distinct eigenvalues on the unit circle. The above list of possibilities ensures that as we change the parameters continuously, the eigenvalues can move off the unit circle only if they collide on the unit circle first. Thus, instabilities develop by eigenvalues “colliding” on the unit circle, however, not all collisions result in instabilities.[20, 21]

In the following sections, we will investigate the development of instabilities for the coupled Mathieu system (A.13), (A.14).

## A.4 Stability of the Mathieu system

We next apply the approach described in the previous section to derive the stability diagram of the coupled Mathieu system. For simplicity, we focus on the two-dimensional version, since in practice the RF fields of a surface trap have non-vanishing components only in the “radial” directions, which we denote by  $x$  and  $y$ . The confinement of the ion in the “axial”, or  $z$  direction is facilitated by the DC fields, which, by Gauss’s law, implies that the DC field has an anti-confining radial component. In other words, the trace of the matrix of second derivatives (Hessian) of the DC potential restricted to the  $x$ - $y$  plane must be negative.

**Coupled Mathieu system** The equations of motion are,

$$\ddot{x}_i + \sum_j A_{ij}x_j + 2 \sum_j Q_{ij}x_j \cos 2\tau = 0. \quad (\text{A.24})$$

In the most general setting, one can investigate the stability properties of (A.24) in terms of the entries of the matrices  $\mathbf{Q}$  and  $\mathbf{A}$ , however, this would result in a hard to visualize stability “diagram” in the large-dimensional space of all possible values of these entries. Instead, we assume that only the overall scale of the matrices  $\mathbf{A}$  and  $\mathbf{Q}$  are changed, and obtain a “ $q$ - $a$ ” plot similar to the ones in the single variable case. As we will next show, this amounts to

---

<sup>2</sup>If some of the eigenvalues are degenerate, we have to consider the Jordan decomposition. See, e.g., [21] for a detailed discussion.

fixing the relative angles between the principal axes of RF and DC, and the ratio of the eigenvalues of  $\mathbf{A}$ .<sup>3</sup> We will obtain similar plots for various angles and eigenvalue ratios.

As mentioned above,  $x$  and  $y$  so that the Hessian of either the RF or the DC potential used in (A.1) is diagonal. Let us assume that the DC Hessian is diagonalized. This means that the  $\mathbf{A}$  matrix resulting from the total DC potential is of the form,

$$\mathbf{A} = a \begin{pmatrix} 1 & 0 \\ 0 & -\alpha \end{pmatrix}, \quad (\text{A.25})$$

where  $a$  and  $\alpha$  are constants to be determined by the electrode geometry and the DC voltages.

The two-dimensional ( $x$ - $y$ ) RF Hessian  $U_{ij}^{\text{RF}}$  is traceless and symmetric, and so is  $Q_{ij}$ . If we were to use a coordinate system  $(\tilde{x}, \tilde{y})$  in which  $U_{ij}^{\text{RF}}$  is diagonal, the RF potential energy would have the form,

$$U^{\text{RF}}(\tilde{x}, \tilde{y}) = \frac{1}{2} U_0^{\text{RF}} (\tilde{x}^2 - \tilde{y}^2) \cos(2\tau), \quad (\text{A.26})$$

and the related  $\mathbf{Q}$  would be given as,

$$\mathbf{Q} = q \begin{pmatrix} 1 & 0 \\ 0 & -1 \end{pmatrix}, \quad (\text{A.27})$$

where  $q$  is a free parameter. The coordinates  $(\tilde{x}, \tilde{y})$  and  $(x, y)$  are related by a rotation,

$$\tilde{x} = x \cos \theta + y \sin \theta \quad (\text{A.28})$$

$$\tilde{y} = -x \sin \theta + y \cos \theta. \quad (\text{A.29})$$

Substituting these in (A.26), we get the RF potential energy in terms of the coordinates along the DC principal axes. This gives,

$$U^{\text{RF}}(x, y) = \frac{1}{2} U_0^{\text{RF}} (x^2 \cos 2\theta - y^2 \cos 2\theta + 2xy \sin 2\theta) \cos(2\tau). \quad (\text{A.30})$$

The resulting  $\mathbf{Q}$  matrix is,

$$\mathbf{Q} = q \begin{pmatrix} \cos 2\theta & \sin 2\theta \\ \sin 2\theta & -\cos 2\theta \end{pmatrix}. \quad (\text{A.31})$$

Thus, the equations of motion in coordinates along the DC principal axes are,

$$\ddot{x} + ax + 2q(cx + dy) \cos 2t = 0 \quad (\text{A.32})$$

$$\ddot{y} - \alpha ay + 2q(dx - cy) \cos 2t = 0, \quad (\text{A.33})$$

where for brevity we replaced  $\cos 2\theta$  and  $\sin 2\theta$  by  $c$  and  $d$ , respectively. Below, we will fix the values of  $\alpha$  and  $\theta$  to get a  $q$ - $a$  stability plot as in the decoupled case, for a set of values of  $\alpha$  and  $\theta$ . In practice, fixing  $\alpha$  and  $\theta$  and varying  $q$  and  $a$  corresponds to fixing the trap geometry and the ratios of the DC voltages, and changing the overall scale of the RF ( $q$ ) and DC ( $a$ ) voltages. Below, we will assume that  $\alpha > 0$ . This means that one of the DC axes is confining (i.e., the DC force along that axis recalls the ion to the trap center), and the other is anti-confining. Since we assume a confining DC force along the  $z$ -direction, at least one of  $x$  and  $y$  must have an anti-confining DC force. In practical designs we do not use designs with two anti-confining directions, hence the assumption  $\alpha > 0$ .

---

<sup>3</sup>Physically, these conditions correspond to fixing the geometry of the electrodes and the relative magnitudes of the DC voltages; changing only the overall DC voltage scale and the RF voltage (possibly also the RF frequency).

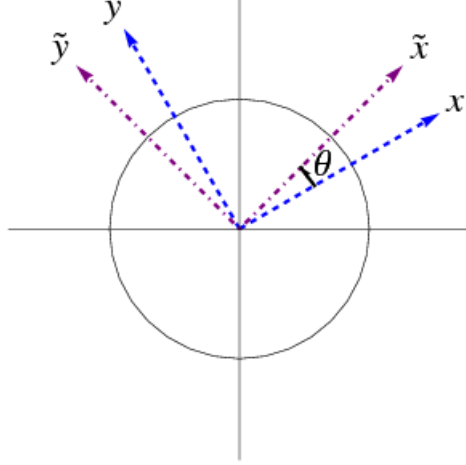


Figure A.1: DC  $(x,y)$  and RF  $(\tilde{x},\tilde{y})$  axes

**The numerics.** We next explore the stability properties of the system (A.32)-(A.33), for various values of  $\alpha$  and  $\theta$ . We proceed by numerically solving (A.32)-(A.33) for four different initial conditions where we set one of  $x(0)$ ,  $y(0)$ ,  $\dot{x}(0)$ ,  $\dot{y}(0)$  to one, and all the others to zero. After obtaining the four solutions over one period of the oscillating RF field (i.e., in terms of the time parameter  $\tau$ , over a time period of  $\Delta\tau = \pi$ ), we obtain the “mapping at a period” described in the previous section. We next obtain the eigenvalues of this matrix, and decide whether the system is stable or unstable by looking at the sizes of the eigenvalues. This procedure corresponds to one “dot” in the  $q$ - $a$  stability plot. Looping over  $q$  and  $a$  values, we obtain a stability diagram for a given value of  $\alpha$  and  $\theta$ .

We present two stability plots below in Figures 2, 3, 4, 7, 8, 9, and demonstrate the “eigenvalue collision” phenomenon in Figures 5, 6, 10, 11. We give a more comprehensive set of stability plots after we present an approximate analytical method for obtaining the stability boundaries.

## A.5 The infinite determinant method

We will describe the infinite determinant method in the setting of the single variable Mathieu equation. Using Floquet’s theorem, we look for a solution to

$$\ddot{x} + (a + 2q \cos 2\tau)x = 0, \quad (\text{A.34})$$

of the form

$$x(\tau) = e^{i\nu\tau} \sum_{n=-\infty}^{\infty} b_n e^{i2n\tau}. \quad (\text{A.35})$$

Here, the infinite sum represents a periodic function with a period equal to the period of the oscillating parameter,  $2q \cos 2\tau$ , and the exponential term in front determines the long time stability of the solution. The system is stable when  $\nu$  is purely real, and unstable when  $\nu$  has a nonvanishing imaginary part.

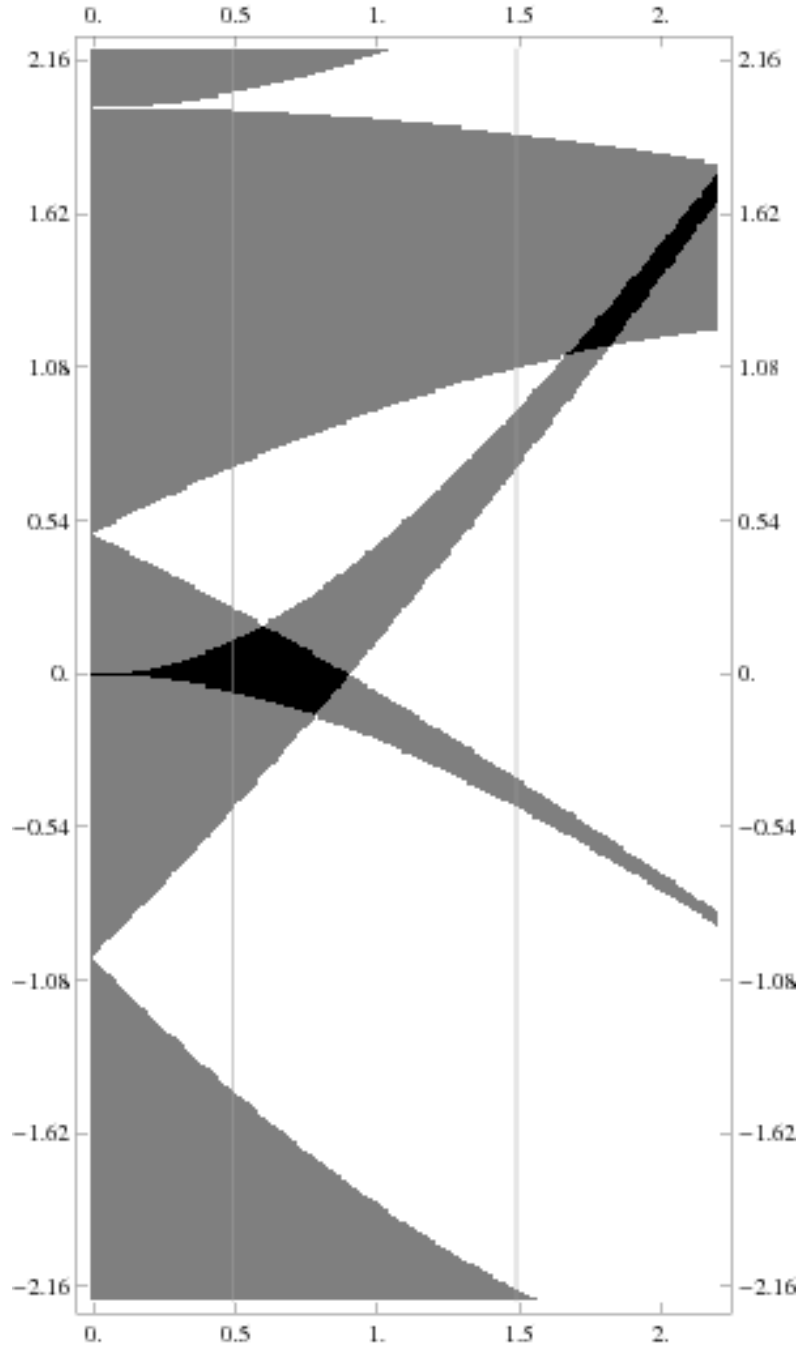


Figure A.2: The number of stable eigenvalues of the “mapping at a period” in the  $q$ - $a$  space, for  $\theta = 0$  degrees between the RF and DC axes, with  $\alpha = 1/2$ . Black: 4 stable eigenvectors (complete stability), gray: 2 stable eigenvectors (partial stability), white: no stable eigenvectors (complete instability). This case corresponds to the classical stability of two decoupled, single-variable Mathieu systems.



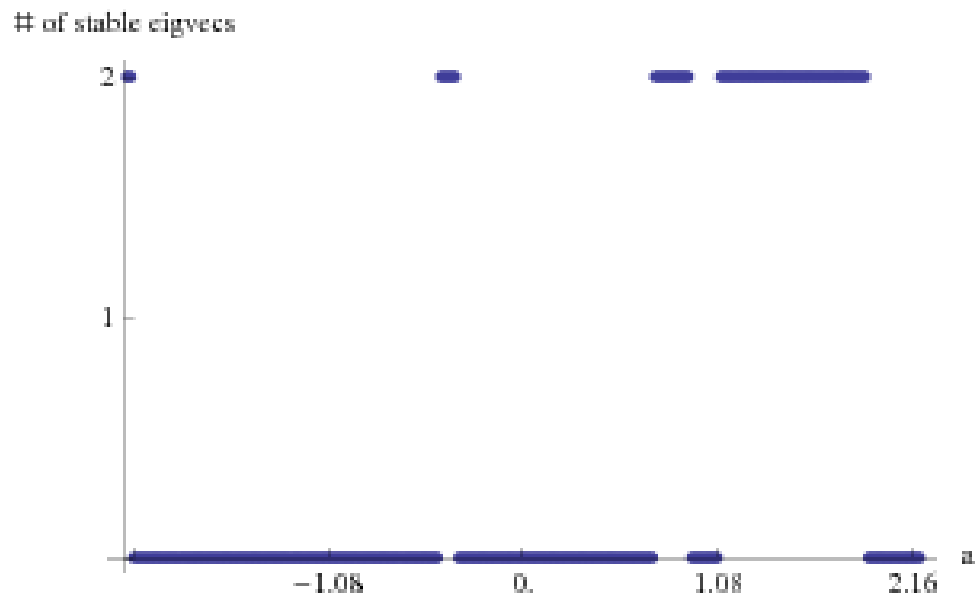


Figure A.3: The number of stable eigenvalues vs.  $a$ , along the line at  $q = 0.5$  in Figure A.2.

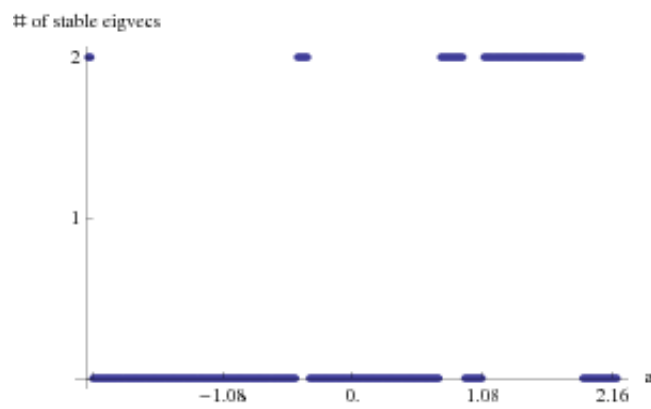


Figure A.4: The number of stable eigenvalues vs.  $a$ , along the line at  $q = 1.5$  in Figure A.2.

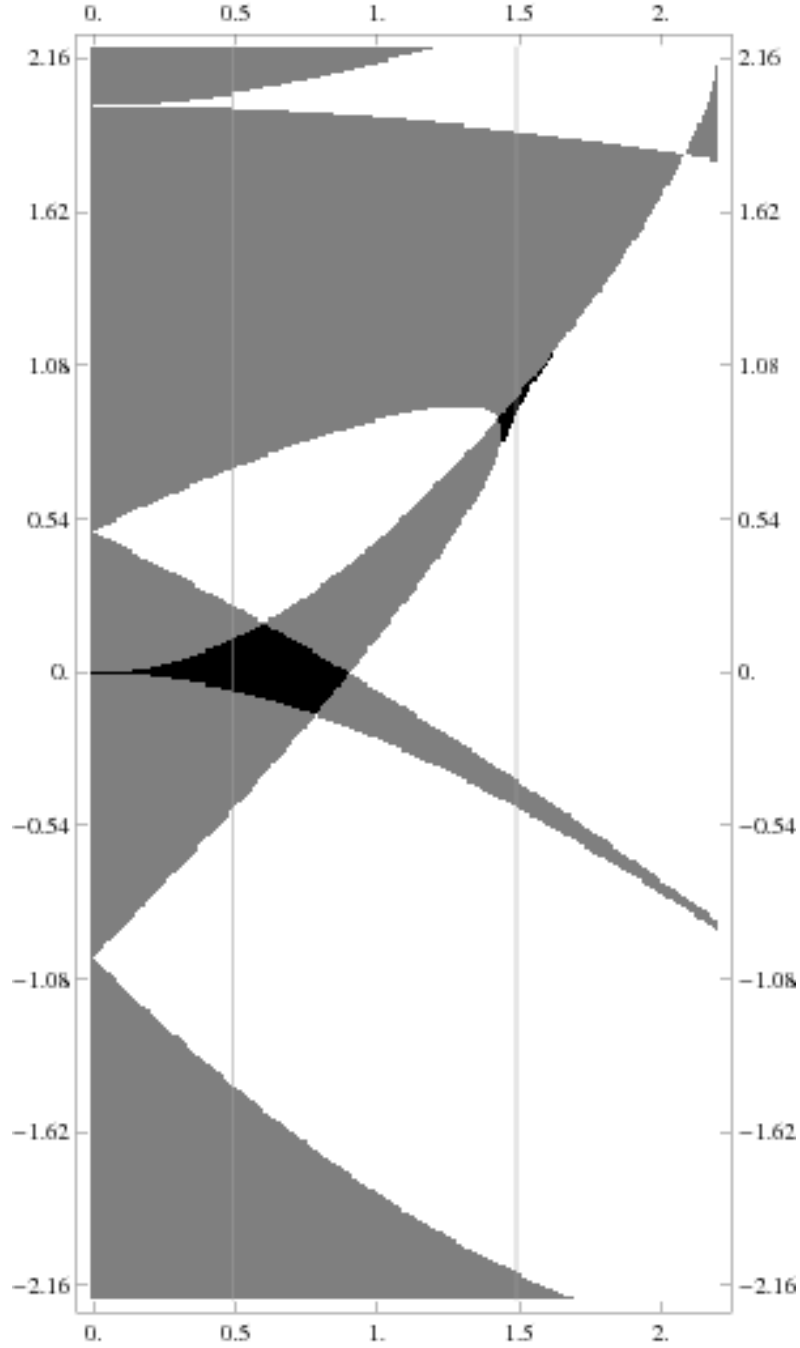


Figure A.5: The number of stable eigenvalues of the “mapping at a period” in the  $q$ - $a$  space, for  $\theta = 6.4$  degrees between the RF and DC axes, with  $\alpha = 1/2$ . Black: 4 stable eigenvectors (complete stability), gray: 2 stable eigenvectors (partial stability), white: no stable eigenvectors (complete instability). This case couples the  $x$  and  $y$  motions, and cannot be investigated by standard, single-variable Mathieu techniques.

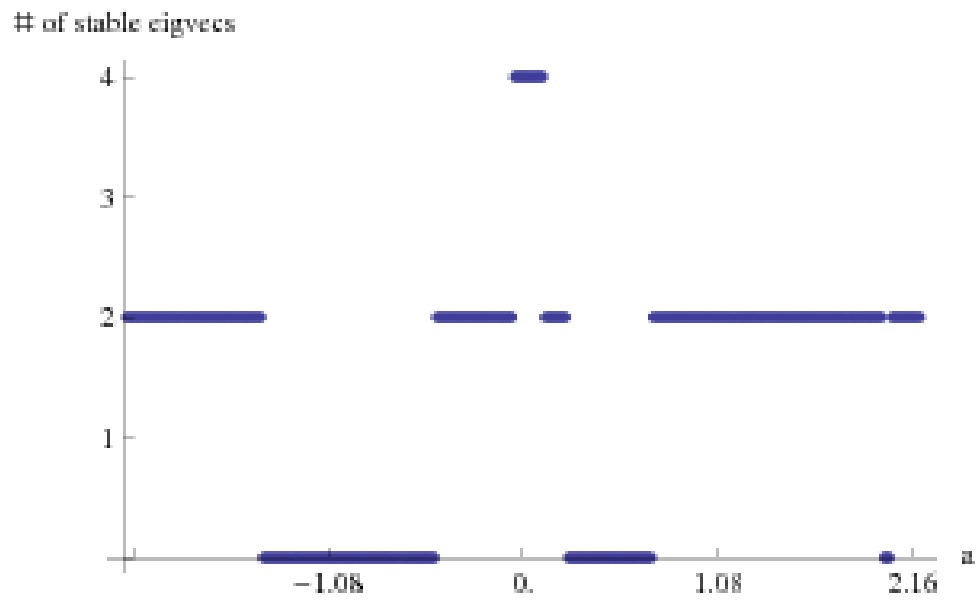


Figure A.6: The number of stable eigenvalues vs.  $a$ , along the line at  $q = 0.5$  in Figure A.5.

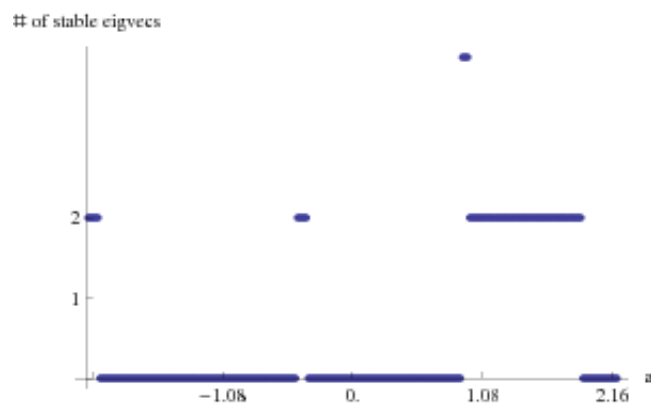


Figure A.7: The number of stable eigenvalues vs.  $a$ , along the line at  $q = 1.5$  in Figure A.5.

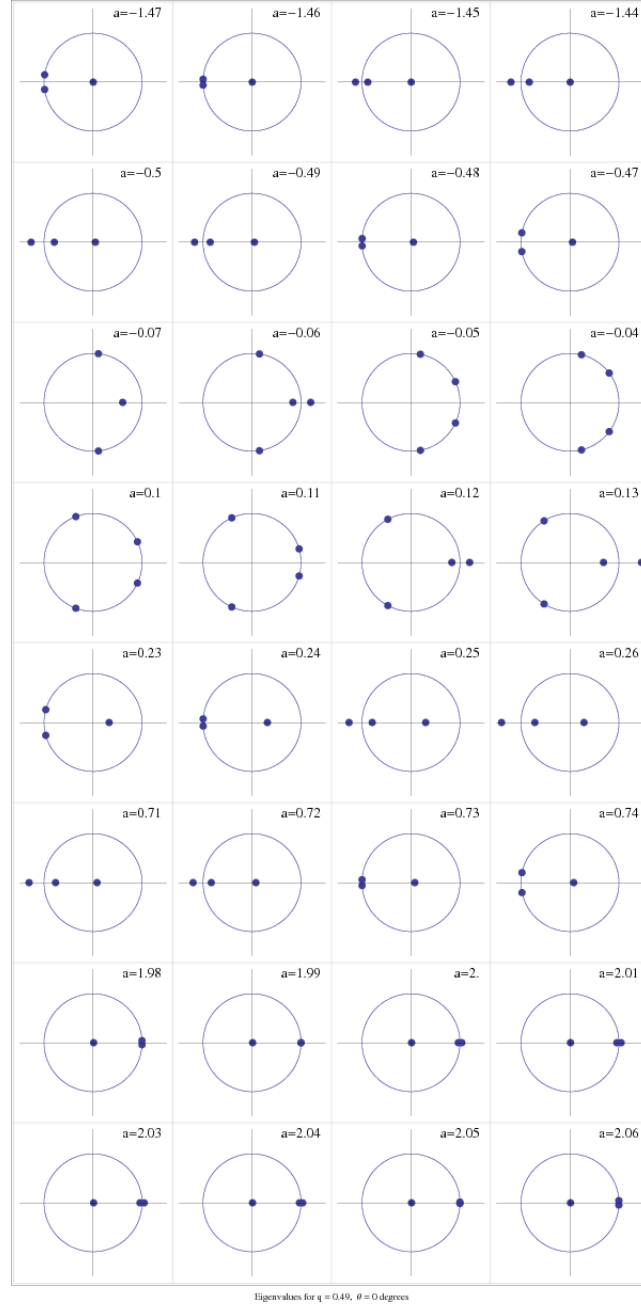


Figure A.8: The evolution of the eigenvalues of the “mapping at a period”, as one moves along the first vertical line (at  $q = 0.5$ ) in Figure A.2. Each row of four plots corresponds to a region in Figure A.2 around a point where a change in the number of stable eigenvectors occurs. Such changes are represented by changes in the darkness of the  $q$ - $a$  area plot in Figure A.2. As described in the text, a change in the number of stable eigenvectors is effected by a “collision” of eigenvalues on the unit circle, with eigenvalues on the unit circle leaving, or eigenvalues off the unit circle getting on the unit circle. In some plots, one of the four eigenvalues is outside the region shown, so only three eigenvalues are seen. In this decoupled case, all collisions happen on the real line.

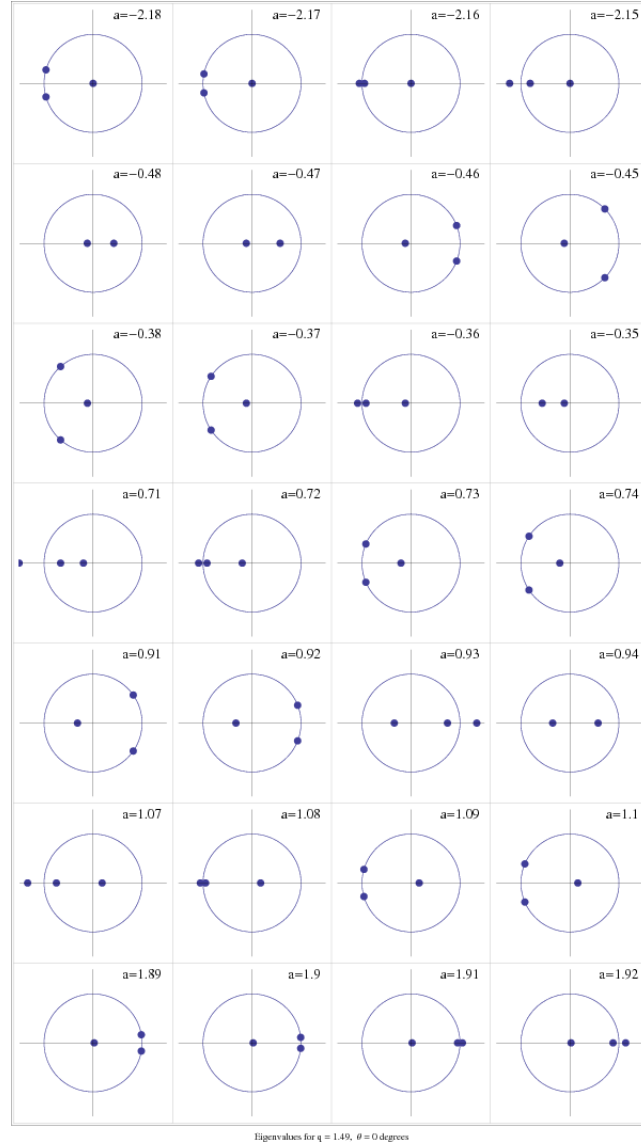


Figure A.9: The evolution of the eigenvalues of the “mapping at a period” as one moves along the second vertical line (at  $q = 1.5$ ) in Figure A.2. As in Figure A.8, each row of four plots corresponds to a change in the number of stable eigenvalues resulting from a “collision” of eigenvalues on the unit circle. Once again, collisions happen only on the real line.

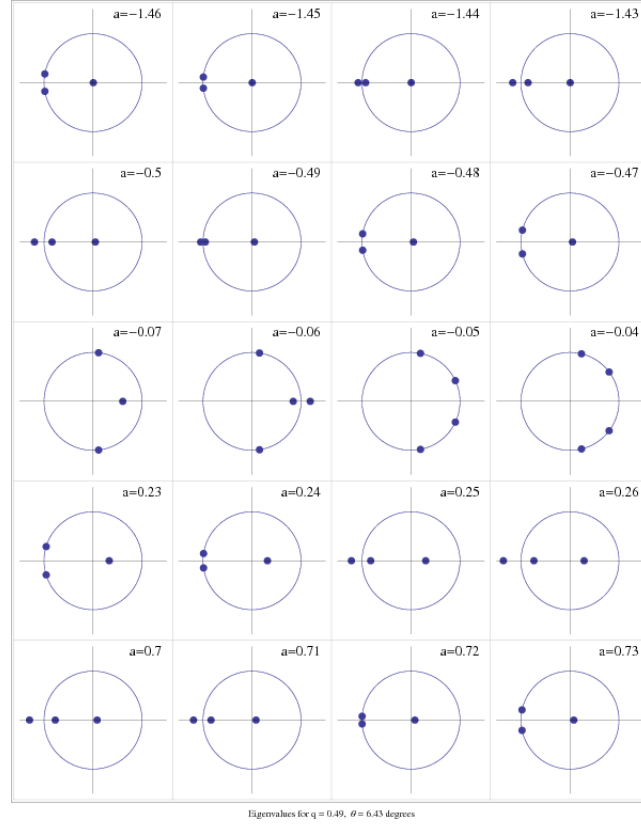


Figure A.10: Similar to Figure A.8, but for a *coupled* system. Each row shows the evolution of the eigenvalues of the “mapping at a period” as one moves along the first vertical line (at  $q = 0.5$ ) in Figure A.5, eigenvalues changes. Such changes are represented by changes in the darkness of the  $q$ - $a$  area plot in Figure A.5. The transitions on this first line ( $q = 0.5$ ) all have analogues in the decoupled case, and the “collisions” of eigenvalues still happen on the real line only.

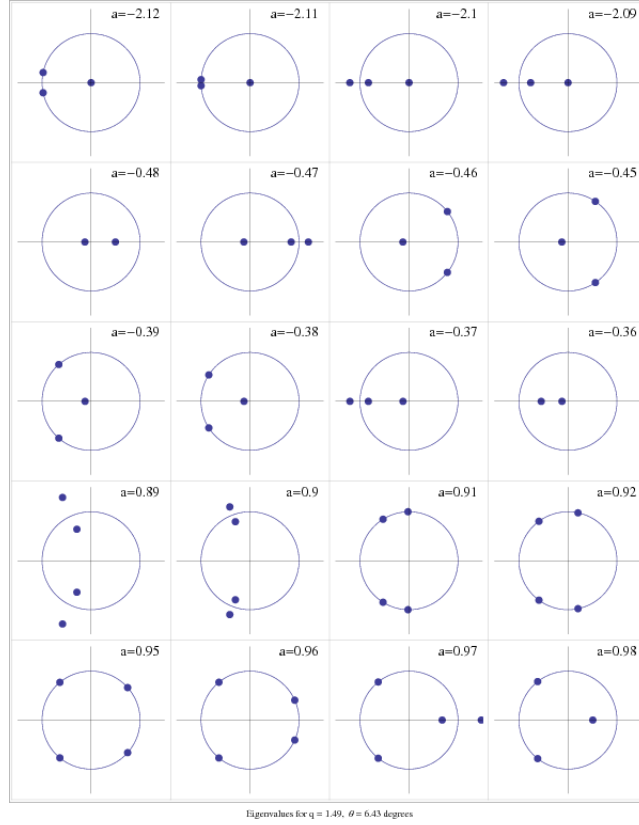


Figure A.11: Similar to Figure A.9, but for a *coupled* system. Each row shows the evolution of the eigenvalues of the “mapping at a period” as one moves along the second vertical line (at  $q = 1.5$ ) in Figure A.5, around a region where the number of stable eigenvalues changes. This time, we encounter a “*combined resonance*” near  $a = 0.9$ , which doesn’t have an analogue in the decoupled case. This is represented as a collision of eigenvalues on the unit circle, *away* from the real line.

Substituting (A.35) into (A.34) and shifting the summation index in two of the terms, we get,

$$e^{i\nu\tau} \sum_{n=-\infty}^{\infty} ((-(\nu + 2n)^2 + a)b_n + q(b_{n-1} + b_{n+1})) e^{i2n\tau} = 0. \quad (\text{A.36})$$

Setting the coefficient of each basis functions  $e^{i2n\tau}$  to zero, we obtain an infinite set of equations for the infinitely many coefficients  $b_n$ . This set of equations has a solution only if the determinant of the infinite matrix of coefficients vanishes, i.e.,  $\det \mathbf{B} = 0$ , where,

$$B_{mn} = \begin{cases} -(\nu + 2n)^2 + a & : m = n \\ q & : m = n \pm 1 \\ 0 & : \text{Otherwise.} \end{cases} \quad (\text{A.37})$$

The determinant of the matrix (A.37) does not converge as it stands, but we could remedy this by obtaining an equivalent set of equations to (A.36) by dividing each equation by the corresponding diagonal entry,  $B_{nn}$ . Since we will be working with a finite-size version of (A.37) in order to extract numerical results, the convergence issue will not be of concern; we thus directly work with (A.37).

This approach gives an equation that relates  $q$ ,  $a$ , and the exponent  $\nu$ . Once again, for a given  $q$  and  $a$ , one can extract the growth factor, this time by solving the determinant equation. By checking whether the equation for  $\nu$  has an imaginary solution, we deduce the stability/instability of the system. For the decoupled case, it is also possible to extract the stability boundaries in a straightforward manner; it turns out [22] that setting the growth factor  $e^{i\nu\pi}$  to  $\pm 1$ , we get equations relating  $q$  and  $a$  on the stability boundaries. In order to obtain the boundaries for higher order stability regions, one needs to work with a better approximation to the infinite matrix  $\mathbf{B}$ , i.e., a matrix of larger size.

The generalization of this approach to the multi-variable case is straightforward, and involves replacing various scalars by vectors/matrices. See [22] for a more detailed discussion. One still gets a determinant equation relating  $a$ ,  $q$  and  $\nu$ , but in this case, not all the stability boundaries can be obtained in a straightforward manner. Setting  $e^{i\nu\pi}$  to  $\pm 1$  gives the stability boundaries for the so-called “natural resonances”, but there is another set of boundaries, those related to “combined resonances”, which cannot be obtained by this method. In [22], a pragmatic but unrigorous approach is proposed to obtain these secondary boundaries, but we do not follow this procedure here.

See Figure A.12 for the stability regions and the boundaries due to the “natural resonances” obtained by the infinite determinant method, superposed with the stability regions obtained by the Floquet analysis (ODE numerics). We show plots for 4 different values of  $\theta$ , and  $\alpha = 1/2$ . While the infinite determinant method as we use it does not give all the boundaries, the ones it does give are accurate. We will give more comprehensive stability plots based on the Floquet method, in the later sections.

## A.6 Method of multiple scales

For a given set of parameters, the Floquet analysis of Section (A.4) gives the stability regions of the coupled Mathieu system numerically. While such results are useful, for asymmetric



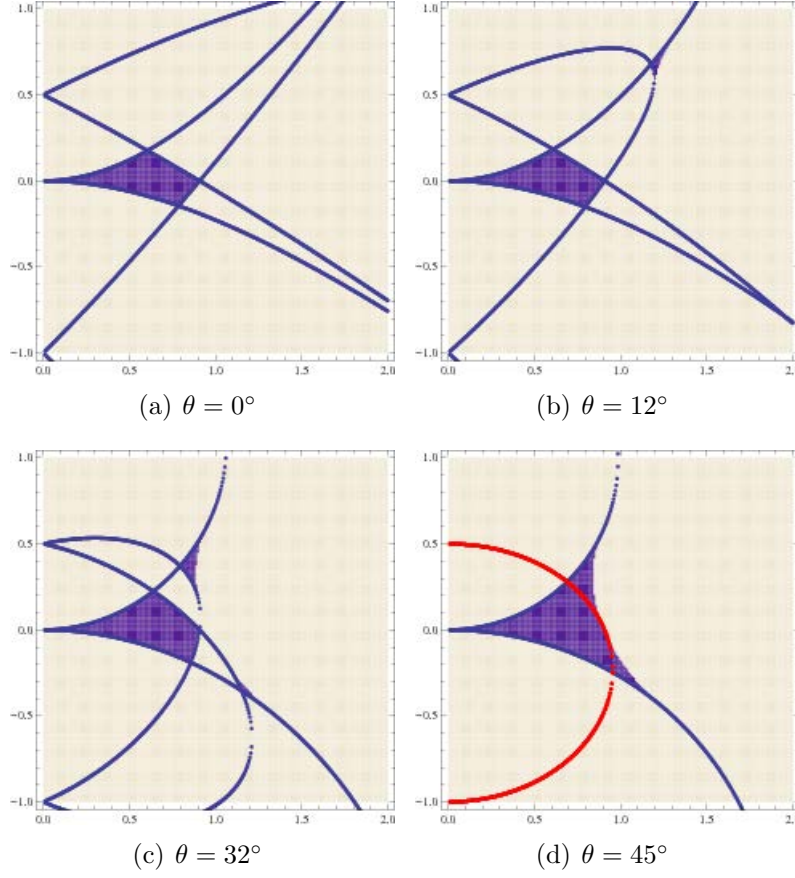


Figure A.12: The stability regions and the stability boundaries obtained by the methods of Section A.5, for  $\alpha = 1/2$ . The stability regions (dark solid regions) were obtained by evaluating the growth factor for given  $q$  ( $x$ -axis) and  $a$  ( $y$ -axis). The boundaries (dark curves in the first three plots, red curves in the last) were obtained by setting the growth factor to  $\pm 1$ , and solving for  $a$  and  $q$ . These are the boundaries pertaining to “natural resonances” which have analogues in the decoupled case. As can be seen, this approach gives the boundaries of the primary stability region in the first three plots, but not all the boundaries of the secondary stability regions, some of which are determined by “combined resonances”. In the last, exceptional plot corresponding to  $\theta = 45^\circ$ , the secondary stability regions are joined with the primary stability region, and the boundaries we obtain coincide with the curves where these regions join.

trap design and characterization, it would be beneficial to have at least approximate analytical formulae for the stability boundaries. Such approximate formulae would enable one to quickly check the stability regions for a particular trap geometry, and guide the trap design.

Multi-scale perturbation theory, or the method of multiple scales, is a useful technique capable of generating such approximate results. Straightforward perturbation theory for an ordinary differential equation involves treating certain parameters in the equation as small, and expanding the unknown solution into a power series in terms of these parameters. One obtains separate equations for each power of the perturbation parameter, and solves the system order by order. While useful in many settings, this approach fails for a variety of equations due to the appearance of so-called “secular terms”, which grow in time in an unbounded manner, invalidating the assumptions in the perturbation analysis after a certain time period.

Multi-scale perturbation theory avoids this problem by expanding not only the solution, but also the independent parameter (time) to a series in the small parameter. This results in a set of *partial* differential equations whose solutions are then restricted by imposing the condition that secular terms do not appear. The absence of secular terms allows the method of multiple scales to give uniformly accurate results for cases where standard perturbation theory gives results valid only for short time intervals.

There is a lot of freedom in the way the equations of multiple scale perturbation theory are set up, and there does not seem to be a standard convention. Below, we will base our approach on the examples given in [23] and [24]. For an elementary introduction to multiple scale perturbation theory, see [25, 23]. For applications to the coupled Mathieu system, see [24]. Note that the analysis in [24] is not immediately applicable to our case, since some of the natural frequencies for the Paul trap are imaginary.

Let us first demonstrate the use of multi-scale perturbation theory for the relatively simple example of single-variable Mathieu equation. We will then work out the multi-scale perturbation analysis of the coupled Mathieu system resulting from asymmetric ion traps.

### A.6.1 Single-variable Mathieu equation

We would like to have approximate formulas for the stability boundaries of the Mathieu equation,

$$\ddot{x} + (a + 2q \cos 2\tau)x = 0. \quad (\text{A.38})$$

This equation has multiple regions of stability separated by regions of instability, but we will focus on the “primary” stability region near the origin of the  $a$ - $q$  space. We will treat  $q$  as a small variable, and perform an expansion in its powers.

As mentioned above, we begin by introducing a set of slowly-varying time variables (the “multiple scales”),

$$T_0 = t, \quad T_1 = qt, \quad T_2 = q^2t, \quad (\text{A.39})$$

etc. We replace the dependent variable  $x$  with a function of the  $T_i$ s,

$$x(t) = x(T_0, T_1, \dots), \quad (\text{A.40})$$

where we made a slight abuse of notation by calling the multivariable version of  $x$  by the same name as the single variable version. Using the chain rule, we get,

$$\frac{d}{dt} = \frac{\partial}{\partial T_0} + q \frac{\partial}{\partial T_1} + q^2 \frac{\partial}{\partial T_2} + \dots$$

Working out the resulting perturbation theory in  $q$ , one gets approximate solutions to (A.10) valid for small values of  $q$ , unless  $a$  is close to certain critical values. These critical values are where the stability boundaries intersect the  $q = 0$  axis. Various approaches exist for dealing with these critical points. We will follow the approach used in [23], where one expands  $a$  into a series as well, around the critical point  $a_0$ ,

$$a = a_0 + a_1 q + a_2 q^2 + \dots \quad (\text{A.41})$$

In order to obtain the stability boundaries, one obtains conditions on  $a_1$ ,  $a_2$ , etc., that ensure that the solutions are bounded. It is noted in [24] that in order to get results that are accurate to order  $q^2$ , it suffices to work with  $T_0$  and  $T_1$ . Accordingly, we will ignore  $T_2$  and higher order terms.

Using the notation  $D_i = \frac{\partial}{\partial T_i}$  and expanding

$$x(T_0, T_1) = x_0(T_0, T_1) + q x_1(T_0, T_1) + q^2 x_2(T_0, T_1) + \dots, \quad (\text{A.42})$$

we have, up to second order in  $q$ ,

$$\frac{dx}{dt} = D_0 x_0 + q(D_1 x_0 + D_0 x_1) + q^2(D_1 x_1 + D_0 x_2) \quad (\text{A.43})$$

$$\frac{d^2 x}{dt^2} = D_0^2 x_0 + q(D_0^2 x_1 + 2D_0 D_1 x_0) + q^2(D_1^2 x_0 + 2D_0 D_1 x_1 + D_0^2 x_2). \quad (\text{A.44})$$

Substituting (A.43) and (A.41) (where  $a_0$  is arbitrary for now) in (A.10), we get,

$$\begin{aligned} & D_0^2 x_0 + q(2D_0 D_1 x_0 + D_0^2 x_1) + q^2(D_1^2 x_0 + 2D_0 D_1 x_1 + D_0^2 x_2) \\ & + (a_0 + q a_1 + q^2 a_2)(x_0 + q x_1 + q^2 x_2) + 2q(x_0 + q x_1 + q^2 x_2) \cos 2\tau = 0. \end{aligned}$$

Collecting terms with similar powers of  $q$  and setting them to zero separately, we get the following partial differential equations.

$$D_0^2 x_0 + a_0 x_0 = 0 \quad (\text{A.45})$$

$$D_0^2 x_1 + a_0 x_1 = -2D_0 D_1 x_0 - a_1 x_0 - 2x_0 \cos 2\tau \quad (\text{A.46})$$

$$D_0^2 x_2 + a_0 x_2 = -2D_0 D_1 x_1 - D_1^2 x_0 - a_1 x_1 - a_2 x_0 - 2x_1 \cos 2\tau \quad (\text{A.47})$$

If  $a$  is away from a set of critical values one can ignore  $a_1$  and  $a_2$ , set  $a = a_0$ , and solve the equations (A.45-A.46) to obtain an approximate solution to (A.45)-(A.47). Such a solution can also help determine, a posteriori, the regime of its validity due to the appearance of “small denominators” near certain critical values of  $a_0$ . See, e.g., [23, 24] for such a discussion. We will skip this step, and note that  $a_0 = 0$  and  $a_0 = 1$  are two critical values that help determine the first stability region.

### A.6.1.1 Expansion around $a = 0$

Setting  $a_0 = 0$ , we get,

$$D_0^2 x_0 = 0 \quad (\text{A.48})$$

$$D_0^2 x_1 = -2D_0 D_1 x_0 - 2x_0 \cos 2T_0 - a_1 x_0 \quad (\text{A.49})$$

$$D_0^2 x_2 = -2D_0 D_1 x_1 - D_1^2 x_0 - 2x_1 \cos 2T_0 - a_2 x_0 - a_1 x_1. \quad (\text{A.50})$$

The general solution to (A.48) is,

$$x_0(T_0, T_1) = A(T_1) + T_0 B(T_1), \quad (\text{A.51})$$

where  $A$  and  $B$  are arbitrary functions. In order to suppress the secular term that grows in time, we set  $B = 0$ . This gives,

$$x_0(T_0, T_1) = A(T_1). \quad (\text{A.52})$$

Substituting (A.52) into (A.49), we get,

$$D_0^2 x_1 = A_0(T_1)(-2 \cos 2T_0 - a_1). \quad (\text{A.53})$$

In order to suppress the secular term in  $x_1$ , we must have  $a_1 = 0$ . Solving (A.53) with this assumption and dropping the secular term analogous to  $B$  in (A.51), we get,

$$x_1(T_0, T_1) = C(T_1) + \frac{1}{2} A(T_1) \cos 2T_0. \quad (\text{A.54})$$

Substituting (A.52) and (A.54) in (A.50) and using  $a_1 = 0$ , we get,

$$\begin{aligned} D_0^2 x_2 = & 2A'(T_1) \sin 2T_0 - A''(T_1) - a_2 A(T_1) - 2C(T_1) \cos 2T_0 \\ & - \frac{A(T_1)}{2} - \frac{A(T_1)}{2} \cos 4T_0. \end{aligned}$$

In order to avoid terms in  $x_2$  that grow linearly in  $T_0$ , we must have,

$$A''(T_1) + (a_2 + \frac{1}{2})A(T_1) = 0.$$

This equation will have non-growing solutions for  $A(T_1)$  only if,

$$a_2 \geq -\frac{1}{2}.$$

Thus, the stability boundary is given by,

$$a = -\frac{1}{2}q^2,$$

with  $a > -q^2/2$  being the stable region.

### A.6.1.2 Expansion around $a = 1$

Setting  $a_0 = 1$  in (A.45)-(A.47), we get,

$$D_0^2 x_0 + x_0 = 0 \quad (\text{A.55})$$

$$D_0^2 x_1 + x_1 = -2D_0 D_1 x_0 - a_1 x_0 - 2x_0 \cos 2T_0 \quad (\text{A.56})$$

$$D_0^2 x_2 + x_2 = -2D_0 D_1 x_1 - D_1^2 x_0 - a_1 x_1 - a_2 x_0 - 2x_1 \cos 2T_0 \quad (\text{A.57})$$

General solution to (A.55) is,

$$x_0(T_0, T_1) = A(T_1) \cos T_0 + B(T_1) \sin T_0. \quad (\text{A.58})$$

Plugging this in (A.56), we get,

$$\begin{aligned} D_0^2 x_1 + x_1 = & 2A' \sin T_0 - 2B' \cos T_0 - a_1 A \cos T_0 - a_1 B \sin T_0 \\ & - A(\cos T_0 + \cos 3T_0) + B(\sin T_0 - \sin 3T_0). \end{aligned} \quad (\text{A.59})$$

The solutions to this equation will have growing parts unless the coefficients of the resonance terms  $\sin T_0$  and  $\cos T_0$  on the right hand side vanish. This gives,

$$2A' + (1 - a_1)B = 0 \quad (\text{A.60})$$

$$2B' + (1 + a_1)A = 0. \quad (\text{A.61})$$

This system will have exponential solutions if  $a_1^2 < 1$ , and oscillatory ones if  $a_1^2 > 1$ . Thus, the formula  $a(q)$  for the stability boundary will have  $\pm 1$  as the coefficient of the term linear in  $q$ . Assuming  $a_1^2 > 1$ , the general solution is given as,

$$A(T_1) = c \sin \lambda t + d \cos \lambda t \quad (\text{A.62})$$

$$B(T_1) = \frac{2\lambda}{a_1 - 1} (-d \sin \lambda t + c \cos \lambda t), \quad (\text{A.63})$$

where  $\lambda = \sqrt{\frac{a_1^2 - 1}{4}}$  and  $c$  and  $d$  are constants. Dropping the resonance terms, (A.59) reduces to,

$$D_0^2 x_1 + x_1 = -(A_0 \cos 3T_0 + B_0 \sin 3T_0), \quad (\text{A.64})$$

whose general solution is,

$$x_1(T_0, T_1) = C(T_1) \cos T_0 + D(T_1) \sin T_0 + \frac{A(T_1)}{8} \cos 3T_0 + \frac{B(T_1)}{8} \sin 3T_0. \quad (\text{A.65})$$

Plugging (A.65) in (A.57), the right hand side of (A.57) ends up having various terms proportional to  $\sin T_0$  and  $\cos T_0$ . Once again, these “resonant” terms will result in solutions for  $x_2$  that grow in time, so for bounded solutions, we set these terms to zero. This gives,

$$2C' + (1 - a_1)D = B'' + B(a_2 + \frac{1}{8}) \quad (\text{A.66})$$

$$2D' + (1 + a_1)C = -A'' - A(a_2 + \frac{1}{8}). \quad (\text{A.67})$$

Recalling  $A'' = -\lambda^2 A$  and  $B'' = -\lambda^2 B$  from above, we get,

$$2C' + (1 - a_1)D = B\left(\frac{1 - a_1^2}{4} + a_2 + \frac{1}{8}\right) \quad (\text{A.68})$$

$$2D' + (1 + a_1)C = A\left(\frac{a_1^2 - 1}{4} - a_2 - \frac{1}{8}\right). \quad (\text{A.69})$$

Combining these equations, using the explicit solution above for  $A$  and  $B$ , and requiring the absence of resonant terms, we get,

$$a_2 = -\frac{1}{8} + \frac{a_1^2 - 1}{4}, \quad (\text{A.70})$$

Finally, we get the formula for the stability boundary as,

$$a = a_0 + a_1 q + a_2 q^2 \quad (\text{A.71})$$

$$a = 1 \pm q - \frac{1}{8} q^2. \quad (\text{A.72})$$

### A.6.2 Two-variable, coupled Mathieu's equations

As discussed in section A.4, the principal axes of the RF and DC fields are not necessarily aligned, but ignoring the motion along the trap axis  $z$ , the transverse equations of motion can be brought into the form,

$$\ddot{x} + ax + q(cx + dy) \cos 2t = 0 \quad (\text{A.73})$$

$$\ddot{y} - \alpha ay + q(dx - cy) \cos 2t = 0, \quad (\text{A.74})$$

after a suitable rotation of the coordinate axes. The constants  $c$  and  $d$  are given in terms of the relative angle  $\theta$  between the RF and DC axes as,  $c = \cos 2\theta$  and  $d = \sin 2\theta$ .

As in the single variable case, we begin the multi-scale analysis by promoting  $x$  and  $y$  to functions of two variables,  $T_0 = t$  and  $T_1 = qt$ , and expanding them to series in  $q$ ,

$$x = x_0(T_0, T_1) + qx_1(T_0, T_1) + q^2 x_2(T_0, T_1) + \dots \quad (\text{A.75})$$

$$y = y_0(T_0, T_1) + qy_1(T_0, T_1) + q^2 y_2(T_0, T_1) + \dots \quad (\text{A.76})$$

If  $a$  is near a critical value  $a_0$  where this straightforward expansion fails to work, we expand  $a$  as well,

$$a = a_0 + a_1 q + a_2 q^2 + \dots \quad (\text{A.77})$$

Working to second order in  $q$ , and collecting terms with similar powers of  $q$ , we get,

$$D_0^2 x_0 + a_0 x_0 = 0 \quad (\text{A.78})$$

$$D_0^2 x_1 + a_0 x_1 = -2D_0 D_1 x_0 - a_1 x_0 - (cx_0 + dy_0) \cos 2 \quad (\text{A.79})$$

$$\begin{aligned} D_0^2 x_2 + a_0 x_2 = & -2D_0 D_1 x_1 - D_1^2 x_0 - a_1 x_1 \\ & - a_2 x_0 - (cx_1 + dy_1) \cos 2T_0 \end{aligned} \quad (\text{A.80})$$

for the  $x$  equation of motion (A.73), and,

$$D_0^2 y_0 - \alpha a_0 y_0 = 0 \quad (\text{A.81})$$

$$D_0^2 y_1 - \alpha a_0 y_1 = -2D_0 D_1 y_0 + \alpha a_1 y_0 - (dx_0 - cy_0) \cos 2T_0 \quad (\text{A.82})$$

$$D_0^2 y_2 - \alpha a_0 y_2 = -2D_0 D_1 y_1 - D_1^2 y_0 + \alpha a_1 y_1 + \alpha a_2 y_0 - (dx_0 - cy_0) \cos 2T_0 \quad (\text{A.83})$$

for the  $y$  equation of motion (A.74). If  $a_0 \neq 0$  and  $\alpha > 0$  as we assumed in Section A.4, one of the zeroth order equations (A.78) and (A.81) has oscillatory solutions, the other exponential ones. This means that the system is unstable, even to zeroth order. However, as we have seen in the Floquet analysis above, there may still exist some special solutions that are bounded in time, and these solutions can be realized by fine-tuning the initial conditions. In practice, the unstable solutions will be excited due to fluctuations, and this partial stability may seem only of academic interest. As in our discussion of the single variable Mathieu equation, we will skip the justification of the critical values of  $a_0$ , and refer to [24] for a justification of the critical values  $a_0 = 0$  and  $a_0 = 1$ . Despite the fact that all solutions around  $q = 0$ ,  $a_0 = 1$  are at least partially unstable, our numerical analysis based on the Floquet theorem shows that the curves separating partial stability from full instability near  $q = 0$  and  $a = 1$  become curves separating full stability from full instability, when extended to intersect the stability curves emanating from  $a = 0$ . Using this observation (to be justified when we present the numerical solutions below), we will derive the curves around  $a_0 = 1$  that bound regions of partial stability to obtain approximate formulas for the boundary of the primary stability region.

#### A.6.2.1 Expansion around $a = 0$

Setting  $a_0 = 0$  in (A.78-A.83), we get,

$$D_0^2 x_0 = 0 \quad (\text{A.84})$$

$$D_0^2 x_1 = -2D_0 D_1 x_0 - a_1 x_0 - cx_0 \cos 2T_0 - dy_0 \cos 2T_0 \quad (\text{A.85})$$

$$D_0^2 x_2 = -2D_0 D_1 x_1 - D_1^2 x_0 - a_1 x_1 - a_2 x_0 - cx_1 \cos 2T_0 \quad (\text{A.86})$$

$$- dy_1 \cos 2T_0. \quad (\text{A.87})$$

Similarly, for  $y(t, T_1)$  we have following set of equations.

$$D_0^2 y_0 = 0 \quad (\text{A.88})$$

$$D_0^2 y_1 = -2D_0 D_1 y_0 + \alpha a_1 y_0 + cy_0 \cos 2T_0 - dx_0 \cos 2T_0 \quad (\text{A.89})$$

$$D_0^2 y_2 = -2D_0 D_1 y_1 - D_1^2 y_0 + \alpha a_1 y_1 + \alpha a_2 y_0 + cy_1 \cos 2T_0 \quad (\text{A.90})$$

$$- dx_1 \cos 2T_0 \quad (\text{A.91})$$

Solving (A.84) and (A.88) and setting the secular terms to zero, we get,

$$\begin{aligned} x_0(T_0, T_1) &= A(T_1) \\ y_0(T_0, T_1) &= C(T_1). \end{aligned}$$

Using these in (A.85) and (A.89), we get,

$$D_0^2 x_1 = -a_1 A(T_1) - (cA(T_1) - dC(T_1)) \cos 2T_0 \quad (\text{A.92})$$

$$D_0^2 y_1 = \alpha a_1 C(T_1) + (cC(T_1) - dA(T_1)) \cos 2T_0. \quad (\text{A.93})$$

In order to avoid secular terms, we pick  $a_1 = 0$ . This gives the general non-secular solution as,

$$x_1(T_0, T_1) = B(T_1) + \frac{1}{4}(cA + dC) \cos 2T_0 \quad (\text{A.94})$$

$$y_1(T_0, T_1) = D(T_1) + \frac{1}{4}(dA - cC) \cos 2T_0. \quad (\text{A.95})$$

Plugging the solutions for  $x_0, x_1, y_0, y_1$  in (A.87) and (A.91), we get equations for  $x_2$  and  $y_2$ . These will have bounded solutions only if the  $T_0$ -independent terms on the right hand side add up to zero. This gives,

$$A'' + \left(a_2 + \frac{1}{8}(c^2 + d^2)\right) A = 0 \quad (\text{A.96})$$

$$C''' + \left(-\alpha a_2 + \frac{1}{8}(c^2 + d^2)\right) C = 0. \quad (\text{A.97})$$

Equations (A.96) and (A.97) will have oscillatory solutions when  $a_2 > -\frac{1}{8}(c^2 + d^2)$  and when  $a_2 < \frac{1}{8\alpha}(c^2 + d^2)$ , respectively. Hence, assuming  $\alpha > 0$ , simultaneous stability occurs for  $-\frac{1}{8}(c^2 + d^2) < a_2 < \frac{1}{8\alpha}(c^2 + d^2)$ . In other words, the stability boundaries around  $a = 0$  are given by,  $a = -\frac{1}{8}(c^2 + d^2)$  and  $a = \frac{1}{8\alpha}(c^2 + d^2)$ .

#### A.6.2.2 Expansion around $a = 1$

For  $a_0 = 1$ , (A.78-A.80) become,

$$D_0^2 x_0 + x_0 = 0 \quad (\text{A.98})$$

$$D_0^2 x_1 + x_1 = -2D_0 D_1 x_0 - a_1 x_0 - (cx_0 + dy_0) \cos 2T_0 \quad (\text{A.99})$$

$$D_0^2 x_2 + x_2 = -2D_0 D_1 x_1 - D_1^2 x_0 - a_1 x_1 - a_2 x_0 \quad (\text{A.100})$$

$$- (cx_1 + dy_1) \cos 2T_0, \quad (\text{A.101})$$

and, (A.81-A.83) become,

$$D_0^2 y_0 - \alpha a_0 y_0 = 0 \quad (\text{A.102})$$

$$D_0^2 y_1 - \alpha a_0 y_1 = -2D_0 D_1 y_0 + \alpha a_1 y_0 - (dx_0 - cy_0) \cos 2T_0 \quad (\text{A.103})$$

$$D_0^2 y_2 - \alpha a_0 y_2 = -2D_0 D_1 y_1 - D_1^2 y_0 + \alpha a_2 y_0 \quad (\text{A.104})$$

$$+ \alpha a_1 y_1 - (dx_0 - cy_0) \cos 2T_0. \quad (\text{A.105})$$

The general solution to (A.98) is,

$$x_0(T_0, T_1) = A(T_1) \cos T_0 + B(T_1) \sin T_0 \quad (\text{A.106})$$



Assuming  $\alpha > 0$ , the solution to (A.102) is exponential,

$$y_0(T_0, T_1) = E(T_1) \exp(\sqrt{\alpha}T_0) + F(T_1) \exp(-\sqrt{\alpha}T_0) \quad (\text{A.107})$$

This shows that the general solution to the coupled system is unstable for  $\alpha > 0$ ,  $a_0 = 1$ . However, as mentioned above, it is still possible to look for stable solutions, and obtain the boundaries of partial stability. This boundary will become a boundary of full stability when it intersects with the stability boundary emanating from  $a = 0$ ,  $q = 0$ .

In order to proceed, we set the coefficients of the exponential solutions to zero,  $E(T_1) = 0 = F(T_1)$ , which gives  $y_0(T_0, T_1) = 0$ . Using the solutions for  $x_0$  and  $y_0$  in (A.99) and setting the coefficients of  $\sin T_0$  and  $\cos T_0$  on the right hand side to zero in order to avoid secular terms, we get,

$$2A' - (a_1 - \frac{c}{2})B = 0 \quad (\text{A.108})$$

$$2B' + (a_1 + \frac{c}{2})A = 0. \quad (\text{A.109})$$

The solution to this system will be oscillatory if  $a_1^2 > \frac{c^2}{4}$  and exponential if  $a_1^2 < \frac{c^2}{4}$ . Thus, the boundary of partial stability is given by,

$$a_1 = \pm \frac{c}{2}. \quad (\text{A.110})$$

The oscillating solutions for  $A$  and  $B$  are given as,

$$A(T_1) = r \sin \lambda t + s \cos \lambda t \quad (\text{A.111})$$

$$B(T_1) = \frac{2\lambda}{a_1 - c/2}(-s \sin \lambda t + r \cos \lambda t), \quad (\text{A.112})$$

where  $\lambda = \sqrt{\frac{a_1^2 - c^2/4}{4}}$ , and  $r$  and  $s$  are constants. With these, the non-secular solution to (A.99) is,

$$\begin{aligned} x_1(T_0, T_1) = & C(T_1) \cos T_0 + D(T_1) \sin T_0 \\ & + \frac{c}{16} A(T_1) \cos 3T_0 + \frac{c}{16} B(T_1) \sin 3T_0. \end{aligned} \quad (\text{A.113})$$

Similarly, the solution for  $y_1$  becomes, after setting the coefficients of the exponential terms to zero,

$$\begin{aligned} y_1(T_0, T_1) = & \frac{d}{2(\alpha + 1)}(-B(T_1) \sin T_0 + A(T_1) \cos T_0) \\ & + \frac{d}{2(\alpha + 9)}(B(T_1) \sin 3T_0 + A(T_1) \cos 3T_0) \end{aligned} \quad (\text{A.114})$$

We substitute (A.113) and (A.114) into (A.100) and collect the resonance terms, i.e., terms proportional to  $\sin T_0$  and  $\cos T_0$ , on the right hand side. Setting the coefficients of these resonances to zero in order to avoid growing solutions for  $x_2$ , we get,

$$2C'(T_1) + D(T_1) \left(-a_1 + \frac{c}{2}\right) = B'' + \beta B \quad (\text{A.115})$$

$$2D'(T_1) + C(T_1) \left(a_1 + \frac{c}{2}\right) = -A''(T_1) - \beta A \quad (\text{A.116})$$

where  $\beta = \left(a_2 + \frac{c}{32} + \frac{d^2(5+\alpha)}{2(9+\alpha)(1+\alpha)}\right)$ . Using equations (A.108) and (A.109), we get  $A'' = -\frac{a_1^2 - c^2/4}{4}A$  and  $B'' = -\frac{a_1^2 - c^2/4}{4}B$ . This gives,

$$2C'(T_1) + D(T_1) \left(-a_1 + \frac{c}{2}\right) = \mu B \quad (\text{A.117})$$

$$2D'(T_1) + C(T_1) \left(a_1 + \frac{c}{2}\right) = -\mu A, \quad (\text{A.118})$$

where  $\mu = -\frac{a_1^2 - c^2/4}{4} + a_2 + c/32 + \frac{d^2(5+\alpha)}{2(9+\alpha)(1+\alpha)}$ . Combining (A.117) and (A.118) with (A.108) and (A.109), we get the decoupled equations,

$$C'' + \frac{a_1^2 - c^2/4}{4}C = -\frac{\mu a_1}{2}A \quad (\text{A.119})$$

$$D'' + \frac{a_1^2 - c^2/4}{4}D = -\frac{\mu a_1}{2}A. \quad (\text{A.120})$$

Now, since the solution (A.111) is in resonance with the left hand sides of these equations, the right hand side must vanish in order to avoid growing solutions. This gives, when  $a_1 \neq 0$ ,

$$\mu = -\frac{a_1^2 - c^2/4}{4} + a_2 + c/32 + \frac{d^2(5+\alpha)}{2(9+\alpha)(1+\alpha)} = 0. \quad (\text{A.121})$$

On the stability boundary (A.110), this gives,  $a_2 = -\frac{c^2}{32} - \frac{d^2(5+\alpha)}{2(1+\alpha)(9+\alpha)}$ . Thus, the stability boundaries starting at  $a = 1$  are given as,

$$a = 1 \pm \left(\frac{c}{2}\right)q - \left(\frac{c^2}{32} + \frac{d^2(5+\alpha)}{2(1+\alpha)(9+\alpha)}\right)q^2. \quad (\text{A.122})$$

## A.7 Results and discussion

In Figures A.13 – A.18, we present the results of the stability analysis via the numerical Floquet method, and compare these results to the stability boundaries obtained from the multi-scale perturbation analysis. We show plots for a range of angles  $\theta$  between the RF and DC axes, and a range of  $\alpha$ s. We do not show the region  $a < 0$ , since  $a < 0$  would correspond to an anti-confining DC field in the axial ( $z$ ) direction, and since there is no RF field in the  $z$  direction, this would result in instability. A few important points are evident from the plots.

- The primary stability region *does not get smaller* when a nonzero angle  $\theta$  is introduced between the RF and DC axes.
- Although the primary stability region does not change appreciably when  $\theta$  is varied, a secondary stability region is highly variable, and joins the primary region to make the latter exceptionally large for the special value of  $\theta = 45^\circ$ .
- The approximate stability boundaries of the primary stability region obtained from multi-scale perturbation theory are more or less accurate, except for the exceptional angle  $\theta = 45^\circ$ .

- The approximate boundaries *underestimate* the stability region obtained from the Floquet analysis. Thus, trusting the approximate boundaries does not lead one to assume that a point in the  $q$ - $a$  space is stable, where in fact it is unstable.

In short, we see that if the primary stability region is the regime of interest, there is no significant change in the stability properties of the system due to a relative angle between the RF and DC axes, unless the angle is close to  $45^\circ$ , in which case the stability region is enhanced. If one would like to work in the secondary stability region, however, one has to take into account the effects of the coupling quite precisely, as the shape and the location of the secondary region is quite sensitively dependent on the relative angle.

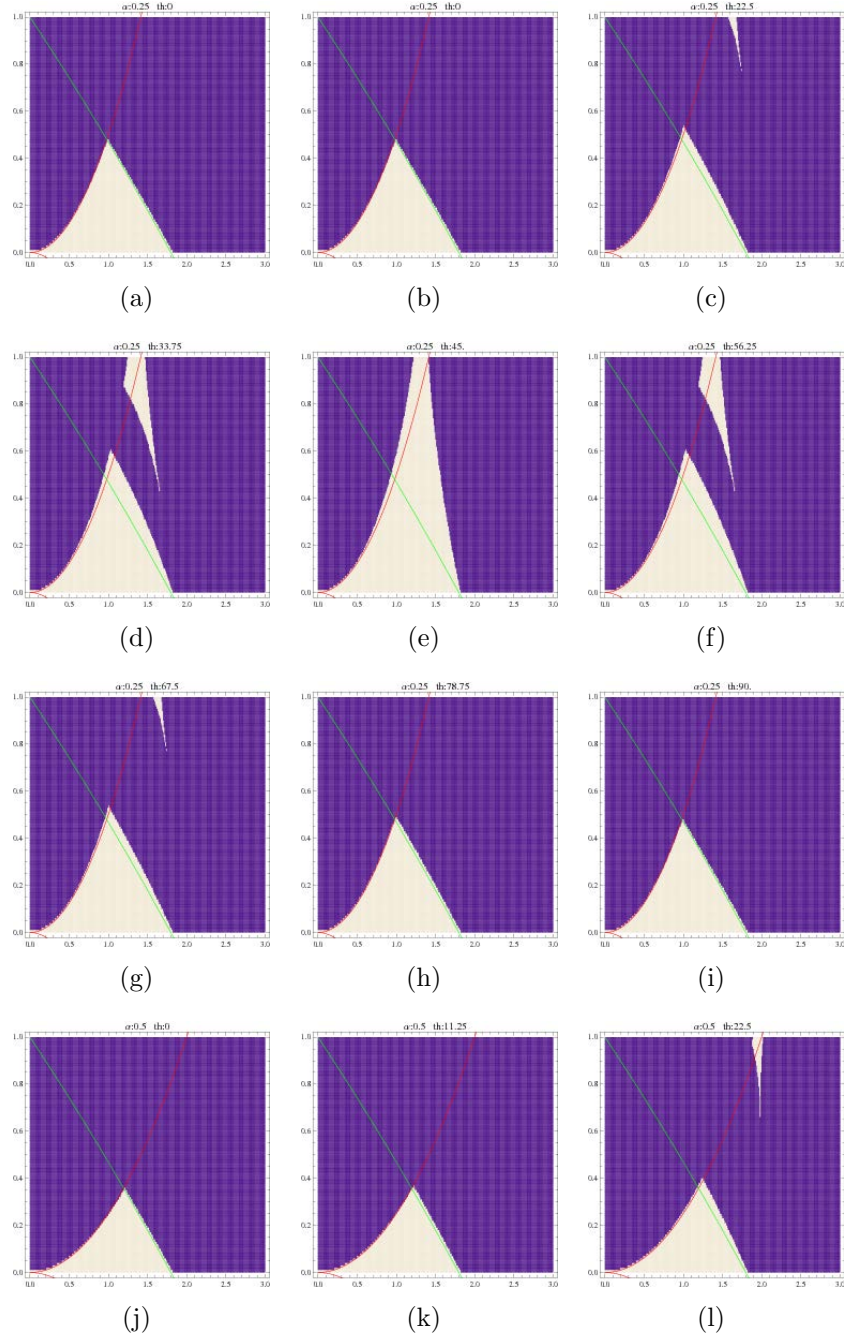


Figure A.13: Stability diagrams for the two-dimensional coupled Mathieu system, superposed with approximate stability boundaries obtained from the multi-scale perturbation analysis. Each plot is an  $a$  vs.  $q$  plot showing the stability region (white) and the instability region (purple/dark) for a specific  $\alpha$  and  $\theta$ . The case  $\theta = 0$  corresponds to a decoupled pair of two one-dimensional Mathieu equations. Plots continue on the following pages.

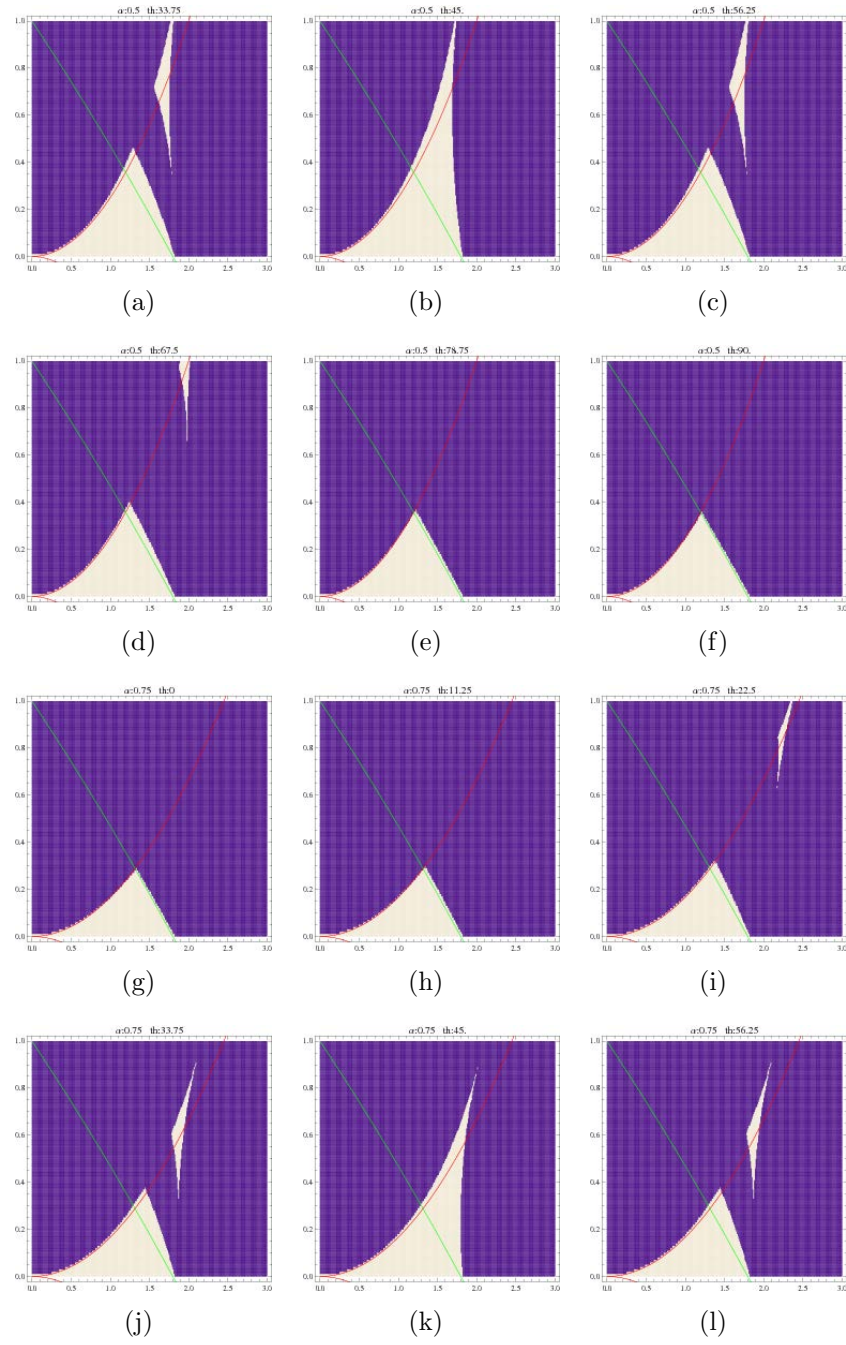


Figure A.14: Stability diagrams for the two-dimensional coupled Mathieu system.

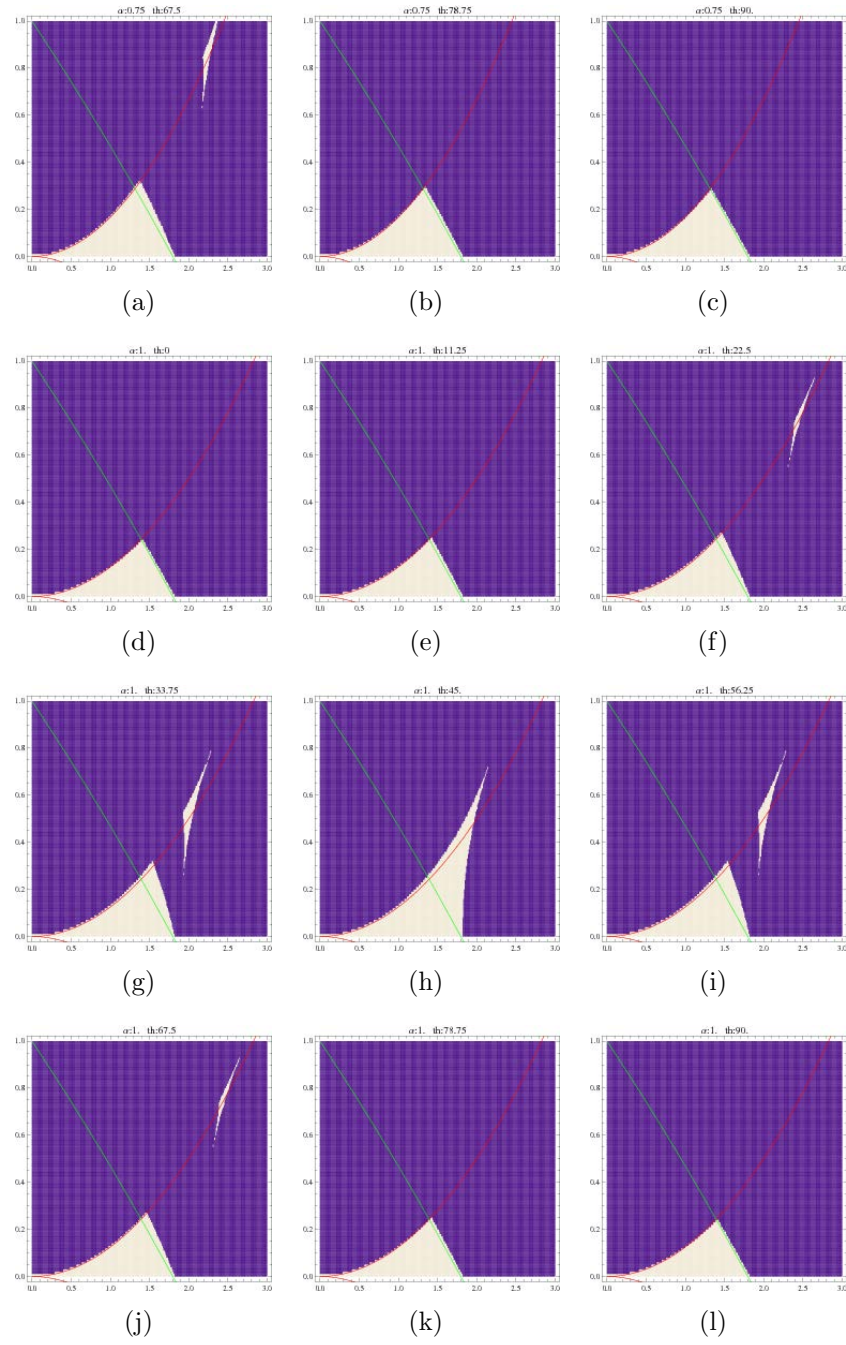


Figure A.15: Stability diagrams for the two-dimensional coupled Mathieu system.

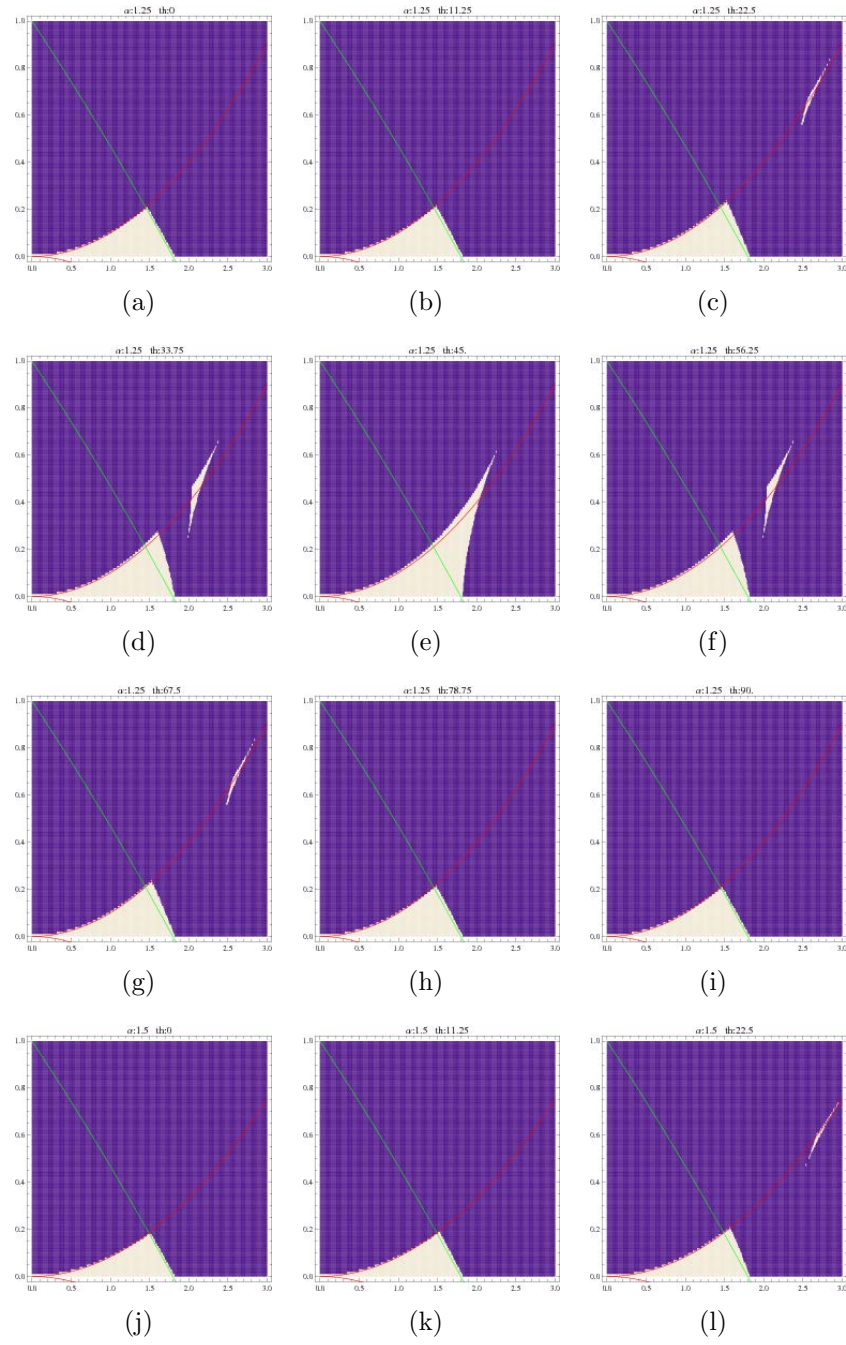


Figure A.16: Stability diagrams for the two-dimensional coupled Mathieu system.

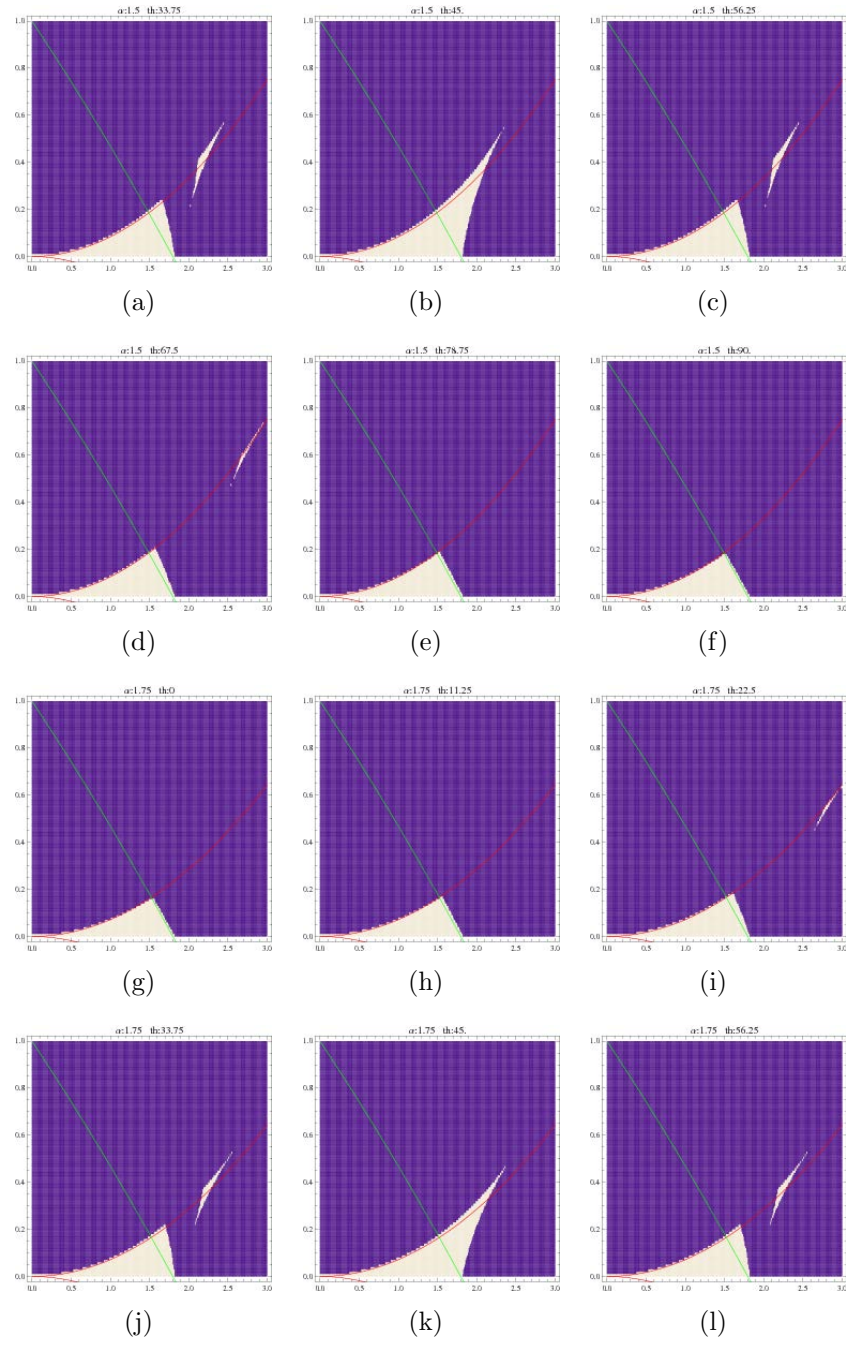


Figure A.17: Stability diagrams for the two-dimensional coupled Mathieu system.



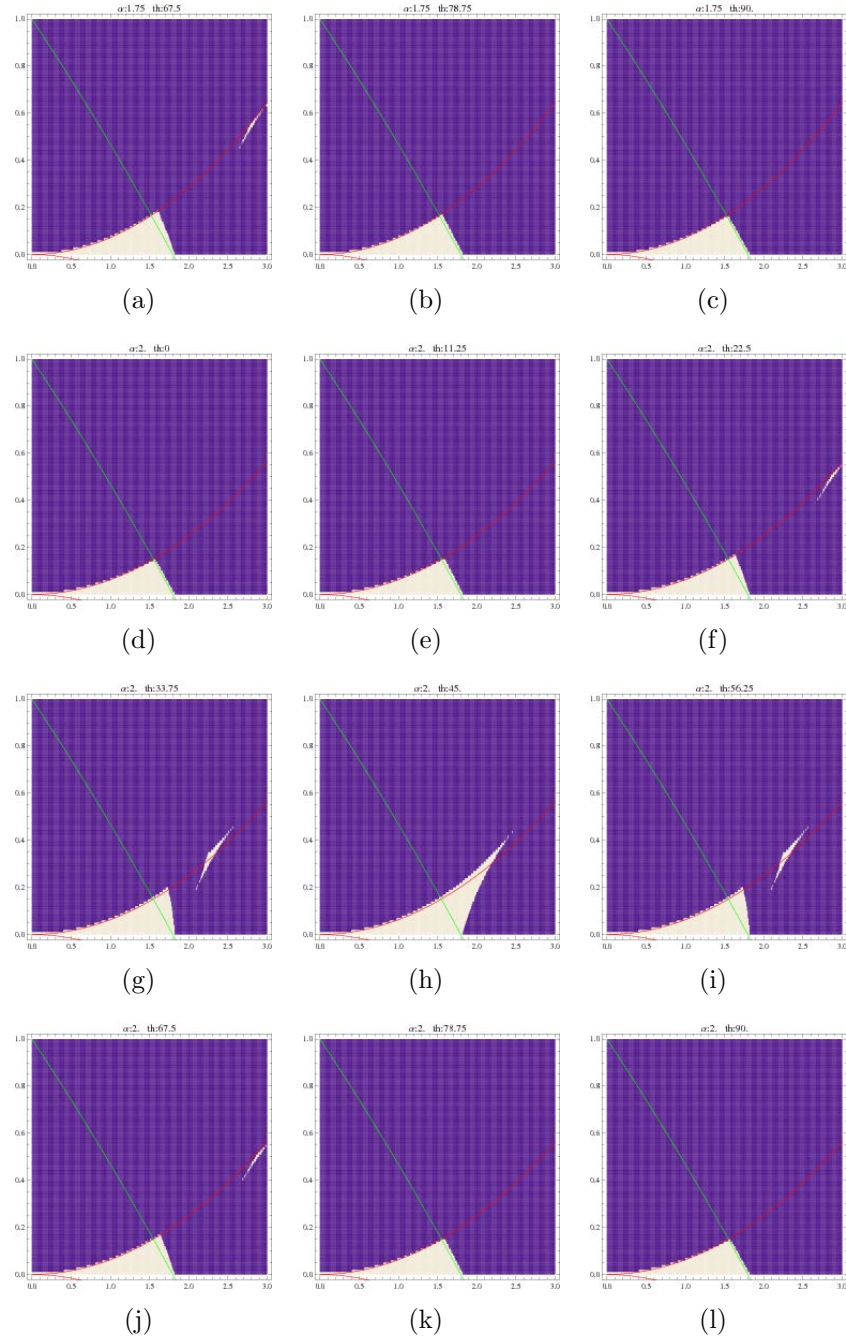


Figure A.18: Stability diagrams for the two-dimensional coupled Mathieu system.

# Appendix B

## Initial goals and results

The initial goals for the first two years of the SMIT II program are listed in Table B.1 for the ion traps and in Table B.2 for the integrated optics. The goals that were not addressed or were only partially achieved are highlighted in orange. The numerical values achieved during SMIT II are in blue. Our effort concentrated on designing, fabricating, and testing reliable, reproducible surface traps. These objectives were largely achieved. In this Appendix the goals and results are described in detail in the order listed in Tables B.1 and B.2.

### B.1 Ion traps

The ion trap packaging goals were largely achieved. The AuSn solder joints for attaching the chip and carrier to the vacuum chamber mounts were typically reliable and reproducible. Auto wirebonding solved many of the initial problems encountered in wiring the chip pads to the carrier pins. Careful crimping of the wires to the carrier and the vacuum feed-throughs was required in order to obtain reliable electrical connections. It was important to carefully ground any floating wires or cable/connector shields.

The vacuum pressures after baking the trap chamber were in the low  $10^{-10}$  torr range during the first year. After adding a Ti sublimation pump the pressures were typically in the low  $10^{-11}$  torr range. After mounting all of the apparatus in the vacuum chamber, the bake out times and cooling times for cryogenic operation are approximately one week at room temperature and one day for cryogenic testing.

Fabricating traps with tungsten and gold surface electrode overlayers is possible at NRC; however, there was not sufficient time to pursue these very important and interesting metal surface studies during SMIT II. Voltage breakdowns and electrode shorts that plagued SMIT I traps have largely been eliminated during the SMIT II program. The wire bonding techniques developed during SMIT II along with the SMIT II fabrication processes have eliminated control electrode shorting problems to the ground layers. There has been no shorting among control electrodes. At times a few of the control electrodes were open; however, these problems have been remedied. Arcing from the RF electrodes was often seen at RF peak voltages above 350V. This arcing was seen at the corners of the RF wirebond pad and across the gap between RF and control electrodes or ground. We did cycle some of the traps several times without incident; however, there has been no systematic study of

reliability with repeated cycling in and out of the vacuum chamber or cryostat.

Backside loading has been a standard feature on all the SMIT II traps. There have been no major problems with ion loading. A recent new Ca oven allows loading at a rate of a few Hz with a vacuum pressure that is in the low  $10^{-10}$  torr range. At this pressure one does not have to turn off the oven in order to obtain long ion lifetimes ( $\sim$ hours with laser cooling). No coatings of the electrodes on the front surface of the trap due to loading have been noted.

Laser access to the trapping locations has been only across the trap surface to date. A new generation of traps will allow laser beam access through a long central slot. Ion measurements have been routine through the top window on the UHV chamber using an excellent, inexpensive lens system designed at GTRI.

The number of trapping zones in the SMIT II traps is now at 22 (including the loading zone). We have loaded 5 ions in one trapping zone. There has not been a concerted effort to trap a larger number of ions. Trapping many ions in long chains of equally spaced ions should be possible, using the arrangements developed by the Monroe group. These long ion chains require an anharmonic trapping well that is easily obtained in the present SMIT II traps.

Crosstalk between neighboring trapping regions is amazingly low in the surface traps designed and tested under SMIT II. A simulation demonstrating low crosstalk for a Gen II SMIT II trap is shown in Figure B.1.

A trap is first formed using three contiguous pairs of electrodes (electrodes 17-22 in Figure B.2) along a linear portion of the trap. This results in a very small  $\beta$  value (see [15]), where  $\beta$  is a measure of the amount of micromotion at the trapping position. For example, when  $\beta = 1$ , the micromotion induced Doppler shifts are sufficient to noticeably broaden the ion fluorescence spectrum and reduce the laser cooling efficiency. The value for a single optimized three electrode trap is shown as the yellow triangle in Figure B.1. The low  $\beta$  value of 0.14 is limited by a lower bound associated with the numerical accuracy of the simulation program.

Next we consider the case where a second ion is trapped in a nearby potential formed by the next series of three electrodes (Zone 2 in Figure B.2) in the linear chain. We assume that this three electrode combination uses the same trapping voltages as used for the initial trap. After turning on the voltages to this second trap, we will need to reset the voltages on the first trap in order to remove micromotion induced by adding the voltages for the second trap. How much will we need to change the voltages in the first trap so that micromotion is again minimized? The results of the simulation for this case is shown by the red points and curve in Figure B.1. Without changing the voltages on the first trap the  $\beta$  value increases to 0.34, slightly in excess of the tolerable level.

Now we change the outer electrode voltages on one rail of the initial trap to compensate for this increased micromotion. A decrease in the compensating voltage used on electrodes 17 and 21 (their voltages are the same by design) from 1.73 to 1.55 V restores the low  $\beta$  value, a change of 10%. The control electrode widths in the Gen II trap are 80  $\mu\text{m}$ , so that the distance between trapping position in this case is 240  $\mu\text{m}$ . Moving the neighboring trap position one further electrode away (using electrodes 25-30 to define the trapping zone) from the initial trap results in the gray points and curve in Figure B.1. Now the fraction change in compensating voltage is less than 3% for an ion separation of 320  $\mu\text{m}$ . Although we have not compared the simulation to experiment, the agreement between simulation and

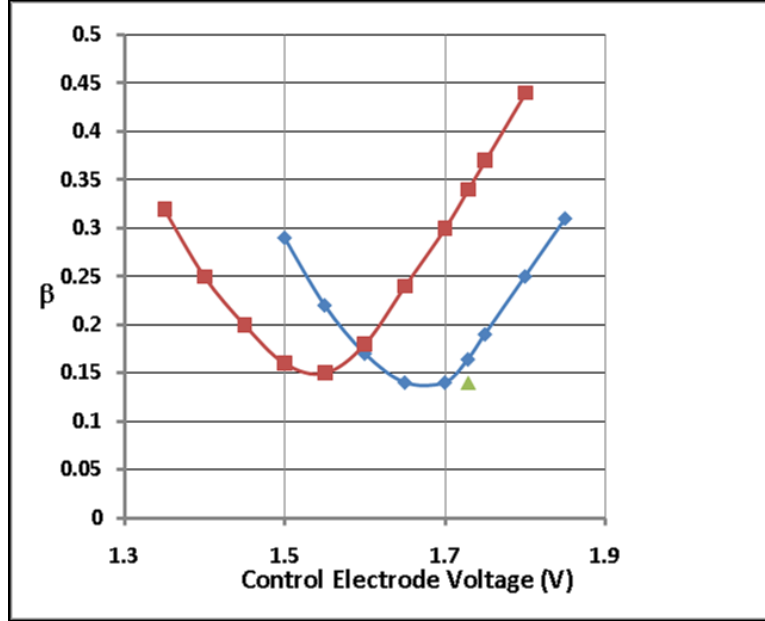


Figure B.1: Beta as a function of a control electrode voltage for the linear section a Gen II SMIT II trap. The green triangle is the low beta value obtained by an optimization algorithm. The value of beta has a lower limit of 0.14 due to numerical limits. The trapping voltages are for a series of three electrode pairs. These voltages are then applied to the neighboring three electrodes as if one were trapping an ion in a well next to the initial well. The resulting beta values as a function of compensating voltage on two electrodes of the initial trap are shown by the red points and curve (a guide to the eye). If the neighboring trap is moved one further electrode width away from the initial trap, very small compensating voltages ( $<3\%$ ) are required to restore the initial small beta value as shown by the blue points and curve.

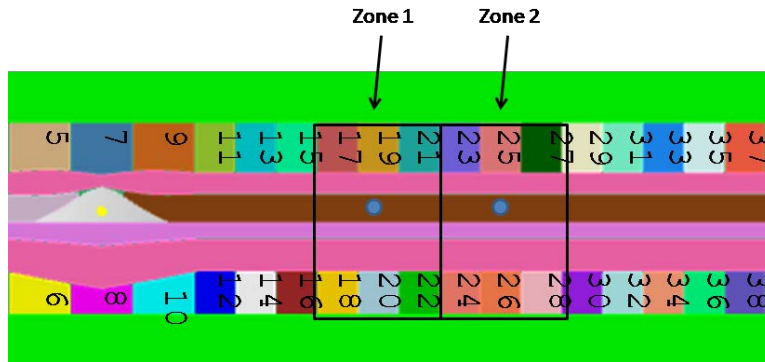


Figure B.2: The Gen II trap was used for a crosstalk study. An ion was trapped in Zone 1. When a second ion was trapped in Zone 2, the influence on the second ion was measured and compensated by adjusting the voltage on electrodes 17 and 21 (which are the same, by design).

experiment has been extremely good in SMIT II. It appears that we have essentially met our goal for crosstalk during SMIT II.

The backside loading for the SMIT II traps has been reliable with loading rates typically for 0.1 to 5 Hz. The loading depends in part on the Ca oven. Our oven design has evolved so that the chamber pressure remains in the  $10^{-11}$  torr range during loading.

The measured secular frequencies in all trap sections that have been studied agree to within 3% of the simulated frequencies for the applied voltages, assuming one is careful to eliminate other charged electrodes or grounds in the chamber. A screen a few mm above the trap is essential to eliminate the effect of charging of the window above the trap. Any floating electrodes tend to charge and shift the voltages required to give a specified secular frequency.

The laser cooled and dark ion lifetimes achieved during SMIT II were much longer than those obtained during SMIT I. The cooled lifetimes at room temperature were in the range of several hours with the oven turned off at pressures in the low  $10^{-11}$  torr range. Dark lifetimes under the same vacuum conditions were typically several minutes. It is not clear why the SMIT II times are so much improved. The fabricated oxides used for SMIT II are "dirtier" but have less stress than those used in SMIT I traps. This or other reasons may have reduced local out-gassing in the SMIT II traps. These surface trap lifetimes are less than multi-level traps used in the field. It is possible that the lower trapping depths for surface traps contribute to these reduced lifetimes.

The GTRI laboratory instrumentation did not progress far enough to make accurate ion heating measurements at room temperature, making the heating measurement goals out of reach during the program period. The laboratory will soon be able to make these measurements. They are planned for early 2011. The ion heating rate at cryogenic temperatures was measured at MIT to be 58 quanta/sec, comparable to the lowest heating rates obtained with surface trap electrodes formed using gold or silver electrodes at MIT.

Rapid, accurate, simulations of complex trap architectures were clearly achieved during SMIT II. For example, the X cross design is possible only because of rapid and accurate simulations developed during SMIT II. The simulations predict voltages for required trap parameters that are found to be accurate experimentally to within a few percent.

No electrode charging has been observed for the SMIT II traps during months of operation. This includes charging from the laser beams that skim the surface. Charging effects would result in shifts in the electrode voltages that are required to minimize micromotion or achieve a specified secular frequency. None of this variability has been observed while the laser beams are at or near the ion height above the trap surface. We have not systematically checked for charging by focusing the lasers at various frequencies directly onto the electrodes at locations near the trapping location. This is an interesting area to explore in the future.

There was not sufficient time during SMIT II to perform gate operations and optimize coherence times.

There was a demonstration of ion transport during SMIT II. However, there was not time to measure heating during ion transport or optimize the transport voltages and time sequences for minimum ion heating. This is a very interesting area for future exploration since the genetic algorithms developed during SMIT II can be used with heating rate constraints in order to minimize heating during transport. One could also explore the possibility that control pulse shaping can be used to re-cool.

Although it is clear that on-chip RF filtering on the control electrodes is required for good trap operation and comparison between measured and simulated trap parameters; there was no systematic study of the degree of filtering achieved by the on-chip control electrode capacitive filters. The control electrode capacitances were made more nearly uniform and as large as possible for the later SMIT II trap generations.

We did not have time to study on-chip control electronics. This is still a very interesting area to explore in the future. Integrated optics

The integrated optics portion of SMIT was making good progress toward all of the goals as the program ended. These goals will be tested in the near future as chips with good micromirrors become available.

Table B.1: Tabulation of the initial SMIT II project trap metrics and goals by year for the first two years. The values of various metrics achieved during SMIT I are entered in red. The numerical values achieved during SMIT II are listed in blue. The objectives that were achieved are in green boxes. The goals that were not addressed or only partially achieved are in orange (both boxes and text).

Objective	Figure(s) of merit	Current state-of-the-art	Goals Year 1	Goals Year 2
<b>Fabrication:</b> Optimize Packaging	Ease of trap start up (install+bake out); local pressure	Rm T $\sim$ 1 wk Cryogenic $\sim$ 1 day Local pressure $10^{-11}$ torr ( $10^{-11}$ torr)	Rm T $\sim$ 1 wk 1 wk Cryogenic $\sim$ 1 day 1 day Local pressure $10^{-11}$ torr ( $10^{-11}$ torr)	Rm T $\sim$ 1 wk 1 wk Cryogenic $\sim$ 1 day 1 day Local pressure $10^{-11}$ torr ( $10^{-11}$ torr)
<b>Fabrication:</b> Fabricate ion trap chips (ITCs) with variable materials	Designed metal coatings of ITC electrodes	Deposited Al Deposited Ag (annealed) electroplated Au	Deposited Al with W over-layer Electroplated Au	Depends on Year 1 results

Objective	Figure(s) of merit	Current state-of-the-art	Goals Year 1	Goals Year 2
<b>Fabrication:</b> Fabricate ITCs with reliable electrical characteristics	Voltage breakdown/shorts of RF and DC electrodes; Q of trap	Rm T > 10 cycles with no shorts/breakdown Cryogenic ~ 20 (6) cycles with no shorts or delamination Q ~ 200 (80) RF > 400 (400) V peak	Rm T > 20 cycles with no shorts/breakdown Cryogenic > 20 cycles with no shorts or delamination Q ~ 200 RF > 400 (300) V peak	Rm T > 20 cycles with no shorts/breakdown Cryogenic > 20 cycles with no shorts or delamination Q ~ 200 RF > 400 (300) V peak Traps have far fewer shorts
<b>Fabrication:</b> Optimize trap design for ion loading, cooling, processing, read-out	Optical access, trap depth	Backside loading for surface traps, In plane and out of plane optical access, Single location readout Trap depth > 0.025 eV	Backside loading for surface traps, In plane and out of plane optical access, Single location readout Trap depth > 0.025 eV	Backside loading for surface traps, In plane and out of plane optical access, Single location readout Trap depth > 0.025 eV
<b>Fabrication:</b> Trap complexity	Number of trap zones and number of ions	Trap zones ~ 20 Trapped ions ~ 8 (straight line)	Trap zones ~ 30(20) Trapped ions ~ 8 (straight line)	Trap zones ~ 40(34) Trapped ions ~ 8 – 10 (5)
<b>Fabrication:</b> Cross talk	Degree of cross talk between electrodes (potentials), cross talk between ions	Not well measured	< 10% (< 10%)	< 3% (< 3%)

Objective	Figure(s) of merit	Current state-of-the-art	Goals Year 1	Goals Year 2
<b>Diagnostics:</b> Facile ion loading	Time between loading events (ions/s in Hz); presence of thru-hole	$\sim 0.1$ Hz (macro-trap); $\sim 0.01$ Hz (micro-trap); robust backside loading slot (GTRI)	Demonstrate 0.1 Hz load rate with backside loading (0.1 - 0.5 Hz)	
<b>Diagnostics:</b> Trap reproducibility	Reproducible control voltages on multiple traps	Note well measured	Measure trap potential reproducibility for constant secular frequency in multi-section linear and junction traps	
<b>Diagnostics:</b> Minimize ion loss (while cooled) at fixed trap location	Ion lifetime(s) while Doppler cooled	Rm T $\sim 10$ (1) min (chip traps) Cryogenic $\sim$ hrs (no trapping during first year)	Rm T $> 10$ ( $\sim 5$ hours) Cryogenic $\sim$ ( $\sim$ hrs) Demonstrate Doppler cooling with asymmetric RF electrodes while minimizing the micromotion	
<b>Diagnostics:</b> Minimize ion heating	Ion heating rate (quanta/s)	$\sim 3$ -10 (7) quanta/ms @ Rm T $\sim 1$ -10 (220) quanta/s (cryogenic) (no trapping during first year)	Perform ion heating measurement using Ca at GTRI, $\sim 3$ quanta/ms Rm T $\sim 10$ quanta/s cryogenic ( $\sim 58$ quanta/s)	



Objective	Figure(s) of merit	Current state-of-the-art	Goals Year 1	Goals Year 2
<b>Diagnostics:</b> Optimize trap design for ion cooling, processing, read-out	Ion secular frequency control and frequency range	<1% control accuracy 1 - 10 MHz freq. range	Simulate ion secular frequency control and range with minimum of micromotion, Simulate ion secular frequencies during junction transport	Simulate ion frequencies, <1% control accuracy 1 - 10 MHz freq. range, linear and junction traps
<b>Diagnostics:</b> Optimize trap design for ion cooling, processing, read-out	Trap electrode and oxide charging relative to applied potentials	< 1% relative to applied potentials (depends on the light wavelength when due to photon charging). Charging effects were measured in SMIT I at NIST with Mg ions	Simulate charging effects from loading zone and laser beam charging of oxides	Demonstrate complex trap with < 1% charging effects
<b>Diagnostics:</b> Optimize trap design for ion cooling, processing, read-out	Coherence time	15 s (NIST)	Optimize coherence time with simulations measurements at NIST and UMD	

Objective	Figure(s) of merit	Current state-of-the-art	Goals Year 1	Goals Year 2
<b>Diagnostics:</b> Demonstrate linear transport of ions	Ion transport rate, Ion survival rate Ion heating and energy gain	Rate $\sim 2^4$ mm/s for straight sections, Ion loss $\sim 0\%$ , Ion heating $< 1$ quanta/s	Measure linear zone-to-zone transfer survival rate	$< 10^{-4}$ loss rate, measure acquired motional quanta ( $10^4$ ) ion transports without loss
<b>Diagnostics:</b> Demonstrate ion transport through junction	Ion survival rate Ion energy gain, Ion cooling required	$\sim 10^3$ loss rate (Michigan T-trap), Very large energy gains (motion over 100s of microns)	Simulate ion transport energy gains and explore kinetic damping	Demonstrate kinetic ion energy extraction
<b>Diagnostics:</b> Demonstrate single and two qubit gates	Gate fidelity	99.3% (Innsbruck, 2 qubit gate)		Demonstrate kinetic ion energy extraction
<b>Electronics:</b> Integrate passive filter components on ITC	Minimize RF pick-up on DC control electrodes	$< 10\%$ pickup in SMIT I traps, $< 1\%$ with external filtering	Simulate and demonstrate $< 1\%$ pick-up with on chip filters	

Objective	Figure(s) of merit	Current state-of-the-art	Goals Year 1	Goals Year 2
<b>Diagnostics:</b> Specify and integrate commercial multiplexing electronics and/or DAC chip for trap electrode control	1. Degree of multiplexing, 2. Integration of electronics with ion chip, 3. Speed, precision, accuracy, and noise floor	No multiplexing No measurements of noise from nearby integrated electronics	Measure noise from DAC multiplexer and/or DAC chips, design noise filters	Design integrated multi-chip electronics near ion chip, Go/no-go decision for integrating control electronics

Table B.2: Summary of integrated optics metrics and goals.

Goal	Metric	Present Value	Project Goal	Year	Comments
A	# of Measurement locations for high speed detection	1	8	2	
A	Measurement time	$\sim 200 \mu s$	$< 100 \mu s$	2	
A	Measurement fidelity	$> 99\%$	$> 99\%$	2	
A	Field-of-view	0.5 mm	$> 3\text{mm}$	2	
B	Coating reflectance on micromirrors	$\sim 90\%$	99.9%	1	Single wavelength between 300-400 nm
B	curved mirror surface roughness	N/A	$< 1 \text{ nm RMS}$	1	
B	Cavity mode beam waist	$\sim 54 \mu m$	$< 2 \mu m$	2	Mundt et al., PRL 89, 103001 (2002)
B	Cooperativity factor	$< 0.1$	$> 2$	3	<i>ibid</i>
B	Atom-photon coupling/atomic decay ( $g/\Gamma$ )	$< 0.05$	$> 10$	3	<i>ibid</i>
B	Collection efficiency of photon into fiber	$< 0.005$	$> 0.1$	4	Moehring et al, Nature 449, 68 (2007)
B	Integration of micro-cavity with ion trap chip	N/A	Demonstrate	4	
C	Multiplexed beam locations	1	$> 5$	2	
C	Intensity fluctuation-induced gate error (geometric phase gate)	3%	$< 0.5\%$	4	

# Appendix C

## Publications and reports

### C.1 Refereed journal publications

1. R. Noek, C. Knoernschild, J. Migacz, T. Kim, P. Maunz, T. Merrill, H. Hayden, C. S. Pai and J. Kim, “Multi-scale optics for enhanced light collection from a point source,” *Optics Letters* **35**, 2460 (2010).
2. T. H. Kim, P. F. Herskind, T. Kim, J. Kim and I. L. Chuang, “A surface electrode point Paul trap,” *Physical Review A* **82**, 043412 (2010).

### C.2 Conference proceedings and presentations

1. J. Kim, C. Knoernschild, C. Kim, J. Migacz, R. Noek, K. McKay, and F. Lu, “Optical MEMS technology for scalable quantum information processor”, Invited Talk, *Frontiers in Optics*, Rochester, NY, October 2008.
2. J. Kim, R.E. Slusher, C. Knoernschild, C.S. Pai, C. Kim and F. Lu, “Microsystems approach to quantum information processing in trapped ions”, Open Poster Session, *Solid State Sensors, Actuators and Microsystems Workshop*, Hilton Head Island, SC, June 2008.
3. R. Slusher, A. Ozakin, F. Shaikh, D. Denison, D. Faircloth, D. Landgren, and J. Wessenberg, “Geometric Compensation for Planar Ion Traps”, *2nd Workshop on Integrated Atomic Systems*, Seattle, WA, February 2009.
4. T. Kim, C. Knoernschild, J. Migacz, R. Noek, M. Silver and J. Kim, “Integrated optics approach to quantum information processing in trapped ions”, Poster Presentation, *2nd Integrated Atomic Systems Workshop*, Seattle, WA, February 2009.
5. T. Kim, J. Migacz, R. Noek, C. Knoernschild, M. Silver and J. Kim, “Integrated optics approach towards ion trap quantum computation”, Poster Presentation, *APS DAMOP Meeting*, Charlottesville, VA, May, 2009.

6. D.L. Faircloth, D.W. Landgren, E.J. Kuster, D.R. Denison, J.G. Maloney, R.T. Lee, "Implementation and Issues Concerning Higher-Order Moment Method Simulations on CUDA-Enabled GPU", Poster Presentation, *nVidia GPU Technology Conference*, San Jose, CA, October 2009.
7. R. Noek, J. Migacz, C. Knoernschild, T. Kim, and J. Kim, "Enhanced light collection from a point fluorescent source using multiscale optics", Contributed Talk, *Frontiers in Optics*, San Jose, CA, October 2009.
8. F. Shaikh, C. Doret, J. Amini, A. Ozakin, C. Volin, D. Denison, D. Faircloth, D. Landgren, C.S. Pai, H. Hayden, D. Geddis, K. Martin, A. Harter, and R. Slusher, "GTRI Microfabricated Ion Trap Program", Poster Presentation, *SQuInt*, Santa Fe, NM, February 2010.
9. T. Kim, P. Maunz, R. Noek, C. Knoernschild, E. Mount, and J. Kim, "Integration of ion trap and optical cavity towards efficient entanglement generation between remote ions", Poster Presentation, *APS DAMOP Meeting*, Houston, TX, May 2010.
10. A. Ozakin, F. Shaikh, D. Faircloth, C. Volin, J. Amini, C. Doret, D. Denison, D. Landgren, D. Geddis, C.S. Pai, H. Hayden, A. Harter, and R. Slusher, "Ion Stability in Asymmetric Surface Electrode Ion Traps", Poster Presentation, *APS DAMOP Meeting*, Houston, TX, May 2010.
11. F. Shaikh, C. Doret, J. Amini, A. Ozakin, C. Volin, D. Denison, D. Faircloth, D. Landgren, C.S. Pai, H. Hayden, D. Geddis, K. Martin, A. Harter, and R. Slusher, "GTRI Microfabricated Ion Trap Program", Poster Presentation, *APS DAMOP Meeting*, Houston, TX, May 2010.
12. R. Noek, C. Knoernschild, J. Migacz, T. Kim, P. Maunz, J. Kim, T. Merrill, H. Hayden and C.S. Pai, "Enhanced light collection from a point source using a micro-mirror for application in trapped ion quantum information processing", Contributed Talk, *APS DAMOP Meeting*, Houston, TX May 2010.
13. J. Kim, "Modular Universal Scalable Ion-Trap Quantum Computer (MUSIQ): Engineering a quantum computer", Invited Talk, *Summer Meeting of the Optical Society of Korea*, Busan, Korea, July 2010.
14. J. Kim, P. Maunz, T. Kim, J. Hussman, R. Noek, A. Mehta, and C. Monroe, "Modular Universal Scalable Ion-Trap Quantum Computer (MUSIQ)", Contributed Talk, *Quantum Communication, Measurement and Computation (QCMC)*, Brisbane, Australia, July 2010.

# Bibliography

- [1] D. Leibbrandt, J. Labaziewicz, R. Clark, I. Chuang, R. Epstein, C. Ospelkaus, J. Wesenberg, J. Bollinger, D. Leibfried, D. Wineland, D. Stick, J. Sterk, C. Monroe, C. Pai, Y. Low, R. Frahm, and R. Slusher, “Demonstration of a scalable, multiplexed ion trap for quantum information processing,” *Quant. Inf. Comput.*, vol. 9, no. 901, 2009.
- [2] R. Blakestad, C. Ospelkaus, A. VanDevender, J. Amini, J. Britton, D. Leibfried, and D. Wineland, “High-fidelity transport of trapped-ion qubits through an x-junction trap array,” *Phys. Rev. Lett.*, vol. 102, no. 153002, 2009.
- [3] M. Rowe, A. Ben-Kish, B. Demarco, D. Leibfried, V. Meyer, J. Beall, J. Britton, J. W. Itano, B. Jelenkovic, C. Langer, T. Rosenband, and D. Wineland, “Transport of quantum states and separation of ions in a dual rf ion trap,” *Quant. Inf. Comput.*, vol. 2, no. 257, 2002.
- [4] W. Hensinger, S. Olmschenk, D. Stick, D. Hucul, M. Yeo, M. Acton, L. Deslauriers, C. Monroe, and J. Rabchuk, “T-junction ion trap array for two-dimensional ion shuttling, storage, and manipulation,” *Appl. Phys. Lett.*, vol. 88, no. 034101, 2006.
- [5] J. Chiaverini, R. Blakestad, J. Britton, J. Jost, C. Langer, D. Leibfried, R. Ozeri, and D. Wineland, “Surface-electrode architecture for ion-trap quantum information processing,” *Quant. Inf. Comput.*, vol. 5, no. 419, 2005.
- [6] S. Seidelin, J. Chiaverini, R. Reichle, J. Bollinger, D. Leibfried, J. Britton, J. Wesenberg, R. Blakestad, R. Epstein, D. Hume, W. Itano, J. Jost, C. Langer, R. Ozeri, N. Shiga, and D. Wineland, “A microfabricated surface-electrode ion trap for scalable quantum information processing,” *Phys. Rev. Lett.*, vol. 96, no. 2115, 2006.
- [7] J. Amini, H. Uys, J. Wesenberg, S. Seidelin, J. Britton, J. Bollinger, D. Leibfried, C. Ospelkaus, A. Vandevender, and D. Wineland, “Toward scalable ion traps for quantum information processing,” *New Jour. of Phys.*, vol. 12, no. 033031, 2010.
- [8] J. Wesenberg, “Electrostatics of surface-electrode ion traps,” *Physical Review A*, vol. 78, no. 6, p. 63410, 2008.
- [9] M. Oliveira and J. Miranda, “Biot-Savart-like law in electrostatics,” *European Journal of Physics*, vol. 22, no. 1, pp. 31–38, 2001.
- [10] M. House, “Analytic model for electrostatic fields in surface-electrode ion traps,” *Physical Review A*, vol. 78, no. 3, p. 33402, 2008.

- [11] R. Churchill, J. Brown, and R. Verhey, *Complex variables and applications*. New York: McGraw-Hill, Inc., 1960.
- [12] J. H. Wesenberg, “Ideal intersections for radio-frequency trap networks,” *Phys. Rev. A*, vol. 79, p. 013416, Jan 2009.
- [13] R. Reichle, S. Seidelin, J. Chiaverini, R. Blakestad, J. Bollinger, J. Britton, D. Epstein, D. Hume, W. M. Itano, J. Jost, E. Knill, C. Langer, D. Leibfried, R. Ozeri, J. Wesenberg, and D. J. Wineland, “Networking surface electrode ion traps for large-scale QIP,” in *Workshop on Trapped Ion Quantum Computing*, vol. Posters: Trap Technology, (Boulder, CO), p. T01, Feb. 2006.
- [14] G. R. Brady, A. R. Ellis, D. L. Moehring, D. Stick, C. Highstrete, K. M. Fortier, M. G. Blain, R. A. Haltli, A. A. Cruz-Cabrera, R. D. Briggs, J. R. Wendt, T. R. Carter, S. Samora, and S. A. Kemme, “Integration of fluorescence collection optics with a microfabricated surface electrode ion trap,” *ArXiv e-prints*, Aug. 2010.
- [15] D. Berkeland, J. Miller, J. Bergquist, W. Itano, and D. Wineland, “Minimization of ion micromotion in a paul trap,” *Jour. App. Phys.*, vol. 83, no. 5025, 1998.
- [16] R. C. Eberhart and J. Kennedy, “A new optimizer using particle swarm theory,” in *Proceedings of the Sixth International Symposium on Micromachine and Human Science*, pp. 39–43, 1995.
- [17] S. Olmschenck, K. Younge, D. Moehring, D. Matsukevich, P. Maunz, and C. Monroe, “Manipulation and detection of a trapped  $\text{yb}^+$  hyperfine qubit,” *Phys. Rev. A.*, vol. 76, no. 052314, 2007.
- [18] E. Abraham and E. Cornell, “Teflon feedthrough for coupling optical fibers into ultra-high vacuum systems,” *Applied Optics*, vol. 37, no. 172, 1998.
- [19] C. Knoernschild, X. Zhang, L. Isenhower, A. Gill, F. Lu, M. Saffman, and J. Kim, “Independent individual addressing of multiple neutral atom qubits with a micromirror-based beam steering system,” *Appl. Phys. Lett.*, vol. 97, no. 134101, 2010.
- [20] V. Arnold, *Mathematical methods of classical mechanics*. Springer, 1989.
- [21] A. Seyranian and A. Mailybaev, *Multiparameter stability theory with mechanical applications*. World Scientific Pub Co Inc, 2003.
- [22] J. Hansen, “Stability diagrams for coupled Mathieu-equations,” *Archive of Applied Mechanics*, vol. 55, no. 6, pp. 463–473, 1985.
- [23] A. Nayfeh, *Perturbation methods*. Wiley Online Library, 1973.
- [24] A. Nayfeh and D. Mook, *Nonlinear oscillations*. Wiley Online Library, 1979.
- [25] J. Kevorkian and J. Cole, *Multiple scale and singular perturbation methods*. Springer Verlag, 1996.